Application of a Thermal Desorption-Differential Mobility Analyzer (TD-DMA) coupled to a nitrate chemical ionization-atmospheric pressure interface-time-of-flight (CI-APi-TOF) for measuring nanoparticles at the CLOUD Chamber at CERN

Dissertation
zur Erlangung des Doktorgrades
der Naturwissenschaften

vorgelegt beim Fachbereich 11 Geowissenschaften / Geographie
der Johann Wolfgang Goethe - Universität
in Frankfurt am Main

DISSERTATION
von

Lucía Caudillo Murillo
aus Mexiko-Stadt

Frankfurt am Main, 2022

vom Fachbereich 11 Geowissenschaften / Geographie der
Johann Wolfgang Goethe - Universität als Dissertation angenommen.

Dekan: Prof. Dr. Jürgen Runge

Gutachter: Prof. Dr. Joachim Curtius

Associate professor Katrianne Lehtipalo

Datum der Disputation:

Table of Content

Abstract

Atmospheric particles play an important role in the radiative balance of the Earth, as well as they affect human health and air quality. Hence, the chemical characterization constitutes a crucial task to determinate their properties, sources and fate. Particularly, the analysis of nanoparticles (d<100 nm) represents an analytical challenge, since these particles are abundant in number but have very little mass.

This accumulative thesis focuses on the chemical characterization of nanoparticles, performed in both laboratory and field studies. Here, I present four manuscripts, two of which are my main project as a lead author.

The first manuscript (Caudillo et al., 2021) focuses on the gas and the particle phase originated from biogenic precursor gases (α-pinene and isoprene). The experiments were performed in the CLOUD chamber at CERN to simulate pure biogenic new particle formation. Both gas and particle phases are measured with a nitrate CI-APi-TOF mass spectrometer, while the TD-DMA is coupled to it for particle-phase measurements, this setup allows a direct comparison as both measurements use the identical chemical ionization and detector. This study demonstrates the suitability of the TD-DMA for measuring newly formed nanoparticles and it confirms that isoprene suppresses new particle formation but contributes to the growth of newly formed particles.

The second manuscript (Caudillo et al., 2022) presents an intercomparison of four different techniques (including the TD-DMA) for measuring the chemical composition of SOA nanoparticles. The measurements were conducted in the CLOUD chamber. The intercomparison was done by contrasting the observed chemical composition, the calculated volatility, and the thermal desorption behavior (for the thermal desorption techniques). The methods generally agreed on the most important compounds that are found in the nanoparticles. However, they did see different parts of the organic spectrum. Potential explanations for these differences are suggested.

The third manuscript (Ungeheuer al., 2022) presents both laboratory and ambient measurements to investigate the ability of lubricant oil to form new particles. These new particles are an important source of ultrafine particles in the areas nearby large airports. The ambient measurements were performed downwind of Frankfurt International Airport, and it was found that the fraction of lubricant oil is largest in the smallest particles. In the laboratory, the main finding was that evaporated lubricant oil nucleates and forms new particles rapidly. The results suggest that nucleation of lubricant oil and subsequent particle growth can occur in the cooling exhaust plumes of aircraft-turbofans.

The fourth manuscript (Wang et al., 2022) is a new particle formation study in the CLOUD chamber at CERN. This study shows that nitric acid, sulfuric acid, and ammonia interact synergistically and rapidly form particles under upper free tropospheric conditions. These particles can grow by condensation (driven by the availability of ammonia) up to CCN sizes and INP particles. The ability of these particles to act as a CCN and INP was also investigated and it was found to be as efficient as for desert dust. This mechanism constitutes an important finding and it can account for previous observations of high concentrations of ammonia and ammonium nitrate over the Asia monsoon region.

1. Aerosols

1.1 Why do we study aerosols?

An aerosol is generally defined as a suspension of liquid or solid particles in a gas, with particle diameters in the range of 10^{-9} to 10^{-4} m (~ 0.001 to 100 μm). Where the lower limit are molecular clusters and the upper limit are particles that can rapidly sediment. Often the terms aerosol, aerosol particles, and particles are used without distinction, although strictly speaking the term "aerosol" is defined as the whole suspension of particles and gas; "aerosol particles" are the particles that float in the gas, and the term "particles" is not limited to an aerosol, it could, for example, also describe dust particles that have settled to a surface, etc. Hinds (1999).

Aerosol particles are important for many reasons, here, are listed three important ones:

1. Climate influence.

   The effects of aerosols on the climate can be direct or indirect with respect to radiative forcing. The direct effects are related to scattering and absorption of radiation (solar and terrestrial) by aerosols. The indirect effect refers to the modification of microphysical properties of clouds due to aerosol particles.

   For example, within the direct effects, particles such as sulfates, nitrates and organic carbon can scatter radiation, therefore they have negative radiative forcing which has a cooling effect, while black carbon particles lead to the opposite effect, they can absorb both solar and terrestrial radiation which leads to a positive radiative forcing, thus they have a warming effect (Ramanathan et al., 2001).

   On the other hand, aerosols can act as Cloud Condensation Nuclei (CCN) or Ice Nucleating Particles (INP). Then, by acting as a CCN or INP, aerosols can modify the microphysical properties of clouds and have an influence on precipitation, by a) Twomey effect: when the CCN concentration increases, the optical depth of the cloud increases and therefore also the albedo increases (Twomey, 1974), b) Albrecht effect: in polluted environments, more droplets with smaller size are formed, which increases the life time of the cloud and therefore, increases the solar radiation reflected from clouds, as well as, modifies the precipitation efficiency (Albrecht, 1989).

   Nowadays one of the biggest uncertainties is the exact radiative forcing of clouds. Current research focuses on better estimates of this effect to predict how the temperature will change for future climate projections.

2. Health effects.

At the present time, it is very well documented and supported by the World Health Organization (WHO) that there is a clear and quantitative relationship between exposure to high concentrations of particles PM_{10} and $PM_{2.5}$ ($d \leq 100$ µm and $d \leq 2.5$ µm, respectively) and an increase mortality or morbidity at both short and long term.

Nevertheless, ultrafine particles (UFP, $d < 100$ nm) are not officially (by WHO) recognized as hazardous for health to the same extent as PM_{10} and $P_{2.5}$. Even though, several epidemiological studies have suggested a link between exposition to UFP and respiratory and cardiovascular problems. Nowadays, WHO has admitted that the number of studies on health effects of UFP has increased, and suggested a suite of good practice advices in order to make the studies comparable in terms of UFP size ranges and other exposure metrics.

UFP particles are an important concern because of their size. The smaller the particles the easier they can penetrate the membranes of the respiratory tract and the alveoli. There, they can either enter the blood circulation or they can even be transported to the brain via the olfactory system.

Schraufnagel (2020), have reported that UFP compared to fine particles ($PM_{2.5}$) cause more pulmonary inflammation and are retained longer in the lung. Their large surface that can potentially increase their toxicity. It has also been reported that depending on the chemical composition and other properties, UFP can cause several diseases such as, bronchial asthma, Chronic Obstructive Pulmonary Disease (COPD), lung fibrosis, and lung cancer (Leikauf et al., 2020), the suggested mechanisms are via oxidative cellular damage, including innate immunity, adaptive immunity, and reactive oxygen species.

Secondary organic aerosols (SOA) constitute an important fraction of UFP. Cardiopulmonary health implications resulting from exposure to SOA have been reported by Tuet et al. (2017). In addition, it was found that SOA may produce oxidative stress in the bronchoalveolar lavage fluid of the mice (Niu et al., 2020), this indicates that SOA particles may trigger acute lung injury in humans, and it potentially can cause further respiratory disease. Pye et al. (2021) showed that SOA is strongly associated with county-level cardiorespiratory death rates in the U.S. independently of the total $PM_{2.5}$ mass.

On the other hand, airport related particles may have implications to the human health. Habre et al. (2018) demonstrated an increased acute systemic inflammation following exposure to UFP from aircraft landing and takeoff activity in the Los Angeles airport. However, Møller et al. (2020) presents a long-term study of the UFP exposure of airport workers and reported that there is no association between outdoor occupational exposure to UFP and ischemic heart disease, and cerebrovascular disease.

Extensive reviews (Ohlwein et al., 2019; HEI, 2013) have assessed studies that present epidemiological evidence related to UFP.

3. Air quality.

In megacities (cities with a population of more than 10 million people) the formation of particles has several sources and pathways. In this process, several parameters are involved, for example: emissions, meteorological conditions, radiative transfer, atmospheric boundary layer depth, topography, chemistry and dynamics of aerosols and precursors.

One parameter related to particles and air quality is visibility. Visibility is defined as the attenuation of light due to absorption and scattering as it passes through a medium. Thus, the presence of particles in the atmosphere reduces the visibility, since they can scatter or absorb the light before it reaches the observer.

In terms of atmospheric particles, air quality standards establish limit values of $PM_{2.5}$ and PM_{10}. These values are concentrations in μgm^{-3} that are based on scientific knowledge in order to avoid, prevent or reduce harmful effects on human health, in a given period (24-hour and annual means). Therefore, especially in cities, $PM_{2.5}$ and PM_{10} are usually monitored. However, very little monitoring is made on UFP due to several reasons: a) there is no existing legislation on limits on UFP concentrations as it exists for $PM_{2.5}$ and PM_{10}, b) usually the monitoring of UFP involves sophisticated instrumentation that are costly.

Besides the health effects (briefly described previously), there have been several studies highlighting the importance of monitoring UFP in megacities. Kulmala et al. (2021) have suggested that in Chinese megacities, atmospheric gas-to-particle conversion is a dominant contributor to haze, since numerous new particle formation events were followed by a haze episode. Huang et al. (2014) investigated the chemical nature and sources of particulate matter at urban locations in China and found that haze pollution events were driven to a large extent by SOA formation, which contributed significantly to $PM_{2.5}$ and to organic aerosol.

Several efforts have been made in order to improve our understanding of the effects of aerosols (especially UFP) on air quality and most likely, in the future, UFP will constitute an important metric within the air quality standards.

1.2 Where do the aerosols come from?

Aerosols originate from primary and secondary sources. Primary particles are directly emitted to the atmosphere as liquids or solids. For example, some primary sources are: biomass burning, incomplete combustion of fossil fuels, volcanic eruptions, wind-driven or traffic-related suspension of road, soil, and mineral dust, sea salt, as well as, biological materials (plant fragments, microorganisms, pollen, etc.) (Pöschl, 2005).

Secondary particles, on the other hand, are not directly emitted as particles, they are formed by gas-to-particle conversion in the atmosphere, under a process called New Particle Formation (NPF). In this process, certain precursor gases undergo chemical reactions that produce condensable vapors. These vapors then have the ability to nucleate, in other words, there is a phase transition (from gas to liquid/solid). NPF produces very small particles that have the potential for further growth.

There are several well-known chemical systems that produce secondary particles. For example: binary nucleation (sulfuric acid-water), ternary nucleation (sulfuric acid-ammonia-water), or sulfuric acid-dimethylamine-water.

This work is specifically focused on the biogenic nucleation, that means, Secondary Organic Aerosol (SOA) which is produced via autoxidation of Volatile Organic Compounds (VOCs). Figure 1, shows a schematic of origin of SOA. VOCs as precursor gases are emitted to the atmosphere, then under certain chemical reactions (oxidation), condensable vapors are produced. These vapors can a) nucleate to form new particles, b) condense on other freshly nucleated pre-existing particles to help them grow and increase their probability to serve as a CCN, or c) condense on the background aerosol (d > 100 nm). It has been estimated that, approximately half of the global submicron atmospheric aerosols are produced by biogenic emissions of VOCs (Dickinson, 2012).

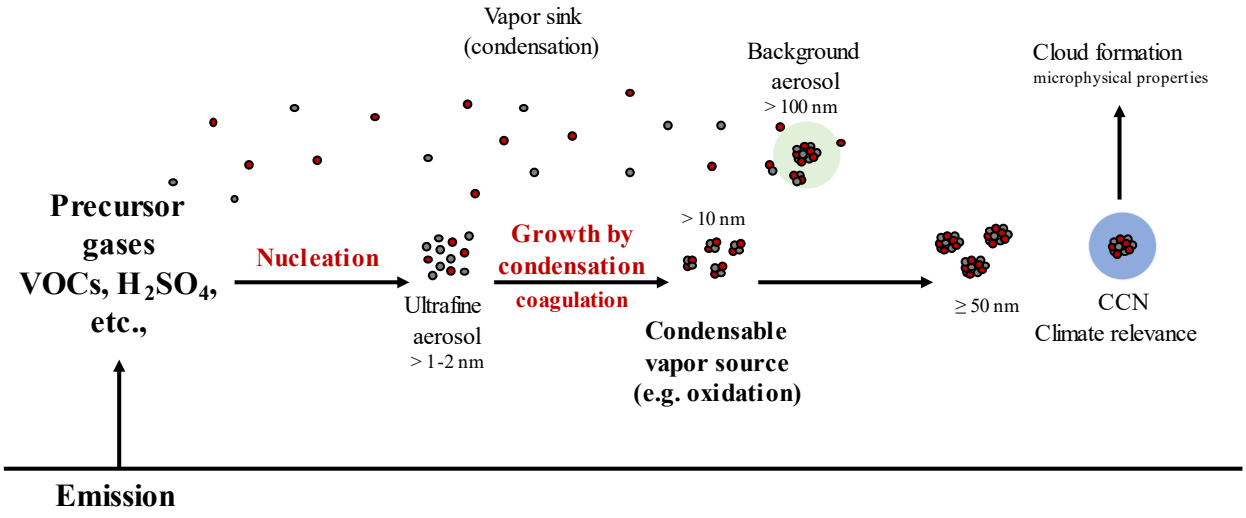

Figure 1. Origin of Secondary Organic Aerosol via New Particle Formation. Condensable vapors are produced by the oxidation of VOCs. These vapors can a) nucleate to form new particles, b) condense on pre-existing particles to help them grow up and increase their probability to serve as a CCN or c) condense on the background aerosol (d > 100 nm) and promote the loss of ultrafine particles. This figure has been taken from Riipinen et al. (2011) and modified.

1.3 Which aerosols do we study specifically?

One of the most important biogenic gases is α-pinene ($C_{10}H_{16}$), which is able to undergo chemical oxidation reactions and form a suite of organic compounds known as: Highly Oxygenated Organic Molecules (HOMs) (Bianchi et al., 2019). These compounds have the ability to nucleate on their own under atmospheric conditions and with no involvement of any other traces gases, such as sulfuric acid (Kirkby et al., 2016).

HOMs can be chemically described as a group of organic compounds that are formed by the gas phase autooxidation involving peroxy radicals (Ehn et al., 2014; Bianchi et al., 2019). Most importantly, they are formed under atmospheric conditions. These compounds have low vapor pressures and therefore play an important role in the formation of new particles due to condensation onto newly formed clusters and growing particles.

Another biogenic gas of our interest is isoprene (C_5H_8). Its emission is estimated between 500 - 600 Tg per year (Guenther et al., 2006; Sindelarova et al., 2014), and therefore it is one of the most important biogenic compounds with the highest emission around the world.

Both α-pinene and isoprene interact in a very interesting way. While α-pinene produces HOMs that can directly contribute to nucleation, isoprene suppresses the nucleation but it contributes to the growth of the newly formed particles. This means that the effect of isoprene in the α-pinene system leads to a) a decrease in the number concentration (Kiendler-Scharr et al., 2009), and b) to a decrease of the nucleation rates compared to the α-pinene system at similar conditions. This is attributed to the alteration of the peroxy radical termination reactions that inhibit the formation of molecules containing 19 to 20 carbon atoms, as reported by Heinritzi et al. (2020).

One of the most important properties that determines if a species can nucleate is volatility. Volatility describes how easily a substance vaporizes (at given temperature and pressure). It is more likely to find vapors with high volatility, while substances with low volatility tend to be abundant in solid or liquid form. In terms of NPF, the volatility can tell us the tendency of a vapor to condense onto a liquid or solid (to nucleate) particle, and therefore contribute to the formation of SOA. In particular, we use the volatility regimes defined in Donahue et al. (2012) and in Schervish and Donahue (2020): ultralow-volatility (ULVOC), extremely low-volatility (ELVOC), low-volatility (LVOC), semi-volatile (SVOC), and intermediate-volatility (IVOC) organic compounds. Figure 2 summarizes the processes involving α-pinene and isoprene, as well as, the influence of these processes on the formation of Secondary Organic Aerosols.

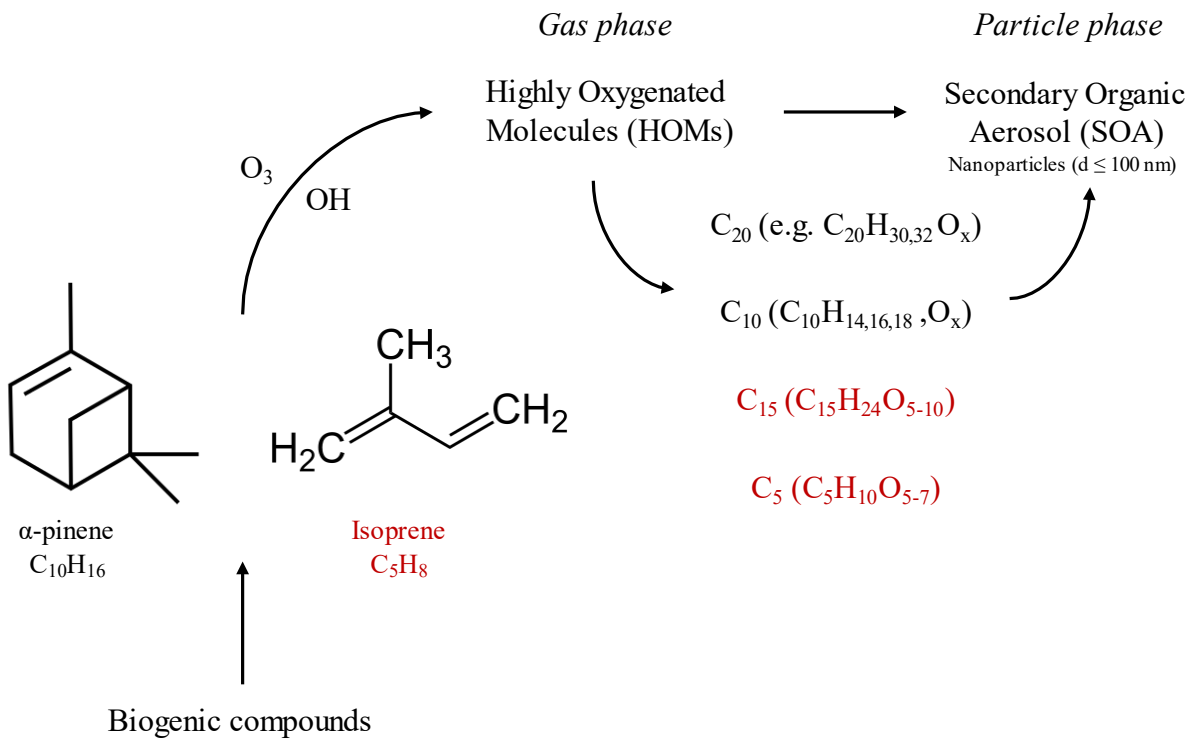

Figure 2. Scheme on the Biogenic New Particle Formation. Biogenic vapors such as α-pinene and isoprene are emitted to the atmosphere. In the atmosphere, they can undergo chemical oxidation reactions. These reactions produce Highly Oxygenated Organic Molecules (HOMs) that due to their low vapor pressure can directly participate on the formation of new particles. Within the suite of organic compounds that participate in this process, C_5 and C_{15} compounds are directly related to isoprene emissions while C_{10} and C_{20} to α-pinene emissions.

2. How does the TD-DMA work?

2.1 General description

The TD-DMA analyzes the chemical composition of nanoparticles in a semi-continuous mode of operation. Figure 3 shows the measurement setup, which together with the design and characterization were previously described by Wagner et al. (2018).

The TD-DMA coupled to a nitrate chemical ionization-atmospheric pressure interface-time-of-flight (CI-APi-TOF) performs the measurement in two steps: collection and evaporation. In the first step, the particles are directly sampled, charged, size selected, and collected on a filament. In the second step, the particles are evaporated, and conducted to the nitrate CI-APi-TOF for chemical composition analysis.

The following sections describe in more detail how the TD-DMA works, as well as what has been measured with it, what the results are and what we have learned from them.

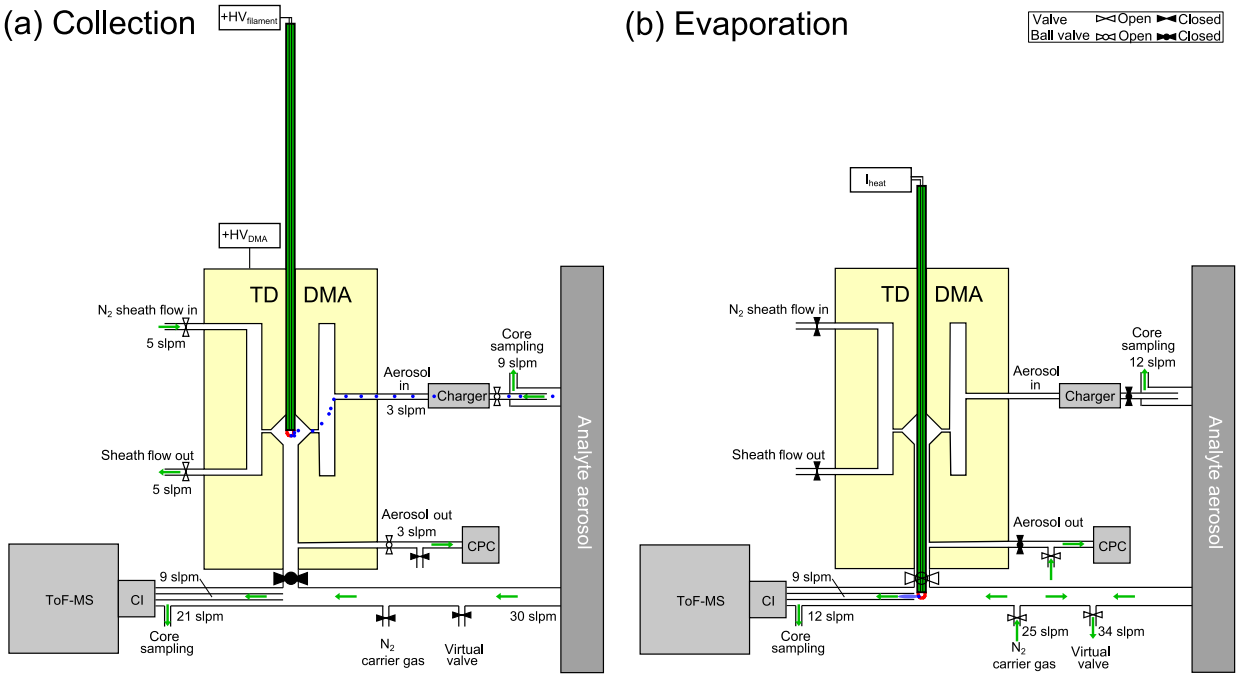

Figure 3. Measurement setup of the TD-DMA coupled to nitrate chemical ionization-atmospheric pressure interface-time-of-flight (CI-APi-TOF). The analysis is performed in two steps: (a) collection and (b) evaporation. In the first step, the particles are sampled, charged, size selected, and collected on a filament. In the second step, the collected particles are evaporated, and conducted through a N_2 carry flow to the nitrate CI-APi-TOF for chemical composition analysis. This figure has been taken from Wagner et al. (2018).

2.2 First step: Particle collection

2.2.1 Sampling and charging

The first step for performing the particle analysis is the sampling. The TD-DMA is directly connected to the CLOUD chamber by using a ½'' sampling port. The sampling inlet line (stainless-steel) has a core sampling system in which the particles are isokinetically sampled from the center of a large tube to reduce losses. Hence, an aerosol flow of approximately 3 lpm is sampled and conducted to a bipolar neutralizer. The use of a neutralizer is essential, because this technique requires the knowledge of the particle size (d_p). The particle size is related to the particle charge state (n_e) and the charge of the particles is necessary for the electrostatic separation to work.

Depending on the size the particle can be neutral, or it can carry one or more (positive or negative) charges. As the charge distribution is generally an unknown property, the main goal of the neutralizer is to bring the whole aerosol particle population into a known bipolar charge equilibrium. For this, the sample is exposed to a bipolar neutralizer which uses ions to produce a known steady state distribution of electrical charge on the particles. The bipolar neutralizer used in this study was the Advance Aerosol Neutralizer Model 3088 TSI, which uses soft X-ray energy for producing the ions (< 9.5 keV). This neutralizer has the big advantage of not using radioactive material and it brings the aerosol to almost identical charge-states as using the well-established radioactive neutralizers (i.e. 85Kr, 210Po and 241 Am) (Lee et al., 2005; TSI, 2010).

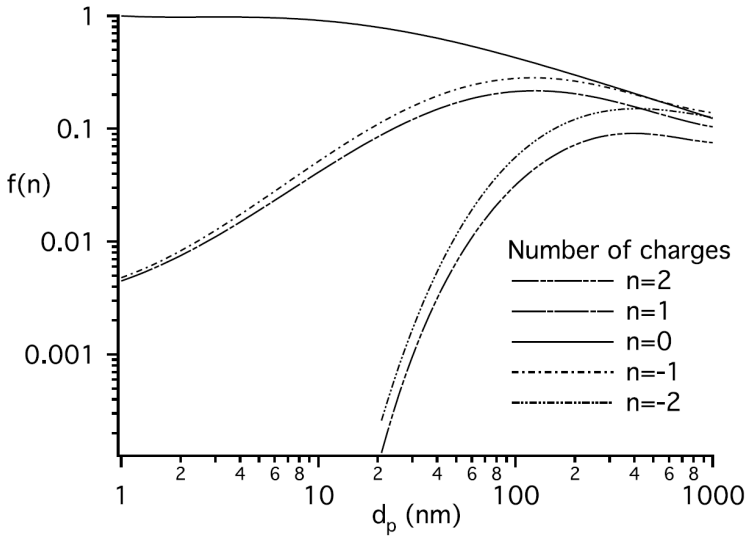

Figure 4. Equilibrium charge distribution for bipolar charging in ambient pressure air calculated using Wiedensohler (1988) approximation to the Fuchs charge distribution, taken from Flagan (2008).

By bringing the whole aerosol particle population to a known charge distribution, the measurement of the charged aerosol fraction at certain size allows to calculate the remaining neutral and oppositely charged fraction, and therefore to derive the entire aerosol distribution reliably. Figure 4 shows the charge distribution for bipolar charging in ambient air, and highlights that, depending on the size the particle can carry 1 or 2 charges of positive or negative sign, or it can be uncharged. For example, most of the particles with diameter < 100 nm have no charge, and only a small fraction (< 20 %) carry a single positive or negative charge. An even lower probability is expected for multiply charged particles. In contrast, multiply charge particles are most likely as the size increases.

Using the neutralizer to produce a known fraction of singly charged particles is essential. The measurements are complicated by the fact that small singly charged particles have the same electric mobility as larger particle with multiple charges. This has to be taken into account for the analysis but up to a size of around 30 nm the fraction of particles that carry two or more charges is negligible compared to the singly charge particles (cf. Fig. 4).

2.2.2 Particle size selection

The TD-DMA has two modes of operation: size selection mode and non-size resolved. In the case of size selection mode, the TD-DMA is suitable for particle sizes in a size range from ~ 10 nm to 30 nm. The characterization and size selection efficiently have been reported in Wagner et al. (2018). For the experiments reported here (in the CLOUD chamber), we did not select any specific size, instead we performed non-size resolved measurements in order to maximize the mass collected.

Regardless of the type of measurement, the procedure of particle collection takes place in the DMA unit. The DMA unit used in this study has a cylindrical geometry (Reischl et al., 1997; Chen et al., 1998) with two electrodes: a central electrode with a positive high voltage and an outer electrode with ground potential. The voltage difference between these two electrodes causes a polarity and consequently an electric field. In this way, only particles with negative charge are selected and proceed further for the next steps of the analysis.

Two flows enter the DMA unit: aerosol flow (q_a) which carries the particles and sheath flow (q_{sh}), these flows travel between the two electrodes, when a specific voltage is applied, only particles with a specific electrical mobility will go through the DMA unit, whereas the electrical mobility is a function of the charge and particle size.

The electrical mobility (Z_p) can be understood as the capacity for a charged particle to move in an electric field, mathematically can be expressed as it follows:

$$Z_P = \frac{n\ e\ C}{3\pi\ \mu\ D_p} \qquad (Eq.1)$$

Number of elementary charges (n), elementary charge of 1.6e-19 Coulomb (e). Cunningham correction factor (C) that accounts for non-continuous effects when calculating drag on small particles, C is a function of Knudsen number, gas mean free path and particle size. Gas viscosity (μ), and particle diameter (D_p).

The electrical mobility of a particle in a DMA can also be related to the specific properties and settings of the DMA such as its dimensions, the voltage between the electrodes and the flows through it. Knutson and Whitby (1975) derivated the transfer function. The transfer function defines the probability that an aerosol particle which enters the DMA unit will leave it, given its electrical mobility.

Thus, Knutson and Whitby (1975) showed theoretically and experimentally that the transfer function has a triangular shape and it is centered at mobility (Z_p^*) with full width at half height (ΔZ_p).

$$Z_P^* = \frac{q_{sh}}{2\pi\, VL}\, In\frac{r_2}{r_1} \qquad (Eq.2)$$

$$\Delta Z_p = \frac{q_a}{q_{sh}}\, Z_p^* \qquad (Eq.3)$$

Sheath flow (q_{sh}), aerosol flow (q_a), V is the voltage applied and L is the classification length in the DMA unit; r_1 and r_2 are the inner and outer radius, respectively. As described by Wagner et al. (2018), DMA's inner radius is 15 mm, outer radius is 20 mm and the classification length is 15 mm.

Consequently, the negatively charged particles are exposed to a well-defined electric field, the particles then move through the DMA unit according to their electrical mobility. The size of the particle and its electrical mobility are inversely proportional, then, smaller particles have higher electrical mobility. Depending on the DMA settings of qsh/L, charged particles of a certain size can be selected by the DMA.

2.2.3 Collection by electrostatic precipitation

Depending on the type of measurement, either size-resolved or non-size-resolved particles are guided through the DMA. The particles are then transmitted and collected on the surface of a wire (called filament), which carries the opposite charge. Thus, the particles are collected by electrostatic precipitation.

A filament of Platinum and Rhodium (Pt/Rh 90:10) serves as the collection surface. This filament is placed inside the central electrode and it is connected to a power supply (by using a copper wire), this provides the positive high voltage needed for the collection. The exact *collection position* of the filament is an important parameter and it is determined in each setup in order to ensure that the maximum fraction of particles is collected.

The fraction of particles transmitted and collected on the filament depends on their size and have been characterized previously by Wagner et al. (2018). Wagner et al. (2018) reported that the TD-DMA transmission efficiency for 15 nm particles is slightly above 50 % and that the collection efficiency is close to 1 for all sizes up to 15 nm and above 50 % for sizes up to 30 nm.

The experiment set-up has been reproduced by me and found similar results on the transmission efficiency of particles larger than 15 nm (Fig. 5a). For the small particles, the transmission efficiency is lower by a factor of two compared to the previous results. The collection efficiency for particles smaller than 15 nm is higher than 80 % and it is similar to the previous results (Fig. 5b). However, the collection efficiency of particles larger than 15 nm differs by a factor of 2 compared to the results reported by Wagner et al. (2018).

Overall, for the TD-DMA, the efficiency at which the selected particles are collected on the filament decreases with increasing size.

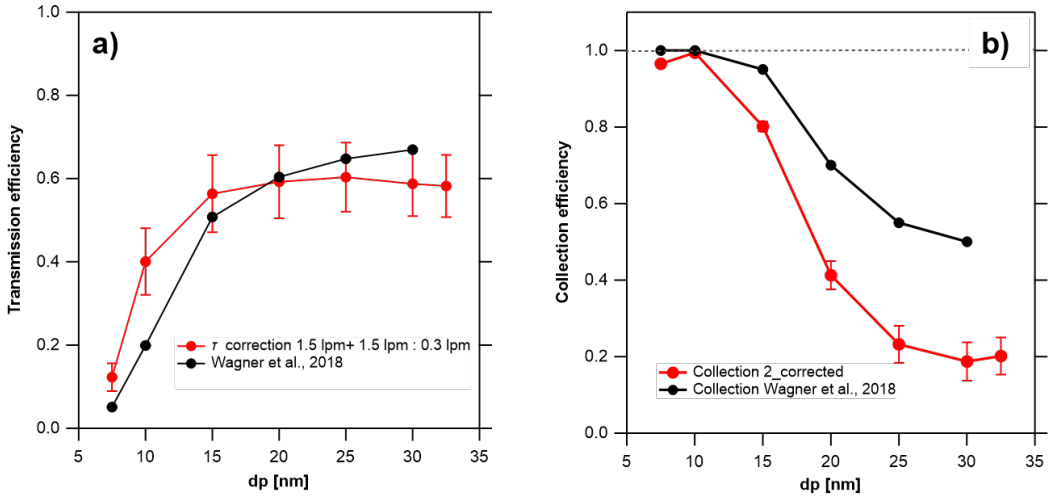

Figure 5. Transmission and collection efficiency for the TD-DMA. The characterization performed by Wagner et al., (2018) is shown in red. The results from the reproduced experiment are shown in black. In general, the transmission efficiency increases with the particle size and the collection efficiency decreases with the size.

2.3 Second step: Particle evaporation and detection

2.3.1 Evaporation

Once enough particles are collected (this depends on the type of measurement and particle load), the filament can be moved from the *collection position* to the *evaporation position*. The evaporation position is placed inside the ½" inlet line that goes directly to the mass spectrometer. The inlet line is flushed with nitrogen, this inert gas does not interfere with the measurements and provide a clean mass spectrum before particle measurements.

Immediately after the filament is placed at the evaporation position, electrical current is gradually applied, this causes an increase in the filament temperature and therefore particles start to evaporate. The vapor is then carried by the nitrogen flow and conducted to the mass spectrometer.

The heating cycle varies depending on the settings since it is an adjustable parameter and the user can decide the voltage ramp applied to the filament. For the biogenic experiments performed in the CLOUD chamber, the heating cycle lasted approximately 1 minute. Nevertheless, we did perform other tests with different heating cycles (see Sec. where we report other measurements, Appendix II).

As soon as the first heating cycle ends, a second heating is performed. This helps us to estimate the background signals due to the heating of the inlet line.

Wagner et al. (2018) estimated the temperature on a Platinum filament (slightly different to the Pt/Rh 90:10 used in this study). This calculation was done based on the Pt filament resistance, and resulted in rough temperatures up to 350 ºC during standard measurements and up to 600 ºC for the background estimation-filament cleaning. Müller (2020) performed several attempts for calculating the temperature of the Pt/Rh 90:10 filament. One attempt was to use the same method as in Wagner et al. (2018), however it was found that the parameters for calculating the resistance at room temperature used for Pt 100 are not valid for Pt/Rh 90:10 and lead to erroneous results. Another attempt was to compare known evaporation temperatures for some chemical species during the CLOUD experiment, but it was recognized that several factors can affect the accuracy of this estimation, for instance: temperature of the nitrogen flow, amount of water in the particles (dry or wet conditions), cluster formation, fragmentation (an extensive explanation is given in Section 6 in Müller (2020).

For the biogenic experiments at the CLOUD chamber, we estimated that the temperature for the Pt/Rh 90:10 filament gradually increased up to approximately 600 ºC in a period of ~ 1 minute. We performed this estimation based on the filament resistance and by intercomparing TD-DMA and FIGAERO thermograms (Caudillo et al., 2022).

Nevertheless, for future measurements it would be desirable to know the precise temperature, for example, by directly measuring it with a sensitive temperature sensor.

2.3.2 Chemical ionization

The vapors that evaporate from the heated particles are carried by a N_2 flow to the nitrate chemical ionization-atmospheric-pressure-interface-time-of-flight (CI-APi-TOF) mass spectrometer. There, the chemical analysis takes place.

Firstly, the species are ionized by a method called Chemical Ionization (CI). CI is a soft ionization technique introduced more than 50 years ago by Munson and Field (1966). In this technique, the ionization of the sample of interest is realized by gas phase ion-molecule reactions rather than by electron impact, proton impact, or fields ionization/desorption (Harrison, 1992). Because CI requires less energy compared to electron impact, less fragmentation can be expected. Therefore, this technique is suitable for identifying especially compounds with large molecular mass. Besides the reactivity for specific compounds, other compounds that are much more abundant (N_2 and O_2) are not ionized.

In our case, the chemical ionization takes place at atmospheric pressure within a unit called ion source. In this unit, nitric acid (HNO_3) is introduced in excess to produce nitrate reagent ions $NO_3^-(HNO_3)_m$ m = 0-2 using a corona discharge needle (Kürten et al., 2011).

This small needle is made of gold-plated metal, which is convenient because HNO_3 does not dissolve or react with it.

Once the reagent ions are formed, they react with the sample and form new clusters. There are some reactions that can occur depending on the analyte. For example, the detection of H_2SO_4 occurs mainly by proton transfer reaction. Sulfuric acid, as a strong acid, donates a proton (H^+) which is transferred to the reagent ion.

The most important ion-molecule reactions that are used for the detection of H2SO4 are (Kürten et al., 2016):

$$(H_2SO_4)_n + (HNO_3)_{m=0-2}\ NO_3^- \rightarrow (H_2SO_4)_{n-1}\,(HNO_3)_{k=0-2}\,HSO_4^- + (m-k+1)(HNO_3)$$

Similarly, the detection of Highly Oxygenated Organic Molecules (HOMs) occurs via clustering with the reagent ion.

$$HOM + (HNO_3)_{m=0-2}\ NO_3^- \rightarrow (HOM)NO_3^- + m(HNO_3)$$

For example,

$$C_{10}H_{16}O_7 + (HNO_3)NO_3^- \rightarrow (C_{10}H_{16}O_7)NO_3^- + HNO_3$$

HOMs possess functional groups such as hydroperoxy (–OOH) or hydroxy (–OH), which provide the hydrogen bonds required for clustering with the reagent ions. Other species that can be detected with this chemical ionization method are, for example: dimethylamine (Simon et al., 2016), iodic acid (He et al., 2021), as well as, methanesulfonic acid (Shen et al., 2022).

One interesting feature is that CI at atmospheric pressure has the advantage of increasing the number of collisions between the reagent ions and the analyte molecules. This, improves the sensitivity and makes feasible to measure compounds at very low concentrations (state the LOD and or concentration range that can be measured).

2.3.3 Detection by mass spectrometry

After being chemically ionized at atmospheric pressure (1 atm), the reagent ions and the charged molecules enter into the next step: the vacuum chamber. In the vacuum chamber, the ions are accelerated and separated according to their mass to charge ratio. This chamber consists of several stages in which the pressure decreases from ~ 1 mbar to approximately 10^{-7} mbar.

Quadrupoles and ion guides are placed in each pressure stage in order to help the ions to follow their way to the detector. Once the ions pass through the vacuum chamber, they enter to the time of flight (TOF) for detection.

TOF is a mass analyzer in which the ions are orthogonally accelerated, reflected and detected by a multi-channel plate detector (Jokinen et al., 2012; Kürten et al., 2014) .

This can be stated mathematically as follows:

Time of flight (t), is determined by: the energy (E) to which an ion is accelerated, the distance (d) that the ion has to travel, and its mass (m), in this case the mass-to-charge ratio.

This can be expressed as in terms of kinetic energy:

$$E = \frac{1}{2}\, mv^2 \qquad (Eq.4)$$

In which mass m, and velocity v can be expressed as follows:

$$m = \frac{2E}{v^2} = \frac{2E\, t^2}{d^2} \qquad (Eq.5) \qquad\qquad v = \sqrt{\frac{2E}{m}} \qquad (Eq.6)$$

From Eq. 6, can be seen that, for a given energy, the smaller the mass the higher velocity. Therefore, ions with different mass but the same kinetic energy will travel with different velocities.

For a given energy (Eq. 5), the mass is proportional to the square of the flight time of the ion. In the TOF, they ions are detected as a function of the time that it takes them to reach the detector. Ions with smaller masses will travel much faster through the TOF and will reach the detector first.

An important parameter in a TOF is the *resolution*. The IUPAC definition (Murray et al., 2013) of *resolution in mass spectrometry* is as $m/\Delta m$, where m is the mass of the ion of interest and Δm is the peak width at specific fraction of the maximum peak height, typically 50 % (but also 5 or 0.5 % are used). In our Nitrate CI-APi-TOF, the resolution is > 8 000.

3. What is the CLOUD Chamber at CERN?

Most of the experiments that were conducted for this thesis were performed at the CLOUD chamber.

The Cosmics Leaving OUtdoor Droplets (CLOUD) chamber is located at the European Organization for Nuclear Research (CERN) in Switzerland-France. The CLOUD chamber (Figure 6) is a 26.1 m^3 cylinder made of stainless-steel and it has been built with high standards of technical performance and cleanliness.

The CLOUD chamber studies how aerosols particles form and grow from gaseous species and how these processes are affected by the galactic cosmic rays (GCR). Therefore, CLOUD also studies the link between galactic cosmic rays and cloud formation under atmospheric conditions. The chamber is based in the diverged pion beam from the Proton Synchrotron (PS), which allows it to be exposed to 3.5 GeV c^{-1} secondary π^+ beam from the PS.

In the CLOUD experiments, we characterize atmospheric systems by measuring the nucleation (*J*) and growth (*GR*) rates at different conditions (precursor gasses concentration, temperature and ionization conditions). By simulating different ionization conditions, we can infer the nucleation and growth processes at any chosen altitude in the troposphere (between ground level and 15 km altitude).

According to the ion conditions, we perform three types of experiments:

I. Nucleation under neutral conditions (*Jn*): to simulate an environment with very low ion concentration, ion pair concentrations of ~ 0 cm^{-3}.
II. Nucleation under galactic cosmic rays (GCR) conditions (*Jgcr*): to simulate ion concentrations at the boundary layer, ion pair concentrations of ~ 700 cm^{-3}, and;
III. Nucleation under beam conditions (*Jπ*): to simulate upper free troposphere conditions, ion pair concentrations of ~ 3000 cm^{-3}.

By performing experiments at different ions conditions, we can also study the role of ion-induced nucleation vs neutral nucleation and its dependence on the temperature and chemical system.

For recreating the chemical systems, many parameters are carefully controlled:

Air: synthetic air made from liquid nitrogen and liquid oxygen, mixed at the ratio 79:21 N_2/O_2.

Gas precursor concentration: the chamber has a gas supply and a distribution system with individual ultra-pure gas suppliers. Depending on the chemical system of interest, the gases are either injected directly or are produced from precursor gases in the chamber. For instance, the biogenic gases, α-pinene and isoprene are regulated by evaporator suppliers, in which dry nitrogen passes through the evaporator containing the precursors in a liquid form, at controlled temperature. Gases such as SO_2 are directly introduced to the chamber from a gas cylinder stored

in a temperature-controlled cabinet. The desired concentrations can be achieved by using Mass Flow Controllers (MFC) and valves, installed as well in the gas system.

Ozone (O_3): ozone is produced by exposing cryogenic O_2 in a fused quartz tube to UV irradiation below 240 nm (UV photolysis).

Ultraviolet light intensity (UV): homogeneous illumination to produce photochemical reactions (UV fibre-optic system). This includes four 200-W Hamamatsu Hg-Xe lamps at wavelengths between 250 and 450 nm and a 4-W KrF excimer UV laser at 248 nm with adjustable power.

Temperature (T): The chamber is surrounded by an insulated thermal housing, which keeps the temperature constant from -65 ºC to +30 ºC. This simulates the full temperature range of the troposphere.

Relative Humidity (RH): The relative humidity is adjusted with a temperature-controlled Nafion humidifier using ultrapure Millipore water.

Internal mixing (fans): The chamber is continuously stirred by two magnetically coupled stainless-steel fans placed at the top and at the bottom of the chamber to provide a homogeneously mixed system.

Clearing field: An internal electric field can be created by applied high voltage (two electrodes ± 30 kV voltages). This high voltage is useful for removing quickly all the ions in the chamber.

Sampling probes for connecting a suite of instruments: the processes happening in the CLOUD chamber can be monitored in real time by a suite of instruments connected via probes around the chamber.

One of the particularities of the CLOUD chamber is that the experiments can be performed under clean conditions with very low level of contaminants, this means, with levels of $H_2SO_4 < 5e^4$ cm^{-3} and total organics < 50 pptv (Kirkby et al., 2016; Schnitzhofer et al., 2014). This allows very precise measurements.

CLOUD represents a large community (CLOUD Collaboration) that cooperates together by a) operating a suite of instruments (mass spectrometers, particle counters, CCN and INP counters, etc.), b) operating the CLOUD chamber and planning experiments, c) analyzing and interpreting the data set. The main goal is to monitor in a very detailed way these processes to gain a picture of these atmospheric processes. As well as, to transfer the results to a global scale through modeling, and comparison with atmospheric observations.

More details about the CLOUD chamber technical performance and characterization can be found in Kirkby et al. (2011), Schnitzhofer et al. (2014), and Duplissy et al. (2016).

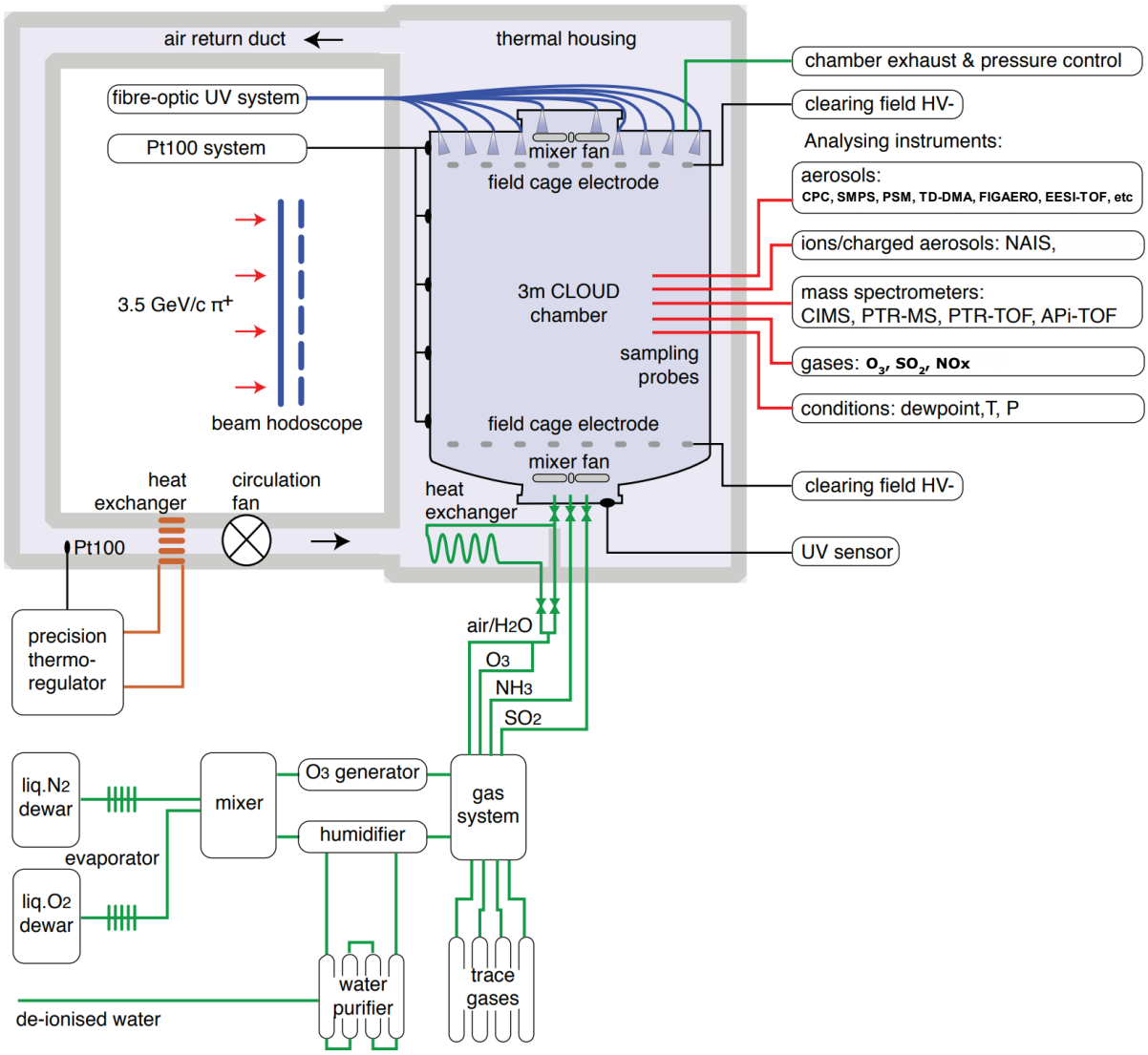

Figure 6. Scheme of the CLOUD chamber at the CERN Proton Synchrotron. The CLOUD chamber is equipped with several systems that carefully control: the temperature, relative humidity, light intensity, gas flows of trace gases into the chamber, internal mixing, clearing field, etc. The contents of the chamber are continuously analyzed by a suite of instruments such as gas monitors, mass spectrometers, and aerosols instruments to measure size, number, and chemical composition. The TD-DMA was coupled to a nitrate chemical ionization-atmospheric pressure interface-time-of-flight (CI-APi-TOF) for measuring the chemical composition of nanoparticles formed in the chamber. This figure has been taken from (Kirkby et al., 2011).

4. Summary of the Publications

4.1 Publications as a lead and second author.

4.1.1 Chemical composition of nanoparticles from α-pinene nucleation and the influence of isoprene and relative humidity at low temperature, Caudillo et al. (2021). Published on Atmospheric Chemistry and Physics on November 25th, 2021.

New Particle Formation (NPF) from biogenic organic precursors is an important atmospheric process. One of the major species is α-pinene, which upon oxidation, can form a suite of products covering a wide range of volatilities. A fraction of the oxidation products is termed Highly Oxygenated Organic Molecules (HOM). These play a crucial role for nucleation and the formation of Secondary Organic Aerosol (SOA). However, measuring the composition of newly formed particles is challenging due to their very small mass. Here, we present results on the gas and particle phase chemical composition for a system where α-pinene was oxidized by ozone, and for a mixed system of α-pinene and isoprene, respectively. The measurements took place at the CERN Cosmics Leaving Outdoor Droplets (CLOUD) chamber at temperatures between -50 °C and -30 °C and at low and high relative humidity (20 % and 60 to 100 % RH). These conditions were chosen to simulate pure biogenic new particle formation in the upper free troposphere. The particle chemical composition was analyzed by the Thermal Desorption-Differential Mobility Analyzer (TD-DMA) coupled to a nitrate chemical ionization time-of-flight mass spectrometer. This instrument can be used for particle and gas phase measurements using the same ionization and detection scheme. Our measurements revealed the presence of $C_{8\text{-}10}$ monomers and $C_{18\text{-}20}$ dimers as the major compounds in the particles (diameter up to ~ 100 nm). Particularly, for the system with isoprene added, C_5 ($C_5H_{10}O_{5\text{-}7}$) and C_{15} compounds ($C_{15}H_{24}O_{5\text{-}10}$) are detected. This observation is consistent with the previously observed formation of such compounds in the gas phase. However, although the C_5 and C_{15} compounds do not easily nucleate, our measurements indicate that they can still contribute to the particle growth at free tropospheric conditions. For the experiments reported here, most likely isoprene might enhance growth at particle sizes larger than 15 nm. Besides the chemical information regarding the HOM formation for the α-pinene (plus isoprene) system, we report on the nucleation rates measured at 1.7 nm and find that the lower $J_{1.7}$ nm values compared with previous studies are very likely due to the higher α-pinene and ozone mixing ratios used in the present study.

4.1.2 An intercomparison study of four different techniques for measuring the chemical composition of nanoparticles. Caudillo et al. (2022). Submitted to Atmospheric Chemistry and Physics on July 13th, 2022, currently in ACPD.

Currently, the complete chemical characterization of nanoparticles (<100 nm) represents an analytical challenge, since these particles are abundant in number but have very little mass. Several methods for particle-phase characterization have been recently developed to better detect and infer more accurately the sources and the fate of ultra-fine particles, but a detailed comparison of different approaches is missing. Here we report on the chemical composition of secondary organic aerosol (SOA) nanoparticles from experimental studies of α-pinene ozonolysis at -50 ºC, -30 ºC, and -10 ºC, and inter-compare the results measured by different techniques. The experiments were performed at the Cosmics Leaving OUtdoor Droplets (CLOUD) chamber at the European Organization for Nuclear Research (CERN). The chemical composition was measured simultaneously by four different techniques: 1) Thermal Desorption-Differential Mobility Analyzer (TD-DMA) coupled to a NO_3^- chemical ionization-atmospheric-pressure-interface-time-of-flight (CI-APi-TOF) mass spectrometer, 2) Filter Inlet for Gases and AEROsols (FIGAERO) coupled to an I^- high-resolution time-of-flight chemical-ionization mass spectrometer (HRToF-CIMS), 3) Extractive Electrospray Na^+ Ionization time-of-flight mass spectrometer (EESI-TOF), and 4) Offline analysis of filters (FILTER) using Ultra-high-performance liquid chromatography (UHPLC) and heated electrospray ionization (HESI) coupled to an Orbitrap high-resolution mass spectrometer (HRMS). The intercomparison was performed by contrasting the observed chemical composition as a function of oxidation state and carbon number, by calculating the volatility and comparing the fraction of volatility classes, and by comparing the thermal desorption behavior (for the thermal desorption techniques: TD-DMA and FIGAERO) and performing positive matrix factorization (PMF) analysis for the thermograms. We found that the methods generally agree on the most important compounds that are found in the nanoparticles. However, they do see different parts of the organic spectrum. We suggest potential explanations for these differences: thermal decomposition, aging, sampling artifacts, etc. We applied PMF analysis and found insights of thermal decomposition in the TD-DMA and the FIGAERO.

4.1.3 Nucleation of jet engine oil vapours is a large source of aviation-related ultrafine particles, Ungeheuer et al. 2022. Submitted to npj Climate and Atmospheric Science on September 26th, 2022.

Ungeheuer et al., 2022 present a comprehensive study of the abilities of lubricant oil to form new particles and contribute as a source of urban ultrafine particles (UFPs) in the areas surrounding large airports.

The experiments involved both laboratory and field work: in the laboratory, lubricant-oil particles were generated and evaporated at 300 ºC in a thermodenuder. In the field, ambient ultrafine particles were sampled downwind of Frankfurt International Airport and the oil fraction in UFPs was quantified. Lubricant oil was found to contribute 20 % (a conservative estimate) to the mass of the very small particles (10-18 nm) sampled near Frankfurt Airport.

The experiments performed at 300 ºC and 20 ºC with a thermodenuder showed a) an increase by a factor of 5 of the number concentration, and b) a decrease in the mean diameter of the size distribution (300 ºC compared to 20 ºC, respectively). These results suggest that nucleation of lubricant oil vapors and subsequent particle growth can occur rapidly in the cooling exhaust plumes of the aircraft-turbofans. These findings might explain the high number concentration of small particles near airports.

This study further suggests that the rapid nucleation of lubricant oil vapors in the cooling aircraft exhaust is related to their gas-phase supersaturation concentration and volatility. To reduce UFPs emissions from aviation, a suite of recommendations is discussed such as: improvement of jet oil recovery, maintenance routines, reducing the total uptime of jet engines by for example electrification of ground handling.

4.2 Publications as a co-author.

4.2.1 Synergistic HNO_3–H_2SO_4–NH_3 upper tropospheric particle formation, Wang et al. (2022). Published on Nature on May 18th, 2022.

In this paper, Wang et al. (2022) report on the NPF experiments performed in the CLOUD chamber with mixtures of nitric acid, sulfuric acid, and ammonia at -50 ºC and 25 % RH. These conditions are representative for the upper troposphere.

It was found that the system HNO_3-H_2SO_4-NH_3 produces new particles at nucleation rates that are orders of magnitude faster than the traditional ternary H_2SO_4-NH_3 nucleation at similar conditions. Because high concentrations of ammonia and ammonium nitrate have been observed in the upper troposphere over the Asia monsoon region, the mechanism suggested by Wang et al. (2022) can explain how these particles are formed: ammonia can be efficiently transported to the upper troposphere, there it mixes with low levels of sulfuric acid and nitric acid, and form particles. Furthermore, these particles can grow by condensation (driven by the availability of ammonia) up to CCN sizes and INP particles.

This mechanism represents an important finding because is linked with anthropogenic ammonia emissions over the Asian monsoon region.

5. Personal contribution to the Publications

Chemical composition of nanoparticles from α-pinene nucleation and the influence of isoprene and relative humidity at low temperature, Caudillo et al. (2021), and an intercomparison study of four different techniques for measuring the chemical composition of nanoparticles. Caudillo et al. (2022).

As a lead author, I participated in the preparation of the CLOUD facility by running the experiments. Together with my Frankfurt colleagues, I installed and operated the Thermal Desorption-Differential Mobility Analyzer (TD-DMA) coupled to a nitrate chemical ionization time-of-flight mass spectrometer. I performed the measurements during the whole campaign and analyzed the data in situ. After the campaign, I performed a deep analysis of the data, including the gas and the particle phase. I organized multiple meetings with my colleagues for discussing and interpreting the results.

Based on the existing computer codes for the data analysis, I prepared my own codes to make them more suitable for TD-DMA data. I produced the majority of the figures and wrote the manuscripts.

For the *intercomparison study*, I coordinated the integration of the data of four different particle phase instruments. I applied the Positive Matrix Factorization (PMF) analysis to the Filter Inlet for Gases and AEROsols (FIGAERO) and the TD-DMA. This constitutes the first time that the PMF method is applied to the TD-DMA data. I did the submission process, and for the published manuscript (Caudillo et al., 2021), I responded accordingly to the referees during the review process.

Nucleation of jet engine oil vapors is a large source of aviation-related ultrafine particles, Ungeheuer et al. (2022).

As a second author, together with Florian Ungeheuer, I planned, set up, and ran the laboratory experiments. I wrote the MATLAB codes to perform the preliminary analysis of the data. These codes were later adapted by Ungeheuer for a deeper analysis.

I performed the data analysis in situ and contributed to the discussion on the results. I commented on the manuscript written by Ungeheuer.

Synergistic HNO_3–H_2SO_4–NH_3 upper tropospheric particle formation, Wang et al. (2022).

I participated in the preparation of the CLOUD facility by running the experiments. Together with my Frankfurt colleagues, I installed and operated the nitrate chemical ionization time-of-flight mass spectrometer. This spectrometer provided the gas-phase sulfuric acid concentration, which was an essential part of the manuscript.

I was involved in the daily discussions during the campaign and, I often prepared and presented the shift reports.

6. Publications

6.1 Chemical composition of nanoparticles from α-pinene nucleation and the influence of isoprene and relative humidity at low temperature, Caudillo et al. (2021).

Atmos. Chem. Phys., 21, 17099–17114, 2021
https://doi.org/10.5194/acp-21-17099-2021

Atmospheric Chemistry and Physics
Open Access
EGU

Chemical composition of nanoparticles from α-pinene nucleation and the influence of isoprene and relative humidity at low temperature

Lucía Caudillo[1], Birte Rörup[2], Martin Heinritzi[1], Guillaume Marie[1], Mario Simon[1], Andrea C. Wagner[3], Tatjana Müller[1,4], Manuel Granzin[1], Antonio Amorim[5], Farnoush Ataei[6], Rima Baalbaki[2], Barbara Bertozzi[7], Zoé Brasseur[2], Randall Chiu[3], Biwu Chu[2], Lubna Dada[8], Jonathan Duplissy[2,9], Henning Finkenzeller[3], Loïc Gonzalez Carracedo[10], Xu-Cheng He[2], Victoria Hofbauer[11], Weimeng Kong[12,13], Houssni Lamkaddam[8], Chuan P. Lee[8], Brandon Lopez[11], Naser G. A. Mahfouz[11], Vladimir Makhmutov[14,26], Hanna E. Manninen[15], Ruby Marten[8], Dario Massabò[16], Roy L. Mauldin[17,11], Bernhard Mentler[18], Ugo Molteni[8,20,21], Antti Onnela[15], Joschka Pfeifer[15], Maxim Philippov[14], Ana A. Piedehierro[22], Meredith Schervish[11], Wiebke Scholz[18], Benjamin Schulze[12], Jiali Shen[2], Dominik Stolzenburg[2], Yuri Stozhkov[14], Mihnea Surdu[8], Christian Tauber[10], Yee Jun Tham[2], Ping Tian[23], António Tomé[24], Steffen Vogt[7], Mingyi Wang[11], Dongyu S. Wang[8], Stefan K. Weber[15], André Welti[22], Wang Yonghong[2], Wu Yusheng[2], Marcel Zauner-Wieczorek[1], Urs Baltensperger[8], Imad El Haddad[8], Richard C. Flagan[12], Armin Hansel[18,19], Kristina Höhler[7], Jasper Kirkby[1,15], Markku Kulmala[2,9,25], Katrianne Lehtipalo[2,22], Ottmar Möhler[7], Harald Saathoff[7], Rainer Volkamer[3], Paul M. Winkler[10], Neil M. Donahue[11], Andreas Kürten[1], and Joachim Curtius[1]

[1]Institute for Atmospheric and Environmental Sciences, Goethe University Frankfurt, 60438 Frankfurt am Main, Germany
[2]Institute for Atmospheric and Earth System Research (INAR)/Physics, Faculty of Science, University of Helsinki, 00014 Helsinki, Finland
[3]Department of Chemistry & CIRES, University of Colorado Boulder, Boulder, CO 80309-0215, USA
[4]Atmospheric Chemistry Department, Max Planck Institute for Chemistry, 55128 Mainz, Germany
[5]CENTRA and FCUL, University of Lisbon, 1749-016 Lisbon, Portugal
[6]Leibniz Institute for Tropospheric Research, 04318 Leipzig, Germany
[7]Institute of Meteorology and Climate Research, Karlsruhe Institute of Technology, 76344 Eggenstein-Leopoldshafen, Germany
[8]Laboratory of Atmospheric Chemistry, Paul Scherrer Institute, 5232 Villigen, Switzerland
[9]Helsinki Institute of Physics (HIP)/Physics, Faculty of Science, University of Helsinki, 00014 Helsinki, Finland
[10]Faculty of Physics, University of Vienna, 1090 Vienna, Austria
[11]Center for Atmospheric Particle Studies, Carnegie Mellon University, Pittsburgh, PA 15213, USA
[12]Division of Chemistry and Chemical Engineering, California Institute of Technology, Pasadena, CA 91125, USA
[13]California Air Resources Board, Sacramento, CA 95814, USA
[14]Lebedev Physical Institute, Russian Academy of Sciences, 119991, Moscow, Russia
[15]CERN, 1211 Geneva, Switzerland
[16]Dipartimento di Fisica, Università di Genova and INFN, 16146 Genoa, Italy
[17]Department of Atmospheric and Oceanic Sciences, University of Colorado Boulder, Boulder, CO 80309, USA
[18]Institute for Ion and Applied Physics, University of Innsbruck, 6020 Innsbruck, Austria
[19]Ionicon Analytik GmbH, 6020 Innsbruck, Austria
[20]Forest Dynamics, Swiss Federal Institute for Forest, Snow and Landscape Research, 8903 Birmensdorf, Switzerland
[21]Department of Chemistry, University of California, Irvine, CA 92697, USA
[22]Atmospheric Composition Unit, Finnish Meteorological Institute, 00560 Helsinki, Finland
[23]Beijing Weather Modification Office, 100089 Beijing, China
[24]IDL, Universidade da Beira Interior, R. Marquês de Ávila e Bolama, 6201-001 Covilhã, Portugal

Published by Copernicus Publications on behalf of the European Geosciences Union.

[25]Aerosol and Haze Laboratory, Beijing Advanced Innovation Center for Soft Matter Science and Engineering, Beijing University of Chemical Technology, Beijing, 100029, China
[26]Moscow Institute of Physics and Technology, National Research University, 117303, Moscow, Russia

Correspondence: Lucía Caudillo (lucia.caudillo@iau.uni-frankfurt.de) and Joachim Curtius (curtius@iau.uni-frankfurt.de)

Received: 16 June 2021 – Discussion started: 7 July 2021
Revised: 15 October 2021 – Accepted: 17 October 2021 – Published: 25 November 2021

Abstract. Biogenic organic precursors play an important role in atmospheric new particle formation (NPF). One of the major precursor species is α-pinene, which upon oxidation can form a suite of products covering a wide range of volatilities. Highly oxygenated organic molecules (HOMs) comprise a fraction of the oxidation products formed. While it is known that HOMs contribute to secondary organic aerosol (SOA) formation, including NPF, they have not been well studied in newly formed particles due to their very low mass concentrations. Here we present gas- and particle-phase chemical composition data from experimental studies of α-pinene oxidation, including in the presence of isoprene, at temperatures (-50 and $-30\,^{\circ}$C) and relative humidities (20 % and 60 %) relevant in the upper free troposphere. The measurements took place at the CERN Cosmics Leaving Outdoor Droplets (CLOUD) chamber. The particle chemical composition was analyzed by a thermal desorption differential mobility analyzer (TD-DMA) coupled to a nitrate chemical ionization–atmospheric pressure interface–time-of-flight (CI-APi-TOF) mass spectrometer. CI-APi-TOF was used for particle- and gas-phase measurements, applying the same ionization and detection scheme. Our measurements revealed the presence of C_{8-10} monomers and C_{18-20} dimers as the major compounds in the particles (diameter up to ~ 100 nm). Particularly, for the system with isoprene added, C_5 ($C_5H_{10}O_{5-7}$) and C_{15} compounds ($C_{15}H_{24}O_{5-10}$) were detected. This observation is consistent with the previously observed formation of such compounds in the gas phase. However, although the C_5 and C_{15} compounds do not easily nucleate, our measurements indicate that they can still contribute to the particle growth at free tropospheric conditions. For the experiments reported here, most likely isoprene oxidation products enhance the growth of particles larger than 15 nm. Additionally, we report on the nucleation rates measured at 1.7 nm ($J_{1.7\,\mathrm{nm}}$) and compared with previous studies, we found lower $J_{1.7\,\mathrm{nm}}$ values, very likely due to the higher α-pinene and ozone mixing ratios used in the present study.

1 Introduction

Approximately half of the global cloud condensation nuclei (CCN) are produced by nucleation (Merikanto et al., 2009; Gordon et al., 2017). In particular, biogenic emissions of volatile organic compounds (VOCs) play an important role in the formation of aerosol particles. The chemical reactions involving VOCs can lead to the formation of highly oxygenated organic molecules (HOMs), which can be described as a class of organic compounds that are formed under atmospherically relevant conditions by gas-phase autoxidation involving peroxy radicals (Ehn et al., 2014; Bianchi et al., 2019). These compounds possess low-saturation vapor pressures and are thus relevant for secondary organic aerosol (SOA) formation, including new particle formation (NPF), due to gas-to-particle partitioning.

Isoprene (C_5H_8) has the highest global emission rate, and many studies have demonstrated the importance of isoprene in terms of SOA formation (Surratt et al., 2006, 2007, 2010; Paulot et al., 2009; Lin et al., 2012; Riva et al., 2016). α-Pinene ($C_{10}H_{16}$), while less abundant, is one of the most commonly observed and prominent contributors to biogenic SOA due to its ability to form HOMs that nucleate on their own under atmospheric conditions (Kirkby et al., 2016; Tröstl et al., 2016). The formation of SOA has been well studied in isoprene and α-pinene systems. The role of HOMs in SOA formation and NPF has also been explored in α-pinene and α-pinene with isoprene systems. However, much less is known about the particle-phase composition of HOMs in these systems and the specific controls particle formation and growth rates, including as a function of temperature and the ratio of isoprene to α-pinene.

Regarding α-pinene studies, Stolzenburg et al. (2018) reported α-pinene dark ozonolysis experiments at $+25$, $+5$, and $-25\,^{\circ}$C and showed that the rapid growth of organic particles is observed across these temperatures and that higher T leads to a faster autoxidation, while lower T leads to an increased partitioning due to decreased vapor pressures. Furthermore, Simon et al. (2020) extended the study of α-pinene gaseous oxidation products to even lower temperatures from $+25$ to $-50\,^{\circ}$C, showing that the oxygen-to-carbon ratio (O : C) and the yield for HOM formation decrease as the temperature decreases, whereas the reduction of volatility com-

pensates for this effect by increasing the nucleation rates at lower temperatures.

Kiendler-Scharr et al. (2009) presented observations at 15 °C of a significant decrease in particle number and volume concentration by the presence of isoprene in an experiment under plant-emitted VOC conditions. Subsequently, McFiggans et al. (2019) showed that isoprene, carbon monoxide, and methane can each suppress aerosol mass and the yield from monoterpenes in mixtures of atmospheric vapors. Recently, a study by Heinritzi et al. (2020) revealed that the presence of isoprene in the α-pinene system suppresses new particle formation by altering the peroxy-radical termination reactions and inhibiting the formation of those molecules needed for the first steps of cluster and particle formation (species with 19 to 20 carbon atoms).

Despite the difficulties in measuring the nanoparticle chemical composition due to their very small mass, there have been several efforts for designing and improving techniques to face this problem. Some particle-phase studies exist that report the chemical composition of newly formed nanoparticles. For instance, Kristensen et al. (2017), measuring at -15 and $+20$ °C, showed an increased contribution of less oxygenated species to α-pinene SOA particles formed from ozonolysis at sub-zero temperatures. Ye et al. (2019) measured the particle-phase chemical composition from α-pinene oxidation between -50 and $+25$ °C with the FIGAERO inlet (Lopez-Hilfiker et al., 2014). They found that during new particle formation from α-pinene oxidation, gas-phase chemistry directly determines the composition of the condensed phase. Highly oxygenated organic molecules are much more abundant in particles formed at higher temperatures, shifting the compounds towards higher O : C and lower volatilities. Additionally, some studies addressing the chemical composition, volatility, and viscosity of organic molecules have provided important insights into their influence on the climate (Huang et al., 2018; Reid et al., 2018; Champion et al., 2019).

Here, we present the results from gas- and particle-phase chemical composition measurements for a system where α-pinene was oxidized to simulate pure biogenic new particle formation at free tropospheric conditions in a range from -50 to -30 °C. The data are further compared to the mixed system of α-pinene and isoprene in order to better understand the partitioning processes. The particle chemical composition was analyzed by a thermal desorption differential mobility analyzer (TD-DMA) (Wagner et al., 2018), coupled to a nitrate chemical ionization–atmospheric pressure interface–time-of-flight (CI-APi-TOF) mass spectrometer. This technique allows for a direct comparison between the gas and particle phase as both measurements are using the identical chemical ionization source and detector.

2 Methods

2.1 The CLOUD chamber at CERN and the experiments

The measurements took place in the Cosmics Leaving Outdoor Droplets (CLOUD) chamber at the European Organization for Nuclear Research (CERN) during the CLOUD14 campaign (September–November 2019). The CLOUD chamber is a stainless-steel cylinder, with a volume of 26.1 m^3, which has been built to the highest technical standards of cleanliness (Kirkby et al., 2011; Duplissy et al., 2016). By precisely controlling several parameters, such as gas concentrations, temperature, relative humidity, ultraviolet light intensity, and internal mixing, specific atmospheric systems can be recreated in order to study the nucleation and growth processes of aerosols at atmospheric conditions. The biogenic gas concentrations, here α-pinene and isoprene, can be regulated by using individual evaporator supplies, in which dry nitrogen passes through the evaporator containing the precursors in a liquid form, at controlled temperature. In this way, the precursors are evaporated and diluted with clean air to achieve the desired concentration in the chamber. Ozone is introduced via a separate gas line. The chamber is continuously stirred by two magnetically coupled stainless-steel fans placed at the top and at the bottom of the chamber to provide a homogeneously mixed system (Voigtländer et al., 2012). In order to promote particle production from ions, galactic cosmic ray (GCR) conditions can be achieved by turning off the high voltage field (30 kV m^{-1}). The equilibrium ion-pair concentration in the chamber due to GCR is around 700 cm^{-3} (Kirkby et al., 2016).

The experiments relevant for this work were done under GCR conditions and in a flow-through mode with continuous addition of the reactants, performed at -50 and -30 °C, at low and high relative humidity to simulate pure biogenic new particle formation at a range of free tropospheric conditions. Isoprene and α-pinene precursor gases were oxidized with O_3 and ·OH (produced from O_3 photolysis in the presence of H_2O and UV light) to induce both dark ozonolysis and photochemistry oxidation reactions. The α-pinene level was between 1 and 8 ppbv, the isoprene level up to 30 ppbv, and O_3 approximately 100 ppbv. The ozonolysis of α-pinene was performed at -50 and -30 °C, while the α-pinene + isoprene experiment was performed at -30 °C only. The experimental overview is discussed in more detail in Sect. 3.1.

2.2 TD-DMA

The particle chemical composition was analyzed by a thermal desorption differential mobility analyzer (TD-DMA) coupled to a nitrate chemical ionization–atmospheric pressure interface–time-of-flight (CI-APi-TOF) mass spectrometer. The TD-DMA design and characterization have been

described in detail by Wagner et al. (2018). This instrument allows for the direct comparison between gas- and particle-phase chemical composition as both measurements use the same ionization scheme and mass spectrometer (the detection technique will be described in Sect. 2.3).

The TD-DMA uses an online and semi-continuous principle for the detection of the chemical composition of nanoparticles. The particles are sampled from the chamber and charged with an X-ray source; a specific size can be selected, and immediately afterwards they are electrostatically collected on a filament. Heating the filament after a defined collection time evaporates the particles into a stream of clean carrier gas (N_2). The particle vapor is analyzed by the nitrate CI-APi-TOF mass spectrometer (Kürten et al., 2014). In order to estimate the instrumental background, two heating profiles are recorded: the first heating cycle evaporates all the particulate material collected; a second heating cycle constrains the background due to the heating of the inlet line. All reported particle-phase signals are corrected based on this background measurement.

For the experiments that are reported in this work, a filament of platinum / rhodium (90 : 10) was used, and an integral, non-size-selective mode of operation was chosen in order to maximize the mass of collected particles. For desorbing the sample, an electric current was applied to the filament and ramped linearly over a duration of approximately 1 min. Due to the very low experimental temperatures, cold sheath flows and isolated inlet lines were installed in order to avoid drastic temperature changes between the CLOUD chamber and the instrument. Evaporation of particulate material before the active heating should therefore not be substantial.

2.3 Nitrate CI-APi-TOF mass spectrometer

The gas-phase and the evaporated particulate material were measured using a nitrate chemical ionization–atmospheric pressure interface–time-of-flight (CI-APi-TOF) mass spectrometer, which has three major components: an atmospheric pressure ion–molecule reactor, where the chemical ionization takes place; an atmospheric pressure interface for transporting the charged ions into the mass classifier; and a time-of-flight mass classifier, where the ions are accelerated, separated according to their mass-to-charge ratio, and detected with a microchannel plate (Jokinen et al., 2012; Kürten et al., 2014). The nitrate CI-APi-TOF mass spectrometer uses nitrate reagent ions $(HNO_3)_n\ NO_3^-$ with $n = 0$–2, which are created by an ion source using a corona discharge needle (Kürten et al., 2011). With this nitrate chemical ionization technique, sulfuric acid, iodic acid, dimethylamine and HOMs can be detected (Kürten et al., 2014; Simon et al., 2016; Kirkby et al., 2016; He et al., 2021). HOMs are detected because of the presence of functional groups such as hydroperoxy (–OOH) or hydroxy (–OH), which provide the hydrogen bonds required for clustering with the reagent ions.

Here the nitrate CI-APi-TOF mass spectrometer data for the gas and particle phase have been corrected for background signals and the mass-dependent transmission efficiency in the mass classifier (Heinritzi et al., 2016). The data analysis and processing were performed using IGOR Pro 7 (WaveMetrics, Inc., USA), Tofware (Version 3.2, Aerodyne Inc., USA) and MATLAB R2019b (MathWorks, Inc., USA).

2.4 Nucleation rates

The particle number size distribution between ~ 1 nm and 1 µm is measured using a suite of particle counters namely a particle size magnifier (PSM; Vanhanen et al., 2011), a condensational particle counter (CPC 3776, TSI), a nano scanning mobility particle sizer (nano-SMPS 3982, TSI), and a home-built long scanning mobility particle sizer (long-SMPS). The PSM measures the size distribution between ~ 1 and 3 nm as well as the total particle number concentration above a defined cutoff, 1.7 nm in this study. The CPC on the other hand is used to measure the total particle number concentration above 2.5 nm. The nano-SMPS and long-SMPS together cover the particle number size distribution between 6 nm and 1 µm. The same setup has been used in previous CLOUD experiments; see for example Lehtipalo et al. (2018) and Heinritzi et al. (2020).

The nucleation rate (J_{dp}), which is defined as the flux of particles of a certain size, is calculated using the method proposed by Dada et al. (2020); see Eq. (9) therein. For this study, the formation of particles with a diameter ≥ 1.7 nm is calculated ($J_{1.7}$) using the derivative of the total concentration of particles measured with the PSM while accounting for size-dependent losses to the chamber wall, by coagulation or via dilution. The error on $J_{1.7}$ is 30 % based on run-to-run repeatability (Dada et al., 2020).

3 Results and discussion

3.1 Experimental overview

An overview of the experiments performed at -30 and -50 °C at low and high relative humidity is shown in Fig. 1. The mixing ratio of ozone was stable at ~ 100 ppbv for all of the experiments reported in this work (not shown). In order to represent pure biogenic new particle formation events, no other trace gases were added to the chamber, and the levels of SO_2, NO_x, and other trace gases were monitored to remain always below the detection limits of the respective measurement devices. By using the TD-DMA, particles were collected in every NPF system (without resolving the particle size); the shaded area in Fig. 1 refers to the period where the particle collection took place.

The upper panel of Fig. 1 displays the size distribution measured by the scanning mobility particle sizer (SMPS). Four different experiments can be categorized as follows:

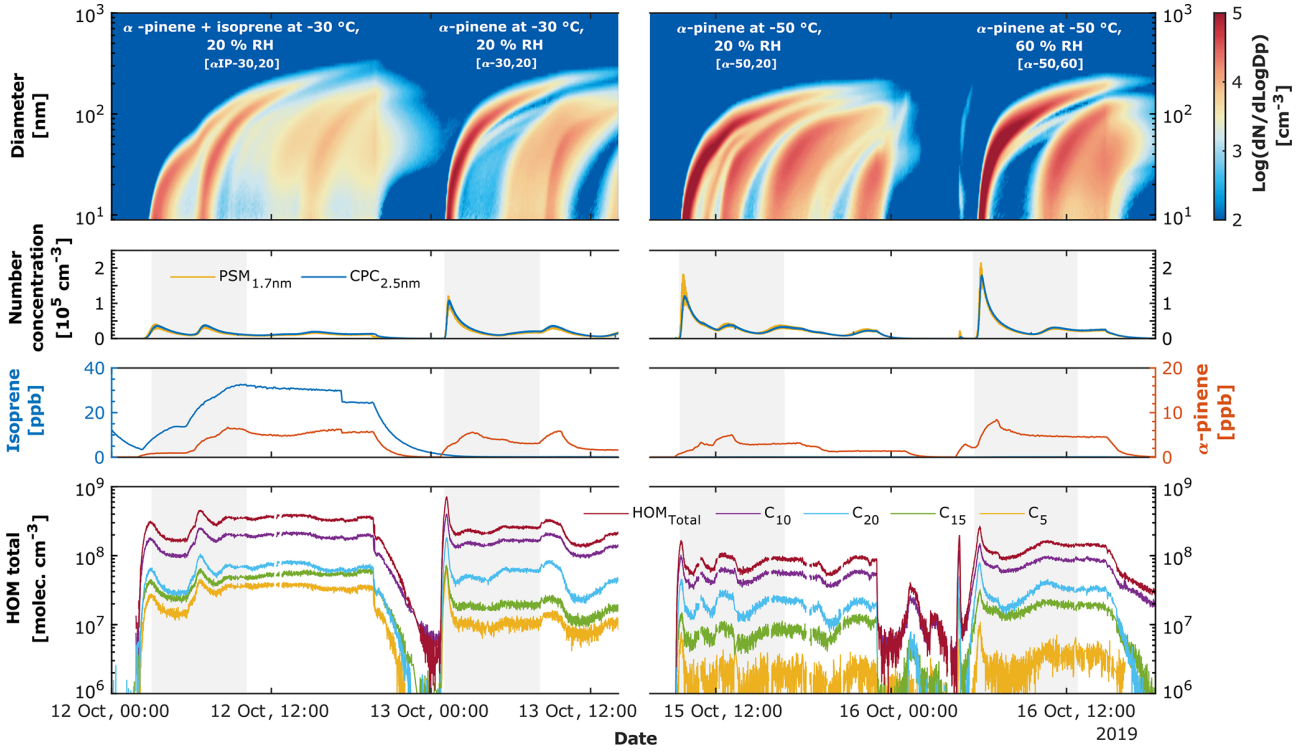

Figure 1. Experimental overview for pure biogenic new particle formation. First panel: particle size distribution for four different experiments: α-pinene + isoprene at −30 °C and 20 % RH (αIP-30,20), α-pinene at −30 °C and 20 % RH (α-30,20), α-pinene at −50 °C and 20 % RH (α-50,20), and α-pinene at −50 °C and 60 % RH (α-50,60). The color scale represents the log 10 of the normalized particle concentration in cubic centimeters (cm^{-3}). Second panel: particle number concentration in cm^{-3} measured by the PSM with a cutoff diameter of 1.7 nm and CPC 2.5 nm. Third panel: mixing ratio in parts per billion by volume (ppbv) for the biogenic precursor gases, isoprene, and α-pinene. Fourth panel: evolution of total HOM concentration in molecules per cubic centimeter (molec. cm^{-3}), measured in the gas phase by the nitrate CI-APi-TOF mass spectrometer. The HOM total is defined as the sum of C_5, C_{10}, C_{15}, and C_{20} carbon classes, which are shown as well. Ozone level is not shown though remains stable over the whole period at ∼ 100 ppbv. The shaded areas refer to the time when the particles were collected using the TD-DMA.

1. α-pinene + isoprene at −30 °C and 20 % RH (*αIP-30,20*),
2. α-pinene at −30 °C and 20 % RH (*α-30,20*),
3. α-pinene at −50 °C and 20 % RH (*α-50,20*), and
4. α-pinene at −50 °C and 60 % RH (*α-50,60*).

The color scale in the upper panel of Fig. 1 indicates that the newly formed particles appear in the smallest size channels of the SMPS soon after the concentration of α-pinene in the chamber is increased. The experiments were performed such that the particles grew rapidly to reach sizes of approximately 100 nm, where they could potentially act as cloud condensation nuclei (CCN) or ice nucleating particles (INPs) and were used for further CCN and INP studies.

The second panel of Fig. 1 shows the particle number concentration measured by the condensation particle counter ($CPC_{2.5\,nm}$) and by the particle size magnifier (PSM) with a cutoff diameter of 1.7 nm. A higher particle number concentration can be observed for the experiments *α-50,20* and *α-50,60* at −50 °C, reaching $\sim 2 \times 10^5$ cm^{-3}. By comparing the experiments at −30 °C, *α-30,20*, and *αIP-30,20* a lower particle concentration is observed for the system where isoprene is present. The reduction is approximately a factor of 3; this can be attributed to the suppression of the new particle formation by isoprene oxidation. This is in line with the results of Kiendler-Scharr et al. (2009), who first reported the decrease in particle number of the nucleated particles. The effect of isoprene in terms of total HOM concentration in the gas phase and on the measured nucleation rates will be discussed in more detail in Sect. 3.4.2.

The third panel of Fig. 1 shows the α-pinene and isoprene mixing ratios. For all of the systems, α-pinene was between 1 and 8 ppbv, while isoprene was only present during experiment *αIP-30,20* up to 30 ppbv. The precursor gases were measured by using a proton transfer reaction time-of-flight (PTR-TOF) mass spectrometer (Graus et al., 2010; Breitenlechner et al., 2017), which is capable of measuring VOCs.

The bottom panel of Fig. 1 shows the total HOM concentration in the gas phase. Here, the total HOM concentra-

tion is defined as the sum of C_5, C_{10}, C_{15}, and C_{20} carbon classes; these classes consider compounds with C_2–C_5, C_6–C_{10}, C_{11}–C_{15}, and C_{16}–C_{20}, respectively, and considered as a HOM such compounds with five or more oxygen atoms, as suggested in Bianchi et al. (2019). The total HOM concentration was measured with a calibrated nitrate CI-APi-TOF mass spectrometer (Kürten et al., 2012). Additionally, a temperature-dependent sampling loss correction factor is applied. From the evolution of these traces, it can be observed that C_5 and C_{15} carbon classes have higher concentrations (approximately by a factor of 2.5) in experiment *αIP-30,20* compared with *α-30,20*, which can be explained by the presence of isoprene. However, possible fragmentation in the α-pinene ozonolysis systems also can lead to some C_5 and C_{15} compounds produced without the presence of isoprene.

3.2 Gas- and particle-phase chemical composition

Figure 2 shows the carbon distribution as an overview of the compounds detected in gas and particle phase for a system where only α-pinene was oxidized (*α-30,20*). C_{8-10} monomers (Fig. 2a) and C_{18-20} (Fig. 2b) dimers are observed in the gas as well as in the particle phase. For instance, some of the signals with the highest intensity correspond to $C_{10}H_{16}O_{3-9}$ and $C_{20}H_{32}O_{5-13}$; in particular $C_{10}H_{16}O_6$ and $C_{10}H_{16}O_7$ have an important presence in both phases. Overall, most of the compounds that are present in the gas phase are detected as well in the particle phase, although their relative contribution to the total signal can differ between the phases. The corresponding carbon distribution for the other systems can be found in Figs. S1 and S2 in the Supplement.

3.2.1 Influence of isoprene on α-pinene system at −30 °C and 20 % RH

Figure 3 shows mass defect plots of gas and particle phase and the intensity difference between each phase at −30 °C. Figure 3a and d display the gas and particle composition of *α-30,20*, while the gas and particle composition of *αIP-30,20* are shown in Fig. 3b and e, respectively. As both phases were measured with the same instrument, they can be directly inter-compared.

The intensity difference is calculated based on the normalized signal (each single signal divided by the total signal for each system and phase). Essentially, the normalized signal can be understood as a measure of the fraction or contribution of every compound in the entire system. By looking at the intensity difference in the gas phase (Fig. 3c), it can be observed that some C_5 and C_{15} contribute significantly more in the system with isoprene added (*αIP-30,20*) that are not as pronounced in the system where only α-pinene was oxidized (*α-30,20*). This observation can be attributed to the presence of isoprene in the system. As described by Heinritzi et al. (2020), C_{15} dimers are formed in the gas phase when C_{10} $RO_2^\bullet$ radicals from α-pinene ozonolysis undergo terminating reactions with C_5 $RO_2^\bullet$ radicals from the isoprene oxidation with ·OH. Additionally, C_{19} and C_{20} dimers contribute more in the system where only α-pinene was oxidized (*α-30,20*).

Figure 3f shows the intensity difference in the particle phase. In contrast with what is observed in the gas phase, the particle-phase effects seem more diverse. There is an increase in the intensity difference for several species in the system with isoprene (*αIP-30,20*), such as C_{4-5}, C_{13-16}, and some C_{17-19} (see Fig. S1 in the Supplement). In particular, a distinct group of C_{15} compounds $C_{15}H_{24}O_{5-10}$ and $C_5H_{10}O_{5-7}$ can be identified in the particle and in the gas phase. A previous study has shown that isoprene can enhance particle growth rates despite its negative effect on nucleation (Heinritzi et al., 2020). The identification of C_{15} dimers in nanometer-sized particles in the present study confirms this with a direct measurement. The suppressing effect of isoprene on nucleation will further be discussed in Sect. 3.4.2. However, isoprene can still contribute to the growth of particles by C_5 or by C_{15} compounds. Additionally, these species can be an important fingerprint to identify SOA formation from a mixture of biogenic vapors containing isoprene.

For the experiments presented in this study, we report in Table 1 the particle growth rates (GRs) determined from the nano-scanning electrical mobility spectrometer (nSEMS) size distributions. The growth rates in 3.2–8 and 5–15 nm were calculated using the 50 % appearance time method described in Stolzenburg et al. (2018). From the calculated values in Table 1, we observe that $GR_{3.2-8\,nm}$ for the α-pinene + isoprene system (*αIP-30,20*) at the first concentration stage is around 18 nm h^{-1} compared to $\sim$ 77 nm h^{-1} for the α-pinene only system (*α-30,20*). This is a factor of $\sim$ 4 difference, while $GR_{5-15\,nm}$ represents a factor of 2 to 3 difference between *αIP-30,20* compared to *α-30,20*. From these values, one would conclude that isoprene does not contribute to the growth in the size range reported here. Nevertheless, by looking at the aerosol mass concentration (see Fig. S3 in the Supplement), the mass reached during the experiment *αIP-30,20* is identical in the presence and absence of isoprene at −30 °C and 20 % RH. Reaching the same mass with a lower number of particles for the experiment with isoprene (*αIP-30,20*) compared to *α-30,20* means that the growth rates at larger sizes (> 15 nm) are higher in the presence of isoprene. This is consistent with the fact that the particle size reached in the presence of isoprene is higher. Most likely, isoprene might enhance growth at larger sizes (> 15 nm) in the present study.

3.2.2 Influence of relative humidity on α-pinene system at −50 °C

Figure 4 shows mass defect plots for the pure α-pinene experiments at −50 °C at low and high relative humidity: the gas and particle phase of α-pinene at −50 °C, 20 % RH (Fig. 4a and d), and the gas and particle phase of α-pinene at −50 °C,

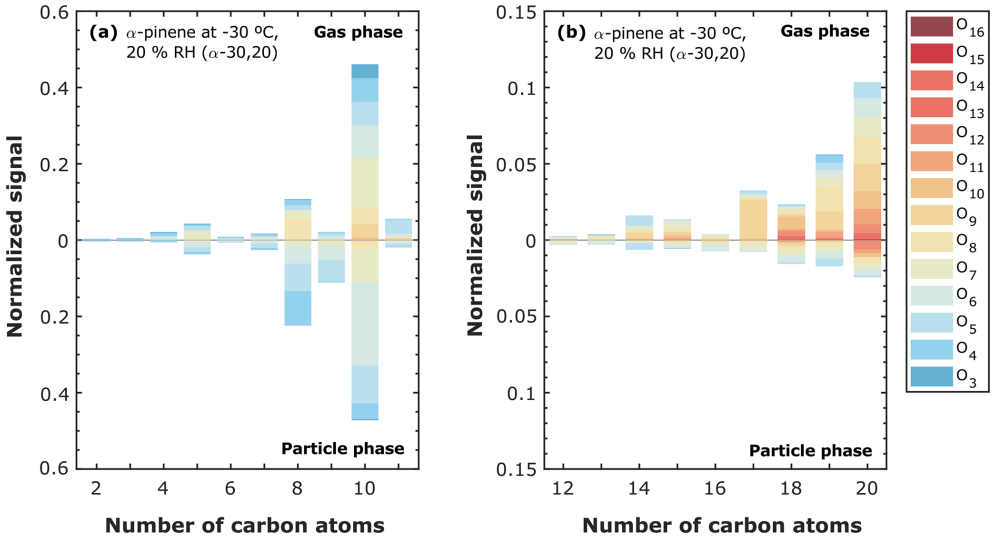

Figure 2. Carbon atom distribution and oxygen atom content in gas- and particle-phase molecules for α-pinene oxidation products at $-30\,^{\circ}$C and 20 % RH (α-30,20). Both phases are measured with a nitrate CI-APi-TOF mass spectrometer, while the TD-DMA is coupled to it for particle-phase measurements. **(a)** Carbon atom distribution C_{2-11} and **(b)** carbon atom distribution C_{12-20}. The level of α-pinene was between 1 and 8 ppbv, and the ozone level was stable at ~ 100 ppbv. The intensities are normalized by the total signal in each system and phase. Each color represents a specific number of oxygen atoms in the range of 3 to 16.

Table 1. Summary of the main parameters for four pure biogenic new particle formation experiments.

Experiment	Isoprene [ppb]	α-pinene [ppb]	Isoprene-to-monoterpene carbon ratio (R)	Ozone [ppb]	T [°C]	RH [%]	HOM total[a] [molec. cm^{-3}]	$J_{1.7}^{a}$ [cm^{-3} s^{-1}]	Growth rate 3.2–8 nm [nm h^{-1}]	Growth rate 5–15 nm [nm h^{-1}]	Mass$_{<15\,nm}$/ Mass$^{b}_{>15\,nm}$ [%]
αIP-30,20	13.71	0.95	14.4	98.58	−30	20	1.50e8	7.29	18.0	22.8	0.29/99.7
	31.38	5.12	6.1	101.56	−30	20	3.04e8	10.10	n/a	39.0	
α-30,20	~ 0	3.35	n/a	102.10	−30	20	2.20e8	23.76	76.9	77.1	0.11/99.9
α-50,20	~ 0	3.04	n/a	100.55	−50	20	6.72e7	51.24	41.1	42.0	0.26/99.7
α-50,60	~ 0	7.72	n/a	110.20	−50	60	8.00e7	79.17	63.4	78.4	0.09/99.9

[a] Run-to-run experimental uncertainties of HOMs is ± 20 %, and for $J_{1.7}$ it is ± 30 %. n/a: not applicable. [b] Mass fraction of particles collected on the filament during the TD-DMA collection time, the calculation of which is based on SMPS mass distributions.

60 % RH (Fig. 4b and e). In both gas and particle phase at high and low RH, we detected C_{8-10} monomers and C_{18-20} dimers. $C_{10}H_{16}O_{4-7}$ and $C_{20}H_{32}O_{5-11}$ are the most prominent signals (see Fig. S2 in the Supplement).

The relative humidity change from 20 % to 60 % does not have a significant influence on the gas-phase composition at temperatures of $-50\,^{\circ}$C (Fig. 4c), meaning that most of the gaseous compounds detected contribute practically equal to the total signal when the humidity changes over the reported range. In contrast, there are changes in the particle-phase signal. The intensity difference (Fig. 4f) does not show a clear humidity effect on the particle chemical composition; however, this comparison is based on the normalized signal (contribution of every compound to the total intensity). When looking only at the total intensity in the particle phase, we do observe an increase by a factor of ~ 3 in the total signal for the system at high RH (*α-50,60*) compared with the system at low RH (*α-50,20*). This observation can likely be attributed to a change in the particle mass size distribution (see Fig. S3 in the Supplement), which indicates that at similar α-pinene and ozone mixing ratio, and the same temperature, the particle mass concentration increases possibly due to the effect of the relative humidity in the system. In addition, a possible impact of relative humidity on particle viscosity can influence particle mass formed; studies by Grayson et al. (2016) and Galeazzo et al. (2021) have reported lower viscosity with higher SOA mass concentration along with RH dependence of viscosity for organic particles.

Our findings are consistent with previous experiments. Saathoff et al. (2009) observed that humidity has a significant influence on α-pinene SOA yields for lower temperatures. Cocker III et al. (2001) reported that the yield of SOA at higher RH for α-pinene ozonolysis (relative to the system at dry conditions) increases possibly due to the uptake

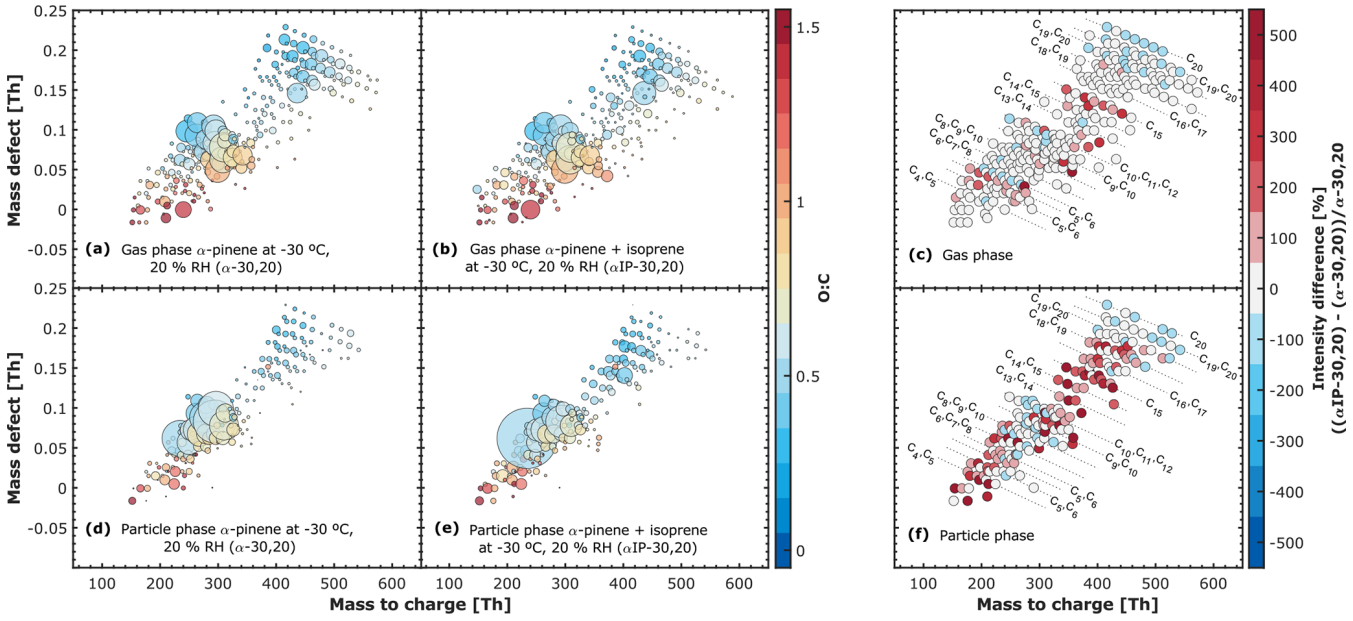

Figure 3. Mass defect plots of gas and particle phase and the intensity difference between each phase. Both phases are measured with a nitrate CI-APi-TOF mass spectrometer, while the TD-DMA is coupled to it for particle-phase measurements. **(a)** Gas and **(d)** particle phase for α-pinene oxidation products at $-30\,^{\circ}$C and 20 % RH (α-30,20). **(b)** Gas and **(e)** particle phase for α-pinene + isoprene oxidation products at $-30\,^{\circ}$C and 20 % RH (αIP-30,20). The level of α-pinene was between 1 and 8 ppbv in both experiments, while isoprene was present only in experiment αIP-30,20 reaching up to 30 ppbv. Ozone levels were $\sim$ 100 ppbv in both experiments. The symbol sizes in **(a)**, **(b)**, **(d)**, and **(e)** are the intensities normalized by the total signal in each system. The intensity difference in the gas phase **(c)** and in the particle phase **(f)** is indicated as $((\alpha\text{IP-30,20}) - (\alpha\text{-30,20}))\,/\,\alpha\text{-30,20}$. The color scale represents the difference in percent.

of water. One explanation for this observation could be that the rate constant value of the α-pinene ozonolysis can be affected by the RH (Zhang et al., 2018). Nevertheless, our semi-continuous particle-phase measurements do not allow any conclusions on the magnitude of the rate constants to be drawn. Continuous particle-phase measurements under different RH conditions are required in order to better understand the RH effect on the SOA formation.

In general, for the experiments presented in this work, most of the compounds that are present in the gas phase are detected as well in the particle phase, although the relative contributions to the total signal can vary depending on the phase. The more oxygenated material in the gas phase, specifically for C_{20} dimers with $n_O > 13$, is not observed in the particle phase. This is probably because of their very low concentrations and the difficulty to distinguish between real particle signal and background. We conjecture that especially at low temperatures this issue might be related to the fact that at lower temperatures, the autoxidation process to form HOMs is slower; therefore, the oxygen content and O : C decrease (Stolzenburg et al., 2018; Ye et al., 2019; Simon et al., 2020). The low contribution of these compounds in the gas phase might be reflected in the particle phase. Additionally, the heating cycle that evaporates all the particulate material collected on the filament can potentially result in the thermal decomposition of some of the larger molecular-weight compounds. Therefore, it is possible that a break-up of some molecules occurs.

3.3 Volatility distribution of particle-phase compounds

Figure 5 shows the volatility distribution of the oxidation products in the particle phase measured by the TD-DMA for the experiments reported in this work (in linear scale Fig. S4 in the Supplement). The volatility calculation was done by using the parametrization introduced by Donahue et al. (2011) and modified by Stolzenburg et al. (2018) and Simon et al. (2020). It is expressed as the logarithm of the saturation mass concentration, $\log_{10} c_i^*$, in micrograms per cubic meters ($\mu g\,m^{-3}$), from the number of carbon and oxygen atoms in the specific molecules. This approximation parameterizes the volatility of a molecule based on its functional groups and a free parameter to distinguish between monomers and dimers.

In Fig. 5 each volatility bin contains the summed intensity of the oxidation products measured in the particle phase, and it is normalized by the total signal. Most of the classes are distributed over the range of the volatility values that are displayed, and at lower temperatures, lower volatilities are observed (experiments *α-50,20* and *α-50,60*). This observation is due to the fact of the strong dependency between saturation concentration and temperature. Essentially, there are no significant differences between the experiments at $-30\,^{\circ}$C

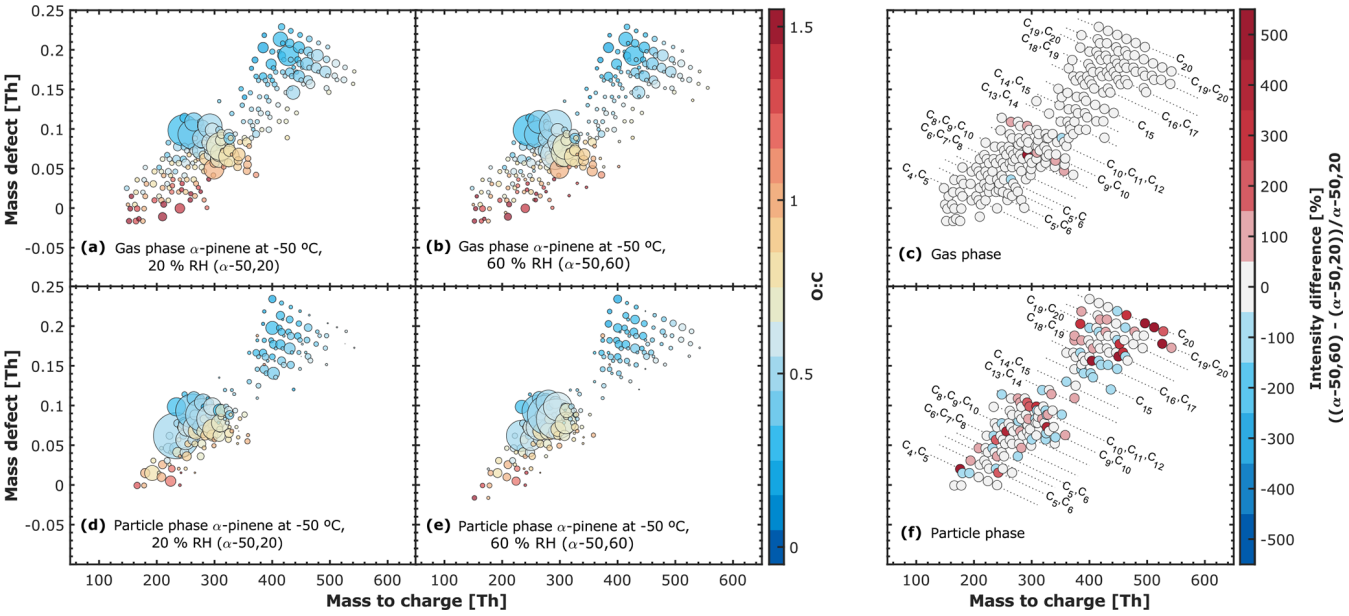

Figure 4. Mass defect plots of gas and particle phase and the intensity difference between each phase. Both phases are measured with a nitrate CI-APi-TOF mass spectrometer, while the TD-DMA is coupled to it for particle-phase measurements. **(a)** Gas and **(d)** particle phase for α-pinene oxidation products at $-50\,^{\circ}$C and 20 % RH (α-50,20). **(b)** Gas and **(e)** particle phase for α-pinene oxidation products at $-50\,^{\circ}$C and 60 % RH (α-50,60). The level of α-pinene was between 1 and 8 ppbv, and ozone levels were $\sim$ 100 ppbv in both experiments. The symbol sizes in **(a)**, **(b)**, **(d)**, and **(e)** are the intensities normalized by the total signal in each system. The intensity difference in the gas phase **(c)** and in the particle phase **(f)** is indicated as ((α-50,60)$-$ (α-50,20)) / α-50,20. The color scale represents the difference in percent.

(*α-30,20* compared with *αIP-30,20*) or between the experiments at $-50\,^{\circ}$C (*α-50,20* compared with *α-50,60*), which indicates that temperature is the main parameter affecting the volatility distribution for the experiments reported here.

We classified the volatility bins according to the regimes proposed by Donahue et al. (2012) and Schervish and Donahue (2020) and calculated the corresponding fractions (Table 2). Overall, the particle-phase-detected compounds correspond mainly to low-volatility organic compounds (LVOCs) and extremely low-volatility compounds (ELVOCs) by explaining more than 80 % of the signals, while ultralow-volatility organic compounds (ULVOCs) represent only a small fraction (between 6 % and 17 %). With this parametrization, we are able to approximate the saturation mass concentration for the particle-phase compounds measured using the TD-DMA in the CLOUD chamber. For this parametrization, we assume that the elemental composition is one of the main parameters to take into account.

3.4 Nucleation rates as a function of the total HOM concentration

Previous CLOUD studies have reported nucleation rates ($J_{1.7\,\mathrm{nm}}$) as a function of the total HOM concentration from α-pinene oxidation for different temperatures and gas mixtures (Kirkby et al., 2016; Heinritzi et al., 2020; Simon et al., 2020). For the experiments discussed in the present study, the nucleation rates have not been reported yet. For this reason, Table 1 gives an overview of the experimental conditions for the experiments *α-30,20*, *αIP-30,20*, *α-50,20*, and *α-50,60*; it further includes the HOM total concentration and derived $J_{1.7\,\mathrm{nm}}$ from the PSM data (see method description in Sect. 2.4).

3.4.1 New particle formation on pure α-pinene experiments

Figure 6 displays pure biogenic $J_{1.7\,\mathrm{nm}}$ vs total HOM concentration at different temperatures for pure α-pinene (Simon et al., 2020) in which it can be seen that the total HOM concentration and their nucleation rates have a strong dependence on the temperature. As the temperature decreases, the nucleation rates increase strongly for a given HOM concentration. In other terms, the total HOM concentration needed to reach the same nucleation rate can be up to 2 orders of magnitude higher for $+25\,^{\circ}$C compared to $-50\,^{\circ}$C. As described by Simon et al. (2020), this can be attributed to the reduction in volatility with decreasing temperature. In other words, at low temperatures, molecules with less oxygen content can lead to the same nucleation rate as more highly oxygenated molecules at higher temperatures. Additionally, Fig. 6 includes the data points at -30 and $-50\,^{\circ}$C from pure α-pinene experiments reported in this study (*α-30,20*, *α-50,20* and *α-50,60*). However, it can be observed that they do not follow the trend at their corresponding temperature.

Table 2. Bin volatility fractions for the different experiments.

Experiment	T [°C]	RH [%]	ULVOCs [%]	ELVOCs [%]	LVOCs [%]	SVOCs [%]	IVOCs [%]
αIP-30,20	−30	20	8.6	28.3	59.1	3.8	0.2
α-30,20	−30	20	5.9	44.1	48.1	1.9	0
α-50,20	−50	20	16.5	36.4	46.1	1.0	0
α-50,60	−50	60	13.8	50.6	34.8	0.8	0

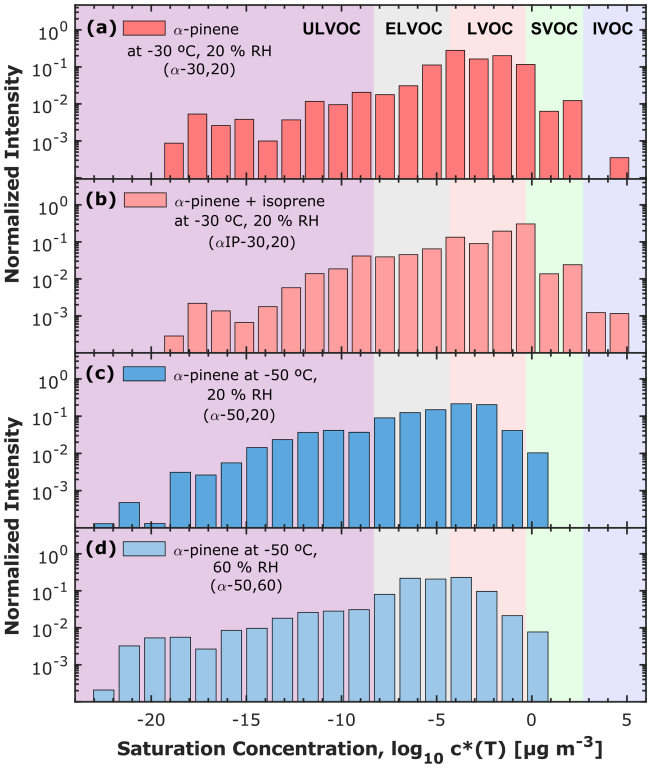

Figure 5. TD-DMA volatility distribution of the measured oxidation products in the particle phase for four different experiments: **(a)** α-pinene at −30 °C and 20 % RH (α-30,20), **(b)** α-pinene + isoprene at −30 °C and 20 % RH (αIP-30,20), **(c)** α-pinene at −50 °C and 20 % RH (α-50,20), and **(d)** α-pinene at −50 °C and 60 % RH (α-50,60). Every individual volatility bin includes the sum of the intensity for the oxidation products normalized by the total signal in each system. Every individual volatility bin is defined at 300 K, shifted, and widened according to their corresponding temperature. The color bands in the background indicate the volatility regimes as in Donahue et al. (2012) and in Schervish and Donahue (2020). The normalized intensity is dimensionless. Nevertheless, it should be noted that the particle-phase signal is given in normalized counts per second integrated over the evaporation time (ncps/s).

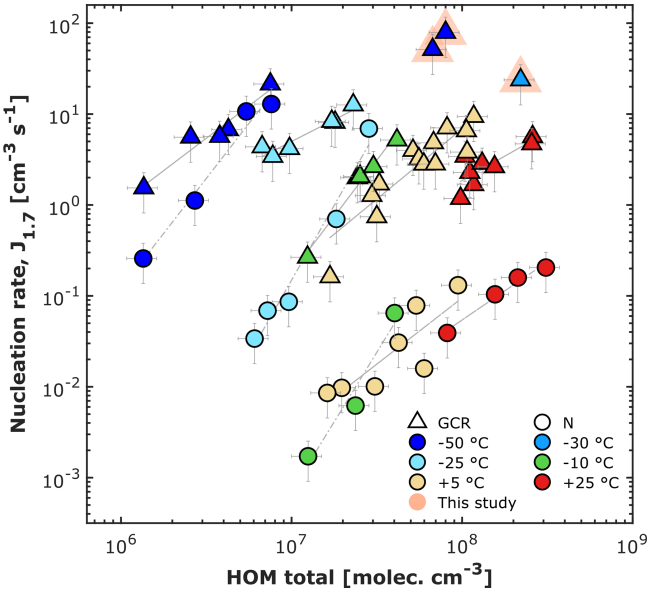

Figure 6. Pure biogenic nucleation rates of pure α-pinene at 1.7 nm diameter against total HOM concentration at different temperatures. The HOM total is defined as the sum of C_5, C_{10}, C_{15} and C_{20} carbon classes. Triangles represent galactic cosmic ray (GCR) conditions, and circles represent neutral conditions. Data points at −50, −25, −10, +5, and +25 °C are from Simon et al. (2020). The points with orange marker on the background are the contribution of this study (experiments α-30,20, α-50,20 and α-50,60). Solid and dashed lines represent power-law fits to GCR and neutral conditions. Bars indicate 1σ run-to-run experimental uncertainty. The overall systematic-scale uncertainty of HOMs of +78 % and −68 % is not shown.

For the pure α-pinene systems (*α-30,20*, *α-50,20*, and *α-50,60*) and complementary pure α-pinene experiments at +5 °C and at −10 °C, we have calculated the HOM yield as described in Simon et al. (2020) and found that the resulting values are higher than previously reported (see Fig. S5 in the Supplement). In order to investigate a possible reason for this finding, we have chosen two representative experiments at −10 °C and 80 % RH to 90 % RH with different levels of α-pinene and ozone. Figure 7 shows the mass defect plots for the gas-phase chemical composition of the oxidation products. In one experiment (Fig. 7a) α-pinene and the ozone mixing ratio were between 0.2 and 0.8 ppbv and 40 and 50 ppbv, respectively, while for the second experiment (Fig. 7b) the mixing ratios were 2 to 3 ppbv and 100 ppbv, respectively. From Fig. 7c, it can be concluded that the formation of HOMs with low oxygen content is favored when

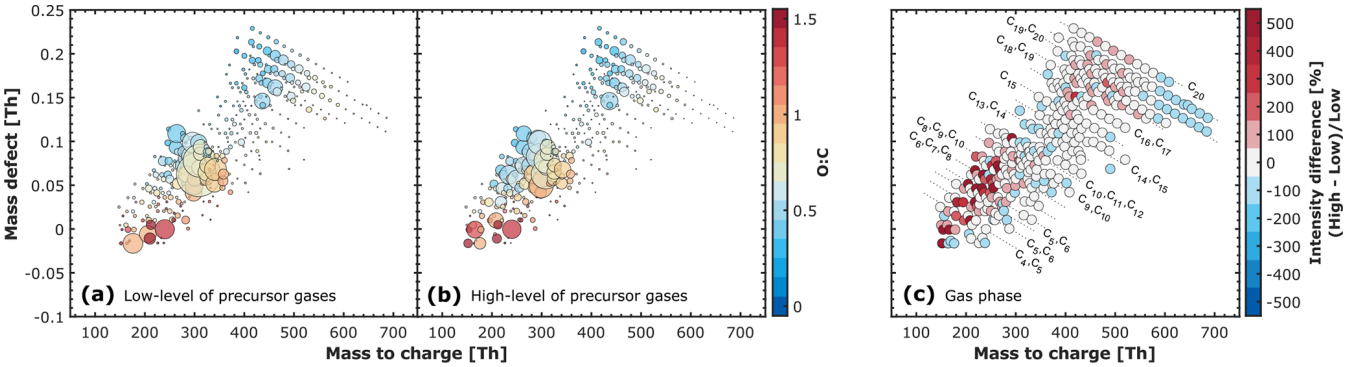

Figure 7. Mass defect plots of gas phase for two different systems and the normalized difference between them. Gas phase is measured with a nitrate CI-APi-TOF mass spectrometer. **(a)** α-Pinene oxidation products at $-10\,^{\circ}$C and 90 % RH at low level of precursor gases and **(b)** α-pinene oxidation products at $-10\,^{\circ}$C and 80 % RH at high level of precursor gases. α-pinene was 0.2–0.8 ppbv and ozone $\sim$ 40–50 ppbv in **(a)**, and α-pinene was 2–3 ppbv and ozone $\sim$ 100 ppbv in **(b)**. The symbol sizes and colors in **(a)** and **(b)** represent the intensities normalized by the total signal in each system. **(c)** The difference between the normalized signals shown in **(a)** and **(b)** is represented by the color scale.

the α-pinene and ozone mixing ratio are higher (relative to the system at low levels of precursor gases). An explanation for this is that the high concentration of RO_2 enhances the terminating reactions before the autoxidation can lead to high oxygen content for the products. As the compounds with low oxygen content tend to have higher saturation vapor pressures, they do not contribute efficiently to new particle formation. For this reason, a given total HOM concentration is not unambiguously tied to a nucleation rate (even at constant temperature). The magnitude of the precursor gas mixing ratio (more specifically the full volatility distribution of the products and not just the simple measure of total HOM concentration) also needs to be taken into account (see Fig. S6 in the Supplement). In summary, the lower $J_{1.7\,\mathrm{nm}}$ values compared with previous studies are very likely due to the higher α-pinene and ozone mixing ratios used in the present study. There are several compounds with low oxygen content that contribute to the total HOM concentration in the gas phase, while these do not contribute to the formation of new particles.

3.4.2 The influence of isoprene on new particle formation

In order to make the present study comparable with other studies that reported a suppression effect of isoprene on biogenic new particle formation, the values of the isoprene-to-monoterpene carbon ratio (R) are also provided in Table 1. Here and in previous studies, R is essentially the ratio between isoprene and α-pinene; for experiment *αIP-30,20*, R is equal to 14.4 and 6.1 (for two steady-state periods in *αIP-30,20*).

Figure 8 shows pure biogenic nucleation rates at 1.7 nm against total HOM concentration at different temperatures for the α-pinene and α-pinene + isoprene systems (Kirkby

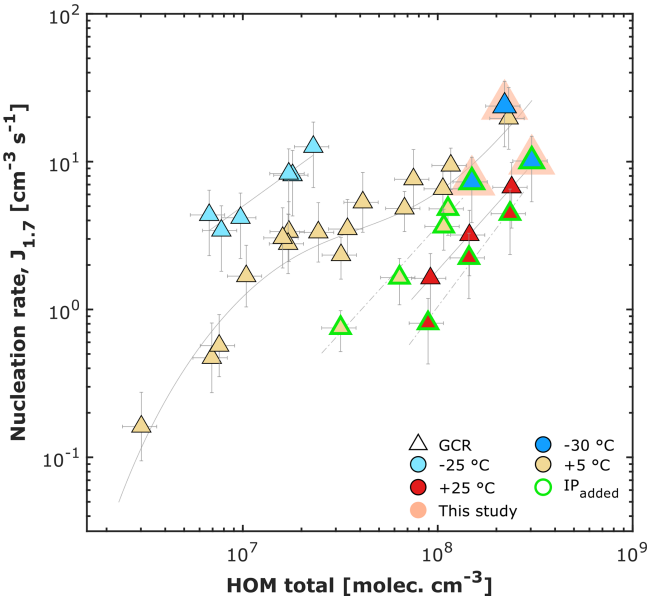

Figure 8. Pure biogenic nucleation rates at 1.7 nm diameter against total HOM concentration at different temperatures for α-pinene and α-pinene + isoprene systems. The HOM total is defined as the sum of C_5, C_{10}, C_{15}, and C_{20} carbon classes. Triangles represent galactic cosmic ray (GCR) conditions. Data points at +5 and +25 °C are from Kirkby et al. (2016) and Heinritzi et al. (2020). Data points at $-25\,^{\circ}$C are from Simon et al. (2020). The value of isoprene-to-monoterpene carbon ratio (R) varies from 1.5 to 6.5 for Heinritzi et al. (2020), and R is equal to 14.4 and 6.1 for this study. The points with orange marker on the background indicate the contribution of this work. Solid lines represent power-law fits to GCR conditions of the systems with α-pinene only, and dashed lines are the power-law fits of the systems with isoprene added. Bars indicate 1σ run-to-run experimental uncertainty. The overall systematic-scale uncertainty of HOMs of +78 % and −68 % is not shown.

et al., 2016; Heinritzi et al., 2020; Simon et al., 2020). How rapidly particles are formed in a pure biogenic system depends strongly on the temperature and on the ion conditions. In general, we observe increasing nucleation rates at lower temperatures and at GCR conditions. The presence of isoprene lowers the nucleation rate (relative to the pure α-pinene system at similar conditions); this is known as isoprene suppression of new particle formation. In this regard, there is a suppression on the new particle formation caused by adding isoprene on an α-pinene system at $-30\,^{\circ}$C and 20 % RH. However, it has been reported that the suppression effect is stronger when α-pinene is lower (and R is higher; see Fig. S7 in the Supplement). For instance, in a plant chamber experiment $R = 19.5$ resulted in no significant new particle formation (Kiendler-Scharr et al., 2009). Additionally, in the Michigan forest with $R = 26.4$, NPF events did not occur frequently (Kanawade et al., 2011). Lee et al. (2016) reported observations of NPF suppression in a rural forest in Alabama, where $R = 2.0$. However, one has to consider that the suppression effect at a given value of R likely decreases as temperature decreases and so does the saturation vapor pressure of the oxidation products.

4 Conclusions

In this study, we demonstrated the suitability of a thermal desorption differential mobility analyzer (TD-DMA) coupled to a nitrate chemical ionization–atmospheric pressure interface–time-of-flight (CI-APi-TOF) mass spectrometer for measuring HOMs in newly formed nano aerosol particles. Together with the nitrate CI-APi-TOF mass spectrometer, this setup is capable of measuring the gas and particle phase, allowing for a direct comparison as both measurements use the identical chemical ionization and detector.

For the pure biogenic NPF experiments performed at -50 and $-30\,^{\circ}$C in the CLOUD chamber at CERN, we detected in the particle phase (diameter up to ~ 100 nm) compounds such as $C_{10}H_{16}O_{3-9}$, and $C_{20}H_{32}O_{5-13}$. Especially for the system with isoprene added, C_5 ($C_5H_{10}O_{5-7}$) and C_{15} compounds ($C_{15}H_{24}O_{5-10}$) can be an important fingerprint to identify secondary organic aerosol from this biogenic source. Based on the elemental composition, we calculated the saturation mass concentration, and according to the volatility regimes, the particle-phase compounds correspond mainly to low-volatility organic compounds (LVOCs), extremely low-volatility compounds (ELVOCs), and ultralow-volatility organic compounds (ULVOCs).

We also showed that at $-30\,^{\circ}$C and an isoprene-to-monoterpene carbon ratio $R = 14.4$ and 6.1, there is a reduction of the nucleation rate (compared to the pure α-pinene system at similar conditions). In this way, isoprene suppresses NPF at $-30\,^{\circ}$C. Nevertheless, this suppression effect can be stronger at higher temperatures and at high R.

Lastly, the lower $J_{1.7}$ values compared with previous studies are very likely due to the higher α-pinene and ozone mixing ratios used in the present study. There are several compounds with low oxygen content that contribute to the total HOM concentration in the gas phase, while these do not contribute to the formation of new particles. For this reason, a given total HOM concentration is not unambiguously tied to a nucleation rate (even at constant temperature). The magnitude of the precursor gas mixing ratio, and thus the full volatility distribution, also needs to be taken into account.

Data availability. Data related to this article are available upon request to the corresponding authors.

Supplement. The supplement related to this article is available online at: https://doi.org/10.5194/acp-21-17099-2021-supplement.

Author contributions. LC, BR, GM, MaS, ACW, TM, MG, FA, RB, BB, ZB, RC, BC, JD, HF, LGC, XCH, VH, WK, HL, CPL, BL, NGAM, VM, HEM, RM, RLM, BM, UM, AO, JP, MP, AAP, WS, BS, JS, DS, YS, MiS, YJT, PT, AT, SV, MW, DSW, SKW, AW, WY, WY, MZW, UB, IEH, RCF, KH, JK, MK, KL, OM, RV, PMW, AK, and JC prepared the CLOUD facility and measurement instruments. LC, BR, GM, ACW, TM, MG, AA, FA, RB, BB, JD, LGC, VH, HL, CPL, NGAM, VM, RM, DM, RLM, BM, UM, WS, BS, DS, MiS, CT, YJT, AT, DSW, SKW, MZW, IEH, JK, RV, and PMW collected the data. LC, BR, MH, GM, FA, LD, RLM, UM, WS, BS, SKW, and RCF analyzed the data. LC, MH, MSim, ACW, TM, MG, LD, RLM, UM, MiS, WS, DS, UB, IEH, RCF, AH, KH, JK, MK, OM, HS, NMD, AK, and JC contributed to the scientific discussion and interpretation of the results. LC, MH, ACW, LD, UB, RCF, HS, NMD, AK, and JC contributed to the writing of the manuscript.

Competing interests. The contact author has declared that neither they nor their co-authors have any competing interests.

Disclaimer. Publisher's note: Copernicus Publications remains neutral with regard to jurisdictional claims in published maps and institutional affiliations.

Acknowledgements. We thank CERN for providing the CLOUD facility to perform the experiments and the CLOUD community for supporting this study. We especially would like to thank Katja Ivanova, Timo Keber, Frank Malkemper, Robert Sitals, Hanna Elina Manninen, Antti Onnela, and Robert Kristic for their contributions to the experiment.

Financial support. This research has been supported by the European Commission, Research Executive Agency (grant no. CLOUD-MOTION (764991)), the Bundesministerium für Bildung

und Forschung (grant no. CLOUD-16, 01LK1601A), the National Science Foundation (grant nos. AGS-1801280, AGS-1801574, and AGS-1801897), and the Schweizerischer Nationalfonds zur Förderung der Wissenschaftlichen Forschung (grant nos. 20020_172602 and BSSGI0_155846).

This open-access publication was funded by the Goethe University Frankfurt.

Review statement. This paper was edited by Kelley Barsanti and reviewed by two anonymous referees.

References

Bianchi, F., Kurtèin, T., Riva, M., Mohr, C., Rissanen, M. P., Roldin, P., Berndt, T., Crounse, J. D., Wennberg, P. O., and Mentel, T. F.: Highly oxygenated organic molecules (HOM) from gas-phase autoxidation involving peroxy radicals: A key contributor to atmospheric aerosol, Chem. Rev., 119, 3472–3509, 2019.

Breitenlechner, M., Fischer, L., Hainer, M., Heinritzi, M., Curtius, J., and Hansel, A.: PTR3: An Instrument for Studying the Lifecycle of Reactive Organic Carbon in the Atmosphere, Anal. Chem., 89, 5824–5831, 10.1021/acs.analchem.6b05110, 2017.

Champion, W. M., Rothfuss, N. E., Petters, M. D., and Grieshop, A. P.: Volatility and Viscosity Are Correlated in Terpene Secondary Organic Aerosol Formed in a Flow Reactor, Environ. Sci. Technol. Lett., 6, 513–519, https://doi.org/10.1021/acs.estlett.9b00412, 2019.

Cocker III, D. R., Clegg, S. L., Flagan, R. C., and Seinfeld, J. H.: The effect of water on gas–particle partitioning of secondary organic aerosol, Part I: α-pinene/ozone system, Atmos. Environ., 35, 6049–6072, https://doi.org/10.1016/j.jes.2017.10.011, 2001.

Dada, L., Lehtipalo, K., Kontkanen, J., Nieminen, T., Baalbaki, R., Ahonen, L., Duplissy, J., Yan, C., Chu, B., Petäjä, T., Lehtinen, K., Kerminen, V.-M., Kulmala, M., and Kangasluoma, J.: Formation and growth of sub-3-nm aerosol particles in experimental chambers, Nat. Protoc., 15, 1013–1040, https://doi.org/10.1038/s41596-019-0274-z, 2020.

Donahue, N. M., Epstein, S. A., Pandis, S. N., and Robinson, A. L.: A two-dimensional volatility basis set: 1. organic-aerosol mixing thermodynamics, Atmos. Chem. Phys., 11, 3303–3318, https://doi.org/10.5194/acp-11-3303-2011, 2011.

Donahue, N. M., Kroll, J. H., Pandis, S. N., and Robinson, A. L.: A two-dimensional volatility basis set – Part 2: Diagnostics of organic-aerosol evolution, Atmos. Chem. Phys., 12, 615–634, https://doi.org/10.5194/acp-12-615-2012, 2012.

Duplissy, J., Merikanto, J., Franchin, A., Tsagkogeorgas, G., Kangasluoma, J., Wimmer, D., Vuollekoski, H., Schobesberger, S., Lehtipalo, K., Flagan, R. C., Brus, D., Donahue, N. M., Vehkamäki, H., Almeida, J., Amorim, A., Barmet, P., Bianchi, F., Breitenlechner, M., Dunne, E. M., Guida, R., Henschel, H., Junninen, H., Kirkby, J., Kürten, A., Kupc, A., Määttänen, A., Makhmutov, V., Mathot, S., Nieminen, T., Onnela, A., Praplan, A. P., Riccobono, F., Rondo, L., Steiner, G., Tome, A., Walther, H., Baltensperger, U., Carslaw, K. S., Dommen, J., Hansel, A., Petäjä, T., Sipilä, M., Stratmann, F., Vrtala, A., Wagner, P. E., Worsnop, D. R., Curtius, J., and Kulmala, M.: Effect of ions on sulfuric acid-water binary particle formation: 2. Experimental data and comparison with QC-normalized classical nucleation theory, J. Geophys. Res.-Atmos., 121, 1752–1775, https://doi.org/10.1002/2015JD023539, 2016.

Ehn, M., Thornton, J. A., Kleist, E., Sipila, M., Junninen, H., Pullinen, I., Springer, M., Rubach, F., Tillmann, R., Lee, B., Lopez-Hilfiker, F., Andres, S., Acir, I.-H., Rissanen, M., Jokinen, T., Schobesberger, S., Kangasluoma, J., Kontkanen, J., Nieminen, T., Kurten, T., Nielsen, L. B., Jorgensen, S., Kjaergaard, H. G., Canagaratna, M., Maso, M. D., Berndt, T., Petaja, T., Wahner, A., Kerminen, V.-M., Kulmala, M., Worsnop, D. R., Wildt, J., and Mentel, T. F.: A large source of low-volatility secondary organic aerosol, Nature, 506, 476–479, https://doi.org/10.1038/nature13032, 2014.

Galeazzo, T., Valorso, R., Li, Y., Camredon, M., Aumont, B., and Shiraiwa, M.: Estimation of secondary organic aerosol viscosity from explicit modeling of gas-phase oxidation of isoprene and α-pinene, Atmos. Chem. Phys., 21, 10199–10213, https://doi.org/10.5194/acp-21-10199-2021, 2021.

Gordon, H., Kirkby, J., Baltensperger, U., Bianchi, F., Breitenlechner, M., Curtius, J., Dias, A., Dommen, J., Donahue, N. M., Dunne, E. M., Duplissy, J., Ehrhart, S., Flagan, R. C., Frege, C., Fuchs, C., Hansel, A., Hoyle, C. R., Kulmala, M., Kürten, A., Lehtipalo, K., Makhmutov, V., Molteni, U., Rissanen, M. P., Stozkhov, Y., Tröstl, J., Tsagkogeorgas, G., Wagner, R., Williamson, C., Wimmer, D., Winkler, P. M., Yan, C., and Carslaw, K. S.: Causes and importance of new particle formation in the present-day and preindustrial atmospheres, J. Geophys. Res.-Atmos., 122, 8739–8760, https://doi.org/10.1002/2017jd026844, 2017.

Graus, M., Müller, M., and Hansel, A.: High resolution PTR-TOF: Quantification and formula confirmation of VOC in real time, J. Am. Soc. Mass Sp., 21, 1037–1044, https://doi.org/10.1016/j.jasms.2010.02.006, 2010.

Grayson, J. W., Zhang, Y., Mutzel, A., Renbaum-Wolff, L., Böge, O., Kamal, S., Herrmann, H., Martin, S. T., and Bertram, A. K.: Effect of varying experimental conditions on the viscosity of α-pinene derived secondary organic material, Atmos. Chem. Phys., 16, 6027–6040, https://doi.org/10.5194/acp-16-6027-2016, 2016.

He, X.-C., Tham, Y. J., Dada, L., Wang, M., Finkenzeller, H., Stolzenburg, D., Iyer, S., Simon, M., Kürten, A., Shen, J., Rörup, B., Rissanen, M., Schobesberger, S., Baalbaki, R., Wang, D. S., Koenig, T. K., Jokinen, T., Sarnela, N., Beck, L. J., Almeida, J., Amanatidis, S., Amorim, A., Ataei, F., Baccarini, A., Bertozzi, B., Bianchi, F., Brilke, S., Caudillo, L., Chen, D., Chiu, R., Chu, B., Dias, A., Ding, A., Dommen, J., Duplissy, J., El Haddad, I., Gonzalez Carracedo, L., Granzin, M., Hansel, A., Heinritzi, M., Hofbauer, V., Junninen, H., Kangasluoma, J., Kemppainen, D., Kim, C., Kong, W., Krechmer, J. E., Kvashin, A., Laitinen, T., Lamkaddam, H., Lee, C. P., Lehtipalo, K., Leiminger, M., Li, Z., Makhmutov, V., Manninen, H. E., Marie, G., Marten, R., Mathot, S., Mauldin, R. L., Mentler, B., Möhler, O., Müller, T., Nie, W., Onnela, A., Petäjä, T., Pfeifer, J., Philippov, M., Ranjithkumar, A., Saiz-Lopez, A., Salma, I., Scholz, W., Schuchmann, S., Schulze, B., Steiner, G., Stozhkov, Y., Tauber, C., Tomé, A., Thakur, R. C., Väisänen, O., Vazquez-Pufleau, M., Wagner, A. C., Wang, Y., Weber, S. K., Winkler, P. M., Wu, Y., Xiao, M., Yan, C., Ye, Q., Ylisirniö, A., Zauner-Wieczorek, M., Zha, Q.,

Zhou, P., Flagan, R. C., Curtius, J., Baltensperger, U., Kulmala, M., Kerminen, V.-M., Kurtén, T., Donahue, N. M., Volkamer, R., Kirkby, J., Worsnop, D. R., and Sipilä, M.: Role of iodine oxoacids in atmospheric aerosol nucleation, Science, 371, 589–595, https://doi.org/10.1126/science.abe0298, 2021.

Heinritzi, M., Simon, M., Steiner, G., Wagner, A. C., Kürten, A., Hansel, A., and Curtius, J.: Characterization of the mass-dependent transmission efficiency of a CIMS, Atmos. Meas. Tech., 9, 1449–1460, https://doi.org/10.5194/amt-9-1449-2016, 2016.

Heinritzi, M., Dada, L., Simon, M., Stolzenburg, D., Wagner, A. C., Fischer, L., Ahonen, L. R., Amanatidis, S., Baalbaki, R., Baccarini, A., Bauer, P. S., Baumgartner, B., Bianchi, F., Brilke, S., Chen, D., Chiu, R., Dias, A., Dommen, J., Duplissy, J., Finkenzeller, H., Frege, C., Fuchs, C., Garmash, O., Gordon, H., Granzin, M., El Haddad, I., He, X., Helm, J., Hofbauer, V., Hoyle, C. R., Kangasluoma, J., Keber, T., Kim, C., Kürten, A., Lamkaddam, H., Laurila, T. M., Lampilahti, J., Lee, C. P., Lehtipalo, K., Leiminger, M., Mai, H., Makhmutov, V., Manninen, H. E., Marten, R., Mathot, S., Mauldin, R. L., Mentler, B., Molteni, U., Müller, T., Nie, W., Nieminen, T., Onnela, A., Partoll, E., Passananti, M., Petäjä, T., Pfeifer, J., Pospisilova, V., Quéléver, L. L. J., Rissanen, M. P., Rose, C., Schobesberger, S., Scholz, W., Scholze, K., Sipilä, M., Steiner, G., Stozhkov, Y., Tauber, C., Tham, Y. J., Vazquez-Pufleau, M., Virtanen, A., Vogel, A. L., Volkamer, R., Wagner, R., Wang, M., Weitz, L., Wimmer, D., Xiao, M., Yan, C., Ye, P., Zha, Q., Zhou, X., Amorim, A., Baltensperger, U., Hansel, A., Kulmala, M., Tomé, A., Winkler, P. M., Worsnop, D. R., Donahue, N. M., Kirkby, J., and Curtius, J.: Molecular understanding of the suppression of new-particle formation by isoprene, Atmos. Chem. Phys., 20, 11809–11821, https://doi.org/10.5194/acp-20-11809-2020, 2020.

Huang, W., Saathoff, H., Pajunoja, A., Shen, X., Naumann, K. H., Wagner, R., Virtanen, A., Leisner, T., and Mohr, C.: α-Pinene secondary organic aerosol at low temperature: chemical composition and implications for particle viscosity, Atmos. Chem. Phys., 18, 2883–2898, https://doi.org/10.5194/acp-18-2883-2018, 2018.

Jokinen, T., Sipilä, M., Junninen, H., Ehn, M., Lönn, G., Hakala, J., Petäjä, T., Mauldin Iii, R. L., Kulmala, M., and Worsnop, D. R.: Atmospheric sulphuric acid and neutral cluster measurements using CI-APi-TOF, Atmos. Chem. Phys., 12, 4117–4125, https://doi.org/10.5194/acp-12-4117-2012, 2012.

Kanawade, V. P., Jobson, B. T., Guenther, A. B., Erupe, M. E., Pressley, S. N., Tripathi, S. N., and Lee, S. H.: Isoprene suppression of new particle formation in a mixed deciduous forest, Atmos. Chem. Phys., 11, 6013–6027, https://doi.org/10.5194/acp-11-6013-2011, 2011.

Kiendler-Scharr, A., Wildt, J., Maso, M. D., Hohaus, T., Kleist, E., Mentel, T. F., Tillmann, R., Uerlings, R., Schurr, U., and Wahner, A.: New particle formation in forests inhibited by isoprene emissions, Nature, 461, 381–384, 2009.

Kirkby, J., Curtius, J., Almeida, J., Dunne, E., Duplissy, J., Ehrhart, S., Franchin, A., Gagné, S., Ickes, L., Kürten, A., Kupc, A., Metzger, A., Riccobono, F., Rondo, L., Schobesberger, S., Tsagkogeorgas, G., Wimmer, D., Amorim, A., Bianchi, F., Breitenlechner, M., David, A., Dommen, J., Downard, A., Ehn, M., Flagan, R. C., Haider, S., Hansel, A., Hauser, D., Jud, W., Junninen, H., Kreissl, F., Kvashin, A., Laaksonen, A., Lehtipalo, K., Lima, J., Lovejoy, E. R., Makhmutov, V., Mathot, S., Mikkilä, J., Minginette, P., Mogo, S., Nieminen, T., Onnela, A., Pereira, P., Petäjä, T., Schnitzhofer, R., Seinfeld, J. H., Sipilä, M., Stozhkov, Y., Stratmann, F., Tomé, A., Vanhanen, J., Viisanen, Y., Vrtala, A., Wagner, P. E., Walther, H., Weingartner, E., Wex, H., Winkler, P. M., Carslaw, K. S., Worsnop, D. R., Baltensperger, U., and Kulmala, M.: Role of sulphuric acid, ammonia and galactic cosmic rays in atmospheric aerosol nucleation, Nature, 476, 429–433, https://doi.org/10.1038/nature10343, 2011.

Kirkby, J., Duplissy, J., Sengupta, K., Frege, C., Gordon, H., Williamson, C., Heinritzi, M., Simon, M., Yan, C., Almeida, J., Tröstl, J., Nieminen, T., Ortega, I. K., Wagner, R., Adamov, A., Amorim, A., Bernhammer, A.-K., Bianchi, F., Breitenlechner, M., Brilke, S., Chen, X., Craven, J., Dias, A., Ehrhart, S., Flagan, R. C., Franchin, A., Fuchs, C., Guida, R., Hakala, J., Hoyle, C. R., Jokinen, T., Junninen, H., Kangasluoma, J., Kim, J., Krapf, M., Kürten, A., Laaksonen, A., Lehtipalo, K., Makhmutov, V., Mathot, S., Molteni, U., Onnela, A., Peräkylä, O., Piel, F., Petäjä, T., Praplan, A. P., Pringle, K., Rap, A., Richards, N. A. D., Riipinen, I., Rissanen, M. P., Rondo, L., Sarnela, N., Schobesberger, S., Scott, C. E., Seinfeld, J. H., Sipilä, M., Steiner, G., Stozhkov, Y., Stratmann, F., Tomé, A., Virtanen, A., Vogel, A. L., Wagner, A. C., Wagner, P. E., Weingartner, E., Wimmer, D., Winkler, P. M., Ye, P., Zhang, X., Hansel, A., Dommen, J., Donahue, N. M., Worsnop, D. R., Baltensperger, U., Kulmala, M., Carslaw, K. S., and Curtius, J.: Ion-induced nucleation of pure biogenic particles, Nature, 533, 521–526, https://doi.org/10.1038/nature17953, 2016.

Kristensen, K., Jensen, L., Glasius, M., and Bilde, M.: The effect of sub-zero temperature on the formation and composition of secondary organic aerosol from ozonolysis of alpha-pinene, Environ. Sci. Proc. Imp., 19, 1220–1234, 2017.

Kürten, A., Rondo, L., Ehrhart, S., and Curtius, J.: Performance of a corona ion source for measurement of sulfuric acid by chemical ionization mass spectrometry, Atmos. Meas. Tech., 4, 437–443, https://doi.org/10.5194/amt-4-437-2011, 2011.

Kürten, A., Rondo, L., Ehrhart, S., and Curtius, J.: Calibration of a Chemical Ionization Mass Spectrometer for the Measurement of Gaseous Sulfuric Acid, J. Phys. Chem. A, 116, 6375–6386, https://doi.org/10.1021/jp212123n, 2012.

Kürten, A., Jokinen, T., Simon, M., Sipilä, M., Sarnela, N., Junninen, H., Adamov, A., Almeida, J., Amorim, A., Bianchi, F., Breitenlechner, M., Dommen, J., Donahue, N. M., Duplissy, J., Ehrhart, S., Flagan, R. C., Franchin, A., Hakala, J., Hansel, A., Heinritzi, M., Hutterli, M., Kangasluoma, J., Kirkby, J., Laaksonen, A., Lehtipalo, K., Leiminger, M., Makhmutov, V., Mathot, S., Onnela, A., Petäjä, T., Praplan, A. P., Riccobono, F., Rissanen, M. P., Rondo, L., Schobesberger, S., Seinfeld, J. H., Steiner, G., Tomé, A., Tröstl, J., Winkler, P. M., Williamson, C., Wimmer, D., Ye, P., Baltensperger, U., Carslaw, K. S., Kulmala, M., Worsnop, D. R., and Curtius, J.: Neutral molecular cluster formation of sulfuric acid–dimethylamine observed in real time under atmospheric conditions, P. Natl. Acad. Sci. USA, 111, 15019–15024, https://doi.org/10.1073/pnas.1404853111, 2014.

Lee, S.-H., Uin, J., Guenther, A. B., de Gouw, J. A., Yu, F., Nadykto, A. B., Herb, J., Ng, N. L., Koss, A., Brune, W. H., Baumann, K., Kanawade, V. P., Keutsch, F. N., Nenes, A., Olsen, K., Goldstein, A., and Ouyang, Q.: Isoprene suppression of new particle formation: Potential mechanisms and

implications, J. Geophys. Res.-Atmos., 121, 14621–614635, https://doi.org/10.1002/2016JD024844, 2016.

Lehtipalo, K., Yan, C., Dada, L., Bianchi, F., Xiao, M., Wagner, R., Stolzenburg, D., Ahonen, L. R., Amorim, A., Baccarini, A., Bauer, P. S., Baumgartner, B., Bergen, A., Bernhammer, A.-K., Breitenlechner, M., Brilke, S., Buchholz, A., Mazon, S. B., Chen, D., Chen, X., Dias, A., Dommen, J., Draper, D. C., Duplissy, J., Ehn, M., Finkenzeller, H., Fischer, L., Frege, C., Fuchs, C., Garmash, O., Gordon, H., Hakala, J., He, X., Heikkinen, L., Heinritzi, M., Helm, J. C., Hofbauer, V., Hoyle, C. R., Jokinen, T., Kangasluoma, J., Kerminen, V.-M., Kim, C., Kirkby, J., Kontkanen, J., Kürten, A., Lawler, M. J., Mai, H., Mathot, S., Mauldin, R. L., Molteni, U., Nichman, L., Nie, W., Nieminen, T., Ojdanic, A., Onnela, A., Passananti, M., Petäjä, T., Piel, F., Pospisilova, V., Quéléver, L. L. J., Rissanen, M. P., Rose, C., Sarnela, N., Schallhart, S., Schuchmann, S., Sengupta, K., Simon, M., Sipilä, M., Tauber, C., Tomé, A., Tröstl, J., Väisänen, O., Vogel, A. L., Volkamer, R., Wagner, A. C., Wang, M., Weitz, L., Wimmer, D., Ye, P., Ylisirniö, A., Zha, Q., Carslaw, K. S., Curtius, J., Donahue, N. M., Flagan, R. C., Hansel, A., Riipinen, I., Virtanen, A., Winkler, P. M., Baltensperger, U., Kulmala, M., and Worsnop, D. R.: Multicomponent new particle formation from sulfuric acid, ammonia, and biogenic vapors, Sci. Adv., 4, eaau5363, https://doi.org/10.1126/sciadv.aau5363, 2018.

Lin, Y.-H., Zhang, Z., Docherty, K. S., Zhang, H., Budisulistiorini, S. H., Rubitschun, C. L., Shaw, S. L., Knipping, E. M., Edgerton, E. S., Kleindienst, T. E., Gold, A., and Surratt, J. D.: Isoprene Epoxydiols as Precursors to Secondary Organic Aerosol Formation: Acid-Catalyzed Reactive Uptake Studies with Authentic Compounds, Environ. Sci. Technol., 46, 250–258, https://doi.org/10.1021/es202554c, 2012.

Lopez-Hilfiker, F. D., Mohr, C., Ehn, M., Rubach, F., Kleist, E., Wildt, J., Mentel, T. F., Lutz, A., Hallquist, M., Worsnop, D., and Thornton, J. A.: A novel method for online analysis of gas and particle composition: description and evaluation of a Filter Inlet for Gases and AEROsols (FIGAERO), Atmos. Meas. Tech., 7, 983–1001, https://doi.org/10.5194/amt-7-983-2014, 2014.

McFiggans, G., Mentel, T. F., Wildt, J., Pullinen, I., Kang, S., Kleist, E., Schmitt, S., Springer, M., Tillmann, R., Wu, C., Zhao, D., Hallquist, M., Faxon, C., Le Breton, M., Hallquist, Å. M., Simpson, D., Bergström, R., Jenkin, M. E., Ehn, M., Thornton, J. A., Alfarra, M. R., Bannan, T. J., Percival, C. J., Priestley, M., Topping, D., and Kiendler-Scharr, A.: Secondary organic aerosol reduced by mixture of atmospheric vapours, Nature, 565, 587–593, https://doi.org/10.1038/s41586-018-0871-y, 2019.

Merikanto, J., Spracklen, D. V., Mann, G. W., Pickering, S. J., and Carslaw, K. S.: Impact of nucleation on global CCN, Atmos. Chem. Phys., 9, 8601–8616, https://doi.org/10.5194/acp-9-8601-2009, 2009.

Paulot, F., Crounse, J. D., Kjaergaard, H. G., Kürten, A., Clair, J. M. S., Seinfeld, J. H., and Wennberg, P. O.: Unexpected epoxide formation in the gas-phase photooxidation of isoprene, Science, 325, 730–733, 2009.

Reid, J. P., Bertram, A. K., Topping, D. O., Laskin, A., Martin, S. T., Petters, M. D., Pope, F. D., and Rovelli, G.: The viscosity of atmospherically relevant organic particles, Nat. Commun., 9, 956, https://doi.org/10.1038/s41467-018-03027-z, 2018.

Riva, M., Budisulistiorini, S. H., Zhang, Z., Gold, A., and Surratt, J. D.: Chemical characterization of secondary organic aerosol constituents from isoprene ozonolysis in the presence of acidic aerosol, Atmos. Environ., 130, 5–13, https://doi.org/10.1016/j.atmosenv.2015.06.027, 2016.

Saathoff, H., Naumann, K. H., Möhler, O., Jonsson, Å. M., Hallquist, M., Kiendler-Scharr, A., Mentel, T. F., Tillmann, R., and Schurath, U.: Temperature dependence of yields of secondary organic aerosols from the ozonolysis of α-pinene and limonene, Atmos. Chem. Phys., 9, 1551–1577, https://doi.org/10.5194/acp-9-1551-2009, 2009.

Schervish, M. and Donahue, N. M.: Peroxy radical chemistry and the volatility basis set, Atmos. Chem. Phys., 20, 1183–1199, https://doi.org/10.5194/acp-20-1183-2020, 2020.

Simon, M., Heinritzi, M., Herzog, S., Leiminger, M., Bianchi, F., Praplan, A., Dommen, J., Curtius, J., and Kürten, A.: Detection of dimethylamine in the low pptv range using nitrate chemical ionization atmospheric pressure interface time-of-flight (CI-APi-TOF) mass spectrometry, Atmos. Meas. Tech., 9, 2135–2145, https://doi.org/10.5194/amt-9-2135-2016, 2016.

Simon, M., Dada, L., Heinritzi, M., Scholz, W., Stolzenburg, D., Fischer, L., Wagner, A. C., Kürten, A., Rörup, B., He, X. C., Almeida, J., Baalbaki, R., Baccarini, A., Bauer, P. S., Beck, L., Bergen, A., Bianchi, F., Bräkling, S., Brilke, S., Caudillo, L., Chen, D., Chu, B., Dias, A., Draper, D. C., Duplissy, J., El-Haddad, I., Finkenzeller, H., Frege, C., Gonzalez-Carracedo, L., Gordon, H., Granzin, M., Hakala, J., Hofbauer, V., Hoyle, C. R., Kim, C., Kong, W., Lamkaddam, H., Lee, C. P., Lehtipalo, K., Leiminger, M., Mai, H., Manninen, H. E., Marie, G., Marten, R., Mentler, B., Molteni, U., Nichman, L., Nie, W., Ojdanic, A., Onnela, A., Partoll, E., Petäjä, T., Pfeifer, J., Philippov, M., Quéléver, L. L. J., Ranjithkumar, A., Rissanen, M. P., Schallhart, S., Schobesberger, S., Schuchmann, S., Shen, J., Sipilä, M., Steiner, G., Stozhkov, Y., Tauber, C., Tham, Y. J., Tomé, A. R., Vazquez-Pufleau, M., Vogel, A. L., Wagner, R., Wang, M., Wang, D. S., Wang, Y., Weber, S. K., Wu, Y., Xiao, M., Yan, C., Ye, P., Ye, Q., Zauner-Wieczorek, M., Zhou, X., Baltensperger, U., Dommen, J., Flagan, R. C., Hansel, A., Kulmala, M., Volkamer, R., Winkler, P. M., Worsnop, D. R., Donahue, N. M., Kirkby, J., and Curtius, J.: Molecular understanding of new-particle formation from α-pinene between -50 and $+25$ °C, Atmos. Chem. Phys., 20, 9183–9207, https://doi.org/10.5194/acp-20-9183-2020, 2020.

Stolzenburg, D., Fischer, L., Vogel, A. L., Heinritzi, M., Schervish, M., Simon, M., Wagner, A. C., Dada, L., Ahonen, L. R., Amorim, A., Baccarini, A., Bauer, P. S., Baumgartner, B., Bergen, A., Bianchi, F., Breitenlechner, M., Brilke, S., Buenrostro Mazon, S., Chen, D., Dias, A., Draper, D. C., Duplissy, J., El Haddad, I., Finkenzeller, H., Frege, C., Fuchs, C., Garmash, O., Gordon, H., He, X., Helm, J., Hofbauer, V., Hoyle, C. R., Kim, C., Kirkby, J., Kontkanen, J., Kürten, A., Lampilahti, J., Lawler, M., Lehtipalo, K., Leiminger, M., Mai, H., Mathot, S., Mentler, B., Molteni, U., Nie, W., Nieminen, T., Nowak, J. B., Ojdanic, A., Onnela, A., Passananti, M., Petäjä, T., Quéléver, L. L. J., Rissanen, M. P., Sarnela, N., Schallhart, S., Tauber, C., Tomé, A., Wagner, R., Wang, M., Weitz, L., Wimmer, D., Xiao, M., Yan, C., Ye, P., Zha, Q., Baltensperger, U., Curtius, J., Dommen, J., Flagan, R. C., Kulmala, M., Smith, J. N., Worsnop, D. R., Hansel, A., Donahue, N. M., and Winkler, P. M.: Rapid growth of organic aerosol nanoparticles over a wide tropospheric

temperature range, P. Natl. Acad. Sci. USA, 115, 9122–9127, https://doi.org/10.1073/pnas.1807604115, 2018.

Surratt, J. D., Murphy, S. M., Kroll, J. H., Ng, N. L., Hildebrandt, L., Sorooshian, A., Szmigielski, R., Vermeylen, R., Maenhaut, W., Claeys, M., Flagan, R. C., and Seinfeld, J. H.: Chemical Composition of Secondary Organic Aerosol Formed from the Photooxidation of Isoprene, J. Phys. Chem. A, 110, 9665–9690, https://doi.org/10.1021/jp061734m, 2006.

Surratt, J. D., Lewandowski, M., Offenberg, J. H., Jaoui, M., Kleindienst, T. E., Edney, E. O., and Seinfeld, J. H.: Effect of Acidity on Secondary Organic Aerosol Formation from Isoprene, Environ. Sci. Technol., 41, 5363–5369, https://doi.org/10.1021/es0704176, 2007.

Surratt, J. D., Chan, A. W., Eddingsaas, N. C., Chan, M., Loza, C. L., Kwan, A. J., Hersey, S. P., Flagan, R. C., Wennberg, P. O., and Seinfeld, J. H.: Reactive intermediates revealed in secondary organic aerosol formation from isoprene, P. Natl. Acad. Sci. USA, 107, 6640–6645, 2010.

Tröstl, J., Chuang, W. K., Gordon, H., Heinritzi, M., Yan, C., Molteni, U., Ahlm, L., Frege, C., Bianchi, F., Wagner, R., Simon, M., Lehtipalo, K., Williamson, C., Craven, J. S., Duplissy, J., Adamov, A., Almeida, J., Bernhammer, A.-K., Breitenlechner, M., Brilke, S., Dias, A., Ehrhart, S., Flagan, R. C., Franchin, A., Fuchs, C., Guida, R., Gysel, M., Hansel, A., Hoyle, C. R., Jokinen, T., Junninen, H., Kangasluoma, J., Keskinen, H., Kim, J., Krapf, M., Kürten, A., Laaksonen, A., Lawler, M., Leiminger, M., Mathot, S., Möhler, O., Nieminen, T., Onnela, A., Petäjä, T., Piel, F. M., Miettinen, P., Rissanen, M. P., Rondo, L., Sarnela, N., Schobesberger, S., Sengupta, K., Sipilä, M., Smith, J. N., Steiner, G., Tomè, A., Virtanen, A., Wagner, A. C., Weingartner, E., Wimmer, D., Winkler, P. M., Ye, P., Carslaw, K. S., Curtius, J., Dommen, J., Kirkby, J., Kulmala, M., Riipinen, I., Worsnop, D. R., Donahue, N. M., and Baltensperger, U.: The role of low-volatility organic compounds in initial particle growth in the atmosphere, Nature, 533, 527–531, https://doi.org/10.1038/nature18271, 2016.

Vanhanen, J., Mikkilä, J., Lehtipalo, K., Sipilä, M., Manninen, H. E., Siivola, E., Petäjä, T., and Kulmala, M.: Particle Size Magnifier for Nano-CN Detection, Aerosol Sci. Technol., 45, 533–542, https://doi.org/10.1080/02786826.2010.547889, 2011.

Voigtländer, J., Duplissy, J., Rondo, L., Kürten, A., and Stratmann, F.: Numerical simulations of mixing conditions and aerosol dynamics in the CERN CLOUD chamber, Atmos. Chem. Phys., 12, 2205–2214, https://doi.org/10.5194/acp-12-2205-2012, 2012.

Wagner, A. C., Bergen, A., Brilke, S., Fuchs, C., Ernst, M., Hoker, J., Heinritzi, M., Simon, M., Bühner, B., Curtius, J., and Kürten, A.: Size-resolved online chemical analysis of nanoaerosol particles: a thermal desorption differential mobility analyzer coupled to a chemical ionization time-of-flight mass spectrometer, Atmos. Meas. Tech., 11, 5489–5506, https://doi.org/10.5194/amt-11-5489-2018, 2018.

Ye, Q., Wang, M., Hofbauer, V., Stolzenburg, D., Chen, D., Schervish, M., Vogel, A. L., Mauldin, R. L., Baalbaki, R., Brilke, S., Dada, L., Dias, A., Duplissy, J., El Haddad, I., Finkenzeller, H., Fischer, L., He, X., Kim, C., Kürten, A., Lamkaddam, H., Lee, C. P., Lehtipalo, K., Leiminger, M., Manninen, H. E., Marten, R., Mentler, B., Partoll, E., Petäjä, T., Rissanen, M. P., Schobesberger, S., Schuchmann, S., Simon, M., Tham, Y. J., Vazquez-Pufleau, M., Wagner, A. C., Wang, Y., Wu, Y., Xiao, M., Baltensperger, U., Curtius, J., Flagan, R., Kirkby, j., Kulmala, M., Volkamer, R., Winkler, P. M., Worsnop, D. R., and Donahue, N. M.: Molecular Composition and Volatility of Nucleated Particles from α-Pinene Oxidation between $-50\,^{\circ}\mathrm{C}$ and $+25\,^{\circ}\mathrm{C}$, Environ. Sci. Technol., 53, 12357–12365, https://doi.org/10.1021/acs.est.9b03265, 2019.

Zhang, G., Fu, H., and Chen, J.: Effect of relative humidity and the presence of aerosol particles on the α-pinene ozonolysis, J. Environ. Sci., 71, 99–107, https://doi.org/10.1016/j.jes.2017.10.011, 2018.

Supplement of Atmos. Chem. Phys., 21, 17099–17114, 2021
https://doi.org/10.5194/acp-21-17099-2021-supplement

Atmospheric Chemistry and Physics
Open Access
EGU

Supplement of

Chemical composition of nanoparticles from α-pinene nucleation and the influence of isoprene and relative humidity at low temperature

Lucía Caudillo et al.

Correspondence to: Lucía Caudillo (lucia.caudillo@iau.uni-frankfurt.de) and Joachim Curtius (curtius@iau.uni-frankfurt.de)

Supplementary Material

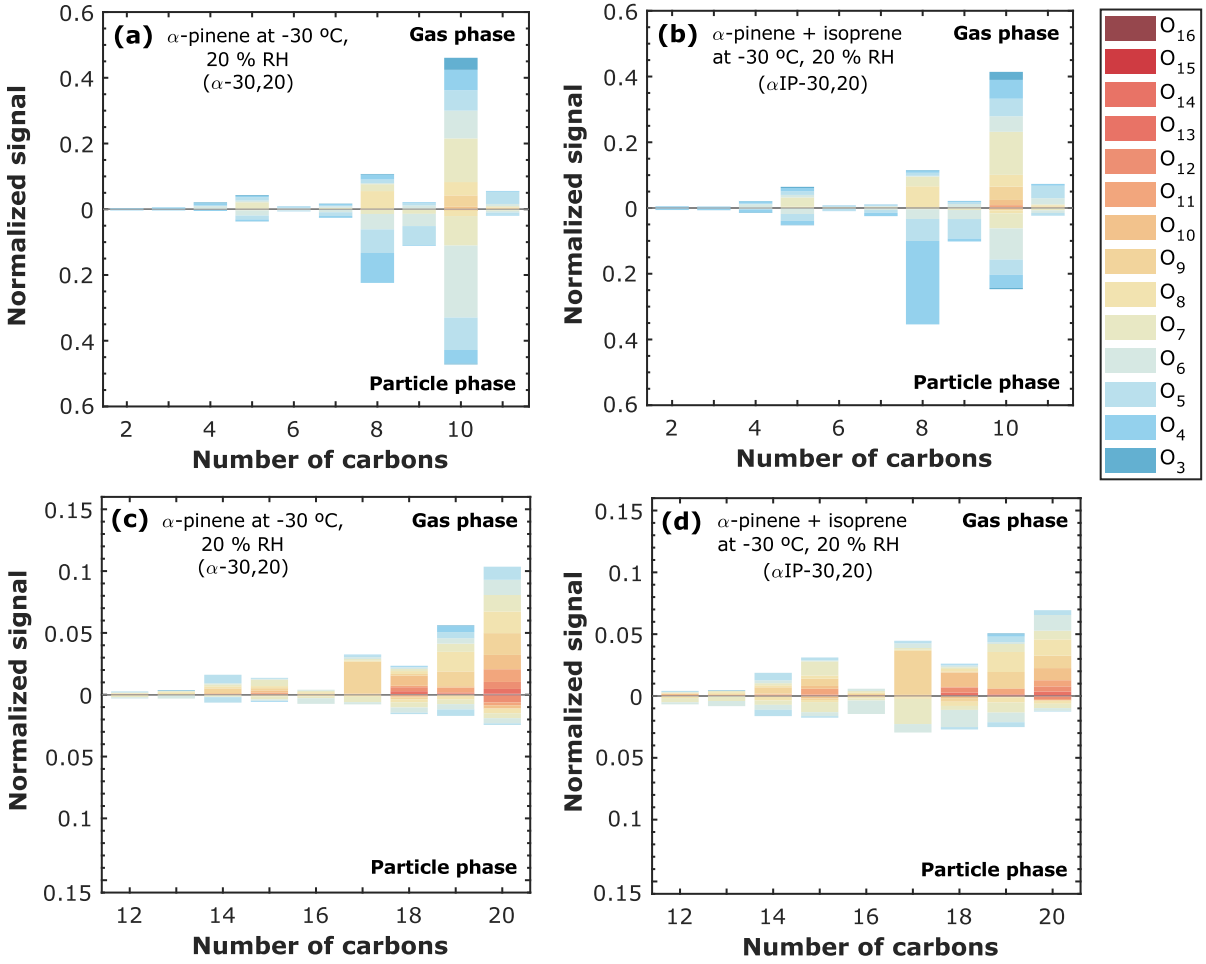

Figure S1. Carbon atom distribution $C_{2\text{-}11}$ and $C_{12\text{-}20}$ and oxygen atom content in gas and particle phase molecules. Both phases are measured with a Nitrate CI-APi-TOF mass spectrometer, while the TD-DMA is coupled to it for particle phase measurements. (a) and (c) α-pinene oxidation products at -30 °C and 20 % RH (α-30,20), (b) and (d) α-pinene + isoprene oxidation products at -30 °C and 20 % RH (αIP-30,20). The level of α-pinene was between 1 and 8 ppbv in (a) (b) (c) and (d), while isoprene level reached up to 30 ppbv in (b) and (d). Ozone level was stable at ~ 100 ppbv for all the experiments. The intensities are normalized by the total signal in each system and phase. Each color represents a specific number of oxygen atoms in the range of 3 to 16.

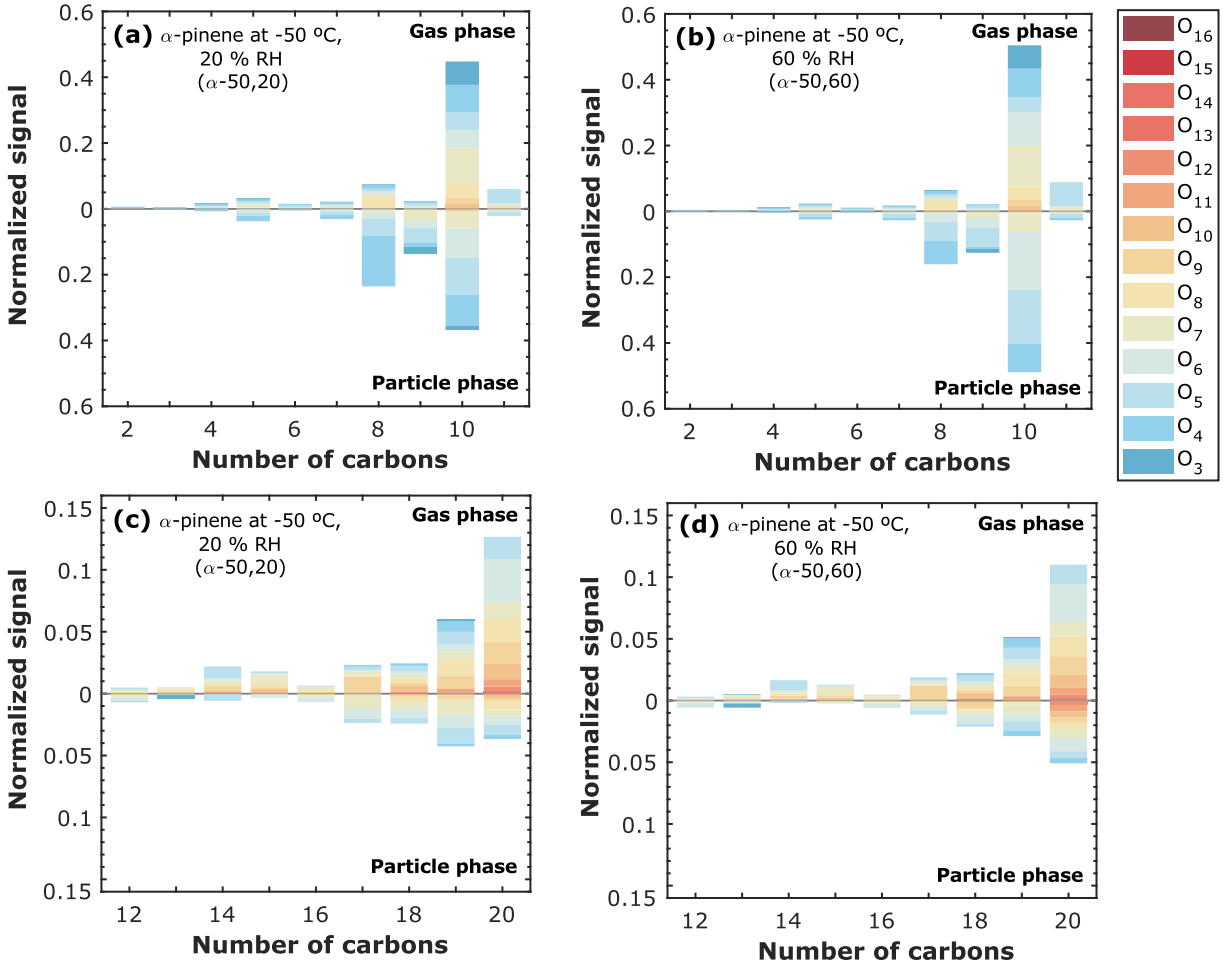

Figure S2. Carbon atom distribution $C_{2\text{-}11}$ and $C_{12\text{-}20}$ and oxygen atom content in gas and particle phase molecules. Both phases are measured with a Nitrate CI-APi-TOF mass spectrometer, while the TD-DMA is coupled to it for particle phase measurements. (a) and (c) α-pinene oxidation products at -50 °C and 20 % RH (α-50,20), (b) and (d) α-pinene oxidation products at -50 °C and 60 % RH (α-50,60). The level of α-pinene was between 1 and 8 ppbv and Ozone level was stable at ~ 100 ppbv for all the experiments. The intensities are normalized by the total signal in each system and phase. Each color represents a specific number of oxygen atoms in the range of 3 to 16.

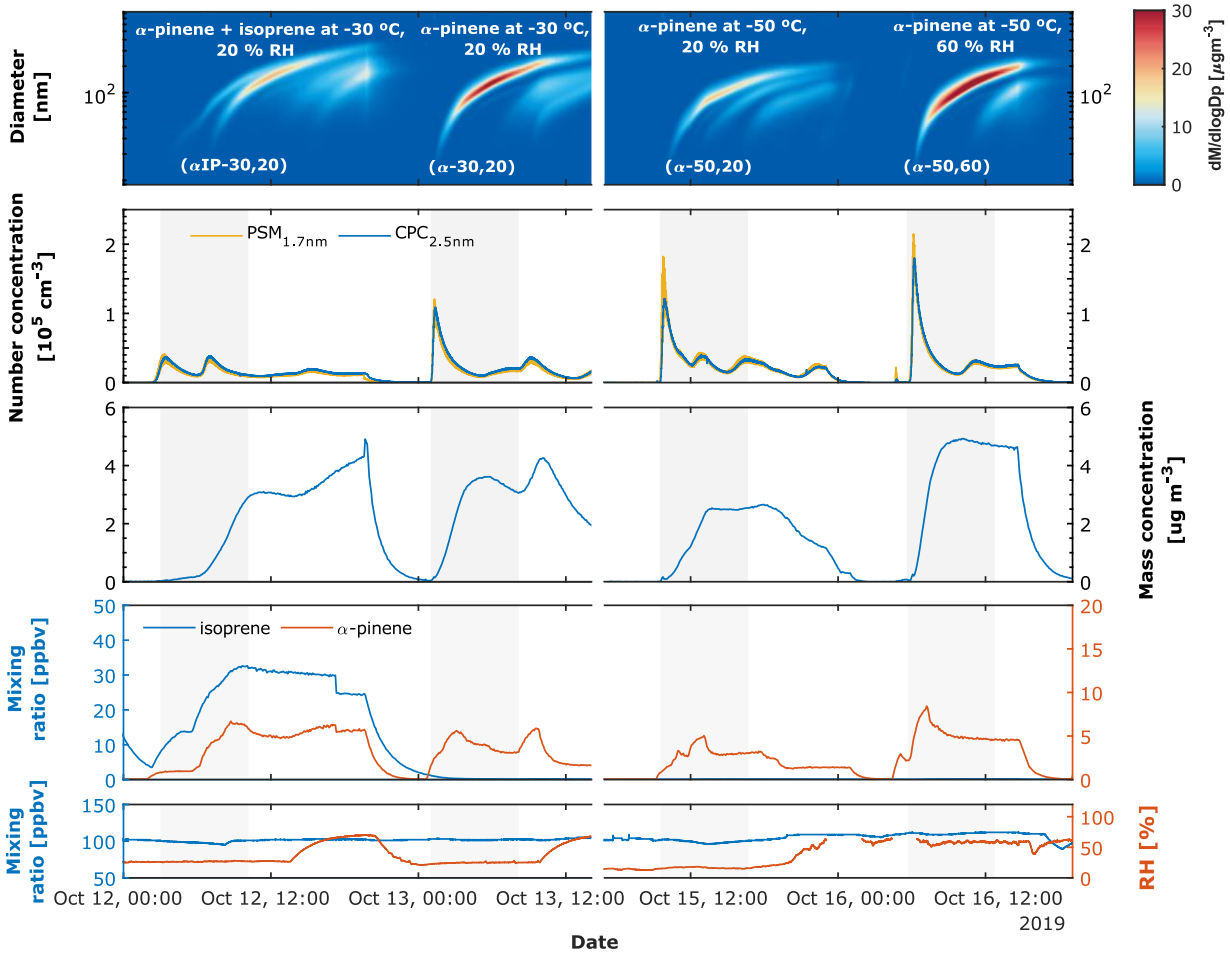

Figure S3. Experimental overview for pure biogenic new particle formation. First panel: particle size distribution for four different experiments: α-pinene + isoprene at -30 °C and 20 % RH (αIP-30,20); α-pinene at -30 °C and 20 % RH (α-30,20); α-pinene at -50 °C and 20 % RH (α-50,20) and α-pinene at -50 °C and 60% RH (α-50,60). The color scale represents the normalized mass concentration in μg m^{-3}. Second panel: Particle number concentration in cm^{-3} measured by the PSM with a cut-off diameter of 1.7 nm and CPC with a cut-off diameter of 2.5 nm. Third panel: Mass concentration in μg m^{-3} (obtained by integrating the normalized mass concentration from the SMPS). Fourth panel: Mixing ratio in ppbv for the biogenic precursor gases, isoprene and α-pinene. Fifth panel: Ozone mixing ratio in ppbv and relative humidity in %. The shaded areas refer to the time where the particles were collected using the TD-DMA.

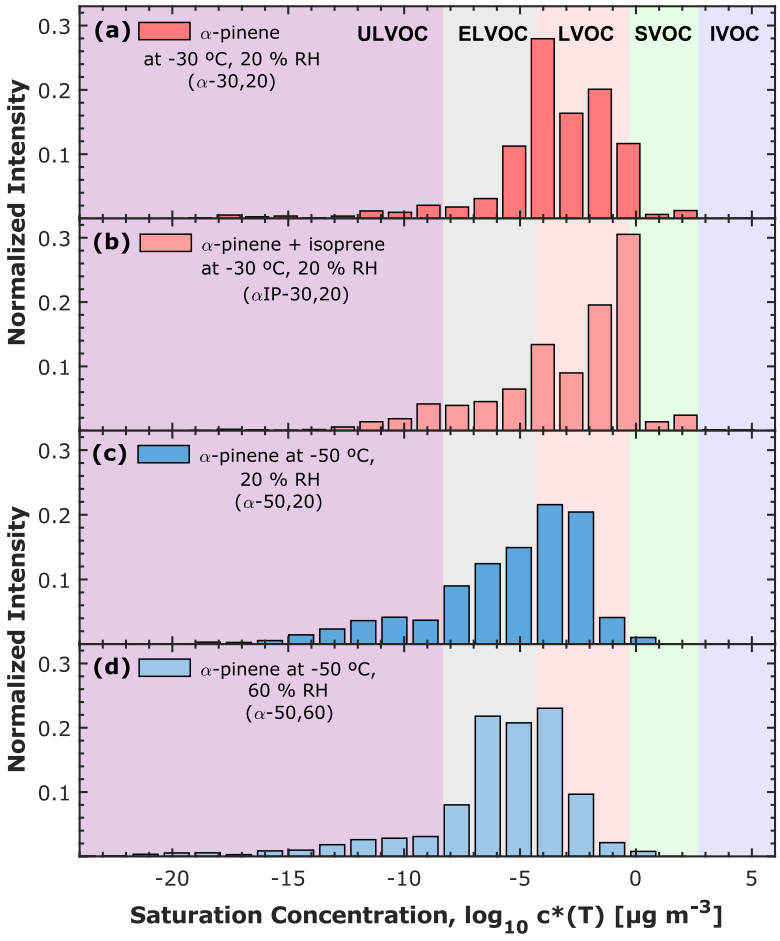

Figure S4. TD-DMA Volatility distribution of the measured oxidation products in the particle phase for four different experiments (Figure 5 in linear scale): (a) α-pinene at -30 °C and 20 % RH (α-30,20); (b) α-pinene + isoprene at -30 °C and 20 % RH (αIP-30,20); (c) α-pinene at -50 °C and 20 % RH (α-50,20) and (d) α-pinene at -50 °C and 60 % RH (α-50,60). Every individual volatility bin includes the sum of the intensity for the oxidation products normalized by the total signal in each system. Every individual volatility bin is defined at 300 K, shifted, and widened according to their corresponding temperature. The color bands in the background indicate the volatility regimes as in Donahue et al. (2012) and in Schervish and Donahue (2020). The normalized intensity is dimensionless. Nevertheless, it should be noted that the particle phase signal is given in normalized counts per second integrated over the evaporation time [ncps. s].

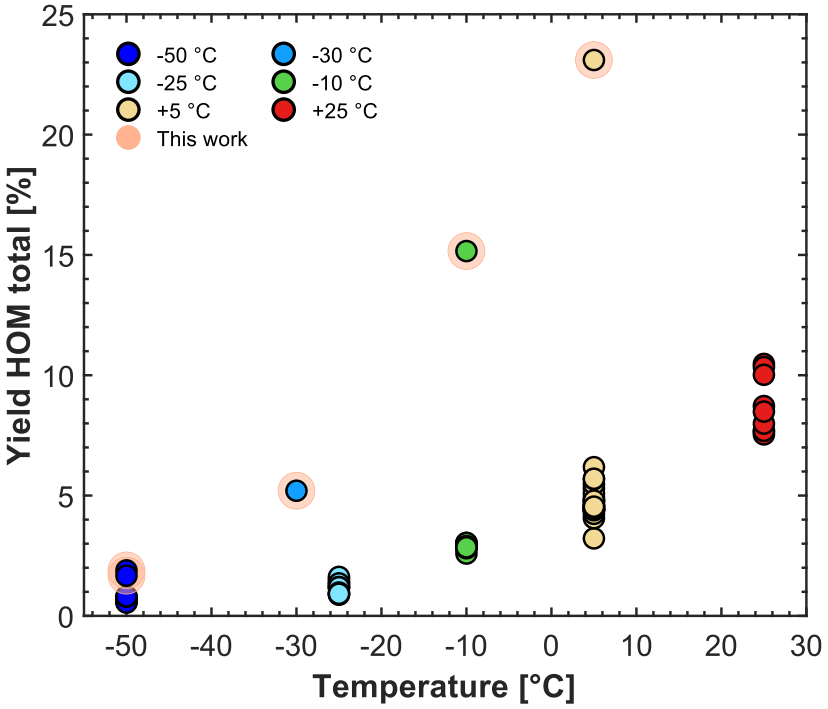

Figure S5. Yield of total HOM as a function of temperature for pure α-pinene systems. Data points at -50 °C, -25 °C, -10 °C, +5 °C and +25 °C are from Simon et al. (2020) and the data points with the orange shadows are the contribution of this study (α-30,20, α-50,20 and α-50,60 and complementary pure α-pinene experiments at +5 °C and at -10 °C). The level of precursor gases from Simon et al., (2020) were 0.2 to 0.8 ppbv for α-pinene and 40 to 50 ppbv for ozone, while for experiments reported here (shown with orange shadows), the mixing ratios were 1 to 8 ppbv for α-pinene and 100 ppbv for ozone.

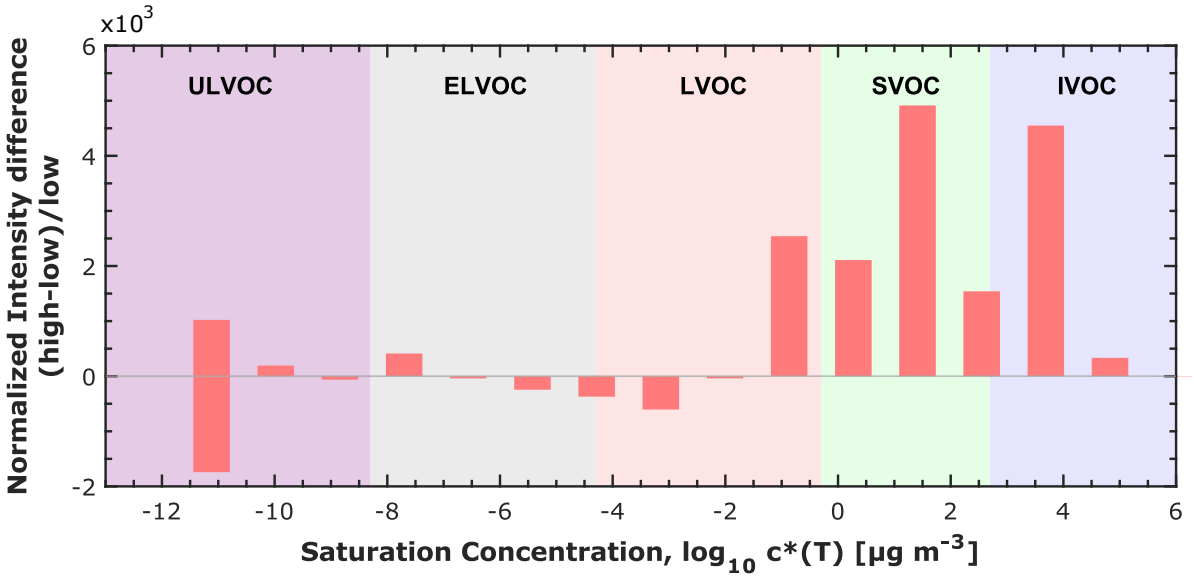

Figure S6. Volatility distribution of gas phase for two different systems and the normalized difference between them. Gas phase is measured with a Nitrate CI-APi-TOF mass spectrometer. Every individual volatility bin includes the normalized intensity difference (high-low)/low, which is calculated based on intensity of the system at high level of precursor gases (α-pinene was 2 - 3 ppbv and Ozone ~ 100 ppbv) and on the system at low level of precursor gases (α-pinene was 0.2 - 0.8 ppbv and Ozone ~ 40 - 50 ppbv). Every individual volatility bin is defined at 300 K, shifted, and widened according to their corresponding temperature. The lowest bin is an overflow bin (which contains the volatility bins with saturation concentration < -11 ug m^{-3}.). The color bands in the background indicate the volatility regimes as in Donahue et al. (2012) and in Schervish and Donahue (2020).

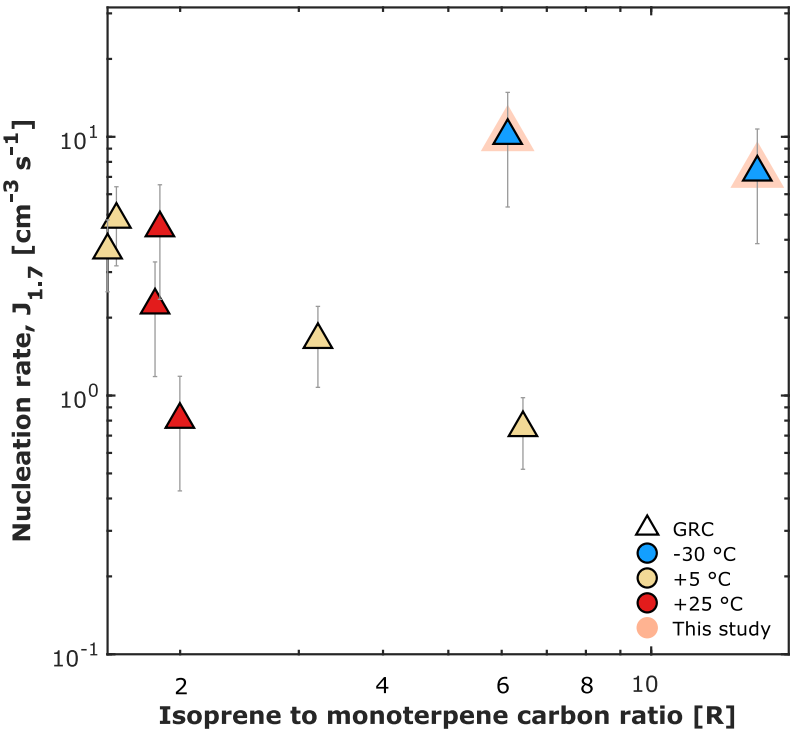

Figure S7. Pure biogenic nucleation rates at 1.7 nm diameter against isoprene-to-monoterpene carbon ratio (*R*) at different temperatures. Triangles represent Galactic Comic Rays (GCR) conditions. Data points at +5 °C and +25 °C are from Heinritzi et al., (2020). The points with the orange shadows are the experiments reported in this study for α-pinene + isoprene oxidation products at -30 °C and 20 % RH (αIP-30,20).

6.2 An intercomparison study of four different techniques for measuring the chemical composition of nanoparticles. Caudillo et al. (2022).

https://doi.org/10.5194/acp-2022-498
Preprint. Discussion started: 26 August 2022

Atmospheric Chemistry and Physics Discussions

An intercomparison study of four different techniques for measuring the chemical composition of nanoparticles

Lucía Caudillo[1], Mihnea Surdu[2], Brandon Lopez[3], Mingyi Wang[3,4], Markus Thoma[1], Steffen Bräkling[5], Angela Buchholz[6], Mario Simon[1], Andrea C. Wagner[1], Tatjana Müller[1,7], Manuel Granzin[1], Martin Heinritzi[1], Antonio Amorim[8], David M. Bell[2], Zoé Brasseur[9], Lubna Dada[2], Jonathan Duplissy[9,10], Henning Finkenzeller[11], Xu-Cheng He[9], Houssni Lamkaddam[2], Naser G. A. Mahfouz[3], Vladimir Makhmutov[12,13], Hanna E. Manninen[14], Guillaume Marie[1], Ruby Marten[2], Roy L. Mauldin[15,3], Bernhard Mentler[16], Antti Onnela[14], Tuukka Petäjä[9], Joschka Pfeifer[1,14], Maxim Philippov[12], Ana A. Piedehierro[17], Birte Rörup[9], Wiebke Scholz[16], Jiali Shen[9], Dominik Stolzenburg[9], Christian Tauber[18], Ping Tian[19], António Tomé[20], Nsikanabasi Silas Umo[21], Dongyu S. Wang[2], Yonghong Wang[9], Stefan K. Weber[1,14], André Welti[17], Marcel Zauner-Wieczorek[1], Urs Baltensperger[2], Richard C. Flagan[4], Armin Hansel[16,22], Jasper Kirkby[1,14], Markku Kulmala[9,10,23], Katrianne Lehtipalo[9,17], Douglas R. Worsnop[9,24], Imad El Haddad[2], Neil M. Donahue[3], Alexander L. Vogel[1], Andreas Kürten[1], Joachim Curtius[1].

[1]Institute for Atmospheric and Environmental Sciences, Goethe University Frankfurt, Frankfurt am Main, 60438, Germany
[2]Laboratory of Atmospheric Chemistry, Paul Scherrer Institute, 5232 Villigen, Switzerland
[3]Center for Atmospheric Particle Studies, Carnegie Mellon University, Pittsburgh, PA 15213, USA
[4]Division of Chemistry and Chemical Engineering, California Institute of Technology, Pasadena, CA 91125, USA
[5]TOFWERK AG, Thun, 3600, Switzerland
[6]Department of Applied Physics, University of Eastern Finland, Kuopio, Finland
[7]Atmospheric Chemistry Department, Max Planck Institute for Chemistry, 55128 Mainz, Germany
[8]CENTRA and Faculdade de Ciências da Universidade de Lisboa, Campo Grande 1749–016, Lisboa, Portugal
[9]Institute for Atmospheric and Earth System Research (INAR) / Physics, Faculty of Science, University of Helsinki, 00014 Helsinki, Finland
[10]Helsinki Institute of Physics, University of Helsinki, 00014 Helsinki, Finland
[11]Department of Chemistry & CIRES, University of Colorado Boulder, Boulder, CO, 80309-0215, USA
[12]Lebedev Physical Institute, Russian Academy of Sciences, 119991, Moscow, Russia
[13]Moscow Institute of Physics and Technology, Moscow, 117303, Russia
[14]CERN, 1211 Geneva, Switzerland
[15]Department of Atmospheric and Oceanic Sciences, University of Colorado Boulder, Boulder, CO 80309, USA
[16]Institute for Ion and Applied Physics, University of Innsbruck, 6020 Innsbruck, Austria
[17]Finnish Meteorological Institute, 00560 Helsinki, Finland
[18]Faculty of Physics, University of Vienna, 1090 Vienna, Austria
[19]Beijing Weather Modification Office, China
[20]IDL, Universidade da Beira Interior, R. Marquês de Ávila e Bolama, Covilhã, 6201-001, Portugal
[21]Institute of Meteorology and Climate Research, Karlsruhe Institute of Technology, Karlsruhe, Germany
[22]Ionicon Analytik GmbH, 6020 Innsbruck, Austria
[23]Aerosol and Haze Laboratory, Beijing Advanced Innovation Center for Soft Matter Science and Engineering, Beijing University of Chemical Technology, Beijing, 100029, P.R. China
[24]Aerodyne Research, Billerica, MA 01821 USA

Correspondence to: Lucía Caudillo (lucia.caudillo@iau.uni-frankfurt.de) and Joachim Curtius (curtius@iau.uni-frankfurt.de)

https://doi.org/10.5194/acp-2022-498
Preprint. Discussion started: 26 August 2022

Atmospheric Chemistry and Physics Discussions

Abstract.

Currently, the complete chemical characterization of nanoparticles (<100 nm) represents an analytical challenge, since these particles are abundant in number but have negligible mass. Several methods for particle-phase characterization have been recently developed to better detect and infer more accurately the sources and fates of ultra-fine particles, but a detailed comparison of different approaches is missing. Here we report on the chemical composition of secondary organic aerosol (SOA) nanoparticles from experimental studies of α-pinene ozonolysis at -50 ºC, -30 ºC, and -10 ºC, and inter-compare the results measured by different techniques. The experiments were performed at the Cosmics Leaving OUtdoor Droplets (CLOUD) chamber at the European Organization for Nuclear Research (CERN). The chemical composition was measured simultaneously by four different techniques: 1) Thermal Desorption-Differential Mobility Analyzer (TD-DMA) coupled to a NO_3^- chemical ionization-atmospheric-pressure-interface-time-of-flight (CI-APi-TOF) mass spectrometer, 2) Filter Inlet for Gases and AEROsols (FIGAERO) coupled to an I^- high-resolution time-of-flight chemical-ionization mass spectrometer (HRToF-CIMS), 3) Extractive Electrospray Na^+ Ionization time-of-flight mass spectrometer (EESI-TOF), and 4) Offline analysis of filters (FILTER) using Ultra-high-performance liquid chromatography (UHPLC) and heated electrospray ionization (HESI) coupled to an Orbitrap high-resolution mass spectrometer (HRMS). Intercomparison was performed by contrasting the observed chemical composition as a function of oxidation state and carbon number, by calculating the volatility and comparing the fraction of volatility classes, and by comparing the thermal desorption behavior (for the thermal desorption techniques: TD-DMA and FIGAERO) and performing positive matrix factorization (PMF) analysis for the thermograms. We found that the methods generally agree on the most important compounds that are found in the nanoparticles. However, they do see different parts of the organic spectrum. We suggest potential explanations for these differences: thermal decomposition, aging, sampling artifacts, etc. We applied PMF analysis and found insights of thermal decomposition in the TD-DMA and the FIGAERO.

1 Introduction

So far there is no well-established instrument and technique to measure the complete chemical composition of ultrafine (< 100 nm) Secondary Organic Aerosol (SOA) particles. However, several analytical techniques have recently been developed in order to better advance our understanding on their chemistry. Techniques that are capable of measuring sub-30 nm particles include the Volatile Aerosol Component Analyzer (VACA) (Curtius et al., 1998), the Thermal Desorption Chemical Ionization Mass Spectrometry (TDCIMS) (Voisin et al., 2003), the Nano Aerosol Mass Spectrometer (NAMS) (Wang et al., 2006), the Aerosol time-of-flight mass spectrometer (Laitinen et al., 2009), the inlet for the size-resolved collection of aerosols (Phares and Collier, 2010), the Chemical Analyzer for Charged Ultrafine Particles (CAChUP) (Gonser and Held, 2013), the Electrostatic Precipitation-Electrospray Ionization Mass Spectrometry (EP-ESI-MS) (He et al., 2015), the Droplet Assisted Inlet Ionization (DAII) (Horan et al., 2017), and the Online Aerosol Chemical Characterization by Extractive Electrospray Ionization−Ultrahigh-Resolution Mass Spectrometer (EESI-Orbitrap) (Lee et al., 2020). Single-particle analysis by mass spectrometry methods based on aerodynamics, light scattering and laser desorption ionization are suitable for particles with larger sizes. These methods include for example, the Aerosol Mass Spectrometer (AMS) described in Jayne et al. (2000), and the suite of single particle methods described in the review by Bzdek et al. (2012). The detection of particles with d < 100 nm using these techniques becomes difficult, because the scattering efficiency decreases when the particle diameter becomes smaller.

Using the Cosmics Leaving OUtdoor Droplets (CLOUD) chamber at the European Organization for Nuclear Research (CERN), we used simultaneously four different techniques for measuring the chemical composition of ultrafine particles and inter-compare the results.

https://doi.org/10.5194/acp-2022-498
Preprint. Discussion started: 26 August 2022

Atmospheric Chemistry and Physics Discussions

1. Thermal Desorption-Differential Mobility Analyzer (TD-DMA) coupled to a NO_3^- chemical ionization-atmospheric-pressure-interface-time-of-flight (CI-APi-TOF) mass spectrometer (Wagner et al., 2018);

2. Filter Inlet for Gases and AEROsols (FIGAERO) coupled to an I^- high-resolution time-of-flight chemical-ionization mass spectrometer (HRToF-CIMS) (Lopez-Hilfiker et al., 2014) ;

3. Extractive Electrospray Na^+ Ionization time-of-flight mass spectrometer (EESI-TOF) (Lopez-Hilfiker et al., 2019); and,

4. Offline analysis of filters (FILTER) using Ultra-high-performance liquid chromatography (UHPLC) and heated electrospray ionization (HESI) coupled to an Orbitrap high-resolution mass spectrometer (HRMS) (Ungeheuer et al., 2021).

None of the techniques presented in this work represents the perfect instrument. In fact, a perfect instrument would be the one that is able to measure quantitatively all the hundreds of organic compounds that are present in the newly formed particles, and identify the molecular structures (including their isomeric and spatial configuration) at high resolution and in real time. Such an ideal instrument does not exist; and at present a combination of techniques is required for a more complete characterization of SOA (Hallquist et al., 2009).

In order to compare the techniques mentioned above and to gain insights into their limitations (e.g., due to decomposition during evaporation, different ionization techniques, etc.), we performed α-pinene ozonolysis experiments at -50 ºC, -30 ºC and -10 ºC. For the experiments at -50 °C and -30 °C TD-DMA, FIGAERO and EESI-TOF were inter-compared while for the experiment at -10 ºC FILTER, FIGAERO and, EESI-TOF were inter-compared. We carried out the in-depth inter-comparison by a) comparing the observed composition as a function of oxidation state and carbon number, b) calculating the volatility and comparing the fraction of ultralow-volatility (ULVOC), extremely low-volatility (ELVOC), low-volatility (LVOC), semi-volatile (SVOC), and intermediate-volatility (IVOC) organic compounds, and c) comparing the thermograms (for the thermal desorption techniques: TD-DMA and FIGAERO), and by performing positive matrix factorization (PMF) analysis to the thermograms.

Because the four techniques provide chemical composition, and more specifically the carbon, hydrogen and oxygen content (CHO), we determined the carbon oxidation state (OSc), which is a metric for the degree of the oxidation of organic species in the atmosphere (Kroll et al., 2011). It is calculated based on the ratios O:C and H:C and is useful to describe organic mixtures upon oxidation processes. In addition, we calculated the volatility (as introduced by Donahue et al. (2011) and modified by Stolzenburg et al. (2018)), and determined to which volatility classes the detected compounds belong. Regarding the thermal desorption methods (TD-DMA and FIGAERO) we investigated the thermal behavior of the detected species. Both instruments collect particles before transferring them to the gas-phase. When a temperature ramp is applied, the species that are adsorbed on the surface gradually desorb (as represented on a thermogram). In order to evaluate whether the thermal desorption methods lead to significant decomposition during evaporation, we applied a method called positive matrix factorization (PMF) (Paatero and Tapper, 1994; Buchholz et al., 2020), in which a dataset matrix is expressed in terms of the sum of factors matrices and a residual matrix. Lastly, we present an overview on the advantages and disadvantages for the different methods. All methods presented here agreed on the most dominant compounds that are found in the nanoparticles. Nevertheless, they do see different parts of the organic spectrum. Therefore, the techniques are complementary. The four techniques described in this work are feasible for measuring SOA and represent an important analytical development.

https://doi.org/10.5194/acp-2022-498
Preprint. Discussion started: 26 August 2022

Atmospheric Chemistry and Physics Discussions

2. Methods

2.1 Experimental approach

2.1.1 The CLOUD chamber experiment

We conducted experiments in the CLOUD chamber at CERN to study pure biogenic new particle formation (NPF), without the presence of nitrogen oxides (NOx). The CLOUD chamber is a stainless-steel cylinder with a volume of 26.1 m^3 which has been extensively described by Kirkby et al. (2011) and Duplissy et al. (2016). To create the particles, NPF was induced by continuously adding α-pinene and ozone into the chamber. The monoterpene concentration was regulated by an evaporation source, in which dry nitrogen (N_2) passes through an evaporator containing liquid α-pinene at a precisely controlled temperature. Ozone was produced by exposing cryogenic O_2 to UV light and was introduced directly into the chamber via a separate line. The relative humidity was adjusted with a temperature-controlled Nafion humidifier using ultrapure Millipore water. All the precursor gases were homogenously mixed in the chamber by two magnetically driven Teflon fans placed at the top and at the bottom of the chamber. The temperature was kept constant by an insulated thermal housing, which surrounds the chamber. The α-pinene mixing ratio was measured by a proton transfer reaction time-of-flight (PTR-TOF) mass spectrometer (Graus et al., 2010; Breitenlechner et al., 2017), whereas ozone was measured by a TEI 49C ozone analyzer (Thermo Environmental Instruments). The experiments relevant for this work were performed at -50 ºC, -30 ºC, and -10 °C. The α-pinene mixing ratio ranged between 1 and 8 ppbv and ozone was approximately 100 ppbv. Figure S1 in the Supplement provides an overview of a representative experiment at -30 ºC.

Table 1 presents the most important features for the instruments used in this work. We categorize the techniques according to certain criteria: continuous or discontinuous operation mode, evaporation method, phase measured, ionization technique, reagent ion, target substances, occurrence of significant thermal decomposition and, whether the technique allows to perform size-resolved analysis of aerosol particles.

2.1.2 Thermal Desorption-Differential Mobility Analyzer (TD-DMA) coupled to a NO_3^- chemical ionization-atmospheric-pressure-interface-time-of-flight (CI-APi-TOF) mass spectrometer

The TD-DMA coupled to a NO_3^- CI-APi-TOF analyzes the chemical composition of nanoparticles in a semi-continuous mode of operation. The design and characterization have been reported by Wagner et al. (2018). This method allows gas-and particle-phase measurements using the same ionization technique. Individual results of gas-and particle-phase comparison of the same chemical system as in this study were reported in Caudillo et al. (2021). While the gas-phase measurement is taking place with the CI-APi-TOF mass spectrometer, the TD-DMA samples particles from the chamber. The particles are charged by an X-Ray source and then collected on a platinum/rhodium (90:10) filament by electrostatic precipitation. After a certain collection time (in this study ~ 4 hours), an electric current is applied to the filament, which causes its direct heating. We estimate based on the filament resistance, that the temperature gradually increased up to approximately 600 ºC in a period of ~ 1 minute (details of the heating curve will be discussed in Section 3.2).

The vapors that evaporate from the heated particles are carried by an N_2 flow to the nitrate CI-APi-TOF for chemical composition analysis. For chemical ionization of the vapors, nitrate reagent ions $(HNO_3)_n NO_3^-$ with n = 0-2 are created by a corona discharge (Kürten et al., 2011; Kürten et al., 2014). Some of the vapor molecules are ionized and subsequently detected by the APi-TOF mass spectrometer. A second heating cycle of the particle collecting filament is performed afterwards (without particle collection) in order to estimate the instrumental background due to the heating of the inlet line; this enables a more accurate particle signal estimation. Besides the particle and background estimations, a second heating up to ~ 600 ºC ensures that the filament is clean and avoids memory effects for the next measurement. With the nitrate ionization technique, sulfuric acid, iodic acid, methane sulfonic acid, and highly oxygenated molecules (HOMs) can be detected.

https://doi.org/10.5194/acp-2022-498
Preprint. Discussion started: 26 August 2022

Atmospheric Chemistry and Physics Discussions

2.1.3 Filter Inlet for Gases and AEROsols (FIGAERO) coupled to an I^- high-resolution time-of-flight chemical-ionization mass spectrometer (HRToF-CIMS)

The Filter Inlet for Gases and AEROsols (FIGAERO) coupled to an I^- high-resolution time-of-flight chemical-ionization mass spectrometer (HRToF-CIMS) was first described by Lopez-Hilfiker et al. (2014) and optimized for CLOUD operation conditions by Wang et al. (2020). FIGAERO uses a multi-port to measure in alternation both gas-and particle-phase following the same general procedure as the TD-DMA/CI-APi-TOF. While the gas-phase is analyzed, particle collection takes place on a polytetrafluoroethylene (PTFE) filter, and after a certain collection time (in this study 15 minutes), the filter is automatically moved into the ion-molecule reactor and exposed to a pure N_2 gas flow. The N_2 flow is gradually heated to evaporate the particles by thermal desorption using a temperature-programmed heating curve. For the measurements reported in this study, the temperature was slowly ramped from room temperature up to 150 ºC in approximately 15 minutes. When the heating cycle ends a new collection starts, and the process repeats (an example of the heating curve is discussed in Section 3.2). The detection technique is based on iodide-molecule adduct ionization. Iodine ions I^-, I_3^- and $(H_2O)I^-$ are generated from a solution of methyl iodide (CH_3I) and a Po-210 ion source (Lee et al., 2014). With this soft ionization technique, the FIGAERO HRToF-CIMS can detect HOMs, organosulfates, and inorganic acids such as sulfuric acid and nitric acid.

2.1.4 Extractive electrospray Na^+ ionization time-of-flight mass spectrometer (EESI-TOF)

The Extractive electrospray ionization time-of-flight mass spectrometer (Lopez-Hilfiker et al., 2019) is a technique used for online particle-phase measurements without particle collection. This technique aims to provide the chemical composition of organic particles in real time. It is also possible to measure the gas-phase by using the dual configuration (Lee et al., 2022). In the beginning of the sampling process, the aerosol sample passes through the inlet line where a carbon denuder is located to remove the gas-phase molecules. The particles then collide with electrospray droplets and the soluble components are extracted and ionized. The EESI-TOF uses here an electrospray solution of pure water doped with 100 ppm NaI and is running in the positive ion mode. This enables the measurements of SOA species as adducts with Na^+. The electrospray droplets are evaporated as they pass through a heated stainless-steel capillary via the Coulomb explosion mechanism and the analytes are detected by a time-of-flight mass spectrometer. With this ionization method, various organic compounds that are relevant for atmospheric SOA particles can be analyzed, with the exception of species that are not oxygenated and organosulfates.

2.1.5 Offline analysis of filters (FILTER) using Ultra-high-performance liquid chromatography (UHPLC) and heated electrospray ionization (HESI) coupled to an Orbitrap high-resolution mass spectrometer (HRMS)

This procedure was optimized and described in detail by Ungeheuer et al. (2021). The method enhances the separation of organic compounds with high-resolution, and enables the determination of the accurate mass. The analysis consists mainly of four steps: sampling, extraction, separation, and detection.

First, the particles were collected from a flow of 5 l min^{-1} on a 47 mm diameter Emfab™ Filter (Pall Life Science, USA). After sampling, the filter was stored at -18 °C to avoid possible losses by evaporation. The filter was cut into small pieces (approximately 3 x 3 mm) and extracted two times in 0.2 ml solution (mixture of 90 % water and 10 % methanol) for 20 min. After each extraction step, the extract was filtered through a syringe filter (PTFE with a pore size of 0.2 µm). For chromatographic separation a gradient of ultrapure water (eluent A, Milli-Q Reference A+, Merck Millipore) and methanol (eluent B, Optima LC/MS Grade, Fisher Scientific) was applied. Both eluents were mixed with 0.1 % formic acid (v/v) for improved chromatographic performance. The injection volume was 5 µl, the flow rate was 400 µl min^{-1}, and the temperature was 40 °C. The gradient started with 1 % eluent B (0-0.5 min), increased linearly to 99 % B (0.5-14 min), stayed at 99 % B (14-16 min), backflushed in 1 min, and equilibrated in 3 min, resulting in a total run time of 20 min. Negative ionization

https://doi.org/10.5194/acp-2022-498
Preprint. Discussion started: 26 August 2022

Atmospheric Chemistry and Physics Discussions

mode was used for the detection, in which the molecular ions $[M\text{-}H]^-$ are produced by deprotonation. The ion source setting used for this purpose were: -3.5 kV spray voltage, 40 psi sheath gas, 8 arbitrary units auxiliary gas, and 262.5 °C capillary temperature. The scan range in full MS was 50-750 *m/z* with a mass resolving power of about 70k at *m/z* 200. For data-dependent MS^2 ($ddMS^2$) the resolution was 17.5k. Fragments were produced in a higher-energy collisional dissociation (HCD) cell with stepped collision energies of 15, 30, and 45 eV.

2.2 Data analysis

2.2.1 Data processing

TD-DMA, FIGAERO and EESI-TOF raw data was processed using IGOR Pro 7 (WaveMetrics, Inc., USA) and Tofware (Version 3.1.2, Aerodyne Inc., USA). The data from the offline method was processed with Compound Discoverer 3.2 (Thermo Fisher Scientific).

TD-DMA data was corrected by the mass-dependent transmission efficiency in the mass classifier (Heinritzi et al., 2016) and normalized by the nitrate reagent ions. FIGAERO raw data was averaged to 1 minute and normalized by the reagent ions. EESI-TOF raw signals were averaged to 10 seconds and normalized by the most abundant electrospray ion ($NaINa^+$). Additionally, for the comparison at -30 ºC and -50 ºC, EESI-TOF and FIGAERO data was averaged during the period where the TD-DMA collected particles. While for the comparison at -10 ºC, the average period corresponded to the time where the particles were collected with the FILTER for the offline analysis.
The postprocessing was done using MATLAB R2022a (MathWorks, Inc., USA).

2.2.2 Positive matrix factorization (PMF) analysis

One of the main questions we want to answer in this work is whether the thermal desorption methods (TD-DMA and FIGAERO) experience significant decomposition during the desorption process. To answer this question, we utilized positive matrix factorization (PMF) analysis. This method was originally described by Paatero and Tapper (1994) for analyzing time series of variable (e.g. mass spectra data) from ambient observations, and it was implemented by Buchholz et al. (2020) to thermal desorption data for identifying different processes during particle evaporation. We therefore applied the same procedure as Buchholz et al. (2020) to the TD-DMA and FIGAERO thermal desorption profiles (for the α-pinene oxidation experiment at -30 ºC and 20 % RH). For the analysis, we processed separately 1-second TD-DMA and 1-second FIGAERO thermograms. Since the FIGAERO measures in a semi-continuous mode, we chose a representative thermogram. Both TD-DMA and FIGAERO data sets were background subtracted. For the TD-DMA background, we used the second heating cycle that is performed immediately after the first heating (described in Section 2.1.2). For the FIGAERO background, we used a period where no significant particle load was present in the chamber (at the beginning of the experiment). We considered only the organic compounds and excluded the reagent ions for this analysis. We ran the PMF software using the CNerror scheme (based on the noise of each ion) and up to 10 different solutions. 4-factor TD-DMA and 6-factor FIGAERO solutions (discussed later in Section 3.2.1) were chosen as the most interpretable results by a) comparing the residuals and by looking at which solution captured the total signal and certain species the best (e.g., $C_8H_{12}O_4$), b) by finding an equilibrium between good reconstructed signal and physically interpretable results. This means, that for the solutions presented here, likely a higher number of factors improve the residuals, nevertheless, we chose the solution with the smallest number of factors that can still provide realistic information.

https://doi.org/10.5194/acp-2022-498
Preprint. Discussion started: 26 August 2022

Atmospheric Chemistry and Physics Discussions

3. Results and discussion

3.1 Chemical composition comparison

Figure 1 shows the OS_C, calculated as $OS_C = 2 \times O{:}C - H{:}C$ (an approximation stated by Kroll et al. (2011)) against the number of carbon atoms for α-pinene oxidation products in the particle-phase at -30 ºC and 20 % RH as measured by three different techniques: TD-DMA, FIGAERO, and EESI-TOF. For all techniques, the highest intensities correspond to compounds with 10 carbon atoms (C_{10}) for which the oxidation state varies between 0.5 and -1.5 depending on the measurement technique. Compounds with more than 10 carbon atoms were also detectable by the TD-DMA, FIGAERO and EESI-TOF. The TD-DMA and FIGAERO detected also compounds with less than 5 carbon atoms and $OS_C > 0$ which, in contrast, are not detected by the EESI-TOF (this feature will be discussed in Section 3.2.1). In order to simplify the comparison, we calculated the fraction of species containing less than 10 carbon atoms ($C_{<10}$), 10 carbon atoms (C_{10}), and more than 10 carbon atoms ($C_{>10}$), since this can provide an insight of the detected fraction of monomers and dimers for each technique (Figure 1d). Approximately 42 %, 32 %, and 23 % of the signals correspond to $C_{<10}$, 47 %, 65 % and, 53 % to C_{10} and, around 11 %, 3 %, and 24 % to $C_{>10}$ measured by the TD-DMA, FIGAERO and EESI-TOF, respectively. Figure S2 in the Supplement displays the results for the experiments at -50 ºC. In every case, C_{10} represents the highest fraction detected by all the techniques in this experiment. Nevertheless, we do see significant differences between the techniques for $C_{<10}$, C_{10}, and $C_{>10}$.

The chemical ionization utilized by the TD-DMA (nitrate, NO_3^-) is more sensitive towards highly oxygenated species, while the FIGAERO (iodide, I^-) detects intermediately oxygenated species with higher sensitivity. In Figures S3 and S4 in the Supplement, we present the results (number of oxygen atoms vs number of carbon atoms) at -30 ºC and -50 ºC, respectively. From the figures (S3 and S4) we observe that more oxygenated species contribute more to the total signal on TD-DMA than in FIGAERO, this observation is consistent with the sensitivity that one would expect according to the chemical ionization. The electrospray ionization (Na^+) for the EESI-TOF is usually more sensitive towards intermediate oxygenated species, even though in the results presented here, it seems to capture very well the whole spectrum.

Besides the reagent ion selectivity, several factors can explain the quantitative differences. For example, both the TD-DMA and FIGAERO detect a lower fraction of $C_{>10}$ (11 % and 3 % compared to 24 % for the EESI-TOF). The TD-DMA and FIGAERO techniques are based on thermal desorption, which may cause decomposition of thermally unstable compounds during evaporation (as discussed in more detail in Section 3.2.1). On the other hand, the resulting fractions of $C_{>10}$ can be influenced by the ionization method employed: chemical ionization and electrospray are soft techniques, for which one can expect little fragmentation. Thus, we presume that thermal decomposition during evaporation could be the most significant factor that explain these differences.

Figure 2 presents the results for the experiment conducted at -10 ºC (α-pinene oxidation products at 80 % RH) for particles collected on a FILTER (Fig. 2a) and later analyzed by the UHPLC-HESI-HRMS method, and as measured by the FIGAERO and EESI-TOF (Fig. 2b and 2c, respectively). Overall, fewer compounds are detected by UHPLC-HESI-HRMS than by FIGAERO and EESI-TOF. The highest intensities in Fig. 2a (FILTER) correspond to $C_8H_{12}O_4$, $C_9H_{14}O_4$, $C_{10}H_{16}O_{3\text{-}6}$, $C_{17}H_{26}O_8$, and $C_{19}H_{28}O_7$. Ions with the same formulas are also detected by the FIGAERO and EESI-TOF, but the contribution to the total signal differs. The results at -10 ºC (number of oxygen atoms vs umber of carbon atoms) are shown in Figure S5 in the Supplement. By applying the UHPLC-HESI-HRMS method, it is possible to distinguish between compounds with identical chemical formula (isomers). For the experiment reported here, two isomers for $C_8H_{12}O_4$, $C_{10}H_{16}O_3$, and $C_{10}H_{16}O_5$, as well as three isomers for $C_{10}H_{16}O_4$ and $C_{10}H_{16}O_6$ were detected. The detection of these isomers is enabled by the chromatographic separation (their interaction with a reversed-phase column results in different retention times and therefore makes the separation feasible). However, complementary experiments are needed to investigate the molecular structure. Furthermore, Figure 2d shows the contributions of the $C_{<10}$, C_{10} and $C_{>10}$ fractions to the total signal for

https://doi.org/10.5194/acp-2022-498
Preprint. Discussion started: 26 August 2022

Atmospheric Chemistry and Physics Discussions

the FILTER, FIGAERO and EESI-TOF. At -10 ºC, the fraction of compounds with more than 10 carbon atoms ($C_{>10}$) has the smallest contribution to the total signal (14 %, 5 % and, 24 % for the FILTER, FIGAERO and EESI-TOF, respectively). The fractions $C_{<10}$ and C_{10} do not seem to have a clear tendency, they both contribute substantially to the total signal in each technique.

3.1.1 Volatility classes

We calculated the volatilities of the detected particle-phase compounds and associated them with defined volatility classes. We used the parametrization introduced in Donahue et al. (2011) and modified by Stolzenburg et al. (2018). This approach has been also discussed in Simon et al. (2020), and Wang et al. (2020). The volatility was calculated from the number of carbon and oxygen atoms in the specific molecules, and it was first defined at 300 K. By using the Clausius–Clapeyron equation, the volatility was then shifted according to the corresponding experimental temperature. The evaporation enthalpy was approximated according to Donahue et al. (2011) and Epstein et al. (2009). Thereafter the volatility was associated with any of the following classes: ultralow-volatility (ULVOC), extremely low-volatility (ELVOC), low-volatility (LVOC), semi-volatile (SVOC), and intermediate-volatility (IVOC) organic compounds.

Figures 3 and 4 show the contribution of each volatility class to the total particle signal for the corresponding experiment and for each technique. The results at - 50 ºC are reported in the Figure S6 in the Supplement. For the experiment at -30 ºC (Fig. 3), LVOC constitute the higher fraction for the TD-DMA, FIGAERO and, EESI-TOF. EESI-TOF detects the highest fraction of ULVOC (~ 12 % compared to 6 %, and 2 % measured by TD-DMA and FIGAERO, respectively). An IVOC fraction (~ 8 %) is only detected by the EESI-TOF. At -10 ºC (Figure 4), semi-volatile organic compounds (SVOC) contribute the most to the total particle signal for the FILTER, FIGAERO and EESI-TOF. Very small fractions of ULVOC are also detected by all the techniques. The EESI-TOF detects a higher fraction of IVOC (20 %) than FILTER and FIGAERO (2 % and 4 %), respectively. Taking into account the particle load (~1-3 ug m^{-3}) and size of the particles (diameter < 100 nm), it is possible that a significant fraction of IVOC measured by the EESI-TOF results from measurement artefacts, as seen in previous studies using EESI (Surdu et al., 2021). Several reasons (or a combination of them) can explain this feature: a) the Na^+ ionization technique may be more sensitive to lower oxygenated organic compounds than the I^- or NO_3^- techniques; b) likely, some amount of the gas-phase broke through the charcoal denuder (although its efficiency is > 99 %) and reached the detector. Lee et al. (2021a) reported that the EESI-TOF is more sensitive toward gas-phase analytes as compared to their particle-phase counterparts and, c) it can possibly occur some ion-induced fragmentation.

Overall, we observed that the contribution of the lowest volatility classes (ULVOC, ELVOC and LVOC) increases as the temperature decrease. This observation reflects two opposing temperature effects, as discussed in Ye et al. (2019) based on FIGAERO results: autoxidation and thus the extent of oxidation is reduced at low temperature, but any given compound is much less volatile at low temperature because of the strong dependency between saturation concentration and temperature.

3.2 Thermal desorption methods: TD-DMA and FIGAERO

Figure 5 shows the thermograms obtained by the FIGAERO and TD-DMA for the species $C_8H_{12}O_4$, $C_9H_{14}O_4$ and $C_{10}H_{16}O_6$ detected in the α-pinene ozonolysis experiment at -30 ºC. In Fig. 5a, c and e, we show a representative thermal desorption profile measured by FIGAERO. During the desorption time (~ 15 minutes), the normalized intensity of $C_9H_{14}O_4$ and $C_{10}H_{16}O_6$ first increased, reached a maximum at about 50-60 ºC, and then gradually decreased (Fig. 5c and e). In contrast, $C_8H_{12}O_4$ (Fig. 5a) shows two maxima (at ~ 50-60 ºC and ~ 120 ºC), which causes a broader signal. In addition, (in Fig.5a) at T > 120 ºC, the signal intensity stays high. In Figure 5b, d and f, we present the TD-DMA thermograms. Two heating cycles are performed in order to estimate the signal coming from the particles and the signal coming from the background due to the inlet line. Based on the filament resistance, we estimated that the temperature gradually increased up to approximately

https://doi.org/10.5194/acp-2022-498
Preprint. Discussion started: 26 August 2022

Atmospheric Chemistry and Physics Discussions

600 ºC in a period of ~ 1 minute. In the first heating cycle, the normalized intensity of $C_9H_{14}O_4$ and $C_{10}H_{16}O_6$ (Fig. 5d and f) rapidly increased, reached a maximum and subsequently decreased (sharp peak). As in Fig. 5a, the thermal profile of $C_8H_{12}O_4$ in TD-DMA (Fig. 5b) shows a broadened signal with a multimodal behavior, in which the $C_8H_{12}O_4$ signal at ~ 250 ºC reached background levels. In the second heating cycle (performed immediately afterwards, without particle collection), the normalized intensity remains stable and close to zero. The particle signal is estimated by subtracting the second heating from the first heating.

3.2.1 Positive matrix factorization results

The results of the PMF analysis of the TD-DMA data are shown in Figure 6 which contains the factor mass spectra (Fig. 6a-d), the factor thermograms (Fig. 6e), and the contribution of each factor to the total signal (Fig. 6f). We found that four factors are the best choice to reconstruct the TD-DMA data and to provide the most interpretable results (the residuals are shown in Fig. S7 in the Supplement). We numbered the factors according to their peak desorption temperatures (Fig. 6e). F1 $_{TD\text{-}DMA}$ which desorbs at the very first stages of the heating cycle, includes organic compounds with molecular masses between 150 and 250 Da (M_{av} = 211.6 Da), with a carbon, hydrogen and oxygen average content (CHO_{ac}) of 9.2, 14.6 and 5.4, respectively. F1 $_{TD\text{-}DMA}$ contains mainly compounds in the monomer region (see Fig. S8 in the Supplement). F2 $_{TD\text{-}DMA}$ desorbs right after F1 $_{TD\text{-}DMA}$. The mass average (M_{av}) is 230.7 Da and the CHO_{ac} is 10.0, 16.1 and 5.9. Compounds in the monomer region also contribute to this factor (see Fig. S8 in the Supplement). F3 $_{TD\text{-}DMA}$ shows a clear contribution of both monomers and dimers for the time when the time series shows a broadened peak. CHO_{ac} is 10.8, 16.7 and 5.5 and M_{av} = 234.5 Da. Lastly, F4 $_{TD\text{-}DMA}$ is dominated (~ 60 % of the signal intensity) by a high signal with molecular mass of 172.18 Da, which corresponds to $C_8H_{12}O_4$. This is reflected by lower values of CHO_{ac} and M_{av} compared to the other factors (CHO_{ac} = 8.6, 12.8, and 4.5, M_{av} = 188.2 Da). By looking closer into F4$_{TD\text{-}DMA}$ (Fig. 6d), we observe that some compounds with mass < 200 Da also contribute to this factor. By integrating each factor thermogram (Fig. 6e), we calculated that F1 $_{TD\text{-}DMA}$ and F2 $_{TD\text{-}DMA}$ contribute to ~ 70 % of the total signal while F3 $_{TD\text{-}DMA}$ and F4 $_{TD\text{-}DMA}$ make up ~ 30 % of the total signal as shown in Figure 6f.

On the other hand, we present in Figure 7 the results from applying PMF to the FIGAERO thermal desorption data for a solution with 6 factors. Figure 7a-f contains the factor mass spectra, Fig. 7g the factor thermograms, and Fig. 7h shows the contribution of each factor to the total particle signal (the residuals and the factors expressed in terms of their oxygen content and mass are shown in Figures S9 and S10 in the Supplement, respectively). F1 $_{FIGAERO}$, F2 $_{FIGAERO}$ and F3 $_{FIGAERO}$ (Fig. 7a-c) show a distinct contribution from monomers, and similar mass spectra, but display different thermal profiles (in Fig. 7g). Specifically, F2 $_{FIGAERO}$ and F3 $_{FIGAERO}$ exhibit well-defined thermal profiles (~ 15 ºC difference in T_{max}). However, F1 $_{FIGAERO}$ shows a broader profile with no distinct maximum. We suspect that F1 $_{FIGAERO}$ can be related to some of the following causes to some extent: a) Limited resolution of the chosen PMF solution at T < 50 ºC, likely to the presence of two neighbouring factors that were not resolved completely; b) interference from volatile material already evaporating at the beginning of the thermogram and, c) adsorption of gaseous compounds. Reason b could be related to the procedure initiating the desorption, where the filter is flushed with N_2 at ambient temperature before starting the heating ramp, which would likely affect the most volatile material. F4 $_{FIGAERO}$ and F5 $_{FIGAERO}$ (Fig. 7d and e) show contribution of both monomers and dimers, with a very similar CHO_{ac} and M_{av}. However, they show different thermogram behavior (~ 20 ºC difference for T_{max}, Fig 7g). F6 $_{FIGAERO}$ shows mainly contributions from compounds with low mass (< 200 Da) and desorbs mainly at the very end of the heating curve. The contribution of each factor to the total signal is shown in Fig 7h.

As mentioned previously, we observed some factors with similar CHO_{ac} and M_{av} but different thermal behavior, possibly due to the presence of isomers. Molecules with the same composition but different structure and functional groups may exhibit different volatilities. In fact, functionality is one of the driving factors that determines volatility (Pankow and Asher, 2008; Wang et al., 2020). The mass spectrometry techniques reported here are not able to determine the molecular

https://doi.org/10.5194/acp-2022-498
Preprint. Discussion started: 26 August 2022

Atmospheric Chemistry and Physics Discussions

structure. We further note that the factors F4 $_{TD\text{-}DMA}$ and F6 $_{FIGAERO}$ desorb mainly at the very last stage of the heating curves, although they both have a clear contribution of compounds with mass < 200 Da, and one of lowest oxygen content of all factors (i.e., the lowest degree of oxidation). We suspect that, F4 $_{TD\text{-}DMA}$ (Fig. 6d) and F6 $_{FIGAERO}$ (Fig. 7g) are comprised primarily of products of thermal decomposition; the heat applied to desorb the particles instead cleaves certain chemical bonds in (larger) molecules before these could desorb. Small compounds are generally expected to desorb before the transmitted thermal energy (i.e., the desorption temperature) is high enough to cause such decomposition. However, F4 $_{TD\text{-}DMA}$ and F6 $_{FIGAERO}$ thermal profiles also exhibit a small peak at lower temperatures (observed more clearly in Fig. 7g at ~ 40-50 °C), which is likely direct desorption. This may suggest that the low temperature peak stems from monomers desorbing directly, while the broad high temperature peak represents decomposing dimers/oligomers which are then detected at the composition of the corresponding monomers. Previous studies applying PMF analysis to FIGAERO thermal desorption data also observed the presence of one or more factors dominated by thermal decomposition products for α-pinene and sesquiterpene derived SOA (Buchholz et al., 2020; Li et al., 2021). Those studies concluded that thermal decomposition was the main volatilization process at desorption temperatures above 100 °C with differences between the observed SOA types.

By applying PMF analysis to thermal desorption data we observed that often, several factors are needed to explain the behavior of a single ion. One example is shown in the thermal profile of $C_8H_{12}O_4$ for both FIGAERO and TD-DMA (in the Supplement Fig. S11), in which all the PMF factors contribute. Particularly, F4 $_{TD\text{-}DMA}$ and F6 $_{FIGAERO}$ explain the $C_8H_{12}O_4$ signal at higher temperature. This is consistent with previous observations. Lopez-Hilfiker et al. (2015) reported a significant contribution of thermal decomposition to the detection of $C_8H_{12}O_4$ in the α-pinene ozonolysis system. However, the presence of the other factors suggests that either there are at least 3 isomers with distinguishable volatility, or that there are different thermal decomposition processes occurring at different desorption temperatures which all form $C_8H_{12}O_4$ as a stable product.

3.3 Advantages and disadvantages

Table 2 summarizes some advantages and disadvantages that should be considered when operating the instruments presented here. When measuring particle chemical composition, the time needed for collecting enough particles (mass) should be carefully considered. This fact becomes a challenge when analyzing nanoparticles, since the small particles do not contribute significantly to the overall SOA mass. For instance, for the experiments reported in this work (see Supplementary Fig. S1), the TD-DMA collection time was around 4 hours, the FIGAERO measured in a semicontinuous mode in which the particle collection lasted 15 minutes and was done every 30 minutes during the whole experiment. In contrast, the EESI-TOF measured continuously (every 10 seconds), whereas, for the offline analysis of FILTERS, the particles were collected during the whole experiment of ~ 8 hours. In addition, the EESI-TOF's total particle signal exhibited a good correlation with the mass concentration calculated from the Scanning Mobility Particle Sizer (SMPS) measurements ($r^2 > 0.94$, Fig. S12 in the Supplementary material). Despite the fact that there is a size-dependence on EESI-TOF sensitivity, EESI-TOF sensitivity decreases as the size of the particles increases (Lee et al., 2021b).

EESI-TOF and FIGAERO provide a faster response (every 10 seconds and every 30 minutes, respectively) than the other two methods, and allows a nearly real time monitoring. This is especially convenient when the chemical composition changes continuously (i.e., in complex environments or during oxidative flow reactor or chamber experiments). In contrast, the particle collection periods for TD-DMA and FILTER (offline analysis) were much longer and depended on the particle load and limit of detection. Besides the low time resolution, a main disadvantage of longer collection times is that aerosol aging may occur during that time. This can potentially change the chemical composition and therefore lead to inaccurate aerosol speciation. Several studies have reported positive and negative artifacts caused by adsorption of gases on the collection surfaces, longer sampling periods, and volatilization of organic species either during collection or during storage (Turpin et al., 1994; Subramanian et al., 2004; Kristensen et al., 2016).

https://doi.org/10.5194/acp-2022-498
Preprint. Discussion started: 26 August 2022

Atmospheric Chemistry and Physics Discussions

The mass spectrometers coupled to TD-DMA and FIGAERO (nitrate CI-APi-TOF and iodide HRToF-CIMS, respectively) can perform gas-phase measurements while the particle collection takes places. EESI-TOF in the dual-configuration can measure both particle-and gas-phase quasi simultaneously. This allows for a direct comparison between gas-and particle-phase. On the other hand, measurements that are size-resolved with respect to the aerosol size distribution (between 10 to 30 nm) are also feasible by the TD-DMA (Wagner et al., 2018). For the experiments presented here, size selective measurements were not performed to maximize the collected mass and to allow the intercomparison with the other methods.

The mass spectrometry techniques presented here (TD-DMA + nitrate CI-APi-TOF, FIGAERO + iodide HRToF-CIMS and Na^+ EESI-TOF) can only identify chemical formulas but with some limitations. Thus, for example, it is not possible for example to provide structural information or identification of isomers. In contrast, the UHPLC-HESI-HRMS offline method has the advantage of being able to distinguish between clusters, molecules, and isomers based on the chromatographic separation. Furthermore, the fragmentation pattern (via MS^2-experiments) can provide hints to interpret the functional groups and can be used for unambiguous compound identification. Hence, UHPLC-HRMS can provide robust analytical insight of the stable compounds.

The thermal desorption methods (TD-DMA and FIGAERO) exhibit significant thermal decomposition of compounds with desorption temperatures above 100 °C. For the EESI this seems to be less of an issue in general but in some specific studies thermal decomposition was found to be relevant (Bell et al., 2021). PMF analysis of the thermal desorption data from the TD-DMA and FIGAERO could separate the contribution of products from thermal decomposition from those directly desorbing. However, even with this method, it is not possible to obtain information about the original compounds decomposing and their true volatility. The observed decomposition temperature can be used as an upper limit for volatility (i.e., their true volatility is lower than that associated with the apparent desorption temperature).

For the FILTER method, the compounds collected on the filter have to be extracted into a liquid phase for the UHPLC separation. The choice of solvents for this extraction will determine which fraction of organic compounds will be analyzed. The water-methanol mixture used in this study will extract polar, hydrophilic compounds similar to the water-soluble organic carbon category. Note that the exposure to water (or other solvents) may lead to chemical reactions, e.g., hydrolysis of (hydro) peroxides. The selective extraction and potential aqueous phase chemistry may explain the smaller number of compounds detected with the FILTER method. However, for the compounds that do get analyzed, a much deeper understanding can be achieved (e.g., separation of isomers).

The ionization technique also plays a role on the final detection. If the ionization technique is not soft enough, this can result in fragmentation and affects the final response in the detection. In principle, the ionization techniques utilized by the instruments reported here are soft, meaning that no significant fragmentation occurs during the detection. Nevertheless, the ionization efficiency is different between the techniques. For example, with the nitrate reagent ion, highly oxygenated species can be better detected, while the ionization techniques used for FIGAERO and EESI-TOF (I^-, and Na^+, respectively) are more sensitive to intermediately oxygenated organic compounds. The UHPLC-HESI-HRMS can be operated in both polarity modes, however, and therefore detect species are either able to donate protons (in the negative mode) or form clusters with protons or sodium (in the positive mode).

The complete characterization of species in the particle-phase in terms of chemical formula and structure represents an analytical challenge. In this sense, the full identification of organic compounds is only possible by combining different techniques.

https://doi.org/10.5194/acp-2022-498
Preprint. Discussion started: 26 August 2022

Atmospheric Chemistry and Physics Discussions

4. Conclusions

In this study, we presented an overview of four different methods for measuring the chemical composition of ultrafine particles and we described their capabilities to detect organic compounds. Specifically, we reported the particle-phase composition from α-pinene ozonolysis at -50 ºC, -30 ºC and -10 ºC. In all the cases, the highest portion of detected compounds correspond to species with 10 and less than 10 carbon atoms (C_{10}, $C_{<10}$). The EESI-TOF generally detected a higher fraction (compared to the other techniques: TD-DMA, FIGAERO and FILTERS) of compounds with more than 10 carbon atoms ($C_{>10}$). In terms of volatility classes, EESI-TOF detected the higher fraction of ULVOC in all the experiments reported here, especially for those at lower temperatures (-50 ºC and -30 ºC). We presume that several factors can explain these differences, i.e., thermal decomposition of large compounds (for the thermal desorption methods), for which we applied positive matrix factorization on the thermal profiles and suggested a 4-Factor solution for TD-DMA and a 6-Factor solution for the FIGAERO. Specifically, we suspect that F4 $_{\text{TD-DMA}}$ and F6 $_{\text{FIGAERO}}$ might be related to thermal decomposition to some extent. The PMF factors dominated by direct desorption can be interpreted as volatility classes, characterized by their T_{max} values (the peak in the respective temperature desorption profiles). Nevertheless, further calibration experiments are needed to determine the relation between T_{max} and saturation concentration. With the offline method UHPLC-HESI-HRMS, we were able to verify the presence of isomers (two isomers for $C_8H_{12}O_4$, $C_{10}H_{16}O_3$, $C_{10}H_{16}O_5$, and three isomers for $C_{10}H_{16}O_4$ and $C_{10}H_{16}O_6$), which represents an important advantage over the online methods reported here.

While the methods generally agree on the most important compounds that are found in the nanoparticles, they all have their strengths and shortcomings. A major limit of these methods is that the measurements of the chemical compounds are not quantitative and only rough estimates of the exact contributions of a compound to the overall chemical composition can be made. However, knowing the limitations of each method and using combinations of the available methods can provide deeper insights into the chemical composition and volatility of nanoparticles.

Data availability. Data related to this article are available upon reasonable request to the corresponding authors.

Supplement The supplement related to this article will be available online.

Author contributions.

L. C., M. S., B. L., M. W., S. B., T. M., M. G., Z. B., L. D., J. Du., H. F., X.-C. H., H. L., N. G. A. M., V. M., H. E. M., G. M., R. M., R. L. M., B. M., A. O., T. P., J. P., M. P., A. A. P., B. R., W. S., J. S., P. T., A. T., N. S. U., D. S. W., S. K. W., A. W., W. Y., M. Z.-W., U. B., J. Kir., M. K., K. L., I. E.-H., N. M. D., A. K., and J. Cu. prepared the CLOUD facility and measurement instruments. L. C., M. S., B. L., M. W., S. B., T. M., M. G., A. A., D. M. B., L. D., J. Du., H. F., X.-C. H., H. L., N. G. A. M., V. M., G. M., R. L. M., B. M., J. S., C. T., A. T., N. S. U., D. S. W., S. K. W., M. Z.-W., and J. Kir. collected the data. L. C., M. S., B. L., M. W., M. T., S. B., A. B., S. K. W., and J. Cu. analyzed the data. L. C., M. S., B. L., M. W., M. T., A. B., M. Sim., A. C. W., M. H., D. M. B., L. D., T. P., D. S., R. C. F., A. H., M. K., K. L., D. W., I. E.-H., N. M. D., A. L. V., A. K., and J. Cu. contributed to the scientific discussion and interpretation of the results. L. C., A. B., U. B., R. C. F., and J. Cu. contributed to the writing of the manuscript.

Competing interests. The authors declare that they have no conflict of interest.

Acknowledgments. We thank CERN for providing the CLOUD facility to perform the experiments and the CLOUD community for supporting this study. We especially would like to thank Katja Ivanova, Timo Keber, Frank Malkemper, Robert Sitals, Hanna Elina Manninen, Antti Onnela, and Robert Kristic for their contributions to the experiment.

https://doi.org/10.5194/acp-2022-498
Preprint. Discussion started: 26 August 2022

Atmospheric Chemistry and Physics Discussions

Financial support. This work was supported by Innovative Training Networks – ITN 400 (CLOUD-Motion H2020-MSCA-ITN-2017 no. 764991 and no. 701647) and by the German Ministry of Science and Education (CLOUD-16, 01LK1601A). European Union's Horizon 2020 research and innovation program through the ATMO-ACCESS Integrating Activity under grant agreement no. 101008004 and, by no. 895875 ("NPF-PANDA"). Deutsche Forschungsgemeinschaft (DFG; German Research Foundation) (grant no. 410009325). US National Science Foundation Award (AGS-1801280, AGS-1801574, AGS-1801897, AGS-1602086, and AGS-18801329). Swiss National Science Foundation (200020_172602 and 20FI20_172622). CERN/FIS-COM/0028/2019, FCT Portuguese national funding agency for science, research and technology. The Jenny and Antti Wihuri Foundation. ACCC Flagship funded by the Academy of Finland grant number 337549, Academy professorship funded by the Academy of Finland (grant no. 302958), Academy of Finland projects no. 325656, 316114, 314798, 325647 and 341349, "Quantifying carbon sink, CarbonSink+ and their interaction with air quality" INAR project funded by Jane and Aatos Erkko Foundation, Jenny and Antti Wihuri Foundation project "Air pollution cocktail in Gigacity", European Research Council (ERC) project ATM-GTP Contract No. 742206, and the Arena for the gap analysis of the existing Arctic Science Co-Operations (AASCO) funded by Prince Albert Foundation Contract No 2859.

https://doi.org/10.5194/acp-2022-498
Preprint. Discussion started: 26 August 2022

Atmospheric Chemistry and Physics Discussions

555 **References**

Bell, D. M., Wu, C., Bertrand, A., Graham, E., Schoonbaert, J., Giannoukos, S., Baltensperger, U., Prevot, A. S. H., Riipinen, I., El Haddad, I., and Mohr, C.: Particle-phase processing of α-pinene NO3 secondary organic aerosol in the dark, Atmos. Chem. Phys. Discuss., 2021, 1-28, 10.5194/acp-2021-379, 2021.

560 Breitenlechner, M., Fischer, L., Hainer, M., Heinritzi, M., Curtius, J., and Hansel, A.: PTR3: An Instrument for Studying the Lifecycle of Reactive Organic Carbon in the Atmosphere, Analytical Chemistry, 89, 5824-5831, 10.1021/acs.analchem.6b05110, 2017.

Buchholz, A., Ylisirniö, A., Huang, W., Mohr, C., Canagaratna, M., Worsnop, D. R., Schobesberger, S., and Virtanen, A.: Deconvolution of FIGAERO–CIMS thermal desorption profiles using positive matrix factorisation to identify chemical and physical processes during
565 particle evaporation, Atmos. Chem. Phys., 20, 7693-7716, 10.5194/acp-20-7693-2020, 2020.

Bzdek, B. R., Pennington, M. R., and Johnston, M. V.: Single particle chemical analysis of ambient ultrafine aerosol: A review, Journal of Aerosol Science, 52, 109-120, https://doi.org/10.1016/j.jaerosci.2012.05.001, 2012.

570 Caudillo, L., Rörup, B., Heinritzi, M., Marie, G., Simon, M., Wagner, A. C., Müller, T., Granzin, M., Amorim, A., Ataei, F., Baalbaki, R., Bertozzi, B., Brasseur, Z., Chiu, R., Chu, B., Dada, L., Duplissy, J., Finkenzeller, H., Gonzalez Carracedo, L., He, X. C., Hofbauer, V., Kong, W., Lamkaddam, H., Lee, C. P., Lopez, B., Mahfouz, N. G. A., Makhmutov, V., Manninen, H. E., Marten, R., Massabò, D., Mauldin, R. L., Mentler, B., Molteni, U., Onnela, A., Pfeifer, J., Philippov, M., Piedehierro, A. A., Schervish, M., Scholz, W., Schulze, B., Shen, J., Stolzenburg, D., Stozhkov, Y., Surdu, M., Tauber, C., Tham, Y. J., Tian, P., Tomé, A., Vogt, S., Wang, M., Wang, D. S., Weber,
575 S. K., Welti, A., Yonghong, W., Yusheng, W., Zauner-Wieczorek, M., Baltensperger, U., El Haddad, I., Flagan, R. C., Hansel, A., Höhler, K., Kirkby, J., Kulmala, M., Lehtipalo, K., Möhler, O., Saathoff, H., Volkamer, R., Winkler, P. M., Donahue, N. M., Kürten, A., and Curtius, J.: Chemical composition of nanoparticles from α-pinene nucleation and the influence of isoprene and relative humidity at low temperature, Atmos. Chem. Phys., 21, 17099-17114, 10.5194/acp-21-17099-2021, 2021.

580 Curtius, J., Sierau, B., Arnold, F., Baumann, R., Busen, R., Schulte, P., and Schumann, U.: First direct sulfuric acid detection in the exhaust plume of a jet aircraft in flight, Geophysical Research Letters, 25, 923-926, https://doi.org/10.1029/98GL00512, 1998.

Donahue, N. M., Epstein, S., Pandis, S. N., and Robinson, A. L.: A two-dimensional volatility basis set: 1. organic-aerosol mixing thermodynamics, Atmospheric Chemistry and Physics, 11, 3303-3318, 2011.
585

Duplissy, J., Merikanto, J., Franchin, A., Tsagkogeorgas, G., Kangasluoma, J., Wimmer, D., Vuollekoski, H., Schobesberger, S., Lehtipalo, K., Flagan, R. C., Brus, D., Donahue, N. M., Vehkamäki, H., Almeida, J., Amorim, A., Barmet, P., Bianchi, F., Breitenlechner, M., Dunne, E. M., Guida, R., Henschel, H., Junninen, H., Kirkby, J., Kürten, A., Kupc, A., Määttänen, A., Makhmutov, V., Mathot, S., Nieminen, T., Onnela, A., Praplan, A. P., Riccobono, F., Rondo, L., Steiner, G., Tome, A., Walther, H., Baltensperger, U., Carslaw, K. S.,
590 Dommen, J., Hansel, A., Petäjä, T., Sipilä, M., Stratmann, F., Vrtala, A., Wagner, P. E., Worsnop, D. R., Curtius, J., and Kulmala, M.: Effect of ions on sulfuric acid-water binary particle formation: 2. Experimental data and comparison with QC-normalized classical nucleation theory, Journal of Geophysical Research: Atmospheres, 121, 1752-1775, 10.1002/2015JD023539, 2016.

Epstein, S. A., Riipinen, I., and Donahue, N. M.: A semiempirical correlation between enthalpy of vaporization and saturation
595 concentration for organic aerosol, Environmental science & technology, 44, 743-748, 2009.

Gonser, S. G., and Held, A.: A chemical analyzer for charged ultrafine particles, Atmos. Meas. Tech., 6, 2339-2348, 10.5194/amt-6-2339-2013, 2013.

600 Graus, M., Müller, M., and Hansel, A.: High resolution PTR-TOF: Quantification and formula confirmation of VOC in real time, Journal of the American Society for Mass Spectrometry, 21, 1037-1044, 10.1016/j.jasms.2010.02.006, 2010.

Hallquist, M., Wenger, J. C., Baltensperger, U., Rudich, Y., Simpson, D., Claeys, M., Dommen, J., Donahue, N. M., George, C., Goldstein, A. H., Hamilton, J. F., Herrmann, H., Hoffmann, T., Iinuma, Y., Jang, M., Jenkin, M. E., Jimenez, J. L., Kiendler-Scharr, A.,
605 Maenhaut, W., McFiggans, G., Mentel, T. F., Monod, A., Prévôt, A. S. H., Seinfeld, J. H., Surratt, J. D., Szmigielski, R., and Wildt, J.: The formation, properties and impact of secondary organic aerosol: current and emerging issues, Atmos. Chem. Phys., 9, 5155-5236, 10.5194/acp-9-5155-2009, 2009.

He, S., Li, L., Duan, H., Naqwi, A., and Hogan, C. J.: Aerosol Analysis via Electrostatic Precipitation-Electrospray Ionization Mass
610 Spectrometry, Analytical Chemistry, 87, 6752-6760, 10.1021/acs.analchem.5b01183, 2015.

Heinritzi, M., Simon, M., Steiner, G., Wagner, A. C., Kürten, A., Hansel, A., and Curtius, J.: Characterization of the mass-dependent transmission efficiency of a CIMS, Atmos. Meas. Tech., 9, 1449-1460, 10.5194/amt-9-1449-2016, 2016.

615 Horan, A. J., Apsokardu, M. J., and Johnston, M. V.: Droplet Assisted Inlet Ionization for Online Analysis of Airborne Nanoparticles, Analytical Chemistry, 89, 1059-1062, 10.1021/acs.analchem.6b04718, 2017.

Jayne, J. T., Leard, D. C., Zhang, X., Davidovits, P., Smith, K. A., Kolb, C. E., and Worsnop, D. R.: Development of an Aerosol Mass Spectrometer for Size and Composition Analysis of Submicron Particles, Aerosol Science and Technology, 33, 49-70,
620 10.1080/027868200410840, 2000.

Kirkby, J., Curtius, J., Almeida, J., Dunne, E., Duplissy, J., Ehrhart, S., Franchin, A., Gagné, S., Ickes, L., Kürten, A., Kupc, A., Metzger, A., Riccobono, F., Rondo, L., Schobesberger, S., Tsagkogeorgas, G., Wimmer, D., Amorim, A., Bianchi, F., Breitenlechner, M., David, A., Dommen, J., Downard, A., Ehn, M., Flagan, R. C., Haider, S., Hansel, A., Hauser, D., Jud, W., Junninen, H., Kreissl, F., Kvashin, A.,

https://doi.org/10.5194/acp-2022-498
Preprint. Discussion started: 26 August 2022

Atmospheric Chemistry and Physics Discussions

Laaksonen, A., Lehtipalo, K., Lima, J., Lovejoy, E. R., Makhmutov, V., Mathot, S., Mikkilä, J., Minginette, P., Mogo, S., Nieminen, T., Onnela, A., Pereira, P., Petäjä, T., Schnitzhofer, R., Seinfeld, J. H., Sipilä, M., Stozhkov, Y., Stratmann, F., Tomé, A., Vanhanen, J., Viisanen, Y., Vrtala, A., Wagner, P. E., Walther, H., Weingartner, E., Wex, H., Winkler, P. M., Carslaw, K. S., Worsnop, D. R., Baltensperger, U., and Kulmala, M.: Role of sulphuric acid, ammonia and galactic cosmic rays in atmospheric aerosol nucleation, Nature, 476, 429-433, 10.1038/nature10343, 2011.

Kristensen, K., Bilde, M., Aalto, P. P., Petäjä, T., and Glasius, M.: Denuder/filter sampling of organic acids and organosulfates at urban and boreal forest sites: Gas/particle distribution and possible sampling artifacts, Atmospheric Environment, 130, 36-53, https://doi.org/10.1016/j.atmosenv.2015.10.046, 2016.

Kroll, J. H., Donahue, N. M., Jimenez, J. L., Kessler, S. H., Canagaratna, M. R., Wilson, K. R., Altieri, K. E., Mazzoleni, L. R., Wozniak, A. S., Bluhm, H., Mysak, E. R., Smith, J. D., Kolb, C. E., and Worsnop, D. R.: Carbon oxidation state as a metric for describing the chemistry of atmospheric organic aerosol, Nature Chemistry, 3, 133-139, 10.1038/nchem.948, 2011.

Kürten, A., Rondo, L., Ehrhart, S., and Curtius, J.: Performance of a corona ion source for measurement of sulfuric acid by chemical ionization mass spectrometry, Atmos. Meas. Tech., 4, 437-443, 10.5194/amt-4-437-2011, 2011.

Kürten, A., Jokinen, T., Simon, M., Sipilä, M., Sarnela, N., Junninen, H., Adamov, A., Almeida, J., Amorim, A., Bianchi, F., Breitenlechner, M., Dommen, J., Donahue, N. M., Duplissy, J., Ehrhart, S., Flagan, R. C., Franchin, A., Hakala, J., Hansel, A., Heinritzi, M., Hutterli, M., Kangasluoma, J., Kirkby, J., Laaksonen, A., Lehtipalo, K., Leiminger, M., Makhmutov, V., Mathot, S., Onnela, A., Petäjä, T., Praplan, A. P., Riccobono, F., Rissanen, M. P., Rondo, L., Schobesberger, S., Seinfeld, J. H., Steiner, G., Tomé, A., Tröstl, J., Winkler, P. M., Williamson, C., Wimmer, D., Ye, P., Baltensperger, U., Carslaw, K. S., Kulmala, M., Worsnop, D. R., and Curtius, J.: Neutral molecular cluster formation of sulfuric acid–dimethylamine observed in real time under atmospheric conditions, Proceedings of the National Academy of Sciences, 111, 15019-15024, 10.1073/pnas.1404853111, 2014.

Laitinen, T., Hartonen, K., Kulmala, M., and Riekkola, M. L.: Aerosol time-of-flight mass spectrometer for measuring ultrafine aerosol particles, Boreal Environ Res, 14, 539-549, 2009.

Lee, B. H., Lopez-Hilfiker, F. D., Mohr, C., Kurtén, T., Worsnop, D. R., and Thornton, J. A.: An Iodide-Adduct High-Resolution Time-of-Flight Chemical-Ionization Mass Spectrometer: Application to Atmospheric Inorganic and Organic Compounds, Environmental Science & Technology, 48, 6309-6317, 10.1021/es500362a, 2014.

Lee, C. P., Riva, M., Wang, D., Tomaz, S., Li, D., Perrier, S., Slowik, J. G., Bourgain, F., Schmale, J., Prevot, A. S. H., Baltensperger, U., George, C., and El Haddad, I.: Online Aerosol Chemical Characterization by Extractive Electrospray Ionization–Ultrahigh-Resolution Mass Spectrometry (EESI-Orbitrap), Environmental Science & Technology, 54, 3871-3880, 10.1021/acs.est.9b07090, 2020.

Lee, C. P., Surdu, M., Bell, D. M., Dommen, J., Xiao, M., Zhou, X., Baccarini, A., Giannoukos, S., Wehrle, G., Schneider, P. A., Prevot, A. S. H., Slowik, J. G., Lamkaddam, H., Wang, D., Baltensperger, U., and El Haddad, I.: High-Frequency Gaseous and Particulate Chemical Characterization using Extractive Electrospray Ionization Mass Spectrometry (Dual-Phase-EESI-TOF), Atmos. Meas. Tech. Discuss., 2021, 1-21, 10.5194/amt-2021-325, 2021a.

Lee, C. P., Surdu, M., Bell, D. M., Lamkaddam, H., Wang, M., Ataei, F., Hofbauer, V., Lopez, B., Donahue, N. M., Dommen, J., Prevot, A. S. H., Slowik, J. G., Wang, D., Baltensperger, U., and El Haddad, I.: Effects of aerosol size and coating thickness on the molecular detection using extractive electrospray ionization, Atmos. Meas. Tech., 14, 5913-5923, 10.5194/amt-14-5913-2021, 2021b.

Lee, C. P., Surdu, M., Bell, D. M., Dommen, J., Xiao, M., Zhou, X., Baccarini, A., Giannoukos, S., Wehrle, G., Schneider, P. A., Prevot, A. S. H., Slowik, J. G., Lamkaddam, H., Wang, D., Baltensperger, U., and El Haddad, I.: High-frequency gaseous and particulate chemical characterization using extractive electrospray ionization mass spectrometry (Dual-Phase-EESI-TOF), Atmos. Meas. Tech., 15, 3747-3760, 10.5194/amt-15-3747-2022, 2022.

Li, Z., Buchholz, A., Ylisirniö, A., Barreira, L., Hao, L., Schobesberger, S., Yli-Juuti, T., and Virtanen, A.: Evolution of volatility and composition in sesquiterpene-mixed and α-pinene secondary organic aerosol particles during isothermal evaporation, Atmos. Chem. Phys., 21, 18283-18302, 10.5194/acp-21-18283-2021, 2021.

Lopez-Hilfiker, F. D., Mohr, C., Ehn, M., Rubach, F., Kleist, E., Wildt, J., Mentel, T. F., Lutz, A., Hallquist, M., Worsnop, D., and Thornton, J. A.: A novel method for online analysis of gas and particle composition: description and evaluation of a Filter Inlet for Gases and AEROsols (FIGAERO), Atmos. Meas. Tech., 7, 983-1001, 10.5194/amt-7-983-2014, 2014.

Lopez-Hilfiker, F. D., Mohr, C., Ehn, M., Rubach, F., Kleist, E., Wildt, J., Mentel, T. F., Carrasquillo, A. J., Daumit, K. E., Hunter, J. F., Kroll, J. H., Worsnop, D. R., and Thornton, J. A.: Phase partitioning and volatility of secondary organic aerosol components formed from α-pinene ozonolysis and OH oxidation: the importance of accretion products and other low volatility compounds, Atmos. Chem. Phys., 15, 7765-7776, 10.5194/acp-15-7765-2015, 2015.

Lopez-Hilfiker, F. D., Pospisilova, V., Huang, W., Kalberer, M., Mohr, C., Stefenelli, G., Thornton, J. A., Baltensperger, U., Prevot, A. S. H., and Slowik, J. G.: An extractive electrospray ionization time-of-flight mass spectrometer (EESI-TOF) for online measurement of atmospheric aerosol particles, Atmos. Meas. Tech., 12, 4867-4886, 10.5194/amt-12-4867-2019, 2019.

Paatero, P., and Tapper, U.: Positive matrix factorization: A non-negative factor model with optimal utilization of error estimates of data values, Environmetrics, 5, 111-126, 1994.

Pankow, J. F., and Asher, W. E.: SIMPOL. 1: a simple group contribution method for predicting vapor pressures and enthalpies of vaporization of multifunctional organic compounds, Atmospheric Chemistry and Physics, 8, 2773-2796, 2008.

https://doi.org/10.5194/acp-2022-498
Preprint. Discussion started: 26 August 2022

Atmospheric Chemistry and Physics Discussions

Phares, D. J., and Collier, S.: Direct Collection of Aerosols by Electrostatic Classification for Size-Resolved Chemical Analysis, Aerosol Science and Technology, 44, 173-181, 10.1080/02786820903482914, 2010.

Simon, M., Dada, L., Heinritzi, M., Scholz, W., Stolzenburg, D., Fischer, L., Wagner, A. C., Kürten, A., Rörup, B., He, X. C., Almeida, J., Baalbaki, R., Baccarini, A., Bauer, P. S., Beck, L., Bergen, A., Bianchi, F., Bräkling, S., Brilke, S., Caudillo, L., Chen, D., Chu, B., Dias, A., Draper, D. C., Duplissy, J., El-Haddad, I., Finkenzeller, H., Frege, C., Gonzalez-Carracedo, L., Gordon, H., Granzin, M., Hakala, J., Hofbauer, V., Hoyle, C. R., Kim, C., Kong, W., Lamkaddam, H., Lee, C. P., Lehtipalo, K., Leiminger, M., Mai, H., Manninen, H. E., Marie, G., Marten, R., Mentler, B., Molteni, U., Nichman, L., Nie, W., Ojdanic, A., Onnela, A., Partoll, E., Petäjä, T., Pfeifer, J., Philippov, M., Quéléver, L. L. J., Ranjithkumar, A., Rissanen, M. P., Schallhart, S., Schobesberger, S., Schuchmann, S., Shen, J., Sipilä, M., Steiner, G., Stozhkov, Y., Tauber, C., Tham, Y. J., Tomé, A. R., Vazquez-Pufleau, M., Vogel, A. L., Wagner, R., Wang, M., Wang, D. S., Wang, Y., Weber, S. K., Wu, Y., Xiao, M., Yan, C., Ye, P., Ye, Q., Zauner-Wieczorek, M., Zhou, X., Baltensperger, U., Dommen, J., Flagan, R. C., Hansel, A., Kulmala, M., Volkamer, R., Winkler, P. M., Worsnop, D. R., Donahue, N. M., Kirkby, J., and Curtius, J.: Molecular understanding of new-particle formation from α-pinene between −50 and +25 °C, Atmos. Chem. Phys., 20, 9183-9207, 10.5194/acp-20-9183-2020, 2020.

Stolzenburg, D., Fischer, L., Vogel, A. L., Heinritzi, M., Schervish, M., Simon, M., Wagner, A. C., Dada, L., Ahonen, L. R., Amorim, A., Baccarini, A., Bauer, P. S., Baumgartner, B., Bergen, A., Bianchi, F., Breitenlechner, M., Brilke, S., Buenrostro Mazon, S., Chen, D., Dias, A., Draper, D. C., Duplissy, J., El Haddad, I., Finkenzeller, H., Frege, C., Fuchs, C., Garmash, O., Gordon, H., He, X., Helm, J., Hofbauer, V., Hoyle, C. R., Kim, C., Kirkby, J., Kontkanen, J., Kürten, A., Lampilahti, J., Lawler, M., Lehtipalo, K., Leiminger, M., Mai, H., Mathot, S., Mentler, B., Molteni, U., Nie, W., Nieminen, T., Nowak, J. B., Ojdanic, A., Onnela, A., Passananti, M., Petäjä, T., Quéléver, L. L. J., Rissanen, M. P., Sarnela, N., Schallhart, S., Tauber, C., Tomé, A., Wagner, R., Wang, M., Weitz, L., Wimmer, D., Xiao, M., Yan, C., Ye, P., Zha, Q., Baltensperger, U., Curtius, J., Dommen, J., Flagan, R. C., Kulmala, M., Smith, J. N., Worsnop, D. R., Hansel, A., Donahue, N. M., and Winkler, P. M.: Rapid growth of organic aerosol nanoparticles over a wide tropospheric temperature range, Proceedings of the National Academy of Sciences, 115, 9122-9127, 10.1073/pnas.1807604115, 2018.

Subramanian, R., Khlystov, A. Y., Cabada, J. C., and Robinson, A. L.: Positive and Negative Artifacts in Particulate Organic Carbon Measurements with Denuded and Undenuded Sampler Configurations Special Issue of Aerosol Science and Technology on Findings from the Fine Particulate Matter Supersites Program, Aerosol Science and Technology, 38, 27-48, 10.1080/02786820390229354, 2004.

Surdu, M., Pospisilova, V., Xiao, M., Wang, M., Mentler, B., Simon, M., Stolzenburg, D., Hoyle, C. R., Bell, D. M., Lee, C. P., Lamkaddam, H., Lopez-Hilfiker, F., Ahonen, L. R., Amorim, A., Baccarini, A., Chen, D., Dada, L., Duplissy, J., Finkenzeller, H., He, X.-C., Hofbauer, V., Kim, C., Kürten, A., Kvashnin, A., Lehtipalo, K., Makhmutov, V., Molteni, U., Nie, W., Onnela, A., Petäjä, T., Quéléver, L. L. J., Tauber, C., Tomé, A., Wagner, R., Yan, C., Prevot, A. S. H., Dommen, J., Donahue, N. M., Hansel, A., Curtius, J., Winkler, P. M., Kulmala, M., Volkamer, R., Flagan, R. C., Kirkby, J., Worsnop, D. R., Slowik, J. G., Wang, D. S., Baltensperger, U., and Haddad, I. e.: Molecular characterization of ultrafine particles using extractive electrospray time-of-flight mass spectrometry, Environmental Science: Atmospheres, 1, 434-448, 10.1039/D1EA00050K, 2021.

Turpin, B. J., Huntzicker, J. J., and Hering, S. V.: Investigation of organic aerosol sampling artifacts in the Los Angeles basin, Atmos. Chem. Phys., 28, 3061-3071, 10.1016/1352-2310(94)00133-6, 1994.
, 1994.

Ungeheuer, F., van Pinxteren, D., and Vogel, A. L.: Identification and source attribution of organic compounds in ultrafine particles near Frankfurt International Airport, Atmos. Chem. Phys., 21, 3763-3775, 10.5194/acp-21-3763-2021, 2021.

Voisin, D., Smith, J. N., Sakurai, H., McMurry, P. H., and Eisele, F. L.: Thermal Desorption Chemical Ionization Mass Spectrometer for Ultrafine Particle Chemical Composition, Aerosol Science and Technology, 37, 471-475, 10.1080/02786820300959, 2003.

Wagner, A. C., Bergen, A., Brilke, S., Fuchs, C., Ernst, M., Hoker, J., Heinritzi, M., Simon, M., Bühner, B., and Curtius, J.: Size-resolved online chemical analysis of nanoaerosol particles: a thermal desorption differential mobility analyzer coupled to a chemical ionization time-of-flight mass spectrometer, Atmospheric Measurement Techniques, 11, 5489-5506, 2018.

Wang, M., Chen, D., Xiao, M., Ye, Q., Stolzenburg, D., Hofbauer, V., Ye, P., Vogel, A. L., Mauldin, R. L., Amorim, A., Baccarini, A., Baumgartner, B., Brilke, S., Dada, L., Dias, A., Duplissy, J., Finkenzeller, H., Garmash, O., He, X.-C., Hoyle, C. R., Kim, C., Kvashnin, A., Lehtipalo, K., Fischer, L., Molteni, U., Petäjä, T., Pospisilova, V., Quéléver, L. L. J., Rissanen, M., Simon, M., Tauber, C., Tomé, A., Wagner, A. C., Weitz, L., Volkamer, R., Winkler, P. M., Kirkby, J., Worsnop, D. R., Kulmala, M., Baltensperger, U., Dommen, J., El-Haddad, I., and Donahue, N. M.: Photo-oxidation of Aromatic Hydrocarbons Produces Low-Volatility Organic Compounds, Environmental Science & Technology, 54, 7911-7921, 10.1021/acs.est.0c02100, 2020.

Wang, S., Zordan, C. A., and Johnston, M. V.: Chemical Characterization of Individual, Airborne Sub-10-nm Particles and Molecules, Analytical Chemistry, 78, 1750-1754, 10.1021/ac052243l, 2006.

Ye, Q., Wang, M., Hofbauer, V., Stolzenburg, D., Chen, D., Schervish, M., Vogel, A. L., Mauldin, R. L., Baalbaki, R., Brilke, S., Dada, L., Dias, A., Duplissy, J., El Haddad, I., Finkenzeller, H., Fischer, L., He, X., Kim, C., Kürten, A., Lamkaddam, H., Lee, C. P., Lehtipalo, K., Leiminger, M., Manninen, H. E., Marten, R., Mentler, B., Partoll, E., Petäjä, T., Rissanen, M. P., Schobesberger, S., Schuchmann, S., Simon, M., Tham, Y. J., Vazquez-Pufleau, M., Wagner, A. C., Wang, Y., Wu, Y., Xiao, M., Baltensperger, U., Curtius, J., Flagan, R., Kirkby, j., Kulmala, M., Volkamer, R., Winkler, P. M., Worsnop, D. R., and Donahue, N. M.: Molecular Composition and Volatility of Nucleated Particles from α-Pinene Oxidation between -50 °C and +25 °C, Environmental Science & Technology, 10.1021/acs.est.9b03265, 2019.

https://doi.org/10.5194/acp-2022-498
Preprint. Discussion started: 26 August 2022

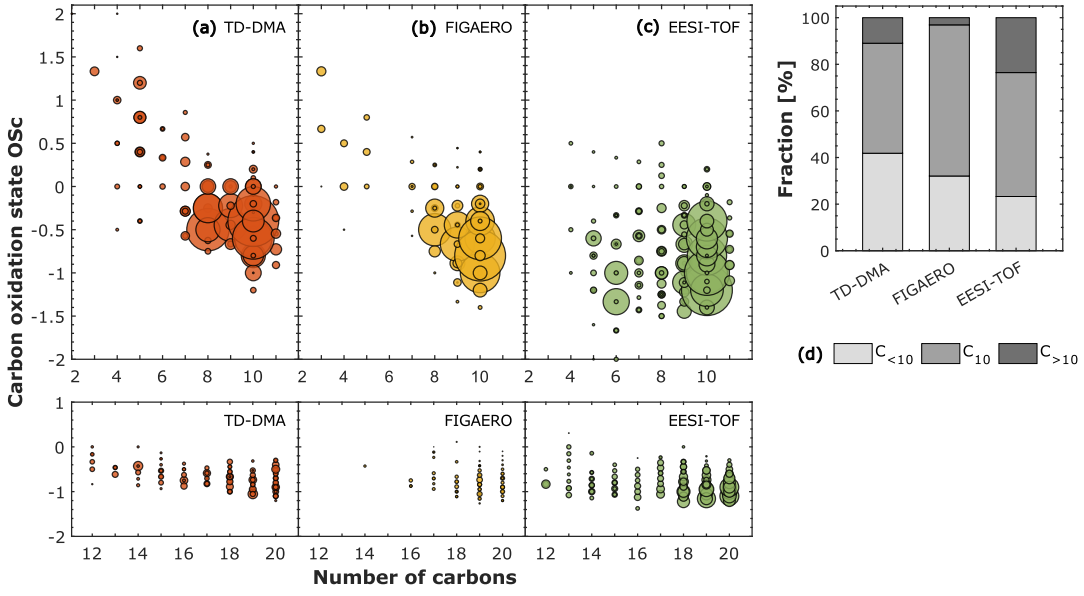

Figure 1. Carbon oxidation state OSc against the number of carbon atoms for α-pinene oxidation products in the particle-phase at -30 °C and 20 % RH measured by three different techniques. (a) TD-DMA: Thermal Desorption-Differential Mobility Analyzer coupled to a NO_3^- chemical ionization-atmospheric-pressure-interface-time-of-flight mass spectrometer. (b) FIGAERO: Filter Inlet for Gases and AEROsols coupled to an I^- high-resolution time-of-flight chemical-ionization mass spectrometer, and (c) EESI-TOF: Extractive Electrospray Na^+ Ionization time-of-flight mass spectrometer. The level of α-pinene was between 1 and 6 ppbv while the ozone level was ~ 100 ppbv. The carbon oxidation state is calculated as follows: OSc = 2xO:C - H:C. The marker sizes in (a), (b), and (c) represent the intensities normalized by the total signal in each system. (d) Fraction of species in the particle-phase containing less than 10 carbon atoms ($C_{<10}$), 10 carbon atoms (C_{10}), and more than 10 carbon atoms ($C_{>10}$). The fraction was calculated by normalizing the intensities by the total signal in each system.

https://doi.org/10.5194/acp-2022-498
Preprint. Discussion started: 26 August 2022

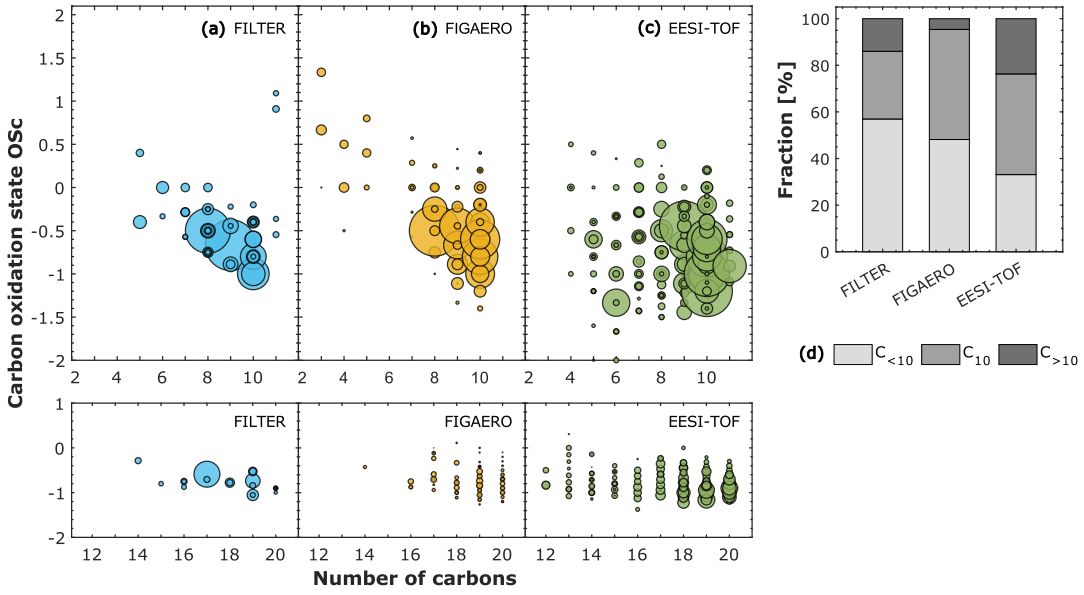

Figure 2. Carbon oxidation state OSc against the number of carbon atoms for α-pinene oxidation products in the particle-phase at -10 °C and 80 % RH measured by three different techniques. (a) FILTER: Offline analysis of filters using Ultra-high-performance liquid chromatography (UHPLC) and heated electrospray ionization (HESI) coupled to an Orbitrap high-resolution mass spectrometer (HRMS). (b) FIGAERO: Filter Inlet for Gases and AEROsols coupled to an I^- high-resolution time-of-flight chemical-ionization mass spectrometer, and (c) EESI-TOF: Extractive Electrospray Na^+ Ionization time-of-flight mass spectrometer. The level of α-pinene was between 1 and 3 ppbv while the ozone level was ~ 100 ppbv. The carbon oxidation state is calculated as follows: OSc = 2*O:C - H:C. The symbol sizes in (a), (b), and (c) represent the intensities normalized by the total signal in each system. (d) Fraction of species in the particle-phase containing less than 10 carbon atoms ($C_{<10}$), 10 carbon atoms (C_{10}), and more than 10 carbon atoms ($C_{>10}$). The fraction was calculated by normalizing the intensities by the total signal in each system.

https://doi.org/10.5194/acp-2022-498
Preprint. Discussion started: 26 August 2022

Atmospheric Chemistry and Physics Discussions

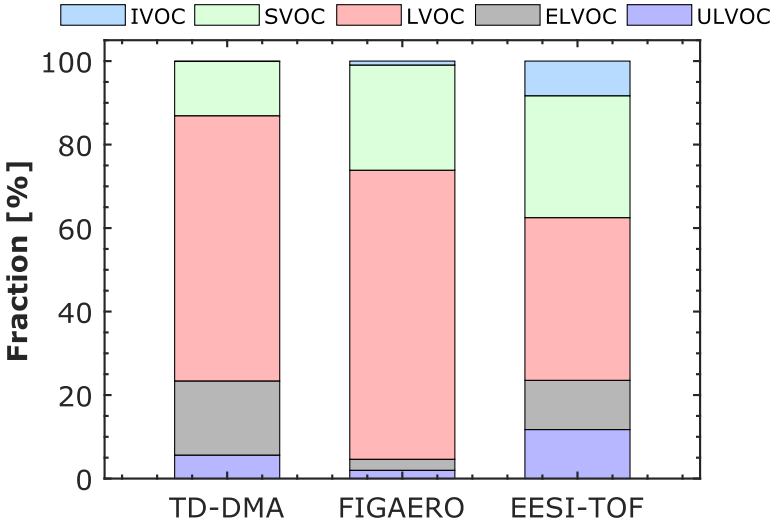

Figure 3. Distribution of volatility classes for α-pinene oxidation products in the particle-phase at -30 ºC and 20 % RH measured by three different techniques: (TD-DMA) Thermal Desorption-Differential Mobility Analyzer coupled to a NO_3^- chemical ionization-atmospheric-pressure-interface-time-of-flight mass spectrometer, (FIGAERO) Filter Inlet for Gases and AEROsols coupled to an I^- high-resolution time-of-flight chemical-ionization mass spectrometer, and (EESI-TOF) Extractive Electrospray Na^+ Ionization time-of-flight mass spectrometer. The level of α-pinene was between 1 and 6 ppbv while the ozone level was ~ 100 ppbv. The volatility classes (ULVOC, ELVOC, LVOC, SVOC, IVOC) were defined as in Donahue et al. (2012) and in Schervish and Donahue (2020).

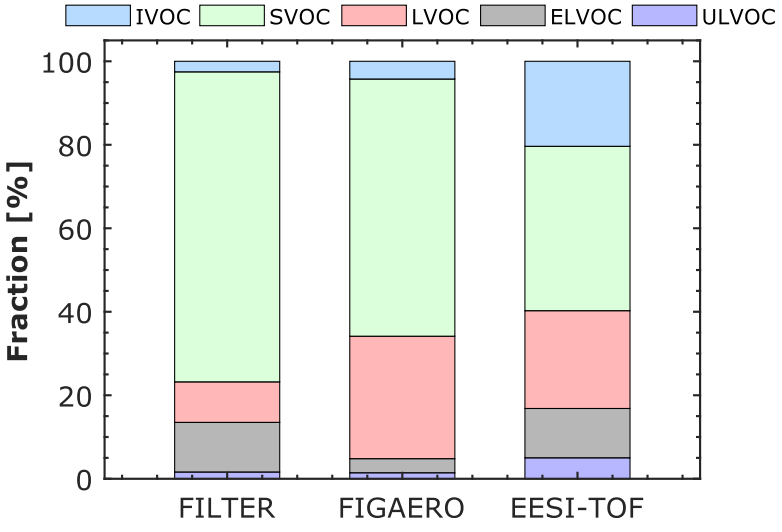

Figure 4. Distribution of volatility classes for α-pinene oxidation products in the particle-phase at -10 ºC and 80 % RH measured by three different techniques: (FILTER) Offline analysis of filters using Ultra-high-performance liquid chromatography and heated electrospray ionization coupled to an Orbitrap high-resolution mass spectrometer, (FIGAERO) Filter Inlet for Gases and AEROsols coupled to an I^- high-resolution time-of-flight chemical-ionization mass spectrometer, and (EESI-TOF) Extractive Electrospray Na^+ Ionization time-of-flight mass spectrometer. The level of α-pinene was between 1 and 3 ppbv while the ozone level was ~ 100 ppbv. The volatility classes (ULVOC, ELVOC, LVOC, SVOC, IVOC) were defined as in Donahue et al. (2012) and in Schervish and Donahue (2020).

https://doi.org/10.5194/acp-2022-498
Preprint. Discussion started: 26 August 2022

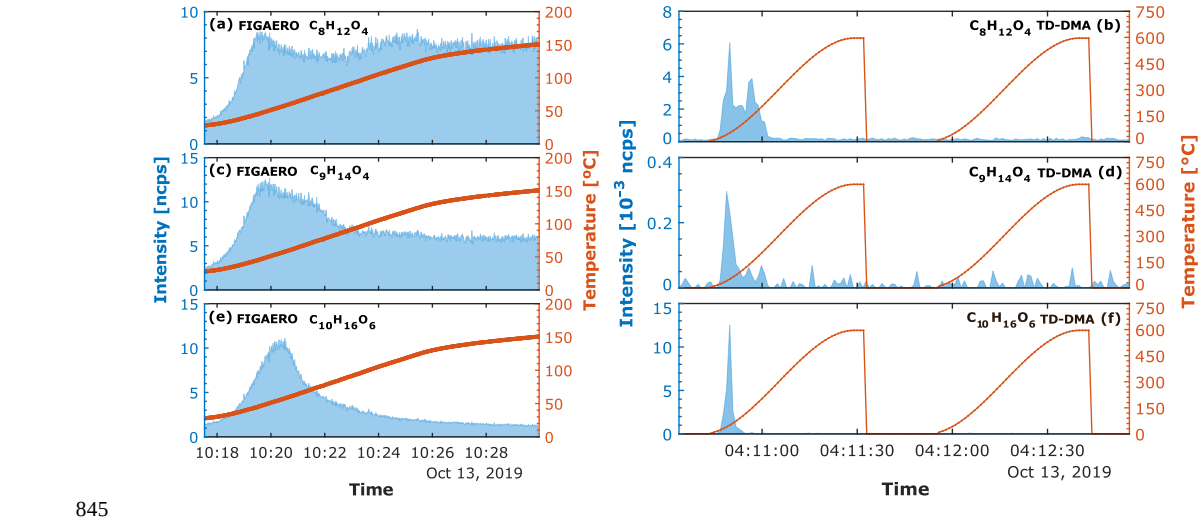

Figure 5. FIGAERO and TD-DMA thermal desorption profiles for three different compounds detected in α-pinene ozonolysis experiment at -30 °C and 20 % RH. (a), (c) and, (e) show FIGAERO thermograms for $C_8H_{12}O_4$, $C_9H_{14}O_4$ and, $C_{10}H_{16}O_6$, respectively. While (b), (d) and, (f) present TD-DMA thermograms for $C_8H_{12}O_4$, $C_9H_{14}O_4$ and, $C_{10}H_{16}O_6$, respectively. FIGAERO and TD-DMA intensities are normalized by the reagent ions and expressed in normalized counts per second (ncps). Both FIGAERO and TD-DMA heating profiles are plotted as a function of temperature. The TD-DMA temperature is an estimate based on the resistance of the filament. For the TD-DMA two heating profiles are needed for determining the particle signal and the background due to the heating of the inlet line.

https://doi.org/10.5194/acp-2022-498
Preprint. Discussion started: 26 August 2022

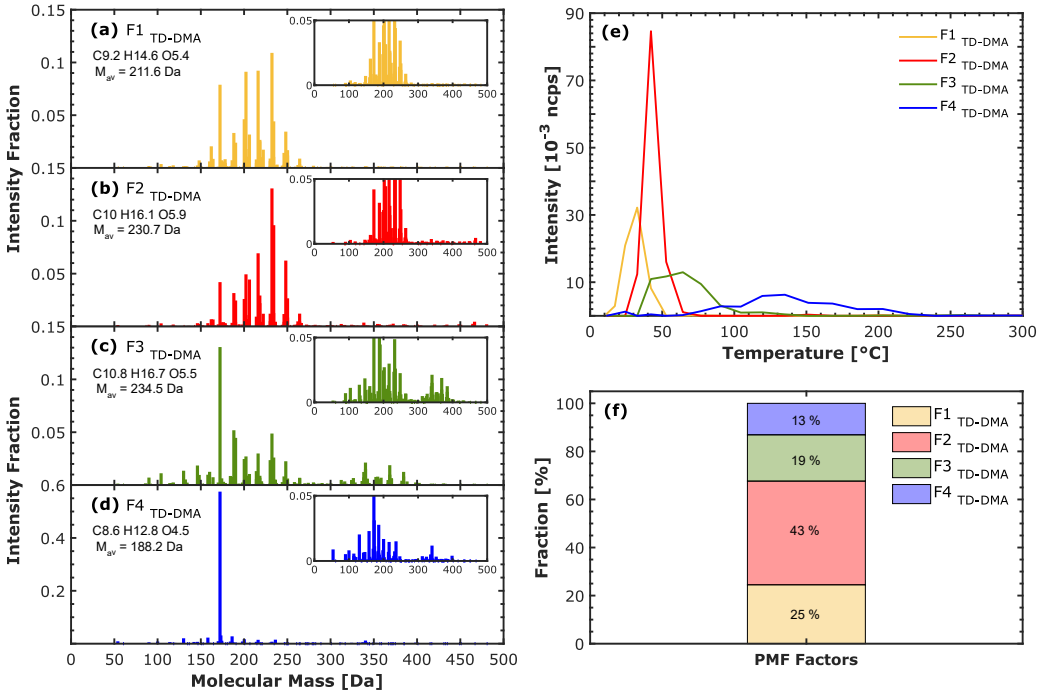

Figure 6. PMF suggested solution on the particle-phase detected by the TD-DMA in α-pinene ozonolysis experiment at -30 °C and 20 % RH. (a), (b), (c) and, (d) Factors mass spectra, (e) Factors thermograms and, (f) Factors fraction. Each factor mass spectrum is normalized and colored according to the order of appearance in the thermogram: F1 TD-DMA (yellow), F2 TD-DMA (red), F3 TD-DMA (green), and F4 TD-DMA (blue). The thermogram (e) is expressed as a function of the temperature, which is an estimation based on the filament resistance. The particle-phase signal has been background corrected.

https://doi.org/10.5194/acp-2022-498
Preprint. Discussion started: 26 August 2022

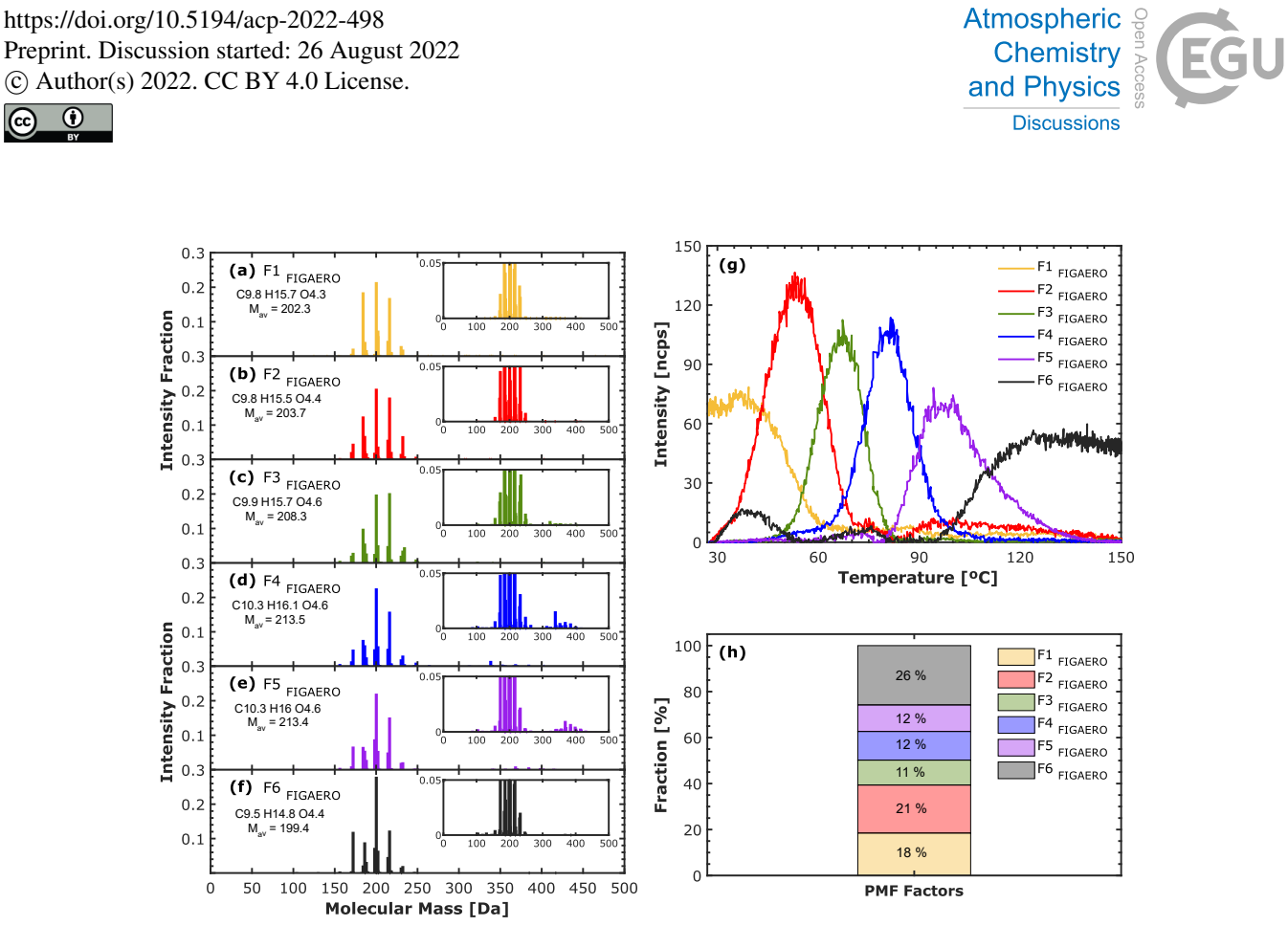

Figure 7. PMF suggested solution on the particle-phase detected by FIGAERO in α-pinene ozonolysis experiment at -30 °C and 20 % RH. (a), (b), (c), (d), (e) and, (f) Factors mass spectra, (g) Factors thermograms and, (h) Factors fraction. Each factor mass spectrum is normalized and colored according to the order of appearance in the thermogram: F1 FIGAERO (yellow), F2 FIGAERO (red), F3 FIGAERO (green), F4 FIGAERO (blue), F5 FIGAERO (purple) and, F6 FIGAERO (black). The thermogram is expressed as a function of the temperature which causes the desorption. The particle-phase signal has been background corrected.

https://doi.org/10.5194/acp-2022-498
Preprint. Discussion started: 26 August 2022

Atmospheric Chemistry and Physics Discussions

Table 1. Instruments for measuring particle-phase chemical composition used in the CLOUD chamber experiments.

	TD-DMA + NO_3^- CI-APi-TOF	**FIGAERO + I^- HRToF-CIMS**	**Na^+ EESI-TOF**	**FILTER UHPLC/HESI/HRMS method**
Continuous or discontinuous	semicontinuos	semicontinuos	continuous	discontinuous - offline
Evaporation method	Thermal desorption	Thermal desorption	Extraction solvent - evaporation	Electrospray solvent - evaporation
Phase measured	Gas and Particle [b]	Gas and Particle [b]	Gas and Particle [b]	Particle
Ionization technique	Chemical ionization	Chemical ionization	Electrospray ionization	Electrospray ionization
Reagent ion	$(HNO_3)NO_3$, NO_3^-	I^-, $(H_2O)I^-$	$(NaI)Na^+$, Na^+	NA negative mode
Target substances	Highly oxygenated	Intermediate oxygenated	Intermediate oxygenated	At least O_1 Any chemical stable species and able to donate protons
Is there thermal fragmentation?	Yes	Yes	No	No
Size resolved for this study?	No[a]	No	No	No
Reference	Wagner et al., 2018	Lopez-Hilfiker et al., 2015	Lopez-Hilfiker et al., 2019	Ungeheuer et al., 2020

[a] TD-DMA can measure both size resolved and non-size resolved. For this work it was chosen the non-size resolved in order to maximize the mass collected and to intercompare with the particle-phase instruments, [b] in this work, only the particle-phase measurements are reported, [c] gas-and particle-phase can be measured by using the dual-EESI-TOF configuration.

https://doi.org/10.5194/acp-2022-498
Preprint. Discussion started: 26 August 2022

Atmospheric Chemistry and Physics Discussions

Table 2. Advantages and drawbacks of four different techniques for measuring the chemical composition of nanoparticles.

Instrument	Advantages	Drawbacks
TD-DMA + NO_3^- CI-APi-TOF	- Size resolved particle collection - Gas-phase can be measured while particle collection, gas and particle intercomparison - Detection immediately after collection	- Resolution might depend on the particle load (collection time ~ 4 hours)* - Thermal fragmentation is possible
FIGAERO + I^- HRToF-CIMS	- Gas-phase can be measure while particle collection, gas and particle intercomparison - Detection immediately after collection - Time resolution 30 min: semicontinuous	- Non-size resolved particle collection - Resolution 30 min: semicontinuous - Thermal fragmentation is possible
Na^+ EESI-TOF	- Continuous measurement, 10 seconds time resolution - Gas-phase can be measure using the dual configuration	- Non-size resolved particle collection - size-dependence sensitivity
FILTER UHPLC-HESI-HRMS method	- Differentiates between clusters and molecules (pre-separation makes sure that the compounds are not fragments) - Identify isomers** using chromatography for separation	- Non-size resolved particle collection - Resolution might depend on the particle load (collection time ~ 8 hours)* - Detection not immediately after collection, first stored - Possible aging, sampling artifacts

950 *Collection period for the experiments reported here for TD-DMA and FILTER. **An assumption about the structure can be expressed by doing complementary experiments.

An intercomparison study of four different techniques for measuring chemical composition of nanoparticles

Supplementary Material

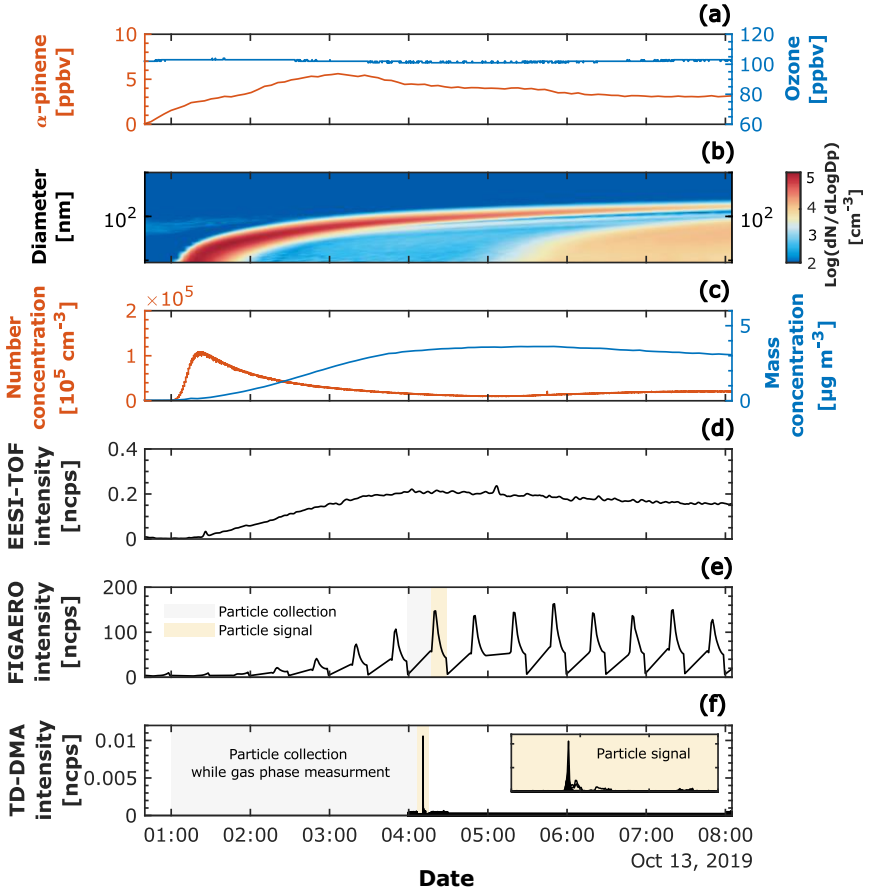

Figure S1. Experimental overview of a representative biogenic new particle formation experiment (α-pinene ozonolysis at -30 °C and 20 % RH), (a) Mixing ratio in ppbv for the precursor gases, α-pinene and ozone. (b) particle size distribution measured by the SMPS, the color scale represents the log 10 of the normalized particle concentration in cubic centimeters (cm^{-3}). (c) Particle number concentration in cm^{-3} measured by the CPC with a cut-off diameter of 2.5 nm and mass concentration in μg m^{-3} (obtained by integrating the normalized mass concentration from the SMPS). (d) particle-phase signal measured continuously by the EESI-TOF. Fifth and sixth panels: Particle-phase measured by FIGAERO and TD-DMA respectively, the gray shaded areas refer to the particle collection period and the yellow shaded areas to the desorption period. FIGAERO measured in a semicontinuous mode in which 15-minute particle collections followed by 15-minute desorption periods were performed during the whole experiment. The TD-DMA collection period was approximately 4 hours while the desorption period lasted around 3 minutes.

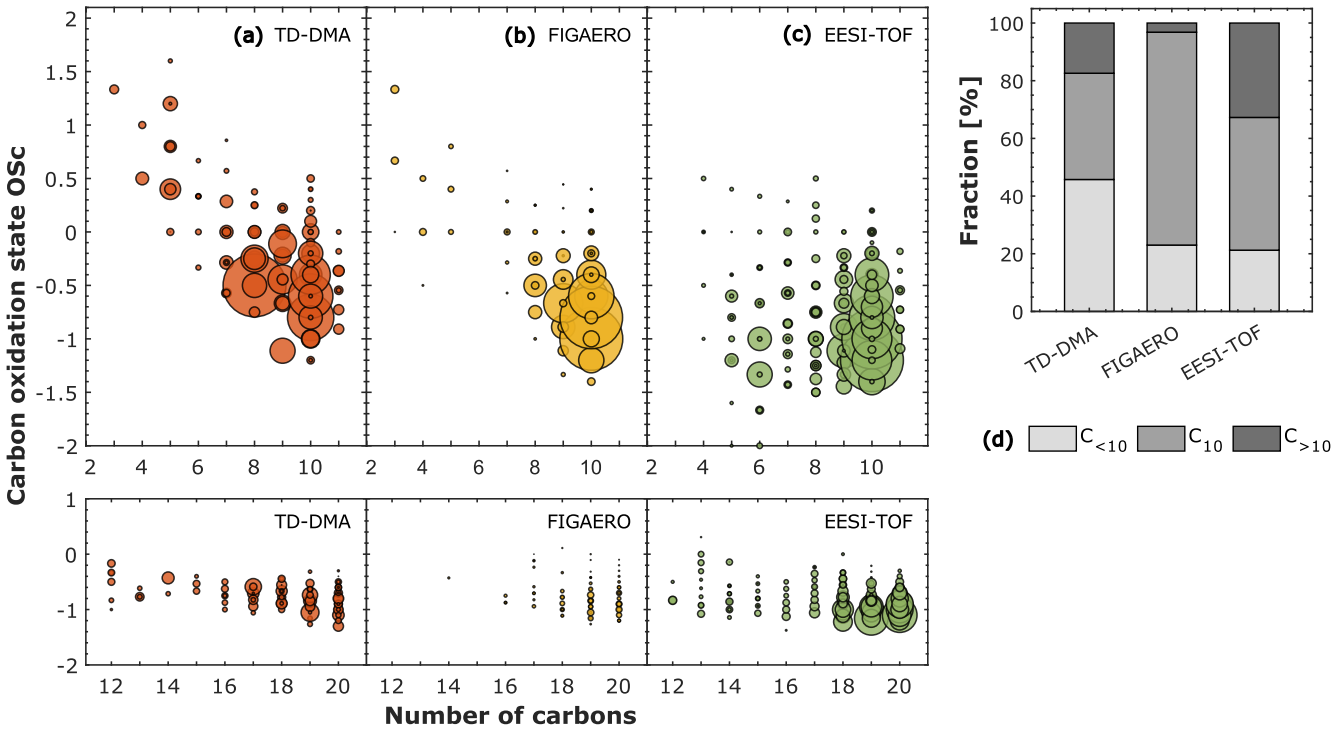

Figure S2. Carbon oxidation state OSc against the number of carbon atoms for α-pinene oxidation products in the particle-phase at -50 ºC and 20 % RH measured by three different techniques. (a) TD-DMA: Thermal Desorption-Differential Mobility Analyzer coupled to a NO_3^- chemical ionization-atmospheric-pressure-interface-time-of-flight mass spectrometer. (b) FIGAERO: Filter Inlet for Gases and AEROsols coupled to an I^- high-resolution time-of-flight chemical-ionization mass spectrometer, and (c) EESI-TOF: Extractive Electrospray Na^+ Ionization time-of-flight mass spectrometer. The level of α-pinene was between 1 and 6 ppbv while the ozone level was ~ 100 ppbv. The carbon oxidation state is calculated as follows: OSc = 2xO:C - H:C. The symbol sizes in (a), (b), and (c) represent the intensities normalized by the total signal in each system. (d) Fraction of species in the particle-phase containing less than 10 carbon atoms ($C_{<10}$), 10 carbon atoms (C_{10}), and more than 10 carbon atoms ($C_{>10}$). The fraction was calculated by normalizing the intensities by the total signal in each system.

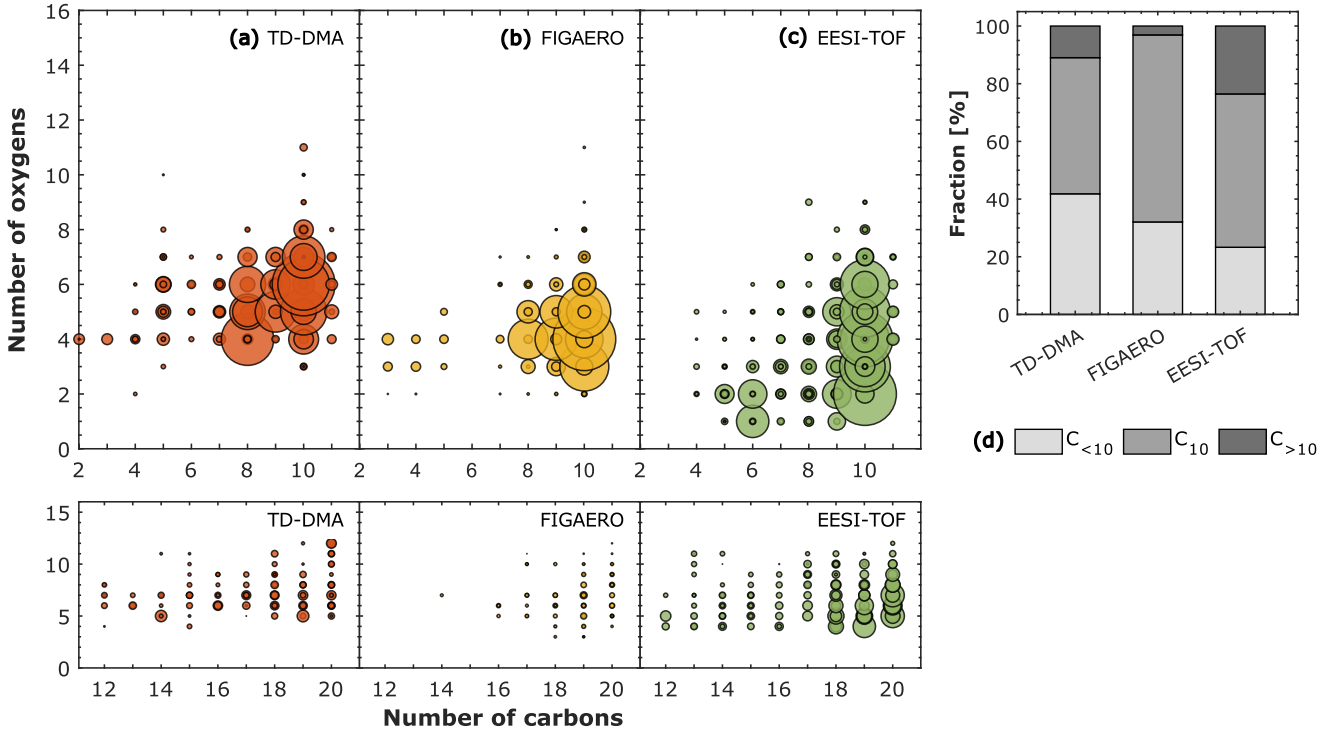

Figure S3. Number of oxygen atoms against the number of carbon atoms for α-pinene oxidation products in the particle-phase at -30 ºC and 20 % RH measured by three different techniques. (a) TD-DMA: Thermal Desorption-Differential Mobility Analyzer coupled to a NO_3^- chemical ionization-atmospheric-pressure-interface-time-of-flight mass spectrometer. (b) FIGAERO: Filter Inlet for Gases and AEROsols coupled to an I^- high-resolution time-of-flight chemical-ionization mass spectrometer, and (c) EESI-TOF: Extractive Electrospray Na^+ Ionization time-of-flight mass spectrometer. The level of α-pinene was between 1 and 6 ppbv while the ozone level was ~ 100 ppbv. The symbol sizes in (a), (b), and (c) represent the intensities normalized by the total signal in each system. (d) Fraction of species in the particle-phase containing less than 10 carbon atoms ($C_{<10}$), 10 carbon atoms (C_{10}), and more than 10 carbon atoms ($C_{>10}$). The fraction was calculated by normalizing the intensities by the total signal in each system.

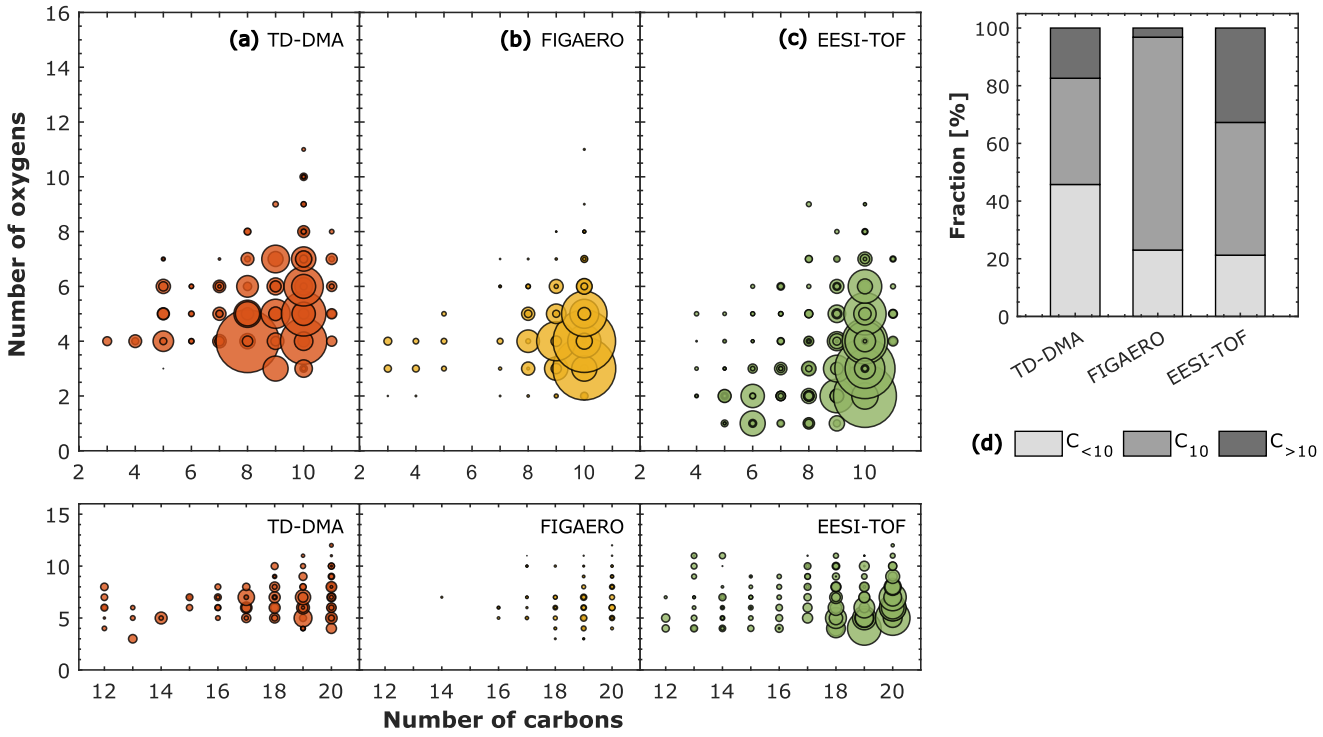

Figure S4. Number of oxygen atoms against the number of carbon atoms for α-pinene oxidation products in the particle-phase at -50 ºC and 20 % RH measured by three different techniques. (a) TD-DMA: Thermal Desorption-Differential Mobility Analyzer coupled to a NO_3^- chemical ionization-atmospheric-pressure-interface-time-of-flight mass spectrometer. (b) FIGAERO: Filter Inlet for Gases and AEROsols coupled to an I^- high-resolution time-of-flight chemical-ionization mass spectrometer, and (c) EESI-TOF: Extractive Electrospray Na^+ Ionization time-of-flight mass spectrometer. The level of α-pinene was between 1 and 6 ppbv while the ozone level was ~ 100 ppbv. The symbol sizes in (a), (b), and (c) represent the intensities normalized by the total signal in each system. (d) Fraction of species in the particle-phase containing less than 10 carbon atoms ($C_{<10}$), 10 carbon atoms (C_{10}), and more than 10 carbon atoms ($C_{>10}$). The fraction was calculated by normalizing the intensities by the total signal in each system.

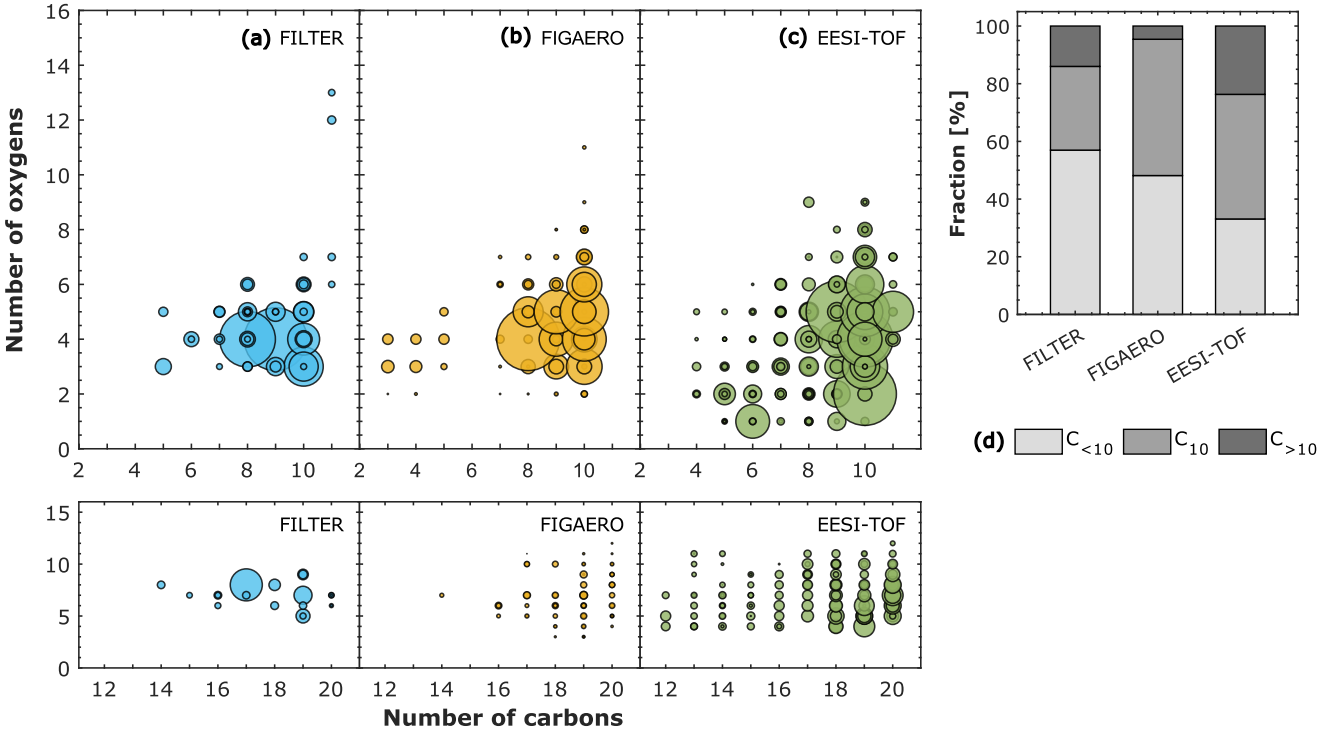

Figure S5. Number of oxygen atoms against the number of carbon atoms for α-pinene oxidation products in the particle-phase at -10 °C and 80 % RH measured by three different techniques. (a) FILTER: Offline analysis of filters using Ultra-high-performance liquid chromatography (UHPLC) and heated electrospray ionization (HESI) coupled to an Orbitrap high-resolution mass spectrometer (HRMS). (b) FIGAERO: Filter Inlet for Gases and AEROsols coupled to an I^- high-resolution time-of-flight chemical-ionization mass spectrometer, and (c) EESI-TOF: Extractive Electrospray Na^+ Ionization time-of-flight mass spectrometer. The level of α-pinene was between 1 and 3 ppbv while the ozone level was ~ 100 ppbv. The symbol sizes in (a), (b), and (c) represent the intensities normalized by the total signal in each system. (d) Fraction of species in the particle-phase containing less than 10 carbon atoms ($C_{<10}$), 10 carbon atoms (C_{10}), and more than 10 carbon atoms ($C_{>10}$). The fraction was calculated by normalizing the intensities by the total signal in each system.

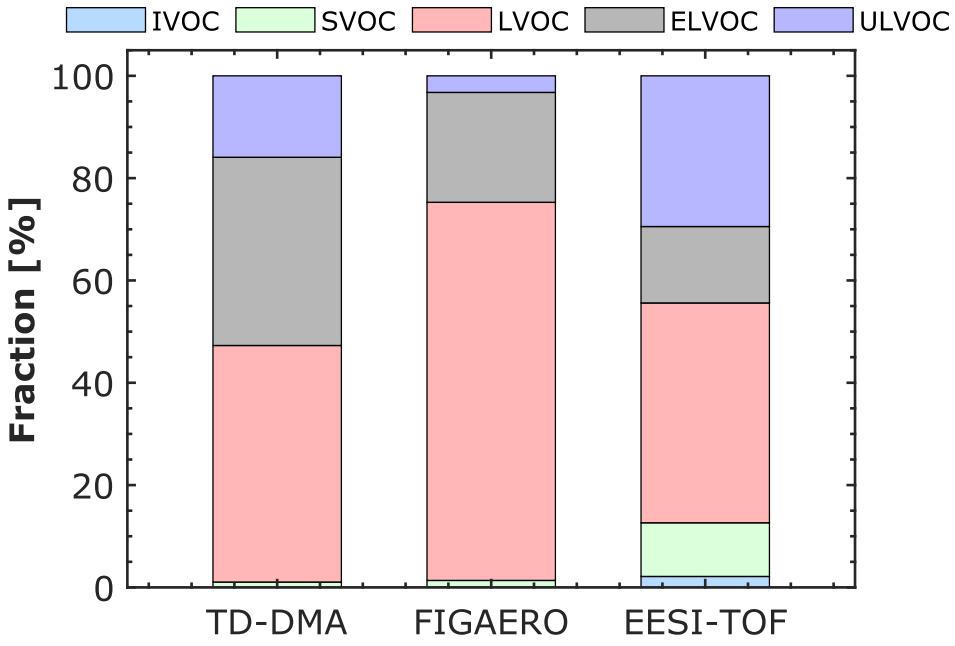

Figure S6. Fraction of volatility regimes for α-pinene oxidation products in the particle-phase at -50 °C and 20 % RH measured by three different techniques: (TD-DMA) Thermal Desorption-Differential Mobility Analyzer coupled to a NO_3^- chemical ionization-atmospheric-pressure-interface-time-of-flight mass spectrometer, (FIGAERO) Filter Inlet for Gases and AEROsols coupled to an I^- high-resolution time-of-flight chemical-ionization mass spectrometer, and (EESI-TOF) Extractive Electrospray Na^+ Ionization time-of-flight mass spectrometer. The level of α-pinene was between 1 and 6 ppbv while Ozone level was ~ 100 ppbv. The volatility regimes (ULVOC, ELVOC, LVOC, SVOC, IVOC) were defined as in Donahue et al. (2012) and in Schervish and Donahue (2020).

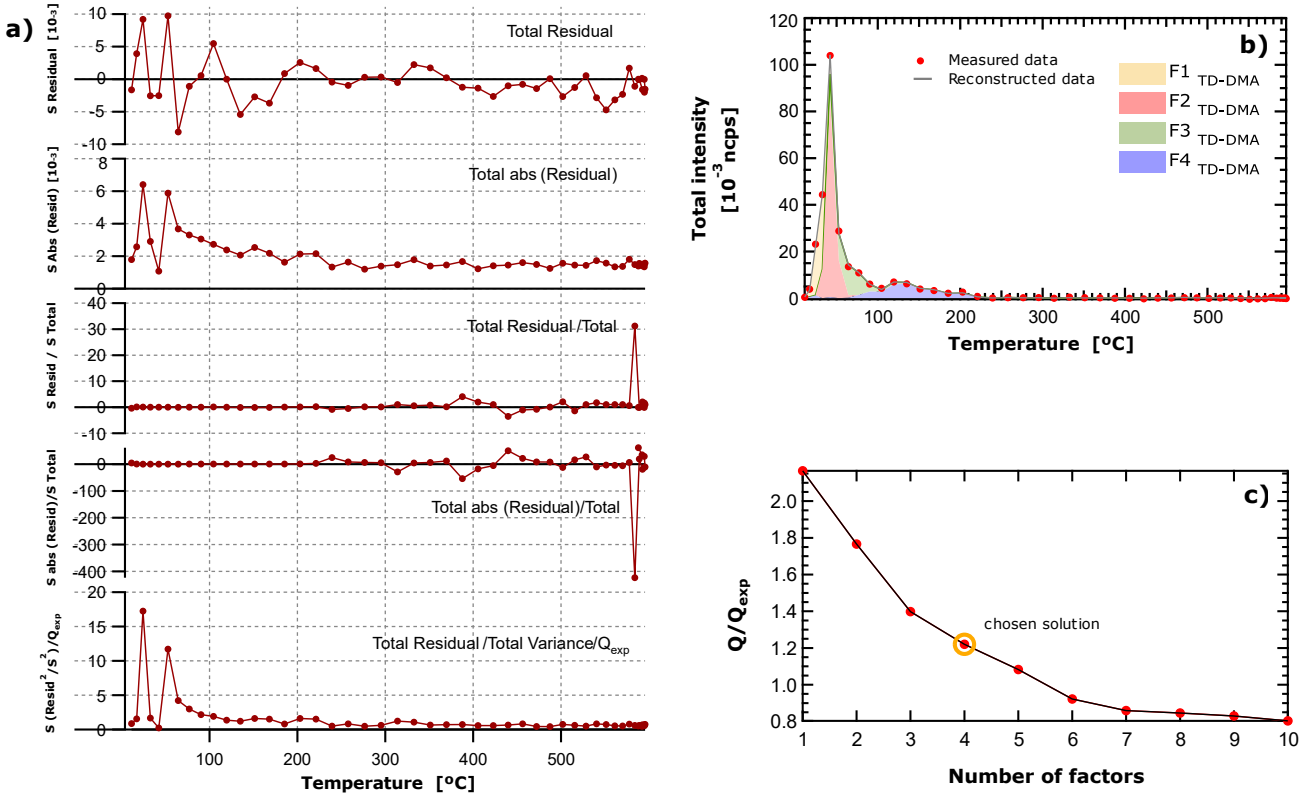

Figure S7. a) Residuals for TD-DMA 4-Factor solution expressed in terms of total residual, absolute residual, variance and Q_{exp} (square of the residual scaled with the error summed over all ions and observations) against the temperature. More details about the calculation and interpretation of these quantities can be found in Buchholz et al. (2020); b) Measured and reconstructed TD-DMA total intensity against the temperature, the contribution of the factors are shown with different colors, and c) Q/Q_{exp} vs Number of factors. Q/Q_{exp} is an optimization parameter based on the residuals and described in Buchholz et al. (2020), in the ideal case Q/Q_{exp} is equal to 1.

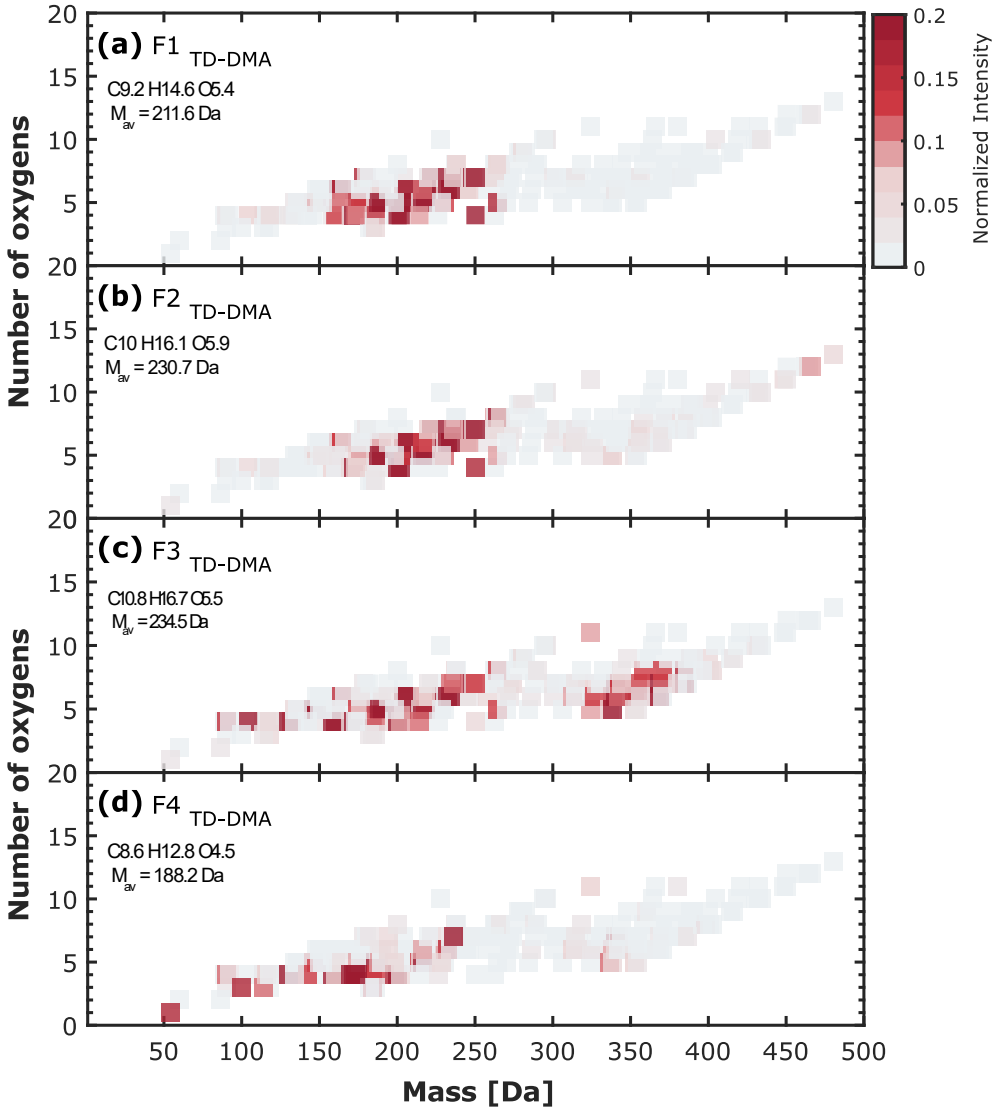

Figure S8. PMF suggested solution on the particle-phase detected by the TD-DMA in α-pinene ozonolysis experiment at -30 ºC and 20 % RH, (a) F1 TD-DMA, (b) F2 TD-DMA, (c) F3 TD-DMA and, (d) F4 TD-DMA are the factors mass spectra expressed in terms of number of oxygens against the neutral ion mass. The colorscale represents the intensity normalized by the total particle signal. The particle-phase signal has been background corrected.

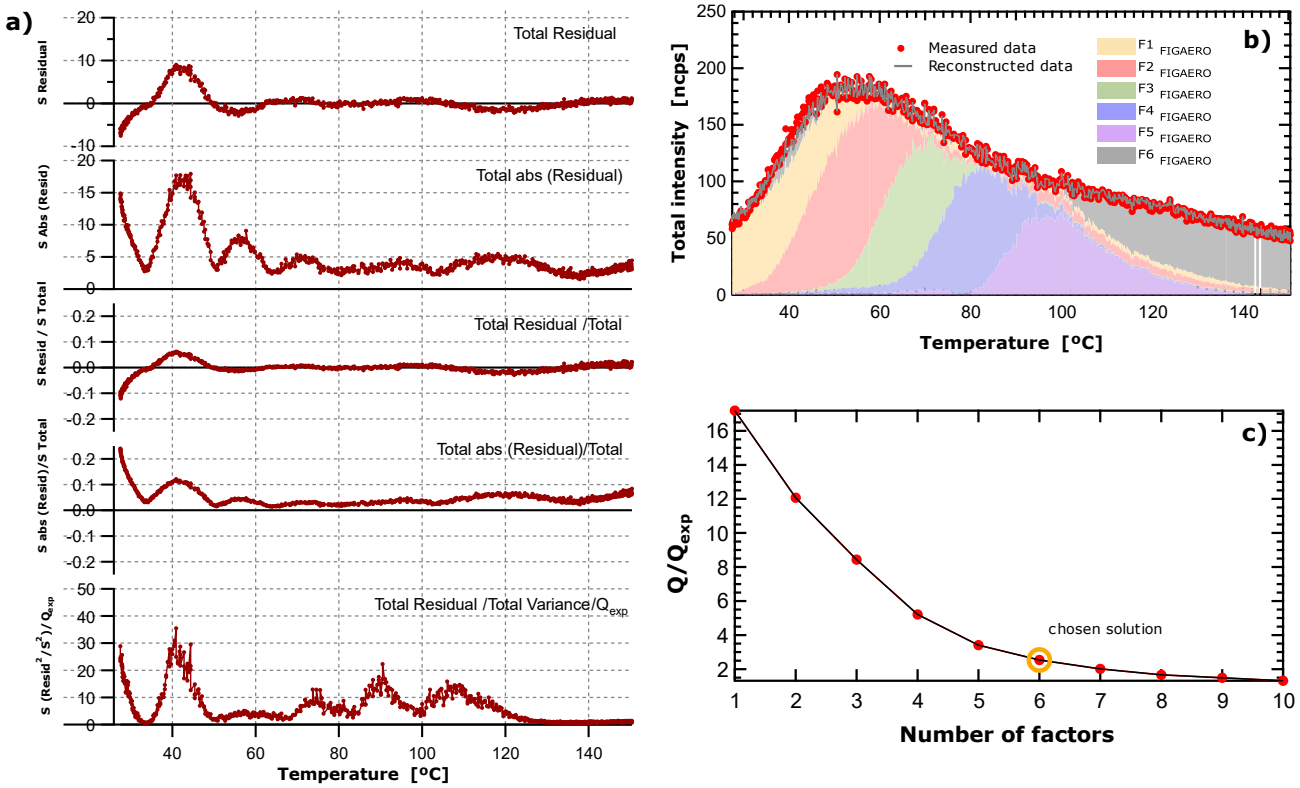

Figure S9. a) Residuals for FIGAERO 6-Factor solution expressed in terms of total residual, absolute residual, variance and Q_{exp} (square of the residual scaled with the error summed over all ions and observations) against the temperature. More details about the calculation and interpretation of these quantities can be found in Buchholz et al. (2020); b) Measured and reconstructed FIGAERO total intensity against the temperature, the contribution of the factors are shown with different colors, and c) Q/Q_{exp} vs Number of factors. Q/Q_{exp} is an optimization parameter based on the residuals and described in Buchholz et al. (2020), in the ideal case Q/Q_{exp} is equal to 1.

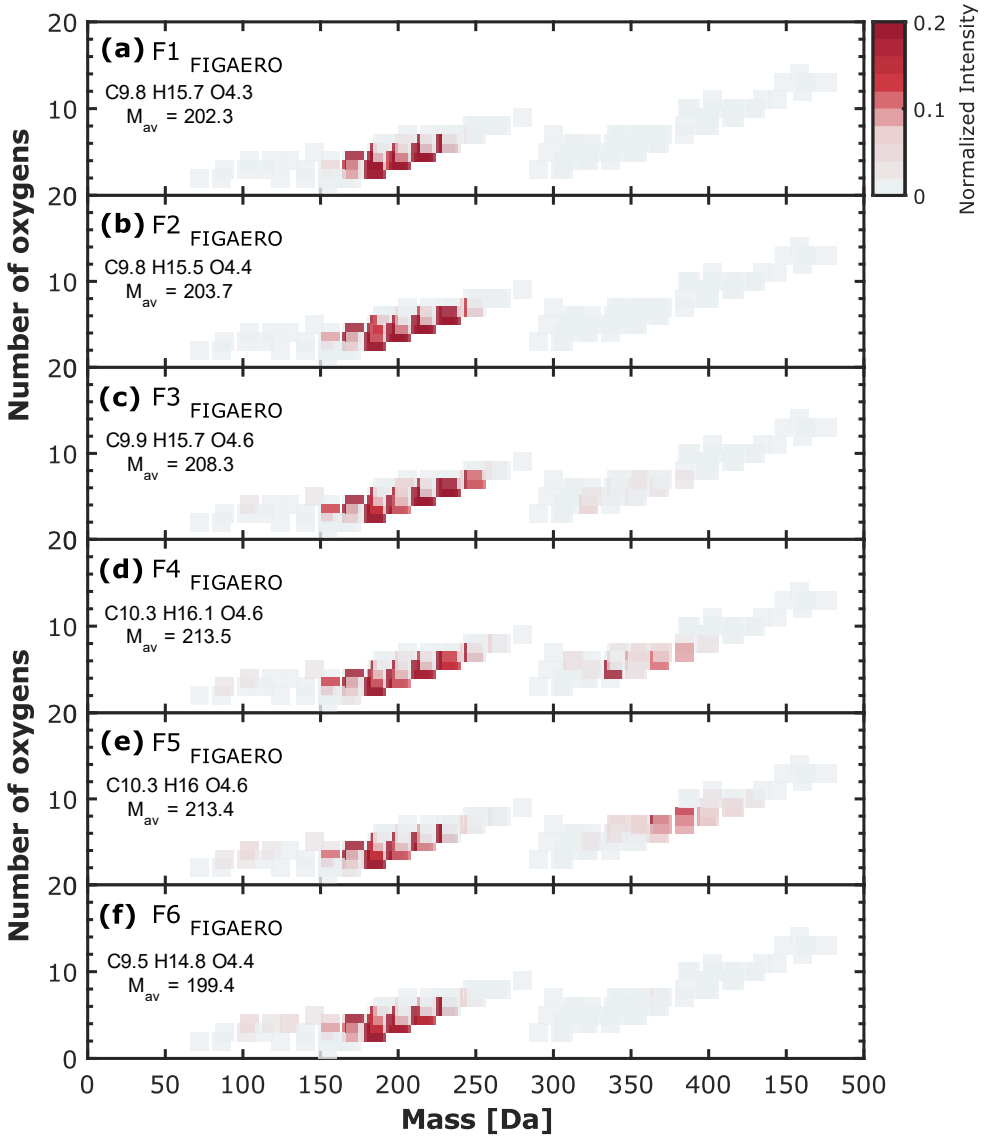

Figure S10. PMF suggested solution on the particle-phase detected by FIGAERO in α-pinene ozonolysis experiment at -30 °C and 20 % RH, (a) F1 FIGAERO, (b) F2 FIGAERO, (c) F3 FIGAERO, (d) F4 FIGAERO, (e) F5 FIGAERO and, (f) F6 FIGAERO are the factors mass spectra expressed in terms of number of oxygens against the neutral ion mass. The colorscale represents the intensity normalized by the total particle signal. The particle-phase signal has been background corrected.

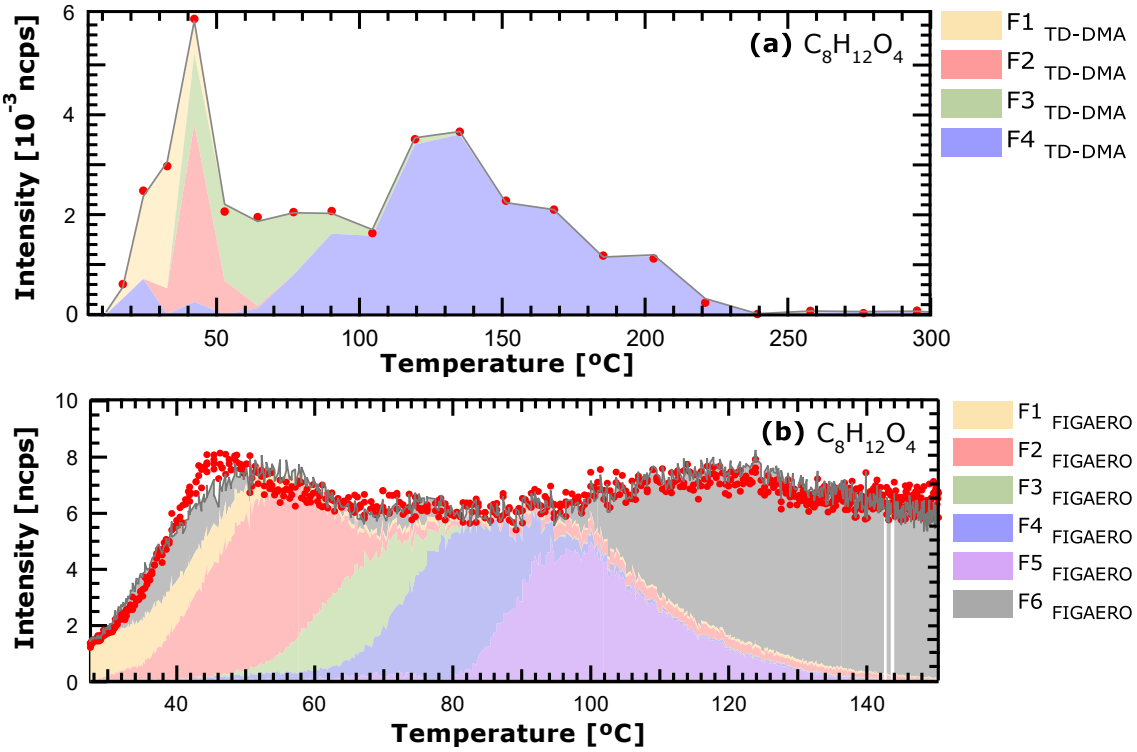

Figure S11. Factor thermograms on the PMF suggested solutions for $C_8H_{12}O_4$ measured by (a) TD-DMA and (b) FIGAERO in the α-pinene ozonolysis experiment at -30 ºC and 20 % RH.

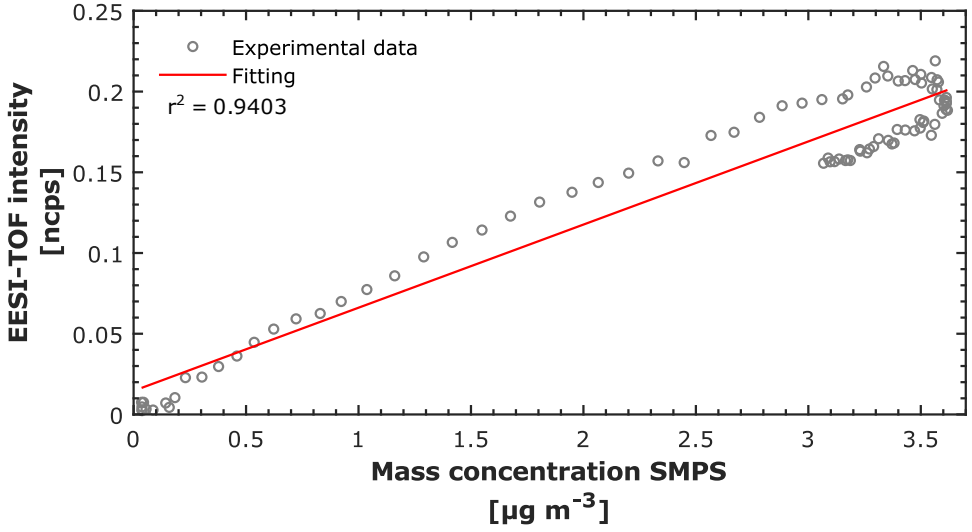

Figure S12. Correlation plot of total EESI intensity in ncps and the mass concentration calculated from the SMPS for the representative experiment shown in Fig. S6. The EESI-TOF particle signal was averaged every 5 minutes for correlation with the SMPS.

Buchholz, A., Ylisirniö, A., Huang, W., Mohr, C., Canagaratna, M., Worsnop, D. R., Schobesberger, S., and Virtanen, A.: Deconvolution
170 of FIGAERO–CIMS thermal desorption profiles using positive matrix factorisation to identify chemical and physical processes during particle evaporation, Atmos. Chem. Phys., 20, 7693-7716, 10.5194/acp-20-7693-2020, 2020.

6.3 Nucleation of jet engine oil vapors is a large source of aviation-related ultrafine particles, Ungeheuer et al. (2022).

Nucleation of jet engine oil vapours is a large source of aviation-related ultrafine particles

Florian Ungeheuer[1], Lucía Caudillo[1], Florian Ditas[3], Mario Simon[1], Dominik van Pinxteren[2], Dogushan Kilic[4,5], Diana Rose[3], Stefan Jacobi[3], Andreas Kürten[1], Joachim Curtius[1], Alexander L. Vogel[1,*]

[1]Institute for Atmospheric and Environmental Sciences, Goethe-University Frankfurt, Frankfurt am Main, 60438, Germany

[2]Atmospheric Chemistry Department (ACD), Leibniz Institute for Tropospheric Research (TROPOS), Leipzig, 04318, Germany

[3]Department for Ambient Air Quality, Hessian Agency for Nature Conservation, Environment and Geology, Wiesbaden, 65203, Germany

[4]The Department of Earth and Environmental Sciences, the Faculty of Science and Engineering, the University of Manchester, Manchester, UK

[5]National Centre for Atmospheric Science, Manchester, UK

*__Email:__ vogel@iau.uni-frankfurt.de

Abstract

Large airports are a major source of ultrafine particles (UFPs), which spread across densely populated residential areas, affecting air quality and human health. Jet engine lubrication oils are traceable in aviation-related UFPs, however, their role in UFP formation and growth remains unclear. Here we show the volatility and new-particle-formation ability of a common synthetic jet oil in the laboratory, and the quantified oil fraction in ambient UFPs downwind of Frankfurt International Airport, Germany. We find that the oil mass fraction is largest in the smallest UFPs (10-18 nm) with 21% on average. Combining ambient particle-phase concentrations and volatility of the jet oil compounds, we determine a lower-limit theoretical gas-phase saturation ratio larger than 1×10^5, indicating the oil´s potential as an efficient nucleating agent. Our results demonstrate that jet oil nucleation is an important mechanism that can explain the abundant observations of high number concentrations of non-refractory UFPs near airports.

Main Text

Introduction

Several studies identified airports as a major source of ultrafine particles (UFPs)[1–8]. Among different engine operation conditions at the airports, take-off is often associated with the highest UFP emissions[9–12,3]. These particles are typically formed via gas-to-particle conversion after combustion[13]. Transmission electron microscopy analysis of UFPs from aviation shows spherical particles with a volatile character under high vacuum[14]. They can be transported large distances

from the source reaching densely populated residential areas, as large airports are usually located in the close vicinity of metropolitan areas[3,15,16]. UFP emissions from airport operations lead to a higher ambient particle number concentration (PNC) in the surrounding of airports, with a limited knowledge of their chemical composition[17,18]. UFP transport and subsequent infiltration to the indoor environment seems to be more relevant than infiltration of $PM_{2.5}$ and PM_{10}[18,19]. The number of particles emitted by jet engines are dominated by particles with a diameter smaller than ~30 nm, which is significantly smaller compared to particles from road traffic emissions[12,20–23]. Jet engine oil constituents (Supplementary Fig. 1) have been identified in UFPs near airports[24–26,2,7]. Lubrication oils are emitted from aircraft engines both for technical purposes (required in venting system) and unintentionally as leaks of the oil circulating system (i.e., due to worn seals)[24].

Due to the small size of UFPs, exposure-related health effects are of importance as they potentially reach the alveoli, penetrate through the pulmonary epithelium in the lower respiratory tract, and translocate the air-blood barrier[27–30]. Animal tests also showed that they can reach the central nervous system via the olfactory nerve circumventing the blood-brain barrier[31]. UFPs can permeate into the respiratory and cardiovascular system within minutes to hours and are still detectable for months after the exposure[32]. Depending on their chemical composition, UFPs can induce oxidative stress, inflammatory reactions, and cell membrane damages[33–35]. Health effects depend on their particle size, mass and number concentration[5], and additionally on individual properties such as surface area, solubility, oxidative potential and the ability to counteract macrophage phagocytosis[36]. Several studies investigated the UFP exposure of airport ground personnel and passengers[37,38] and health effects due to UFP exposure near the airport[6]. A recent cohort study reported a 12% increased risk of developing a malignant brain tumour in the Los Angeles airport area for each increase of UFP exposure by 6,700 particles cm^{-3} [39]. This finding is supported by a study from Toronto, which reports a hazard ratio of 1.112 in developing a malignant brain tumour per UFP increase of 10,000 particles cm^{-3}, adjusted for other air pollutants and socio-demographic factors[40]. A study of the health effects from long-term UFP exposure of airport workers reported no association to cardiovascular disease[41].

Ultrafine and fine particle emissions by jet engines during flight have also been investigated[42,43]. Here the focus has been put on determining emission indices for particle emissions at cruise and their role for contrail and cirrus formation[44]. Black carbon (soot) emissions have been discussed to dominate the formation of ice crystals in contrails, especially in the soot-rich regime characterized by soot particle number emission indices, EIs, in excess of $\sim 10^{14}$ $(kg\text{-}fuel)^{-1}$ [44]. Recent studies have shown that soot formation by aircraft engines burning plant-based bio-fuels blended with petroleum-based conventional kerosene (Jet A) or blends of synthetic fuels (Fischer-Tropsch) with Jet A fuel, both significantly reduces the soot formation[43,45], which is likely explained by the near zero aromatic contents of the bio and synthetic fuels. Ultrafine volatile particles were assumed to be mostly

composed of sulphuric acid and organic fuel components that nucleate in the young exhaust plume[46,47], but jet lubrication oil has so far not been suggested as an important source of the freshly formed particles in the exhaust plume in flight.

In our previous study on airport-related UFPs, we showed that jet engine lubrication oils dominate the spectrum of detected organic compounds after a non-target analysis[26]. Following this non-target study, here we describe the nucleation ability of jet oil vapours in laboratory experiments and by quantification of jet engine oil constituents in three ambient UFP size fractions (< 56 nm) downwind Frankfurt International Airport.

Results

Volatility and new-particle formation of jet engine lubrication oil

We compared particle-number size distributions (PNSD) of ambient UFPs with laboratory-generated jet oil particles. In the ambient measurements at Frankfurt-Schwanheim (Supplementary Fig. 2) we observe a distinct difference between UFPs from the airport and the city centre (Fig. 1A). Air masses transported from Frankfurt Airport show a ~15-times higher PNC of UFPs at ~18 nm compared to air masses from the city centre. For larger UFPs, this difference becomes less pronounced. In the laboratory, we studied the PNSD of lubrication oil particles passing a thermodenuder at 20 °C and 300 °C in order to investigate the volatility and nucleation capability of the jet oil compounds. When the jet oil particles (mean diameter of 27 nm) pass the thermodenuder at 300 °C, we observe a more than fivefold increase of the particle number concentration compared to the experiment at 20 °C, and a reduction of the mean diameter down to ~10 nm of the measured particles (Fig. 1B). Although the particles passed the thermodenuder, it is important to mention that the PNSD measurement was conducted downstream the heating section at room temperature. The volatility of the jet oil at 300 °C is evident as the mass fraction of jet oil is reduced by ~99% compared to the 20 °C control experiment (Fig. 1C). Downstream the heating section of the thermodenuder the majority of oil vapours in the gas phase are likely lost to the surfaces of the tubing. However, a small fraction of the oil vapours nucleates and forms new particles downstream of the thermodenuder within a few seconds, when the temperature of the sampling flow reaches a point at which the oil vapour becomes supersaturated. Rapid growth of particles to sizes >10 nm allows escaping the “valley of death” in the nucleation mode[48], in which small particles are efficiently scavenged by coagulation. The thermodenuder experiment demonstrates that jet engine oil particles are volatile UFPs at 300 °C, and it can be assumed that the oil partitions entirely to the gas phase if exposed to operating temperatures of aircraft turbofan engines (>>300 °C[49]).

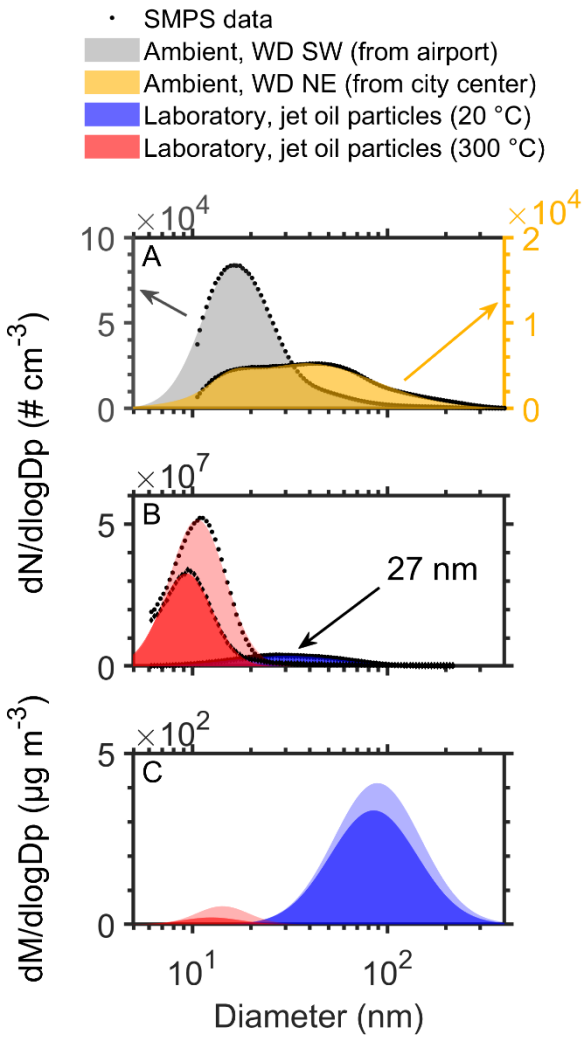

Figure 1. Ambient particle size distribution (A) at the monitoring site during wind direction from the airport (grey) and the city (yellow), averaged over three days (05:00–23:00 CET). Number-size (B) and mass-size distribution (C) from two laboratory experiments, each with jet oil nanoparticles generated from a methanolic solution, native at 20 °C (blue & light blue) and after heating to 300 °C (red & light red). Measurement data (black dots) were fitted using a lognormal distribution.

Remarkably, the particle diameter of the freshly nucleated oil particles in our laboratory experiment appears in the same size region as the ambient UFPs downwind of Frankfurt Airport. Certainly, these laboratory experiments do not reflect the full complexity of jet engine emissions in the atmosphere. In real emission plumes, non-volatile particulate matter (nvPM) could scavenge nucleation by providing surface for condensation of oil vapours. However, earlier studies describe aviation-related UFPs as volatile under high vacuum[14], therefore, it appears likely that a large number of particles smaller than 30 nm, which are observed downwind of airports[23,12], are formed via nucleation of gaseous jet oil emissions.

Fraction of lubrication oil in ambient UFP samples

We quantified jet engine oil constituents from ambient particle samples in order to determine the oil fraction in UFPs near Frankfurt Airport. Therefore, we collected UFP samples downwind the airport at Frankfurt-Schwanheim when air masses arrived from the airport (Fig. 2A-D). Using a cascade impactor (Nano-MOUDI), we sampled UFPs during seven periods (18 – 54 hours) in three different UFP size bins (10-18 nm, 18-32 nm, 32-56 nm) for subsequent chemical analysis. From the continuous measurements of the PNSD we calculated the mass concentration (oil density = 1 g cm^{-3}) for the three investigated particle size bins (Fig. 2B-D). Particle mass concentration of the two smallest size bins (< 32 nm) increased significantly when the wind direction falls within the airport sector during its operating hours, compared to periods of other wind directions or non-operating hours. The variability of larger UFPs (>32 nm) does not show this behaviour (Fig. 2D-G). This is in accordance with previous studies, which state that aircraft-related particle emissions are primarily < 30 nm, while particle emissions from on-road vehicles are dominated by particles > 30 nm[3,12,22,23]. The particle number concentration (< 32 nm) reaches the rural background level around midnight. Hence, we consider the nighttime periods between 00:00 – 05:00 CET adjacent to each sampling day as the mean rural background particle mass concentration that is unaffected by UFPs from the airport (black bars in Fig. 2B-D). Subtraction of the mean background mass from the mass during UFP sampling results in the total accumulated UFP mass on each impactor stage that can be attributed to the airport (Supplementary Fig. 3). This approach of mass closure cannot be applied to the largest stage (32-56 nm), because the particle mass concentration reaches sometimes higher values during non-operating than during operating hours (Fig. 2D).

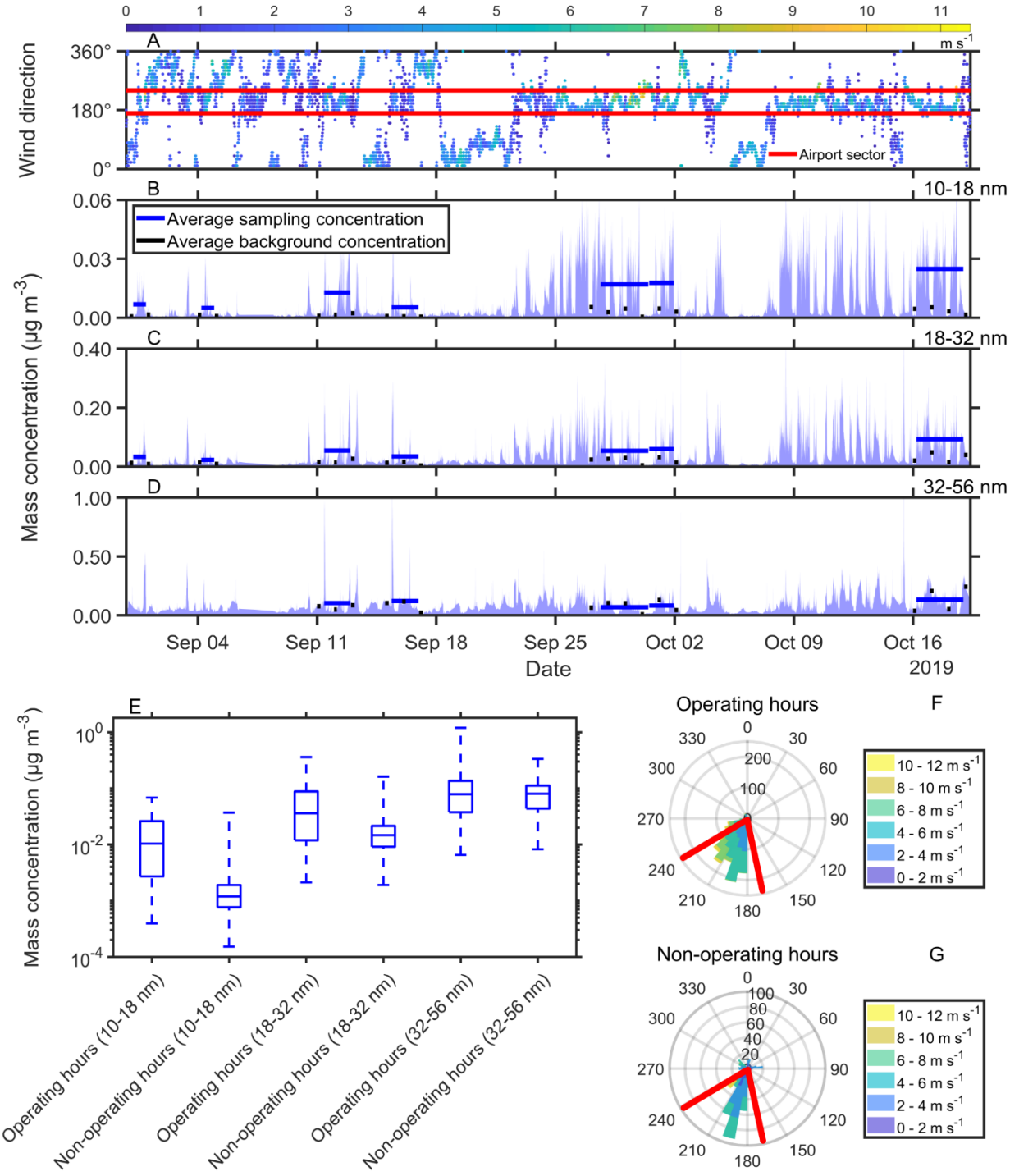

Figure 2. Overview of the UFP mass concentrations derived from PNSD measurements and wind direction at Frankfurt Airport. Wind direction (A) with wind speed indicated by the colour code. The wind data is provided by the meteorological station at Frankfurt Airport (International Civil Aviation Organization, ICAO, code: EDDF) of the German weather service (DWD). The ambient UFP mass concentration (µg m^{-3}) in the size ranges 10-18 nm (B), 18-32 nm (C) and 32-56 nm (D), and the Nano-MOUDI sampling intervals (horizontal lines), indicating the average mass concentration

during sampling hours (blue) and the average background mass concentration (black). Boxplots in (E) show the spread of the total mass concentrations (µg m^{-3}) for particles in 10-18 nm, 18-32 nm and 32-56 nm during airport operating- and non-operating hours. The wind roses depict the prevailing wind directions during filter sampling at airport operating hours (F). Furthermore, the wind directions during the non-operating hour periods used for SMPS background correction are shown (G).

We quantified the jet oil concentration of the individual impactor stages by adding authentic standards to aliquots of the filter extracts (standard addition method). Furthermore, we corrected for particle losses in the Nano-MOUDI based on an experimentally determined loss function of the three nano stages (see methods). We find that jet engine oils contribute on average 21 ± 7% to the UFP mass in the 10-18 nm size bin. The jet-oil mass fraction of individual samples in the 10-18 nm size bin varies between 10 and 38%, with generally higher values for short sampling intervals. The contribution of jet engine oil to the total mass of the 18-32 nm particles is only 5 ± 2% on average. Because the background subtraction could not be applied on the largest stage, we used the non-background corrected SMPS mass of the 32-56 nm stage and find a mean of 9% for the oil fraction of this size bin (Supplementary Table S2). Hence, the smallest particle stage shows consistently the highest mass fraction of jet engine lubrications oils. The calculation of the fractional oil contribution on all three stages did take into account particle wall losses and evaporative losses (pressure in sampling stages < 200 mbar). In fact, we observe a bias in the molecular composition of jet oil from the ambient samples, which can be well explained by evaporation of the semi-volatile additives during Nano-MOUDI sampling (Supplementary Table S3). We evaluated the sampling efficiency of the Nano-MOUDI toward semi-volatiles based on pure ethyl oleate UFPs ($C_{20}H_{38}O_2$, 98%, Sigma-Aldrich) from an atomized solution. Although the generated PNSD covered the whole Nano-MOUDI range, we only detected the compound on the 32-56 nm stage (with the lowest pressure difference of the three Nano-MOUDI stages), and even on this stage we observed a loss of >99% of mass of the ethyl-oleate-UFPs. The vapour pressure of ethyl oleate is 8.10E-03 Pa (EPI Suite[50]), which is similar to the vapour pressure of the N-phenyl-1-naphthylamine additive. The other additives and the jet oil esters exhibit lower vapour pressures (Supplementary Table S3). Therefore, it can be stated that the vapour pressure – and with this regard the volatilization of semi-volatile compounds – is the most important sampling loss process in the Nano-MOUDI. Fortunately, the jet oil esters are extremely low volatile, and therefore evaporation of this compound class during sampling is negligible.

Lubrication oil base stock esters in the volatility basis set

The observed new-particle formation downstream the thermodenuder and the largest mass fraction of lubrication oil in the smallest ambient UFPs suggests that lubrication oil emissions from jet engines play a pivotal role in nucleation and early growth of new particles. We further evaluated

this hypothesis by classifying the oils' synthetic esters into the volatility basis set (VBS[51–53]). Figure 3A shows the quantified ambient particle-phase concentration of single esters from two different jet oil base stocks: pentaerythritol esters ($C_{27\text{-}38}H_{48\text{-}70}O_8$) and trimethylolpropane esters ($C_{27\text{-}34}H_{50\text{-}64}O_6$). We used the SIMPOL.1 model[54] to estimate the vapour pressures of the different esters. We then calculated their saturation mass concentration C_i^* (at 293.15 K), which is the inverse of the gas-to-particle partitioning constant [Eq. 1], and assigned them to volatility classes[55]. In the ambient UFP samples, we measured particle-phase concentrations of the esters between 0.01 and 4 ng m^{-3}. Following, we calculated the theoretical gas-phase concentration, assuming that the esters' partitioning would shift entirely to the gas phase at ambient temperatures [Eq. 2]. As the lubrication oil concentration is not corrected for atmospheric dilution between the airport and the measurement station at Frankfurt-Schwanheim, the gas-phase concentration in the engine exhaust plumes at high temperatures (>300 °C) is certainly higher than this lower limit concentration downwind of the airport. However, we still observe a large saturation ratio of the theoretical gas-phase concentration [Eq. 3], which we derived from ambient particle-phase concentrations (Fig. 3B). The three largest pentaerythritol esters, which fall into the region of ultra-low volatility, reach a saturation ratio of up to $3x10^5$. Although this calculation is a lower-limit estimate, it supports the hypothesis that the synthetic esters from lubrication oils can initiate rapid nucleation in the exhaust plume of aircraft engines. Based on the theoretical gas-phase concentration, we also determined the temperature at which each single ester compound reaches gas-phase supersaturation ($S_i^* > 1$) during cool-down of the exhaust plume [Eq. 6] (Fig. 3C). At around 60 °C, the ultra-low volatility pentaerythritol esters ($C_{36}H_{66}O_8$ - $C_{38}H_{70}O_8$) are the first compounds that reach $S_i^* > 1$, although their ambient concentration is an order of magnitude lower than the extremely low-volatile ester $C_{29}H_{52}O_8$. Based on our measurements we observe that all synthetic esters reach supersaturation at ambient temperature, except the three most volatile trimethylolpropane esters $C_{27\text{-}29}H_{50\text{-}54}O_6$.

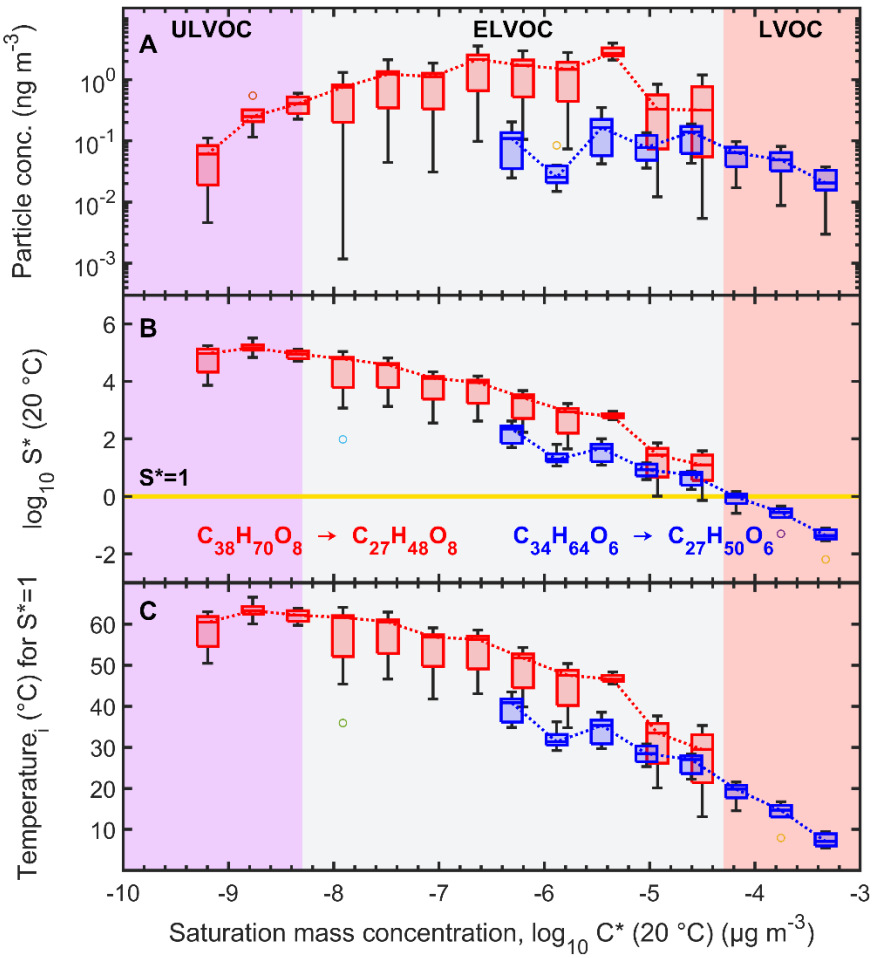

Figure 3. (A) Quantified particle concentration (ng m^{-3}) of each synthetic ester compound ($C_{27\text{-}38}H_{48\text{-}70}O_8$; $C_{27\text{-}34}H_{50\text{-}64}O_6$) plotted against the $\mathbf{log_{10}}\,\boldsymbol{C_i^*}$ at 20 °C (ULVOC: ultra low-volatility-, ELVOC: extremely low-volatility-, LVOC: low-volatility organic compound). The boxes show the spread of the ambient observations as interquartile range. (B) Resulting gas-phase saturation ratio $\boldsymbol{S_i^*(20\,°C)}$ of the theoretical gas-phase concentration when all particle-phase compounds of (A) would partition to the gas phase. Values of $\boldsymbol{S_i^*(20\,°C)}$ above 1 (yellow line) indicate supersaturation. (C) The approximate temperature at which the different jet oil esters reach $\boldsymbol{S_i^* = 1}$.

Discussion

The low concentration of the three ultra-low volatility organic compounds (ULVOCs) and higher concentrations of extremely-low volatility organic compounds (ELVOCs) creates ideal conditions for initial nucleation by the jet oil ULVOCs, followed by rapid growth due to condensation from a large gas-phase reservoir of jet oil ELVOCs. The critical temperatures at which the compounds reach supersaturation suggests that nucleation and particle growth occurs in the near-field during cool down of hot exhaust behind the turbofan (Fig. 4), and can explain the large volatile fraction (at

elevated temperatures) of UFPs from aviation. To which extent the emission of nvPM from turbofan engines can scavenge this nucleation and growth needs further evaluation.

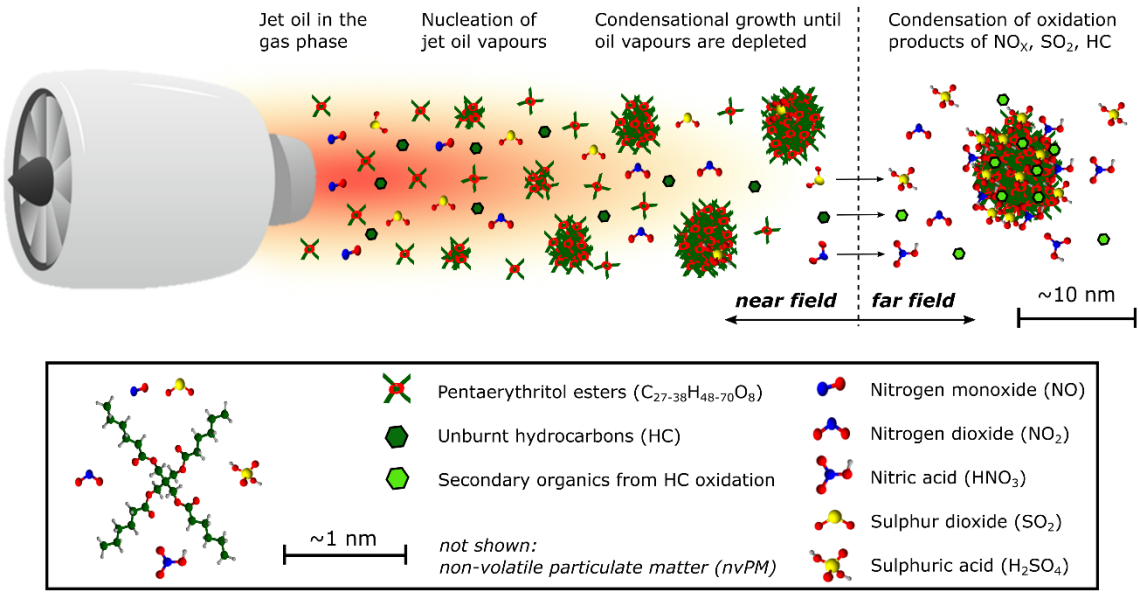

Figure 4. Conceptual illustration of the UFP formation from the emissions of aircraft turbofans, via fast nucleation and growth of jet oil vapours in the near field. Non-volatile emissions (nvPM) are not shown, as observations indicate that the majority of UFPs near airports are spherical and volatile. Dimensions are not true to scale.

In fact, the reduction of nvPM emissions (e.g. soot) from aircraft engines in the last decades – and with this the reduction of the condensational sink – might have led to an increase of the number concentration of volatile UFPs that are formed via nucleation of gaseous oil vapours or sulphuric acid. Nevertheless, the determined high gas-phase saturation ratios of the ULVOC synthetic esters suggest that nucleation can occur despite the presence of the condensation sink from nvPM. The dynamics of formation and condensation of semi-volatile oxidation products (e.g. from incomplete combustion) are not investigated in this study, but are complementary for understanding the UFP composition. Hence, the above-mentioned Nano-MOUDI sampling artefacts are critical, as low- and semi-volatile oxidation products, which can contribute to UFP mass, are lost during sampling. Despite these uncertainties and considering that our results are lower-limit estimates, they substantiate the main finding that jet-oil vapours reach gas-phase supersaturation in cooling emission plumes leading to rapid nucleation and formation of UFPs around 10-20 nm.

Our observations of lubrication oil emissions being an important source for UFPs implies that this source will not be addressed by replacing traditional jet-fuels with sustainable aviation fuels (SAF)[45], and should therefore also be taken into account in the current endeavour to eliminate UFP

emissions from aviation. Accordingly, the air/oil separator should be optimized with regard to an improved jet oil recovery, and thus preventing oil emissions. In addition, developing advanced maintenance routines and reducing the total uptime of jet engines at airports (e.g. through electrification of ground handling) could also reduce oil emissions. Furthermore, evaluation of the toxicological properties of jet oil UFPs should be conducted in order to assess their health effects, also considering detrimental and potentially neurotoxic substances that are either directly emitted (e.g. organophosphates as lubrication oil additives[56,57]), or which are formed through thermal transformation of the utilized trimethylolpropane esters (e.g. trimethlyolpropane phosphate)[26,58]. Furthermore, lubricant oil emissions during cruise and their possible effects on cirrus cloud formation needs further investigation, as the oil effect (e.g. as an organic coating on soot particles) has not been studied, yet.

Materials and Methods

Jet engine oil thermodenuder measurements

We used thermodenuder measurements in order to determine the volatility of jet oil UFPs, as the new international aircraft particulate matter standard only considers the number and mass concentration of nvPM[59]. We determined the particle-number size distribution of Mobil Jet™ Oil II UFPs, formed using an atomizer with 0.04 g L^{-1} jet oil solved in ultra-pure methanol. The resulting PNSD at 20 °C and 300 °C was measured using a scanning-mobility particle sizer (SMPS, TSI, model: 3938, Shoreview, MN, USA). The remaining jet engine oil fraction after the heating section was determined by comparing the particle mass derived from the PNSD measurements at both temperatures.

Impactor sampling and molecular characterization

Detailed information on sampling technique, sample preparation and extraction procedure can be found elsewhere[26]. Briefly, we used a Micro Orifice Uniform Deposition Impactor (Nano-MOUDI, Model 115, MSP, Minneapolis, MN, USA) at an air-quality monitoring site in Frankfurt-Schwanheim and sampled particles on the three nano-stages < 56 nm. All stages were equipped with aluminium foils (TSI, diameter 47 mm and thickness 0.015 mm), and the upper ten stages were coated with Apiezon® grease to minimize the bounce-off of larger particles.

In the period of August to October 2019, we sampled UFPs for 18 - 54 hours during airport operating hours (5:00 – 23:00 CET) and during southerly wind direction. Without an active sampling airflow, we collected field blanks for 115 hours on the three nano-stages to estimate possible background concentrations regarding the target compounds. We stored the filters until analysis at −20 °C. Due to the extensive sampling time span, we assume that our UFP samples represent aircraft engines

of several types under various operating states. This is essential for covering the average UFP emission of the whole airport and not of individual engines or certain engine operating states.

We quantified the additives and jet oil esters using standard addition with authentic and surrogate standards, respectively (Supplementary Fig. 4 and 5). Targeted measurements of the jet engine oil constituents were carried out by using ultra-high performance liquid chromatography (UHPLC)/heated electrospray ionization (HESI) coupled to an Orbitrap high-resolution mass spectrometer (HRMS). Chromatographic separation of the jet engine oil constituents was accomplished using a C_{18}-reversed phase column. Using the standard addition method, we quantified 23 compounds in 25 ambient filter samples including 3 blank samples. Most of these compounds belong to the group of pentaerythritol- or trimethylolpropane esters, which are utilized as jet engine oil base stocks. Finally, we determined the jet engine oil mass of the deposited UFPs after field blank correction.

Experimental loss determination in the Nano-MOUDI

Since sampling UFPs with a Nano-MOUDI is accompanied by particle losses, we determined a loss factor for each Nano-MOUDI stage (Supplementary Fig. 6-8). The loss of particles with an aerodynamic diameter between 32-56 nm is 28% and for 18-32 nm particles 40%, respectively. We were not able to experimentally determine a loss factor for the smallest size bin of 10-18 nm particles, due to insufficient deposited mass. We calculated the loss under the assumption that particle diffusivity is the main driving force for sampling losses of extremely low-volatile compounds in the UFP size range. We determined the dependency between particle diameter and diffusion coefficient at 17.2 kPa and 20 °C (sampling condition of the 18-32 nm stage). In order to fit the experimentally determined particle losses of the two larger stages, we applied a damping term on the diffusion coefficient equation (Supplementary Fig. 8). Based on the experimentally determined losses of the two upper nano stages, we calculated a loss of ~58% for the smallest stage. This loss factor can be considered as a conservative estimate, as it is only based on particle diffusive losses and not including losses due to evaporation after impaction (see main text). By implementing these loss factors, we corrected the quantified jet oil filter mass and determined the mass fraction of jet engine lubrication oils in airport-related UFPs.

Ambient SMPS measurements

The PNSD at the sampling site was determined using a SMPS including an electrostatic classifier (TSI, model: 3082), a Differential Mobility Analyser (DMA, TSI, model: 3081) and a Condensation Particle Counter (CPC, TSI, model: 3772). Ambient air was sampled through a stainless-steel tube (inner diameter: 20 mm, length 1.6 m), using a $PM_{2.5}$ inlet head at a flow rate of 1 $m^3\ h^{-1}$. Prior entering the SMPS, the aerosol passes a Nafion dryer (1.2 m length, flow rate of 0.3 $m^3\ h^{-1}$) to stabilize the relative humidity below 40%. The actual sample flow of the SMPS is 1 L min^{-1}, the

additional bypass is used to minimize residence time and particle losses in the inlet system. The PNSD was measured in the size range of 10 – 500 nm at a temporal resolution of 5 minutes. Particle losses due to sedimentation, inertial impaction and diffusion have been calculated and corrected based on[60]. The UFP mass was determined by integration assuming spherical particles. We calculated the particle mass for each filter collection interval exclusively during airport operating hours by converting the PNSD into a volume distribution averaged over the sampling period using a unit density of 1 g cm^{-3} and the Nano-MOUDI sampling flow rate of 0.6 m^3 h^{-1}. The particle density was chosen according to the analysed jet engine oil densities (see safety data sheets) and aircraft turbine engine studies[61]. Consequently, conversion of the measured mobility diameter to aerodynamic diameter is not necessary[62]. We analysed the SMPS data of seven filter sampling periods as no data is available for one sampling period due to an instrument failure.

Volatility and saturation ratio of jet oil esters

The volatility of compounds strongly determines their gas-to-particle partitioning behaviour. Hence, evaluation of the jet oil base stocks using semi-empirical group contribution methods (SIMPOL.1 model[54]) and the volatility basis set (VBS[51,52]) enables the grouping of the single ester compounds to volatility classes (ULVOC: ultra low-volatility-, ELVOC: extremely low-volatility-, LVOC: low-volatility organic compound). Compound classification is based on their volatility expressed as the logarithm of the saturation mass concentration ($\log_{10} C_i^*$), where the volatility is differentiated by one decade in C_i^*, which is also assumed as uncertainty. The saturation mass concentration (C_i^* (µg m^{-3}) is calculated as the inverse of the gas-to-particle phase partitioning constant (K_p)[51] taking into account the weight fraction of the absorbing organic material (om) phase (f_{om}), the compounds molecular weight (MW_{om}, g mol^{-1}), their activity coefficient (ζ_i), and vapour pressure ($p_{L,i}^0$, Torr)[51,63]:

$$\frac{1}{\zeta_i * C_i^*} = K_p = \frac{f_{om} * 760 * R * T}{MW_{om} * \zeta_i * p_{L,i}^0 * 10^6} \quad [1]$$

We calculated K_p assuming the absorbing organic phase consists only of the respective substance ($f_{om} = 1$), which leads to an ideal absorption affinity of the molecules passing from the gas phase to the particle phase ($\zeta_i = 1$). The compound's affinity to the particle phase inversely correlates with $\zeta_i = 1$ [64]. *R* is the gas constant (8.2 x 10^{-5} m^3 atm mol^{-1} K^{-1}) and *T* (K) the temperature.

We converted the quantified base stock ester concentrations in the particle phase ($\frac{m_i}{V}$ (g m^{-3})) to gas phase number concentrations (c_i^v (m^{-3})) using the ideal gas law (m_i: quantified ester mass; M_i: molecular mass in g mol^{-1}):

$$c_i^v = \frac{m_i * N_A}{V * M_i} \quad [2]$$

In order to determine whether jet oil constituents reach gas-phase supersaturation, we calculated their gas-phase saturation ratio (S_i^*)[65]:

$$S_i^* = \frac{c_i^v * M_i * 10^6}{C_i^* * N_A} \quad [3]$$

Accounting for the temperature dependence of the saturation vapour pressure, C_i^* can be described according to the Clausius-Clapeyron equation:

$$\log_{10} C_i^*(T) = \log_{10} C_i^*(293.15\ K) + \frac{\Delta H_i^{vap}}{R * \ln(10)} * (\frac{1}{293.15\ K} - \frac{1}{T}) \quad [4]$$

where R = 8.314 * 10^{-3} kJ K^{-1} mol^{-1}. The evaporation enthalpy ΔH_i^{vap} (kJ mol^{-1}) can be approximated by:

$$\Delta H_i^{vap} = -11 * \log_{10} C_i^*(293.15\ K) + 129 \quad [5]$$

Despite the large uncertainties of this approach[66], it still can be used to describe a simple estimate of the temperature dependence of the oil partitioning. Finally, we combined [Eq. 3] and [Eq. 4] to calculate the approximate temperature at which the jet oil esters reach gas-phase supersaturation ($S_i^* = 1$) in a cooling engine exhaust plume [Eq. 6].

$$T_i^{S^*=1} = -\frac{1}{\log_{10}(\frac{c_i^v * M_i * 10^6}{N_A * C_i^*(293.15\ K)}) * \frac{R * \ln(10)}{\Delta H_i^{vap}} - \frac{1}{293.15\ K}} \quad [6]$$

Data availability: The data shown in this study is available at 10.5281/zenodo.6876277.

References

1. Hu, S. *et al.* Aircraft emission impacts in a neighborhood adjacent to a general aviation airport in southern California. *Environ. Sci. Technol.* **43,** 8039–8045; 10.1021/es900975f (2009).
2. Yu, Z. *et al.* Identification of lubrication oil in the particulate matter emissions from engine exhaust of in-service commercial aircraft. *Environ. Sci. Technol.* **46,** 9630–9637; 10.1021/es301692t (2012).
3. Keuken, M. P., Moerman, M., Zandveld, P., Henzing, J. S. & Hoek, G. Total and size-resolved particle number and black carbon concentrations in urban areas near Schiphol airport (the Netherlands). *Atmos. Environ.* **104,** 132–142; 10.1016/j.atmosenv.2015.01.015 (2015).
4. Stafoggia, M. *et al.* Particle number concentrations near the Rome-Ciampino city airport. *Atmos. Environ.* **147,** 264–273; 10.1016/j.atmosenv.2016.09.062 (2016).
5. Yu, Z. *et al.* Evaluation of PM emissions from two in-service gas turbine general aviation aircraft engines. *Atmos. Environ.* **160,** 9–18; 10.1016/j.atmosenv.2017.04.007 (2017).
6. Habre, R. *et al.* Short-term effects of airport-associated ultrafine particle exposure on lung function and inflammation in adults with asthma. *Environ. Int.* **118,** 48–59; 10.1016/j.envint.2018.05.031 (2018).
7. Fushimi, A., Saitoh, K., Fujitani, Y. & Takegawa, N. Identification of jet lubrication oil as a major component of aircraft exhaust nanoparticles. *Atmos. Chem. Phys.* **19,** 6389–6399; 10.5194/acp-19-6389-2019 (2019).
8. Rivas, I. *et al.* Source apportionment of particle number size distribution in urban background and traffic stations in four European cities. *Environ. Int.* **135,** 105345; 10.1016/j.envint.2019.105345 (2020).
9. Zhu, Y., Fanning, E., Yu, R. C., Zhang, Q. & Froines, J. R. Aircraft emissions and local air quality impacts from takeoff activities at a large International Airport. *Atmos. Environ.* **45,** 6526–6533; 10.1016/j.atmosenv.2011.08.062 (2011).
10. Hsu, H.-H. *et al.* The relationship between aviation activities and ultrafine particulate matter concentrations near a mid-sized airport. *Atmos. Environ.* **50,** 328–337; 10.1016/j.atmosenv.2011.12.002 (2012).
11. Hsu, H.-H. *et al.* Contributions of aircraft arrivals and departures to ultrafine particle counts near Los Angeles International Airport. *Sci. Total Environ.* **444,** 347–355; 10.1016/j.scitotenv.2012.12.010 (2013).
12. Pirhadi, M. *et al.* Relative contributions of a major international airport activities and other urban sources to the particle number concentrations (PNCs) at a nearby monitoring site. *Environ. Pollut.* **260,** 114027; 10.1016/j.envpol.2020.114027 (2020).
13. Pekkanen, J. & Kulmala, M. Exposure assessment of ultrafine particles in epidemiologic time-series studies. *Scand. J. Work Environ. Health* **30 Suppl 2,** 9–18 (2004).
14. Mazaheri, M., Bostrom, T. E., Johnson, G. R. & Morawska, L. Composition and morphology of particle emissions from in-use aircraft during takeoff and landing. *Environ. Sci. Technol.* **47,** 5235–5242; 10.1021/es3046058 (2013).
15. Hudda, N. & Fruin, S. A. International Airport Impacts to Air Quality: Size and Related Properties of Large Increases in Ultrafine Particle Number Concentrations. *Environ. Sci. Technol.* **50,** 3362–3370; 10.1021/acs.est.5b05313 (2016).
16. Zhang, X., Karl, M., Zhang, L. & Wang, J. Influence of Aviation Emission on the Particle Number Concentration near Zurich Airport. *Environ. Sci. Technol.* **54,** 14161–14171; 10.1021/acs.est.0c02249 (2020).

17. Hudda, N., Simon, M. C., Zamore, W. & Durant, J. L. Aviation-Related Impacts on Ultrafine Particle Number Concentrations Outside and Inside Residences near an Airport. *Environ. Sci. Technol.* **52,** 1765–1772; 10.1021/acs.est.7b05593 (2018).

18. Hudda, N., Durant, L. W., Fruin, S. A. & Durant, J. L. Impacts of Aviation Emissions on Near-Airport Residential Air Quality. *Environ. Sci. Technol.* **54,** 8580–8588; 10.1021/acs.est.0c01859 (2020).

19. Chen, C. *et al.* Outdoor-to-indoor transport of ultrafine particles: Measurement and model development of infiltration factor. *Environ. Pollut.* **267,** 115402; 10.1016/j.envpol.2020.115402 (2020).

20. Riley, E. A. *et al.* Ultrafine particle size as a tracer for aircraft turbine emissions. *Atmos. Environ.* **139,** 20–29; 10.1016/j.atmosenv.2016.05.016 (2016).

21. Masiol, M., Harrison, R. M., Vu, T. V. & Beddows, D. C. S. Sources of sub-micrometre particles near a major international airport. *Atmos. Chem. Phys.* **17,** 12379–12403; 10.5194/acp-17-12379-2017 (2017).

22. Shirmohammadi, F. *et al.* Emission rates of particle number, mass and black carbon by the Los Angeles International Airport (LAX) and its impact on air quality in Los Angeles. *Atmos. Environ.* **151,** 82–93; 10.1016/j.atmosenv.2016.12.005 (2017).

23. Stacey, B. Measurement of ultrafine particles at airports: A review. *Atmos. Environ.* **198,** 463–477; 10.1016/j.atmosenv.2018.10.041 (2019).

24. Yu, Z. *et al.* Characterization of lubrication oil emissions from aircraft engines. *Environ. Sci. Technol.* **44,** 9530–9534; 10.1021/es102145z (2010).

25. Timko, M. T. *et al.* Particulate Emissions of Gas Turbine Engine Combustion of a Fischer−Tropsch Synthetic Fuel. *Energ. Fuel.* **24,** 5883–5896; 10.1021/ef100727t (2010).

26. Ungeheuer, F., van Pinxteren, D. & Vogel, A. L. Identification and source attribution of organic compounds in ultrafine particles near Frankfurt International Airport. *Atmos. Chem. Phys.* **21,** 3763–3775; 10.5194/acp-21-3763-2021 (2021).

27. Oberdörster, G. *et al.* Extrapulmonary translocation of ultrafine carbon particles following whole-body inhalation exposure of rats. *J. Toxicol. Environ. Health Part A* **65,** 1531–1543; 10.1080/00984100290071658 (2002).

28. Oberdörster, G., Oberdörster, E. & Oberdörster, J. Nanotoxicology: an emerging discipline evolving from studies of ultrafine particles. *Environ. Health. Persp.* **113,** 823–839; 10.1289/ehp.7339 (2005).

29. Kreyling, W. G. *et al.* Air-blood barrier translocation of tracheally instilled gold nanoparticles inversely depends on particle size. *ACS nano* **8,** 222–233; 10.1021/nn403256v (2014).

30. Lu, D. *et al.* Chemical multi-fingerprinting of exogenous ultrafine particles in human serum and pleural effusion. *Nat. Commun.* **11,** 2567; 10.1038/s41467-020-16427-x (2020).

31. Oberdörster, G. *et al.* Translocation of inhaled ultrafine particles to the brain. *Inhal. Toxicol.* **16,** 437–445; 10.1080/08958370490439597 (2004).

32. Miller, M. R. *et al.* Inhaled Nanoparticles Accumulate at Sites of Vascular Disease. *ACS nano* **11,** 4542–4552; 10.1021/acsnano.6b08551 (2017).

33. Nel, A., Xia, T., Mädler, L. & Li, N. Toxic potential of materials at the nanolevel. *Science (New York, N.Y.)* **311,** 622–627; 10.1126/science.1114397 (2006).

34. Jonsdottir, H. R. *et al.* Non-volatile particle emissions from aircraft turbine engines at ground-idle induce oxidative stress in bronchial cells. *Commun. Biol.* **2,** 90; 10.1038/s42003-019-0332-7 (2019).

35. Ohlwein, S., Kappeler, R., Kutlar Joss, M., Künzli, N. & Hoffmann, B. Health effects of ultrafine particles: a systematic literature review update of epidemiological evidence. *Int. J. Public Health* **64,** 547–559; 10.1007/s00038-019-01202-7 (2019).

36. Chalupa, D. C., Morrow, P. E., Oberdörster, G., Utell, M. J. & Frampton, M. W. Ultrafine particle deposition in subjects with asthma. *Environ. Health. Persp.* **112,** 879–882; 10.1289/ehp.6851 (2004).

37. Møller, K. L. *et al.* Occupational exposure to ultrafine particles among airport employees--combining personal monitoring and global positioning system. *PloS one* **9,** e106671; 10.1371/journal.pone.0106671 (2014).

38. Ren, J., Cao, X. & Liu, J. Impact of atmospheric particulate matter pollutants to IAQ of airport terminal buildings: A first field study at Tianjin Airport, China. *Atmos. Environ.* **179,** 222–226; 10.1016/j.atmosenv.2018.02.019 (2018).

39. Wu, A. H. *et al.* Association between Airport-Related Ultrafine Particles and Risk of Malignant Brain Cancer: A Multiethnic Cohort Study. *Cancer Res.* **81,** 4360–4369; 10.1158/0008-5472.CAN-21-1138 (2021).

40. Weichenthal, S. *et al.* Within-city Spatial Variations in Ambient Ultrafine Particle Concentrations and Incident Brain Tumors in Adults. *Epidemiology (Cambridge, Mass.)* **31,** 177–183; 10.1097/EDE.0000000000001137 (2020).

41. Møller, K. L. *et al.* Cardiovascular disease and long-term occupational exposure to ultrafine particles: A cohort study of airport workers. *Int. J. Hyg. Environ. Health* **223,** 214–219; 10.1016/j.ijheh.2019.08.010 (2020).

42. Brock, C. A. *et al.* Ultrafine particle size distributions measured in aircraft exhaust plumes. *J. Geophys. Res.* **105,** 26555–26567; 10.1029/2000JD900360 (2000).

43. Voigt, C. *et al.* Cleaner burning aviation fuels can reduce contrail cloudiness. *Commun. Earth. Environ.* **2**; 10.1038/s43247-021-00174-y (2021).

44. Kärcher, B., Burkhardt, U., Bier, A., Bock, L. & Ford, I. J. The microphysical pathway to contrail formation. *J. Geophys. Res. Atmos.* **120,** 7893–7927; 10.1002/2015JD023491 (2015).

45. Moore, R. H. *et al.* Biofuel blending reduces particle emissions from aircraft engines at cruise conditions. *Nature* **543,** 411–415; 10.1038/nature21420 (2017).

46. Anderson, B. E., Cofer, W. R., Barrick, J. D., Bagwell, D. R. & Hudgins, C. H. Airborne observations of aircraft aerosol emissions II: Factors controlling volatile particle production. *Geophys. Res. Lett.* **25,** 1693–1696; 10.1029/98GL00661 (1998).

47. Curtius, J. *et al.* First direct sulfuric acid detection in the exhaust plume of a jet aircraft in flight. *Geophys. Res. Lett.* **25,** 923–926; 10.1029/98GL00512 (1998).

48. Wang, M. *et al.* Rapid growth of new atmospheric particles by nitric acid and ammonia condensation. *Nature* **581,** 184–189; 10.1038/s41586-020-2270-4 (2020).

49. El-Sayed, A. F. *Aircraft propulsion and gas turbine engines* (CRC Press Taylor & Francis Group, Boca Raton, FL, 2017).

50. United States Environmental Protection Agency. *US EPA. [2021]. Estimation Programs Interface Suite™ v 4.11* (Washington, DC, USA,).

51. Donahue, N. M., Robinson, A. L., Stanier, C. O. & Pandis, S. N. Coupled partitioning, dilution, and chemical aging of semivolatile organics. *Environ. Sci. Technol.* **40,** 2635–2643; 10.1021/es052297c (2006).

52. Donahue, N. M., Epstein, S. A., Pandis, S. N. & Robinson, A. L. A two-dimensional volatility basis set: 1. organic-aerosol mixing thermodynamics. *Atmos. Chem. Phys.* **11,** 3303–3318; 10.5194/acp-11-3303-2011 (2011).

53. Donahue, N. M., Kroll, J. H., Pandis, S. N. & Robinson, A. L. A two-dimensional volatility basis set – Part 2: Diagnostics of organic-aerosol evolution. *Atmos. Chem. Phys.* **12,** 615–634; 10.5194/acp-12-615-2012 (2012).

54. Pankow, J. F. & Asher, W. E. SIMPOL.1: a simple group contribution method for predicting vapor pressures and enthalpies of vaporization of multifunctional organic compounds. *Atmos. Chem. Phys.* **8,** 2773–2796; 10.5194/acp-8-2773-2008 (2008).

55. Stolzenburg, D. *et al.* Rapid growth of organic aerosol nanoparticles over a wide tropospheric temperature range. *Proc. Natl. Acad. Sci. U S A* **115,** 9122–9127; 10.1073/pnas.1807604115 (2018).

56. Duarte, D. J., Rutten, J. M. M., van den Berg, M. & Westerink, R. H. S. In vitro neurotoxic hazard characterization of different tricresyl phosphate (TCP) isomers and mixtures. *Neurotoxicology* **59,** 222–230; 10.1016/j.neuro.2016.02.001 (2017).

57. Hageman, G., Mackenzie Ross, S. J., Nihom, J. & van der Laan, G. Aerotoxic syndrome: A new occupational disease caused by contaminated cabin air? In *Occupational Neurotoxicology,* edited by M. Aschner (Elsevier Science & Technology, San Diego, 2022), Vol. 7, pp. 77–132.

58. Keefer, E. W., Gramowski, A., Stenger, D. A., Pancrazio, J. J. & Gross, G. W. Characterization of acute neurotoxic effects of trimethylolpropane phosphate via neuronal network biosensors. *Biosens. Bioelectron.* **16,** 513–525; 10.1016/S0956-5663(01)00165-8 (2001).

59. International Civil Aviation Organization (ICAO). Environmental Report Aviation And Environment. Destination Green The Next Chapter. International Civil Aviation Organization (ICAO), 2019.

60. Weiden, S.-L. von der, Drewnick, F. & Borrmann, S. Particle Loss Calculator – a new software tool for the assessment of the performance of aerosol inlet systems. *Atmos. Meas. Tech.* **2,** 479–494; 10.5194/amt-2-479-2009 (2009).

61. Durdina, L. *et al.* Determination of PM mass emissions from an aircraft turbine engine using particle effective density. *Atmos. Environ.* **99,** 500–507; 10.1016/j.atmosenv.2014.10.018 (2014).

62. Seinfeld, J. H. & Pandis, S. N. *Atmospheric Chemistry and Physics. From Air Pollution to Climate Change.* 3rd ed. (Wiley, s.l., 2016).

63. Pankow, J. F. An absorption model of gas/particle partitioning of organic compounds in the atmosphere. *Atmos. Environ.* **28,** 185–188; 10.1016/1352-2310(94)90093-0 (1994).

64. Williams, B. J., Goldstein, A. H., Kreisberg, N. M. & Hering, S. V. In situ measurements of gas/particle-phase transitions for atmospheric semivolatile organic compounds. *Proc. Natl. Acad. Sci. U S A* **107,** 6676–6681; 10.1073/pnas.0911858107 (2010).

65. Donahue, N. M. *et al.* How do organic vapors contribute to new-particle formation? *Faraday Discuss.* **165,** 91–104; 10.1039/c3fd00046j (2013).

66. Epstein, S. A., Riipinen, I. & Donahue, N. M. A semiempirical correlation between enthalpy of vaporization and saturation concentration for organic aerosol. *Environ. Sci. Technol.* **44,** 743–748; 10.1021/es902497z (2010).

Acknowledgements

We thank Anett Dietze of the Leibniz Institute for Tropospheric Research (TROPOS) for filter preparation and weighing.

This research has been supported by the Deutsche Forschungsgemeinschaft (DFG; German Research Foundation) (grant no. 410009325).

Author Contributions: F.U. wrote the paper; designed research, performed the field sampling, sample preparation, measurements, lab experiments and majority of data analysis; L.C. performed lab experiments and analysed data; F.D., D.R. performed SMPS measurements; D.v.P., S.J., D.K., A.K., J.C. advised on data interpretation; A.L.V. designed research, advised on data analysis, data interpretation and manuscript writing; edited and revised the manuscript; and directed the project administration. All authors commented on the manuscript and contributed to the scientific discussion.

Competing Interest Statement: The authors declare that they have no conflict of interest.

Supplementary information: The supplement related to this article is available online at:[…]

6.4 Synergistic HNO_3–H_2SO_4–NH_3 upper tropospheric particle formation, Wang et al. (2022).

Article

Synergistic HNO_3–H_2SO_4–NH_3 upper tropospheric particle formation

https://doi.org/10.1038/s41586-022-04605-4

Received: 28 July 2021

Accepted: 2 March 2022

Published online: 18 May 2022

Open access

Check for updates

Mingyi Wang[1,2,7], Mao Xiao[3], Barbara Bertozzi[4], Guillaume Marie[5], Birte Rörup[6], Benjamin Schulze[7], Roman Bardakov[8,9], Xu-Cheng He[6], Jiali Shen[6], Wiebke Scholz[10], Ruby Marten[3], Lubna Dada[3,6], Rima Baalbaki[6], Brandon Lopez[1,11], Houssni Lamkaddam[3], Hanna E. Manninen[12], António Amorim[13], Farnoush Ataei[14], Pia Bogert[4], Zoé Brasseur[6], Lucía Caudillo[5], Louis-Philippe De Menezes[12], Jonathan Duplissy[6,15], Annica M. L. Ekman[8,9], Henning Finkenzeller[16], Loïc Gonzalez Carracedo[17], Manuel Granzin[5], Roberto Guida[12], Martin Heinritzi[5], Victoria Hofbauer[1,2], Kristina Höhler[4], Kimmo Korhonen[18], Jordan E. Krechmer[19], Andreas Kürten[5], Katrianne Lehtipalo[6,20], Naser G. A. Mahfouz[1,21], Vladimir Makhmutov[22,23], Dario Massabò[24], Serge Mathot[12], Roy L. Mauldin[1,2,25], Bernhard Mentler[10], Tatjana Müller[5,26], Antti Onnela[12], Tuukka Petäjä[6], Maxim Philippov[22], Ana A. Piedehierro[20], Andrea Pozzer[26], Ananth Ranjithkumar[27], Meredith Schervish[1,2], Siegfried Schobesberger[18], Mario Simon[5], Yuri Stozhkov[22], António Tomé[28], Nsikanabasi Silas Umo[4], Franziska Vogel[4], Robert Wagner[4], Dongyu S. Wang[3], Stefan K. Weber[12], André Welti[20], Yusheng Wu[6], Marcel Zauner-Wieczorek[5], Mikko Sipilä[6], Paul M. Winkler[17], Armin Hansel[10,29], Urs Baltensperger[3], Markku Kulmala[6,15,30,31], Richard C. Flagan[7], Joachim Curtius[5], Ilona Riipinen[9,32], Hamish Gordon[1,11], Jos Lelieveld[26,33], Imad El-Haddad[3], Rainer Volkamer[16], Douglas R. Worsnop[6,19], Theodoros Christoudias[33], Jasper Kirkby[5,12], Ottmar Möhler[4] & Neil M. Donahue[1,2,11,34] ✉

New particle formation in the upper free troposphere is a major global source of cloud condensation nuclei (CCN)[1–4]. However, the precursor vapours that drive the process are not well understood. With experiments performed under upper tropospheric conditions in the CERN CLOUD chamber, we show that nitric acid, sulfuric acid and ammonia form particles synergistically, at rates that are orders of magnitude faster than those from any two of the three components. The importance of this mechanism depends on the availability of ammonia, which was previously thought to be efficiently scavenged by cloud droplets during convection. However, surprisingly high concentrations of ammonia and ammonium nitrate have recently been observed in the upper troposphere over the Asian monsoon region[5,6]. Once particles have formed, co-condensation of ammonia and abundant nitric acid alone is sufficient to drive rapid growth to CCN sizes with only trace sulfate. Moreover, our measurements show that these CCN are also highly efficient ice nucleating particles—comparable to desert dust. Our model simulations confirm that ammonia is efficiently convected aloft during the Asian monsoon, driving rapid, multi-acid HNO_3–H_2SO_4–NH_3 nucleation in the upper troposphere and producing ice nucleating particles that spread across the mid-latitude Northern Hemisphere.

Intense particle formation has been observed by airborne measurements as a persistent, global-scale band in the upper troposphere over tropical convective regions[1,2,4]. Upper tropospheric nucleation is thought to provide at least one-third of global CCN[3]. Increased aerosols since the industrial revolution, and their interactions with clouds, have masked a large fraction of the global radiative forcing by greenhouse gases. Projections of aerosol radiative forcing resulting from future reductions of air pollution are highly uncertain[7]. Present-day nucleation involves sulfuric acid (H_2SO_4) over almost all the troposphere[8]. However, binary nucleation of H_2SO_4–H_2O is slow and, so, ternary or multicomponent nucleation with extra vapours such as ammonia (NH_3)[9] and organics[10,11] is necessary to account for observed new-particle-formation rates[3,8,12].

Ammonia stabilizes acid–base nucleation and strongly enhances particle formation rates[9]. However, ammonia is thought to be extremely scarce in the upper troposphere because its solubility in water and reactivity with acids should lead to efficient removal in convective clouds. However, this assumption is not supported by observation. Ammonia vapour has been repeatedly detected in the Asian monsoon upper troposphere, with mixing ratios of up to 30 pptv (2.5×10^8 cm^{-3}) for a three-month average[5] and up to 1.4 ppbv (1.2×10^{10} cm^{-3}) in hotspots[6].

A list of affiliations appears at the end of the paper.

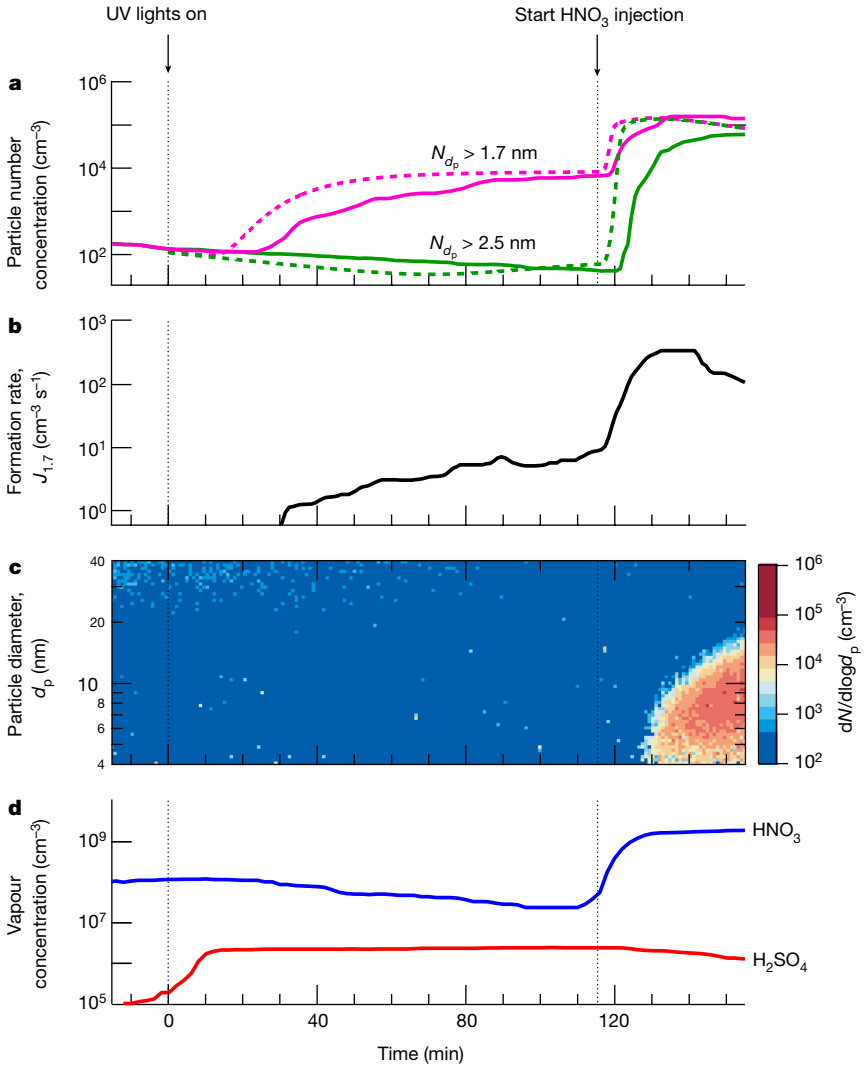

Fig. 1 | Example experiment showing nitric acid enhancement of H_2SO_4–NH_3 particle formation. a, Particle number concentrations versus time at mobility diameters >1.7 nm (magenta) and >2.5 nm (green). The solid magenta trace is measured by a $PSM_{1.7}$ and the solid green trace is measured by a $CPC_{2.5}$. The fixed experimental conditions are about 6.5×10^8 cm^{-3} NH_3, 223 K and 25% relative humidity. A microphysical model reproduces the main features of the observed particle formation (dashed lines; see text for details). **b**, Particle formation rate versus time at 1.7 nm ($J_{1.7}$), measured by a PSM. **c**, Particle size distribution versus time, measured by an SMPS. **d**, Gas-phase nitric acid and sulfuric acid versus time, measured by an I^- CIMS and a NO_3^- CIMS, respectively. Sulfuric acid through SO_2 oxidation started to appear soon after switching on the UV lights at time = 0 min, building up to a steady state of 2.3×10^6 cm^{-3} after a wall-loss-rate timescale of around 10 min. The subsequent H_2SO_4–NH_3 nucleation led to a relatively slow formation rate of 1.7-nm particles. The particles did not grow above 2.5 nm because of their slow growth rate and corresponding low survival probability against wall loss. Following injection of 2.0×10^9 cm^{-3} nitric acid into the chamber after 115 min, while leaving the production rate of sulfuric acid and the injection rate of ammonia unchanged, we observed a sharp increase in particle formation rate (panel **b**), together with rapid particle growth of 40 nm h^{-1} (panel **c**). The overall systematic scale uncertainties of ±30% on particle formation rate, −33%/+50% on sulfuric acid concentration and ±25% on nitric acid concentration are not shown.

The release of dissolved ammonia from cloud droplets may occur during glaciation[13]. Once released in the upper troposphere, ammonia can form particles with nitric acid, which is abundantly produced by lightning[14,15]. These particles will live longer and travel farther than ammonia vapour, with the potential to influence the entire upper troposphere and lower stratosphere of the Northern Hemisphere[6].

Fundamental questions remain about the role and mechanisms of nitric acid and ammonia in upper tropospheric particle formation. Recent CLOUD (Cosmics Leaving Outdoor Droplets) experiments at CERN have shown that nitric acid and ammonia vapours below 278 K can condense onto newly formed particles as small as a few nanometres in diameter, driving rapid growth to CCN sizes[16]. At even lower temperatures (below 258 K), nitric acid and ammonia can directly nucleate to form ammonium nitrate particles, although pure HNO_3–NH_3 nucleation is too slow to compete with H_2SO_4–NH_3 nucleation under comparable conditions. However, the results we present here show that, when all three vapours are present, a synergistic interaction drives nucleation rates orders of magnitude faster than those from any two of the three components. Once nucleated through this multi-acid–ammonia mechanism, the particles can grow rapidly by co-condensation of NH_3 and HNO_3 alone, both of which may be far more abundant than H_2SO_4 in the upper troposphere.

Particle formation measurements in CLOUD

Here we report new-particle-formation experiments performed with mixtures of sulfuric acid, nitric acid and ammonia vapours in the CLOUD chamber[9] at CERN between September and December 2019 (CLOUD 14; see Methods for experimental details). To span ranges typical of the upper troposphere, we established quasi-steady-state

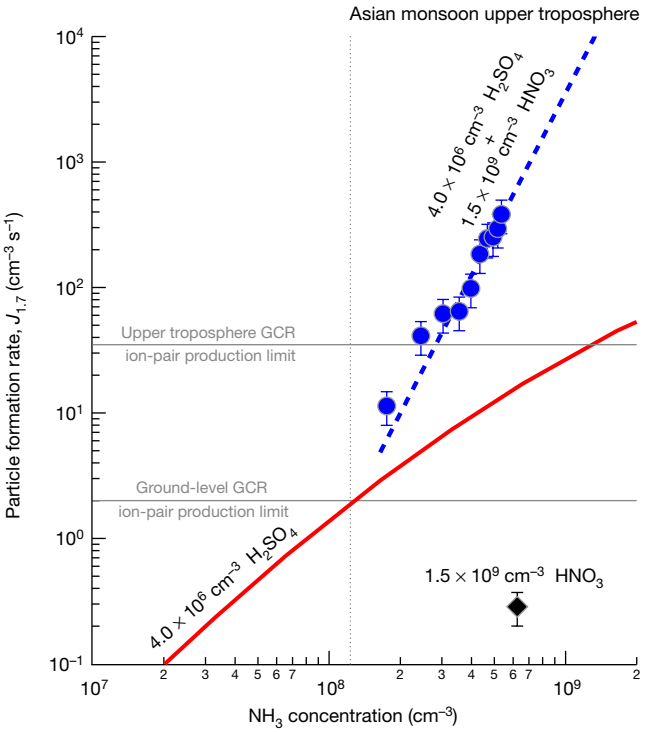

Fig. 2 | Particle formation rates at 1.7 nm ($J_{1.7}$) versus ammonia concentration at 223 K and 25% relative humidity. The chemical systems are HNO_3–NH_3 (black), H_2SO_4–NH_3 (red) and HNO_3–H_2SO_4–NH_3 (blue). The black diamond shows the CLOUD measurement of HNO_3–NH_3 nucleation at 1.5×10^9 cm^{-3} HNO_3, 6.5×10^8 cm^{-3} NH_3 and with H_2SO_4 below the detection limit of 5×10^4 cm^{-3}. The red solid curve is $J_{1.7}$ versus ammonia concentration at 4.0×10^6 cm^{-3} sulfuric acid from a H_2SO_4–NH_3 nucleation parameterization on the basis of previous CLOUD measurements[18,19]. The blue circles show the CLOUD measurements of HNO_3–H_2SO_4–NH_3 nucleation at 4.0×10^6 cm^{-3} H_2SO_4, 1.5×10^9 cm^{-3} HNO_3 and $(1.6–6.5) \times 10^8$ cm^{-3} NH_3. The data are fitted by a power law, $J_{1.7} = k[NH_3]^{3.7}$ (blue dashed curve). The vertical grey dotted line separates ammonia concentrations measured in different regions in the upper troposphere[5]; the region to the right indicates the Asian monsoon conditions. The horizontal grey solid lines show $J_{1.7}$ upper limits for ion-induced nucleation resulting from the GCR ionization rate of around 2 ion pairs cm^{-3} s^{-1} at ground level and 35 ion pairs cm^{-3} s^{-1} in the upper troposphere. Among the three nucleation mechanisms, H_2SO_4–NH_3 nucleation dominates in regions with low ammonia (below around 1.0×10^8 cm^{-3}, or 12 pptv), whereas HNO_3–H_2SO_4–NH_3 nucleation dominates at higher ammonia levels characteristic of the Asian monsoon upper troposphere. The bars indicate 30% estimated total error on the particle formation rates. The overall systematic scale uncertainties are −33%/+50% for sulfuric acid and ±25% for nitric acid concentrations.

vapour concentrations in the chamber of $(0.26–4.6) \times 10^6$ cm^{-3} sulfuric acid (through photochemical oxidation of SO_2), $(0.23–4.0) \times 10^9$ cm^{-3} nitric acid (through either photochemical oxidation of NO_2 or injection from an evaporator) and $(0.95–6.5) \times 10^8$ cm^{-3} ammonia (through injection from a gas bottle). In an extreme experiment to simulate hotspot conditions in the Asian monsoon anticyclone, we raised sulfuric acid, nitric acid and ammonia to maximum concentrations of 6.2×10^7 cm^{-3}, 3.8×10^9 cm^{-3} and 8.8×10^9 cm^{-3}, respectively. The experiments were conducted at 223 K and 25% relative humidity, representative of upper tropospheric conditions.

Figure 1 shows the evolution of a representative new-particle-formation experiment in the presence of around 6.5×10^8 cm^{-3} ammonia. The top three panels show particle number concentrations above 1.7 nm and above 2.5 nm (Fig. 1a), particle formation rate at 1.7 nm ($J_{1.7}$) (Fig. 1b) and particle size distribution (Fig. 1c). The bottom panel shows HNO_3 and H_2SO_4 vapour concentrations (Fig. 1d). We switched on the ultraviolet (UV) lights at $t = 0$ min to oxidize SO_2 with OH radicals and form H_2SO_4. Sulfuric acid started to appear shortly thereafter and built up to a steady state of 2.3×10^6 cm^{-3} over the wall-loss timescale of about 10 min. Under these conditions, the data show a modest formation rate of 1.7-nm particles from H_2SO_4–NH_3 nucleation, consistent with previous CLOUD measurements[8]. These particles grew only slowly (about 0.5 nm h^{-1} at this H_2SO_4 and particle size[17]). No particles reached 2.5 nm within 2 h, owing to their slow growth rate and low survival probability against wall loss.

At $t = 115$ min, we raised the nitric acid concentration to 2.0×10^9 cm^{-3}, through direct injection instead of photochemical production, so that we could independently control the nitric acid and sulfuric acid concentrations. The particle number increased 30-fold and 1,300-fold for particles larger than 1.7 nm and 2.5 nm, respectively. In addition, these newly formed particles grew much more rapidly (40 nm h^{-1}), reaching 20 nm within 30 min. This experiment shows that nitric acid can substantially enhance particle formation and growth rates for fixed levels of sulfuric acid and ammonia.

We also conducted model calculations on the basis of known thermodynamics and microphysics (Methods). Our model results (dashed traces in Fig. 1a) consistently and quantitatively confirm the experimental data: sulfuric acid and ammonia nucleation produces only 1.7-nm particles, whereas addition of nitric acid strongly enhances the formation rates of both 1.7-nm and 2.5-nm particles.

We conducted two further experiments under conditions similar to Fig. 1 but holding the concentrations of a different pair of vapours constant while varying the third. For the experiment shown in Extended Data Fig. 1, we started by oxidizing NO_2 to produce 1.6×10^9 cm^{-3} HNO_3 in the presence of about 6.5×10^8 cm^{-3} NH_3 and then increased H_2SO_4 from 0 to 4.9×10^6 cm^{-3} by oxidizing progressively more injected SO_2. For the experiment shown in Extended Data Fig. 2, we first established 4.6×10^6 cm^{-3} H_2SO_4 and 4.0×10^9 cm^{-3} HNO_3, and then increased NH_3 from 0 to about 6.5×10^8 cm^{-3}. We consistently observed relatively slow nucleation when only two of the three vapours are present, whereas addition of the third vapour increased nucleation rates by several orders of magnitude.

Figure 2 shows particle formation rates measured by CLOUD at 1.7-nm mobility diameter ($J_{1.7}$) versus ammonia concentration, at 223 K. The $J_{1.7}$ data were all measured in the presence of ions from galactic cosmic rays (GCR) and − so − represent the sum of neutral and ion-induced channels. The black diamond shows the measured $J_{1.7}$ of 0.3 cm^{-3} s^{-1} for HNO_3–NH_3 nucleation with 1.5×10^9 cm^{-3} nitric acid, about 6.5×10^8 cm^{-3} ammonia and sulfuric acid below the detection limit of 5×10^4 cm^{-3} (this is the event shown in Extended Data Fig. 1). At this same ammonia concentration, we measured $J_{1.7} = 6.1$ cm^{-3} s^{-1} at 2.3×10^6 cm^{-3} H_2SO_4, demonstrating the much faster rate of H_2SO_4–NH_3 nucleation (not shown). This measurement is consistent with models on the basis of previous CLOUD studies of H_2SO_4–NH_3 nucleation[18,19], as illustrated by the model simulations for 4.0×10^6 cm^{-3} sulfuric acid (red solid curve). The blue circles show our measurements of $J_{1.7}$ for HNO_3–H_2SO_4–NH_3 nucleation at 4.0×10^6 cm^{-3} sulfuric acid and $(1.6–6.5) \times 10^8$ cm^{-3} ammonia, in the presence of 1.5×10^9 cm^{-3} nitric acid (the event shown in Extended Data Fig. 2). The blue dashed curve is a power law fit to the measurements, indicating a strong sensitivity to ammonia concentration ($J_{1.7} = k[NH_3]^{3.7}$).

The vertical grey dotted line in Fig. 2 separates ammonia concentrations measured in different regions in the upper troposphere[5]; Asian monsoon conditions are to the right of this vertical line. Our results indicate that H_2SO_4–NH_3 nucleation is probably responsible for new particle formation in regions with ammonia concentrations below around 10^8 cm^{-3} (12 pptv), but that HNO_3–H_2SO_4–NH_3 nucleation probably dominates at higher ammonia levels in the Asian monsoon upper troposphere. Our nucleation rate measurements confirm that the stronger sulfuric acid is favoured by ammonia in the ammonia-limited regime, so nitric acid will evaporate from the clusters, as it may be displaced by

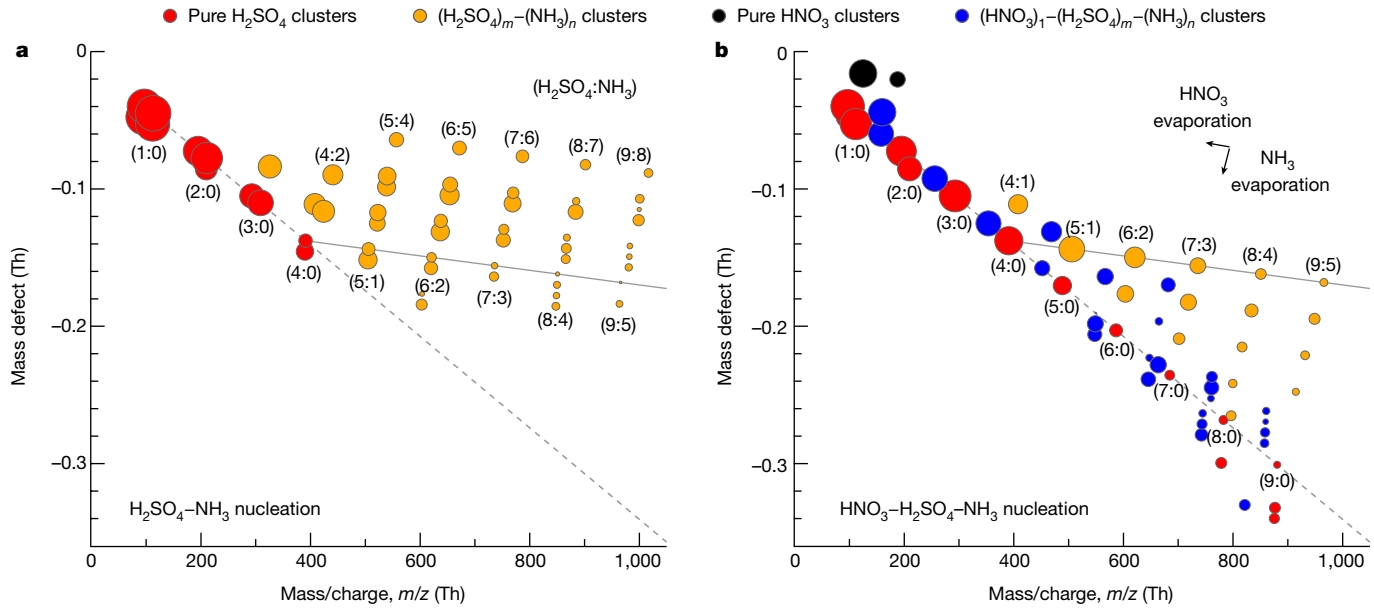

Fig. 3 | Molecular composition of negatively charged clusters during H_2SO_4–NH_3 and HNO_3–H_2SO_4–NH_3 nucleation events at 223 K and 25% relative humidity. Mass defect (difference from integer mass) versus mass/charge (m/z) of negatively charged clusters measured with an APi-TOF mass spectrometer for 1.7×10^6 cm^{-3} sulfuric acid and 6.5×10^8 cm^{-3} ammonia (**a**) and 2.0×10^7 cm^{-3} sulfuric acid, 3.2×10^9 cm^{-3} nitric acid and 7.9×10^9 cm^{-3} ammonia (**b**). The symbol colours indicate the molecular composition as shown. The symbol area is proportional to the logarithm of signal rate (counts per second). The labels (m:n) near the symbols indicate the number of sulfuric acid $(H_2SO_4)_m$ and ammonia $(NH_3)_n$ molecules in the clusters, including both neutral and charged species. The grey dashed lines follow clusters that contain pure H_2SO_4 molecules with an HSO_4^- ion (or SO_4 instead of H_2SO_4 and/or SO_4^- instead of HSO_4^- for pure H_2SO_4 clusters falling below this line in **b**). The grey solid lines follow the 1:1 H_2SO_4–NH_3 addition starting at $(H_2SO_4)_4$–$(NH_3)_0$. Nearly all clusters in panel **a** lie above this line, whereas nearly all clusters in panel **b** fall below it. Most clusters containing HNO_3 lack NH_3 by the time they are measured (they fall near the (m:0) grey dashed line), but the marked difference between **a** and **b** indicates that the nucleating clusters had distinctly different compositions, probably including relatively weakly bound HNO_3–NH_3 pairs in **b**. It is probable that nucleating clusters in the CLOUD chamber at 223 K contain HNO_3–H_2SO_4–NH_3 with a roughly 1:1 acid–base ratio. However, during the transmission from the chamber to the warm APi-TOF mass spectrometer at 293 K, the clusters lose HNO_3 and NH_3, leaving a less volatile core of H_2SO_4 with depleted NH_3. The evaporation of a single NH_3 or HNO_3 molecule from a cluster displaces it on the mass defect plot by a vector distance indicated by the black arrows in **b**.

sulfuric acid. However, as ammonia increases from 1.6 to 6.5×10^8 cm^{-3}, we observe sharp increases in $J_{1.7}$ for HNO_3–H_2SO_4–NH_3 nucleation from 10 to 400 cm^{-3} s^{-1} and in the ratio of particle formation rates (HNO_3–H_2SO_4–NH_3:H_2SO_4–NH_3) from 4 to 30. Our nucleation model (as in Fig. 1) yields slightly higher $J_{1.7}$ than that observed, as shown in Extended Data Fig. 3, but the formation rate variation with ammonia, nonetheless, shows a similar slope.

CLOUD has previously shown that ions enhance nucleation for all but the strongest acid–base clusters; HNO_3–H_2SO_4–NH_3 is probably not an exception. However, the ion enhancement is limited by the GCR ion-pair production rate. We show with the horizontal grey solid lines in Fig. 2 the upper limits on $J_{1.7}$ for ion-induced nucleation of about 2 cm^{-3} s^{-1} at ground level and 35 cm^{-3} s^{-1} in the upper troposphere. Our experimental nucleation rates for HNO_3–H_2SO_4–NH_3 are mostly above upper tropospheric GCR ion production rates. This is confirmed by similar $J_{1.7}$ measured during a neutral nucleation experiment, in which an electric field was used to rapidly sweep ions from the chamber. Thus, for this nucleation scheme, the neutral channel will often prevail over the ion-induced channel in the Asian monsoon upper troposphere. However, when ammonia is diluted away outside the Asian monsoon anticyclone, ions may enhance the nucleation rate up to the GCR limit near 35 cm^{-3} s^{-1}.

In a formal sense, the new-particle-formation mechanism could be one of two types: formation of stable H_2SO_4–NH_3 clusters, followed by nano-Köhler-type activation by nitric acid and ammonia[16]; or else true synergistic nucleation of nitric acid, sulfuric acid and ammonia[9]. In a practical sense, it makes little difference because coagulation loss is a major sink for all small clusters in the atmosphere[20], so appearance of 1.7-nm particles by means of any mechanism constitutes new particle formation. Regardless, we can distinguish between these two possibilities from our measurements of the molecular composition of negatively charged clusters using an atmospheric pressure interface time-of-flight (APi-TOF) mass spectrometer. In Fig. 3, we show cluster mass defect plots during H_2SO_4–NH_3 and HNO_3–H_2SO_4–NH_3 nucleation events at 223 K. The marked difference between Fig. 3a, b indicates that nitric acid changes the composition of the nucleating clusters down to the smallest sizes; thus, the mechanism is almost certainly synergistic HNO_3–H_2SO_4–NH_3 nucleation.

In Fig. 3a, the predominant ions are one of several deprotonated sulfuric acid species, including HSO_4^-, SO_4^-, HSO_5^-, SO_5^- and so on, resulting in a group of points for clusters with similar molecular composition but different mass and mass defect. In the figure, we use the labels (m:n) to indicate the number of sulfuric acid and ammonia molecules in the $(H_2SO_4)_m$–$(NH_3)_n$ clusters, including both neutral and charged species. The mass defect plot closely resembles those previously measured for H_2SO_4–NH_3 nucleation[21]. Negative-ion-induced nucleation proceeds with the known acid–base stabilization mechanism, in which sulfuric acid dimers form as a first step (with HSO_4^- serving as a conjugate base for the first H_2SO_4) and then clusters subsequently grow by 1:1 H_2SO_4–NH_3 addition (that is, as ammonium bisulfate)[9]. We use a grey line to illustrate the 1:1 addition path, beginning at $(H_2SO_4)_4$–$(NH_3)_0$. Clusters larger than the sulfuric acid tetramers mostly contain several ammonia molecules and, so nearly all clusters in Fig. 3a lie above the grey line.

Figure 3b shows a pronounced change in the cluster APi-TOF signal during HNO_3–H_2SO_4–NH_3 nucleation. In addition to pure $(H_2SO_4)_m$–$(NH_3)_n$ clusters, we observe clusters with one extra HNO_3 molecule (or NO_3^- ion), that is, $(HNO_3)_1$–$(H_2SO_4)_m$–$(NH_3)_n$, and the pure nitric acid

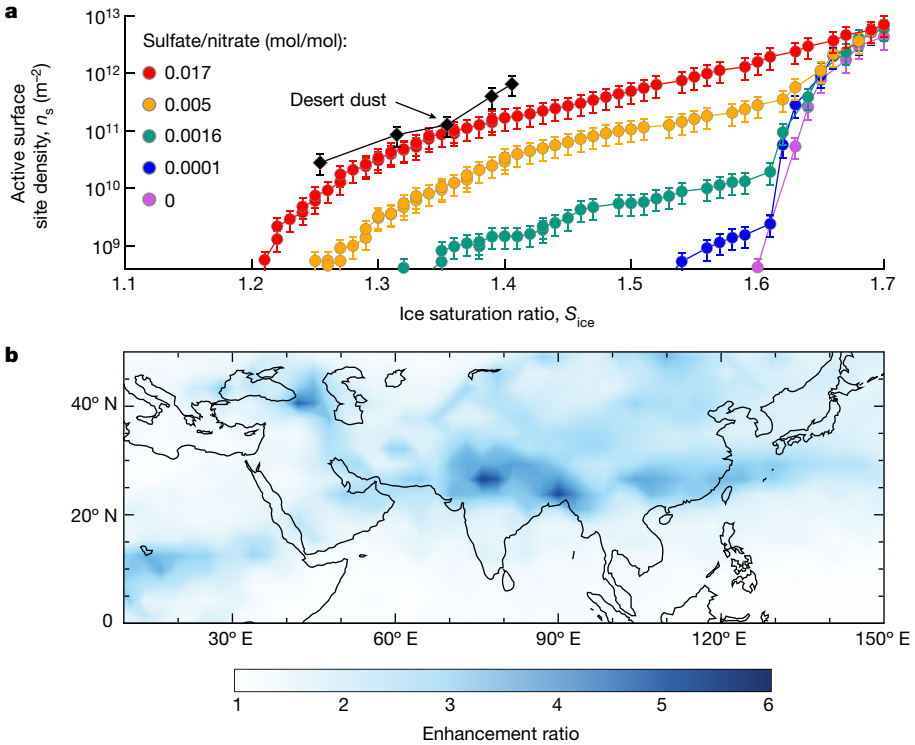

Fig. 4 | Ice nucleation properties and modelled regional contribution of upper tropospheric particles formed from HNO_3–H_2SO_4–NH_3 nucleation. **a**, Active surface site density versus ice saturation ratio, measured by the mINKA instrument at CLOUD, at 233 K and 25% relative humidity. Pure ammonium nitrate particles (purple points) show homogeneous freezing. However, addition of only small amounts of sulfate creates highly ice-nucleation-active particles. At around 1.7% sulfate fraction (red points), the ice nucleating efficiency is comparable with desert dust particles[24]. **b**, Simulation of particle formation in a global model (EMAC) with efficient vertical transport of ammonia into the upper troposphere during the Asian monsoon. Including multi-acid HNO_3–H_2SO_4–NH_3 nucleation (on the basis of the blue dashed curve in Fig. 2) enhances particle number concentrations (nucleation mode) over the Asian monsoon region by a factor of 3–5 compared with the same model with only H_2SO_4–NH_3 nucleation (from Dunne et al.[8], similar to the red solid curve in Fig. 2).

monomer and dimer. In sharp contrast with Fig. 3a, all these clusters are deficient in NH_3, falling below the same grey line as in Fig. 3a. The most deficient contain up to nine bare acids, that is, $(H_2SO_4)_9$ or $(H_2SO_4)_8$–$(HNO_3)_1$. Figure 3b almost certainly does not represent the true cluster composition in the chamber because binary nucleation of H_2SO_4 does not proceed under these exact conditions of H_2SO_4, NH_3, temperature and relative humidity (as demonstrated by Fig. 3a). We can interpret Fig. 3b as follows. It is probable that clusters in the CLOUD chamber (223 K) contain HNO_3–H_2SO_4–NH_3 with a roughly 1:1 acid–base ratio, representing partial neutralization. However, during the transmission from the cold chamber to the warm APi-TOF mass spectrometer (about 293 K), the clusters lose relatively weakly bound HNO_3 and NH_3 molecules but not the lower-volatility H_2SO_4 molecules. Regardless of the interpretation, however, the notable difference between Fig. 3a, b indicates that the sampled clusters had very different compositions and that nitric acid participated in the formation of clusters as small as a few molecules.

Ice nucleation measurements

Nitric acid and ammonia not only enhance the formation rate of new particles but also drive their rapid growth to sizes at which they may act as CCN or ice nucleating particles (INP), above around 50 nm. To assess their effect on cirrus clouds, we measured the ice nucleation ability of particles formed from HNO_3–H_2SO_4–NH_3 nucleation in the CLOUD chamber. Simulating 'hotspot' conditions, we first formed pure ammonium nitrate particles by means of HNO_3–NH_3 nucleation and then increased the H_2SO_4 fraction in the particles by oxidizing progressively more SO_2. We measured their ice nucleation ability using the online continuous flow diffusion instrument, mINKA (Methods and Extended Data Fig. 4). As shown in Fig. 4a, pure ammonium nitrate particles (purple data points) nucleate ice only at high ice saturation ratios (S_{ice}), characteristic of homogeneous nucleation (shown by a steep increase of ice activation above S_{ice} = 1.60 at 215 K). This indicates that pure ammonium nitrate particles, formed by means of HNO_3–NH_3 nucleation, are probably in a liquid state initially, albeit at a relative humidity below the deliquescence point[22]. However, addition of sulfate, with a particulate sulfate-to-nitrate molar ratio as small as 10^{-4}, triggers crystallization of ammonium nitrate. For these particles, we observed a small heterogeneous ice nucleation mode at S_{ice} of 1.54 (blue data points), with other conditions and the particle size distribution held almost constant. Moreover, as the sulfate molar fraction progressively rises to just 0.017 (still almost pure but now solid ammonium nitrate), an active surface site density (n_s) of 10^{10} m^{-2} is reached at S_{ice} as low as 1.26. This is consistent with previous findings, in which particles were generated through nebulization, with a much larger particle diameter and a much higher sulfate-to-nitrate ratio[23]. Our measurements show that HNO_3–H_2SO_4–NH_3 nucleation followed by rapid growth from nitric acid and ammonia condensation — which results in low sulfate-to-nitrate ratio — could provide an important source of INP that are comparable with typical desert dust particles at nucleating ice[24].

Atmospheric implications

Our findings suggest that HNO_3–H_2SO_4–NH_3 nucleation may dominate new particle formation in the Asian monsoon region of the upper troposphere, with a 'flame' of new particles in the outflow of convective

clouds, in which up to 10^{10} cm^{-3} ammonia[6] mixes with low (background) levels of sulfuric acid and nitric acid. Without this mechanism, particle formation through the traditional ternary H_2SO_4–NH_3 nucleation would be much slower and most probably rate-limited by the scarce sulfuric acid. Furthermore, by co-condensing with nitric acid, the convected ammonia also drives the growth of the newly formed particles. Given typical acid-excess conditions in the upper troposphere, condensational growth is governed by the availability of ammonia. Consequently, particles will steadily (and rapidly) grow until ammonia is depleted after several *e*-folding times set by the particle condensation sink. On the basis of condensation sinks generally observed in the tropical upper troposphere[4], this timescale will be several hours. Within this time interval, given the observed ammonia levels, newly formed particles will be able to grow to CCN sizes and even small admixtures of sulfuric acid will render these particles efficient INP.

Our laboratory measurements provide a mechanism that can account for recent observations of abundant ammonium nitrate particles in the Asian monsoon upper troposphere[6]. To evaluate its importance on a global scale, we first parameterized our experimentally measured $J_{1.7}$ for HNO_3–H_2SO_4–NH_3 nucleation as a function of sulfuric acid, nitric acid and ammonia concentrations (Methods). The parameterization is obtained using a power-law dependency for each vapour (Extended Data Fig. 5), given that the critical cluster composition is associated with the exponents according to the first nucleation theorem[25]. Then we implemented this parameterization in a global aerosol model (EMAC, see Methods for modelling details). The EMAC model predicts that HNO_3–H_2SO_4–NH_3 nucleation at 250 hPa (11 km, approximately 223 K) produces an annual average exceeding 1,000 cm^{-3} new particles over an extensive area (Extended Data Fig. 6). This corresponds to an increase in particle number concentration (Fig. 4b) up to a factor of five higher than in a control simulation with only ternary H_2SO_4–NH_3 nucleation[8]. The strongest increase occurs mostly over Asia, in which ammonia is ample because of deep convection from ground sources.

However, another global model (TOMCAT, see Methods) shows much lower ammonia mixing ratios in the upper troposphere than EMAC (<1 pptv compared with <100 pptv, respectively), although with a broadly similar spatial distribution (Extended Data Fig. 7a, b). This large variability of upper tropospheric ammonia is also indicated by recent field measurements on local[6,26] and global[5,27] scales. In view of its importance for both H_2SO_4–NH_3 and HNO_3–H_2SO_4–NH_3 nucleation, there is an urgent need to improve upper tropospheric measurements of ammonia, as well as improve knowledge of its sources, transport and sinks.

We thus turned to a cloud-resolving model to estimate the ammonia vapour fraction remaining after deep convection (see Methods). We show in Extended Data Fig. 8 that around 10% of the boundary layer ammonia can be transported into the upper troposphere and released as vapour by a base-case convective cloud. The sensitivity tests further illustrate that the key factor governing the fraction of ammonia remaining in the cloud outflow is the retention of ammonia molecules by ice particles (Extended Data Fig. 8e), whereas cloud water pH (Extended Data Fig. 8c) and cloud water content (Extended Data Fig. 8d) only play minor roles once glaciation occurs. Given that more than 10 ppbv of ammonia is often observed in the Asian boundary layer[28], it is plausible that the observed 1.4 ppbv (10^{10} cm^{-3}) ammonia in the upper troposphere[6] is indeed efficiently transported by the convective systems.

Although the ammonium–nitrate–sulfate particles are formed locally, they can travel from Asia to North America in just three days by means of the subtropical jet stream, as the typical residence time of Aitken mode particles ranges from one week to one month in the upper troposphere[29]. As a result, these particles can persist as an intercontinental band, covering more than half of the mid-latitude surface area of the Northern Hemisphere (Extended Data Fig. 6). In summary, synergistic nucleation of nitric acid, sulfuric acid and ammonia could provide an important source of new CCN and ice nuclei in the upper troposphere, especially over the Asian monsoon region, and is closely linked with anthropogenic ammonia emissions[27].

Online content

Any methods, additional references, Nature Research reporting summaries, source data, extended data, supplementary information, acknowledgements, peer review information; details of author contributions and competing interests; and statements of data and code availability are available at https://doi.org/10.1038/s41586-022-04605-4.

1. Clarke, A. et al. Nucleation in the equatorial free troposphere: favorable environments during PEM-Tropics. *J. Geophys. Res. Atmos.* **104**, 5735–5744 (1999).
2. Weigel, R. et al. In situ observations of new particle formation in the tropical upper troposphere: the role of clouds and the nucleation mechanism. *Atmos. Chem. Phys.* **11**, 9983–10010 (2011).
3. Gordon, H. et al. Causes and importance of new particle formation in the present-day and pre-industrial atmospheres. *J. Geophys. Res. Atmos.* **122**, 8739–8760 (2017).
4. Williamson, C. J. et al. A large source of cloud condensation nuclei from new particle formation in the tropics. *Nature* **574**, 399–403 (2019).
5. Höpfner, M. et al. First detection of ammonia (NH_3) in the Asian summer monsoon upper troposphere. *Atmos. Chem. Phys.* **16**, 14357–14369 (2016).
6. Höpfner, M. et al. Ammonium nitrate particles formed in upper troposphere from ground ammonia sources during Asian monsoons. *Nat. Geosci.* **12**, 608–612 (2019).
7. Intergovernmental Panel on Climate Change. *Climate Change 2013: The Physical Science Basis* (Cambridge Univ. Press, 2013).
8. Dunne, E. M. et al. Global atmospheric particle formation from CERN CLOUD measurements. *Science* **354**, 1119–1124 (2016).
9. Kirkby, J. et al. Role of sulphuric acid, ammonia and galactic cosmic rays in atmospheric aerosol nucleation. *Nature* **476**, 429–433 (2011).
10. Andreae, M. O. et al. Aerosol characteristics and particle production in the upper troposphere over the Amazon Basin. *Atmos. Chem. Phys.* **18**, 921–961 (2018).
11. Lehtipalo, K. et al. Multicomponent new particle formation from sulfuric acid, ammonia, and biogenic vapors. *Sci. Adv.* **4**, eaau5363 (2018).
12. Zhao, B. et al. High concentration of ultrafine particles in the Amazon free troposphere produced by organic new particle formation. *Proc. Natl Acad. Sci.* **117**, 25344–25351 (2020).
13. Ge, C., Zhu, C., Francisco, J. S., Zeng, X. C. & Wang, J. A molecular perspective for global modeling of upper atmospheric NH_3 from freezing clouds. *Proc. Natl Acad. Sci.* **115**, 6147–6152 (2018).
14. Martin, R. V. et al. Space-based constraints on the production of nitric oxide by lightning. *J. Geophys. Res. Atmos.* **112**, D09309 (2007).
15. Lelieveld, J. et al. The South Asian monsoon—pollution pump and purifier. *Science* **361**, 270–273 (2018).
16. Wang, M. et al. Rapid growth of atmospheric nanoparticles by nitric acid and ammonia condensation. *Nature* **580**, 184–189 (2020).
17. Stolzenburg, D. et al. Enhanced growth rate of atmospheric particles from sulfuric acid. *Atmos. Chem. Phys.* **20**, 7359–7372 (2020).
18. Kürten, A. New particle formation from sulfuric acid and ammonia: nucleation and growth model based on thermodynamics derived from CLOUD measurements for a wide range of conditions. *Atmos. Chem. Phys.* **19**, 5033–5050 (2019).
19. Xiao, M. et al. The driving factors of new particle formation and growth in the polluted boundary layer. *Atmos. Chem. Phys.* **21**, 14275–14291 (2021).
20. Ehrhart, S. & Curtius, J. Influence of aerosol lifetime on the interpretation of nucleation experiments with respect to the first nucleation theorem. *Atmos. Chem. Phys.* **13**, 11465–11471 (2013).
21. Schobesberger, S. et al. Molecular understanding of atmospheric particle formation from sulfuric acid and large oxidized organic molecules. *Proc. Natl Acad. Sci.* **110**, 17223–17228 (2013).
22. Martin, S. T. Phase transitions of aqueous atmospheric particles. *Chem. Rev.* **100**, 3403–3454 (2000).
23. Wagner, R. et al. Solid ammonium nitrate aerosols as efficient ice nucleating particles at cirrus temperatures. *J. Geophys. Res. Atmos.* **125**, e2019JD032248 (2020).
24. Ullrich, R. et al. A new ice nucleation active site parameterization for desert dust and soot. *J. Atmos. Sci.* **74**, 699–717 (2017).
25. Oxtoby, D. W. & Kashchiev, D. A general relation between the nucleation work and the size of the nucleus in multicomponent nucleation. *J. Chem. Phys.* **100**, 7665–7671 (1994).
26. Kille, N. et al. The CU mobile solar occultation flux instrument: structure functions and emission rates of NH_3, NO_2 and C_2H_6. *Atmos. Meas. Tech.* **10**, 373–392 (2017).
27. Nault, B. A. et al. Chemical transport models often underestimate inorganic aerosol acidity in remote regions of the atmosphere. *Commun. Earth Environ.* **2**, 93 (2021).
28. Warner, J. X., Wei, Z., Strow, L. L., Dickerson, R. R. & Nowak, J. B. The global tropospheric ammonia distribution as seen in the 13-year AIRS measurement record. *Atmos. Chem. Phys.* **16**, 5467–5479 (2016).
29. Williams, J., Reus, M. D., Krejci, R., Fischer, H. & Ström, J. Application of the variability-size relationship to atmospheric aerosol studies: estimating aerosol lifetimes and ages. *Atmos. Chem. Phys.* **2**, 133–145 (2002).

[1]Center for Atmospheric Particle Studies, Carnegie Mellon University, Pittsburgh, PA, USA. [2]Department of Chemistry, Carnegie Mellon University, Pittsburgh, PA, USA. [3]Laboratory of Atmospheric Chemistry, Paul Scherrer Institute, Villigen, Switzerland. [4]Institute of Meteorology and Climate Research, Karlsruhe Institute of Technology, Karlsruhe, Germany. [5]Institute for Atmospheric and Environmental Sciences, Goethe University Frankfurt, Frankfurt am Main, Germany. [6]Institute for Atmospheric and Earth System Research (INAR), University of Helsinki, Helsinki, Finland. [7]Present address: Division of Chemistry and Chemical Engineering, California Institute of Technology, Pasadena, CA, USA. [8]Department of Meteorology, Stockholm University, Stockholm, Sweden. [9]Bolin Centre for Climate Research, Stockholm University, Stockholm, Sweden. [10]Institute for Ion Physics and Applied Physics, University of Innsbruck, Innsbruck, Austria. [11]Department of Chemical Engineering, Carnegie Mellon University, Pittsburgh, PA, USA. [12]CERN, the European Organization for Nuclear Research, Geneva, Switzerland. [13]CENTRA and Faculdade de Ciências da Universidade de Lisboa, Campo Grande, Lisbon, Portugal. [14]Leibniz Institute for Tropospheric Research, Leipzig, Germany. [15]Helsinki Institute of Physics, University of Helsinki, Helsinki, Finland. [16]Department of Chemistry & CIRES, University of Colorado Boulder, Boulder, CO, USA. [17]Faculty of Physics, University of Vienna, Vienna, Austria. [18]Department of Applied Physics, University of Eastern Finland, Kuopio, Finland. [19]Aerodyne Research, Inc., Billerica, MA, USA. [20]Finnish Meteorological Institute, Helsinki, Finland. [21]Atmospheric and Oceanic Sciences, Princeton University, Princeton, NJ, USA. [22]P. N. Lebedev Physical Institute of the Russian Academy of Sciences, Moscow, Russia. [23]Moscow Institute of Physics and Technology (National Research University), Moscow, Russia. [24]Department of Physics, University of Genoa & INFN, Genoa, Italy. [25]Department of Atmospheric and Oceanic Sciences, University of Colorado Boulder, Boulder, CO, USA. [26]Atmospheric Chemistry Department, Max Planck Institute for Chemistry, Mainz, Germany. [27]School of Earth and Environment, University of Leeds, Leeds, UK. [28]Institute Infante Dom Luíz, University of Beira Interior, Covilhã, Portugal. [29]Ionicon Analytik Ges.m.b.H., Innsbruck, Austria. [30]Joint International Research Laboratory of Atmospheric and Earth System Sciences, Nanjing University, Nanjing, China. [31]Aerosol and Haze Laboratory, Beijing Advanced Innovation Center for Soft Matter Science and Engineering, Beijing University of Chemical Technology, Beijing, China. [32]Department of Environmental Science (ACES), Stockholm University, Stockholm, Sweden. [33]Climate and Atmosphere Research Center, The Cyprus Institute, Nicosia, Cyprus. [34]Department of Engineering and Public Policy, Carnegie Mellon University, Pittsburgh, PA, USA. ✉e-mail: nmd@andrew.cmu.edu

Methods

The CLOUD facility

We conducted our measurements at the CERN CLOUD facility, a 26.1-m^3, electropolished, stainless-steel CLOUD chamber that allows new-particle-formation experiments under the full range of tropospheric conditions with scrupulous cleanliness and minimal contamination[9,30]. The CLOUD chamber is mounted in a thermal housing, capable of keeping the temperature constant in the range 208 K and 373 K with a precision of ±0.1 K (ref. [31]). Photochemical processes are initiated by homogeneous illumination with a built-in UV fibre-optic system, including four 200-W Hamamatsu Hg-Xe lamps at wavelengths between 250 and 450 nm and a 4-W KrF excimer UV laser at 248 nm with adjustable power. New particle formation under different ionization levels is simulated with and without the electric fields (±30 kV), which can artificially scavenge or preserve small ions produced from ground-level GCR. Uniform spatial mixing is achieved with magnetically coupled stainless-steel fans mounted at the top and bottom of the chamber. The characteristic gas mixing time in the chamber during experiments is a few minutes. The loss rate of condensable vapours and particles onto the chamber walls is comparable with the ambient condensation sink. To avoid contamination, the chamber is periodically cleaned by rinsing the walls with ultra-pure water and heating to 373 K for at least 24 h, ensuring extremely low contaminant levels of sulfuric acid $<5 \times 10^4$ cm^{-3} and total organics <50 pptv (refs. [32,33]). The CLOUD gas system is also built to the highest technical standards of cleanliness and performance. The dry air supply for the chamber is provided by boil-off oxygen (Messer, 99.999%) and boil-off nitrogen (Messer, 99.999%) mixed at the atmospheric ratio of 79:21. Highly pure water vapour, ozone and other trace gases such as nitric acid and ammonia can be precisely added at the pptv level from ultra-pure sources.

Instrumentation

Gas-phase sulfuric acid was measured using a nitrate chemical ionization APi-TOF (nitrate-CI-APi-TOF) mass spectrometer[34,35] and an iodide chemical ionization time-of-flight mass spectrometer equipped with a Filter Inlet for Gases and Aerosols (I-FIGAERO-CIMS)[36,37]. The nitrate-CI-APi-TOF mass spectrometer is equipped with an electrostatic filter in front of the inlet to remove ions and charged clusters formed in the chamber. A corona charger is used to ionize the reagent nitric acid vapour in a nitrogen flow[38]. Nitrate ions are then guided in an atmospheric pressure drift tube by an electric field to react with the analyte molecules in the sample flow. Sulfuric acid is quantified for the nitrate-CI-APi-TOF with a detection limit of about 5×10^4 cm^{-3}, following the same calibration and loss correction procedures described previously[9,32,39]. FIGAERO is a manifold inlet for a CIMS with two operating modes. In the sampling mode, a coaxial core sampling is used to minimize the vapour wall loss in the sampling line. The total flow is maintained at 18.0 slpm and the core flow at 4.5 slpm; the CIMS samples at the centre of the core flow with a flow rate of 1.6 slpm. Analyte molecules are introduced into a 150-mbar ion-molecule reactor, chemically ionized by iodide ions that are formed in a Po-210 radioactive source and extracted into the mass spectrometer. The sulfuric acid calibration coefficient for the I-FIGAERO-CIMS is derived using the absolute sulfuric acid concentrations measured with the pre-calibrated nitrate-CI-APi-TOF.

Gas-phase nitric acid was also measured using the I-FIGAERO-CIMS. Nitric acid concentration was quantified by measuring HNO_3/N_2 mixtures with known nitric acid concentrations, following similar procedures described previously[16]. The HNO_3/N_2 mixture was sourced from flowing 2 slpm ultra-pure nitrogen through a portable nitric acid permeation tube, at constant 40 °C. The permeation rate of nitric acid was determined by passing the outflow of the permeation tube through an impinger containing deionized water and analysing the resulting nitric acid solution through spectrophotometry.

Gas-phase ammonia was either measured or calculated. We measured ammonia using a proton transfer reaction time-of-flight mass spectrometer (PTR3-TOF-MS, or PTR3 for short)[40]. As a carrier gas for the primary ions, we used argon (ultra-high purity 5.0) to ensure that ammonium ions could not be artificially formed in the region of the corona discharge. Although the theoretical detection limit from peak height and width would be even smaller, the lowest concentration we were able to measure during the first fully ammonia-free runs of the beginning of the campaign was 10^9 cm^{-3}. An explanation for this is that, when concentrations of ammonia are low, effects of wall interaction of the highly soluble ammonia become important and the decay of ammonia in the inlet line becomes very slow. To reduce inlet wall contacts, we used a core-sampling technique directly in front of the instrument to sample only the centre 2 slpm of the 10 slpm inlet flow, but owing to frequent necessary on-site calibrations of volatile organic compounds, a Teflon ball valve was placed within the sample line that probably influenced measurements during times of low ammonia concentrations. At concentrations above about 2×10^9 cm^{-3} ammonia, however, the response of the instrument was very fast, so that, for example, changes in the chamber ammonia flow rate were easily detectable. Off-site calibrations showed a humidity-independent calibration factor of 0.0017 ncps/ppb. Calibrated data from the PTR3 agree very well with the Picarro above 10^{10} cm^{-3} (detection limit of the Picarro). The PTR3 also provides information about the overall cleanliness of the volatile organic compounds in the chamber. The technique was extensively described previously[40].

For ammonia concentrations below 10^9 cm^{-3}, we calculated concentration using the calibrated ammonia injection flow and an estimated first-order wall-loss rate. The wall-loss rate (k_{wall}) for ammonia inside the CLOUD chamber is confirmed to be faster than for sulfuric acid[41], and can be determined from the following expression[42]:

$$k_{wall} = \frac{A}{V}\frac{2}{\pi}\sqrt{k_e D_i} = C_{wall}\sqrt{D_i} \quad (1)$$

in which A/V is the surface-to-volume ratio of the chamber, k_e is the eddy diffusion constant (determined by the turbulent mixing intensity, not the transport properties of the gases) and D_i is the diffusion coefficient for each gas. C_{wall} is thus referred to as an empirical parameter of experiment conditions in the chamber. Here we first determine the k_{wall} for sulfuric acid and nitric acid to be 1.7×10^{-3} and 1.9×10^{-3} s^{-3}, respectively, by measuring their passive decay rates and subtracting the loss rate of chamber dilution for both (1.2×10^{-3} s^{-1}), as well as the loss rate of dimer formation for sulfuric acid (around 1.6×10^{-3} s^{-1} for 5×10^6 cm^{-3} H_2SO_4). The k_{wall} for sulfuric acid agrees with our measurements from previous campaigns[43]. We then derive the C_{wall} for sulfuric acid and nitric acid both to be 2.0×10^{-4} $torr^{-0.5}$ cm^{-1} $s^{-0.5}$, with $D_{H_2SO_4}$ of 74 torr cm^2 s^{-1} and D_{HNO_3} of 87 torr cm^2 s^{-1} (ref. [44]). Finally, we calculate the k_{wall} for ammonia to be 2.7×10^{-3} s^{-1}, with D_{NH_3} of 176 torr cm^2 s^{-1} (ref. [44]). Ammonia desorption from the chamber surface is a strong function of the temperature and is believed to be negligible at low temperatures[30]. Even after a long time exposure, ammonia desorption should be less than 1.6×10^6 cm^{-3}, according to previous parameterization of ammonia background contamination in the CLOUD chamber[41].

The composition of negatively charged ions and clusters were determined using an APi-TOF mass spectrometer[45]. The APi-TOF mass spectrometer is connected to the CLOUD chamber by means of a 1-inch (21.7-mm inner diameter) sampling probe, with coaxial core sampling to minimize the wall losses in the sampling line. The total sample flow is maintained at 20 slpm and the core sample flow for the APi-TOF mass spectrometer at 0.8 slpm. Because this instrument only measures charged clusters, the measurements were made during GCR conditions. Owing to a large temperature difference between the cold chamber (223 K) and the warm APi-TOF mass spectrometer (around 293 K), HNO_3–H_2SO_4–NH_3 clusters probably lose relatively

weakly bonded HNO_3 and NH_3 molecules. This resembles the chemical ionization process of detecting ammonia with the nitrate-CI-APi-TOF, in which HNO_3 and NH_3 molecules rapidly evaporate from the resulting ammonia nitrate cluster in the CI-APi-TOF vacuum regions[46].

Gas monitors were used to measure ozone (O_3, Thermo Environmental Instruments TEI 49C), sulfur dioxide (SO_2, Thermo Fisher Scientific Inc. 42i-TLE) and nitric oxide (NO, ECO Physics, CLD 780TR). Nitrogen dioxide (NO_2) was measured by a cavity attenuated phase shift nitrogen dioxide monitor (CAPS NO_2, Aerodyne Research Inc.) and a home-made cavity enhanced differential optical absorption spectroscopy (CE-DOAS) instrument. The relative humidity of the chamber was determined by dew point mirrors (EdgeTech).

Particle number concentrations were monitored by condensation particle counters (CPCs), including an Airmodus A11 nano Condensation Nucleus Counter (nCNC), consisting of a particle size magnifier (PSM) and a laminar-flow butanol-based CPC[47], as well as a butanol TSI 3776 CPC. Particle size distributions between 1.8 nm and 500 nm were measured by a nano-scanning electrical mobility spectrometer (nSEMS), a nano-scanning mobility particle sizer (nano-SMPS) and a long-SMPS. The nSEMS used a new, radial opposed migration ion and aerosol classifier (ROMIAC), which is less sensitive to diffusional resolution degradation than the DMAs[48], and a soft X-ray charge conditioner. After leaving the classifier, particles were first activated in a fast-mixing diethylene glycol stage[49] and then counted with a butanol-based CPC. The nSEMS transfer function that was used to invert the data to obtain the particle size distribution was derived using 3D finite element modelling of the flows, electric field and particle trajectories[50,51]. The two commercial mobility particle size spectrometers, nano-SMPS and long-SMPS, have been fully characterized, calibrated and validated in several previous studies[52–54].

Particle-phase chemical composition was quantified using a high-resolution time-of-flight aerosol mass spectrometer (HR-ToF-AMS, Aerodyne Research). The working principles of the HR-ToF-AMS have been explained in detail previously[55,56]. In brief, particles are focused by an aerodynamic lens and flash-vaporized by impact onto a hot surface at 600 °C under a high vacuum. The vapours are then ionized by 70-eV electrons and the ions are detected with a ToF mass spectrometer. Ionization efficiency calibrations were conducted before and after the campaign and the variation is within 30%. The particle collection efficiency was considered constant during the experiments because temperature and relative humidity in the chamber were fixed and the particle composition was dominated by ammonium nitrate.

INP were measured in real time at 215 K, as a function of ice saturation ratio (S_{ice}), by the mobile ice nucleation instrument of the Karlsruhe Institute of Technology (mINKA). mINKA is a continuous flow diffusion chamber with vertical cylindrical geometry[57], on the basis of the design of INKA[58,59]. A detailed description of the continuous flow diffusion chamber working principle is presented elsewhere[57]. Here, predefined scans of the water vapour saturation ratios were performed in the diffusion chamber every 30 min. For each scan, S_{ice} steadily increased from 1.2 to 1.8 while the temperature was kept constant. The errors associated to temperature and S_{ice} inside the diffusion chamber were derived from the uncertainty of the thermocouples attached to the instrument walls (±0.5 K)[59].

Determination of particle formation rate

The particle formation rate, $J_{1.7}$, is determined at 1.7-nm mobility diameter (1.4-nm physical diameter), here using a PSM. At 1.7 nm, a particle is normally considered to be above its critical size and, therefore, thermodynamically stable. $J_{1.7}$ is calculated using the flux of the total concentration of particles growing past a specific diameter (here at 1.7 nm), as well as correction terms accounting for aerosol losses owing to dilution in the chamber, wall losses and coagulation. Details were described previously[47].

Nucleation model

The nucleation model is on the basis of the thermodynamic model for H_2SO_4–NH_3 nucleation described in detail previously[18,19]. It is developed from the general dynamic equations[60], to calculate the production and losses for each cluster/particle size to determine the formation rates of the acid–base clusters. For HNO_3–H_2SO_4–NH_3 nucleation, we simplify the model simulations by extrapolating nano-Köhler-type activation by nitric acid and ammonia to clusters down to sulfuric acid trimers. Eighty size bins, ranging from one ammonium sulfate cluster to 300 nm, are used to capture the evolution of the size and composition of polydisperse particles.

In brief, we calculate the equimolar condensation flux of nitric acid and ammonia on the basis of the supersaturation of gas-phase nitric acid and ammonia over particle-phase ammonium nitrate[39,60]:

$$\Phi_i^v = k_c\,[C_i^v - a_i\,C_i^0] \tag{2}$$

in which Φ_i^v is the net condensation flux of nitric acid or ammonia, with vapour concentration C_i^v and saturation concentration C_i^0. The term a_i is the activity of species i at the condensed-phase surface of the particle and k_c is the condensation sink for vapours resulting from interaction with particles. The saturation concentrations of nitric acid and ammonia are estimated on the basis of the dissociation constant K_p (ref. [60]). When the vapours are unsaturated, particle-phase ammonium nitrate will evaporate to nitric acid and ammonia to reach the equilibrium.

We also include the Kelvin term ($K_{i,p}$) in the simulation to account for the increased activity ($a_i = a'_i\,K_{i,p}$) of a small curved cluster/particle:

$$K_{i,p} = 10^{(d_{K10}/d_p)} \tag{3}$$

in which $K_{i,p}$ scales with a 'Kelvin diameter' (d_{K10}) for decadal change and d_p is the diameter of the small cluster/particle. The Kelvin diameter for ammonium nitrate is estimated to be 5.3 nm by fitting the data from previous CLOUD experiments according to:

$$S = 10^{(d_{K10}/d_{act})} \tag{4}$$

in which S is the saturation ratio, calculated by means of dividing the product of measured concentrations of nitric acid and ammonia by the dissociation constant K_p and d_{act} is the activation diameter, at which the thermodynamic energy barrier for condensation is overcome and particles start to grow rapidly.

Determination of ice nucleation ability

During the experiments, aerosol particles were continuously sampled from the CLOUD chamber into the mINKA ice nucleation instrument, using an actively cooled sampling line for a consistent temperature profile. Particles were then subject to well-controlled ice supersaturated conditions; the ones that nucleated ice were selectively detected and counted by an optical particle counter (custom-modified Climet CI-3100, lower detection limit of about 1 µm) located at the outlet of the instrument. Background ice crystals were quantified before each saturation scan (for 2 min) and subtracted from the total ice number concentration of the corresponding measurement. The fraction of INP (f_{ice}) was calculated as the ratio of ice crystals number concentration to the total number of particles larger than 10 nm in diameter. The ice nucleation active surface site density (n_s)[61] was calculated as the ratio of ice number concentration to the total surface area of particles larger than 10 nm in diameter. The overall uncertainty of n_s is estimated to be ±40% (ref. [24]). Particle number and surface area concentrations were measured by the SMPS described in the 'Instrumentation' section.

In Extended Data Fig. 4, we provide a detailed summary of the measurement data recorded during the 'hotspot condition' experiment shown in Fig. 4a, in which we investigated the heterogeneous crystallization and ice nucleation ability of ammonium nitrate/sulfate particles produced directly from new particle formation. We first formed pure ammonium nitrate particles through nucleation of nitric acid and

ammonia vapours at 223 K and 15–30% relative humidity (over liquid water). When the evolution of the particle size distribution (Extended Data Fig. 4a) levelled off at a median diameter of around 100 nm, we turned on the UV lights and progressively injected SO_2 at 03:33 to gradually increase sulfuric acid concentration (Extended Data Fig. 4b). Consequently, in Extended Data Fig. 4c, aerosol mass spectrometer measurements show that particle composition was dominated by ammonium nitrate over the course of the experiment, whereas sulfate appeared approximately 1 h after the injection of SO_2. Finally, we show ice nucleation measurements in Extended Data Fig. 4d. Each vertical trajectory represents a saturation ratio scan in mINKA, colour-coded by the measured ice active fraction (f_{ice}). In each scan, we use a horizontal black dash to indicate an ice onset threshold corresponding to f_{ice} of 10^{-3}. Circles indicate the corresponding scans shown in Fig. 4a.

When the particulate sulfate-to-nitrate molar ratio is smaller than 0.0001, the ice nucleation threshold is detected at an ice saturation ratio (S_{ice}) of about 1.6, consistent with the homogeneous freezing threshold of aqueous solution droplets[62]. This finding shows that, if particles presented as absolutely pure ammonium nitrate (NH_4NO_3), they would exist as supercooled liquid droplets even at very low relative humidity, consistent with previous studies[22,63]. As the particulate sulfate-to-nitrate molar ratio gradually increases to about 0.017, the ice nucleation onset shifts to a lower S_{ice} of 1.2, caused by heterogeneous ice nucleation on crystalline ammonium nitrate particles[23]. Crystalline salts are known to be efficient INP at low temperatures when their deliquescence occurs at higher relative humidity compared with the humidity range of their heterogeneous ice nucleation activity[64]. The fact that the addition of sulfate can promote the crystallization of ammonium nitrate has already been observed in previous studies with particles nebulized in large sizes (around 1 μm) from bulk solutions of ammonium nitrate/sulfate[6,23,65]. But it is evidenced here for the first time in an in situ particle nucleation and crystallization experiment representative of upper tropospheric conditions.

Particle formation rate parameterization

According to the first nucleation theorem for multicomponent systems[25], we parameterize the particle formation rates ($J_{1.7}$) for the HNO_3–H_2SO_4–NH_3 nucleation scheme with the empirical formula:

$$J_{1.7} = k\,[H_2SO_4]^a\,[HNO_3]^b[NH_3]^c \quad (5)$$

in which vapour concentrations are in units of cm^{-3} and k, a, b and c are free parameters. This method has been validated by previous observations that the particle formation rates ($J_{1.7}$) vary as a product of power-law functions of nucleating vapours. For example, $J_{1.7}$ for ternary sulfuric acid, ammonia (and water) nucleation follows a cubic dependency on sulfuric acid[8] and a linear[8] or quadratic[19] dependency on ammonia; $J_{1.7}$ for multicomponent nucleation of sulfuric acid, biogenic oxidized organics and ammonia follows a quadratic dependency on sulfuric acid, a linear dependency on both organics[66] and ammonia[11]. The prefactor k accounts for effects of external conditions, such as temperature and relative humidity, thus differs in different environments.

To isolate variables, here we fit the power-law exponents for sulfuric acid, nitric acid and ammonia, respectively, to the dataset of experiments in which only the corresponding vapour concentration was varied. The red triangles, blue circles and yellow squares in Extended Data Fig. 5a–c (same experiments in Extended Data Fig. 1, Fig. 1 and Extended Data Fig. 2), respectively, show that $J_{1.7}$ depends on $[H_2SO_4]^3$ for sulfuric acid between 2.6×10^5 and 2.9×10^6 cm^{-3} (or 0.008 and 0.09 pptv), on $[HNO_3]^2$ for nitric acid between 2.3×10^8 and 1.7×10^9 cm^{-3} (or 7 and 52 pptv) and on $[NH_3]^4$ for ammonia between 1.7×10^8 and 4.9×10^8 cm^{-3} (or 5 and 15 pptv). The third power exponent for sulfuric acid is consistent with previously reported parameterizations for ternary H_2SO_4–NH_3 nucleation[8,19]. The fourth power exponent for ammonia, however, is larger than those in ternary[8,19] or multicomponent systems[11], which emphasizes the critical role of ammonia and suggests further bonding between ammonia and nitric acid molecules in the nucleating clusters. Next, we verify the exponents by refitting the product of $[H_2SO_4]^3$, $[HNO_3]^2$ and $[NH_3]^4$ to the full dataset. Extended Data Fig. 5d shows good consistency ($R^2 = 0.9$) of the parameterization among the three experiments, with a slope of 3.4×10^{-71} s^{-1} cm^{24} being the prefactor k:

$$J_{1.7} = 3.4 \times 10^{-71}[H_2SO_4]^3[HNO_3]^2[NH_3]^4 \quad (6)$$

This parameterization is representative of new particle formation in the Asian monsoon upper troposphere because our experimental conditions of 223 K and 25% relative humidity, as well as concentrations of sulfuric acid[67,68] and nitric acid[69,70], are within the upper tropospheric range, with ammonia[5,6] typical of Asian monsoon regions. One caveat, however, is that the cosmic radiation was at the ground level in our chamber, as shown with grey dot-dashed horizontal line in Extended Data Fig. 5d. The ion-pair production rate can be up to ten times higher in the ambient upper troposphere[71], potentially leading to further enhancement of $J_{1.7}$ by ion-induced nucleation, although the neutral channel dominates in our experiments.

Estimated temperature dependence of the particle formation rate

We did not cover the full temperature range in the upper troposphere, instead focusing on 223 K. However, to make the parameterization in the previous section more applicable for model simulations while not overstating the role of this mechanism, we provide some constraints on the temperature dependence of $J_{1.7}$ for HNO_3–H_2SO_4–NH_3 nucleation. Broadly, it is certain that particle formation involving HNO_3 will have a strong temperature dependence, becoming much slower as T increases.

We first present the temperature dependence of $J_{1.7}$ for pure HNO_3–NH_3 nucleation with the expression:

$$J_{1.7} = k(T)f([HNO_3], [NH_3]) \quad (7)$$

in which $k(T)$ is an empirical temperature-dependent rate constant and has the Arrhenius form

$$k(T) = e^{\left(-\frac{1}{T}\frac{E}{R}\right)}, \quad (8)$$

in which T is the absolute temperature (in Kelvin), E is the activation energy and R is the universal gas constant. $f([HNO_3],[NH_3])$ is a function of the ammonia and nitric acid concentrations (including the pre-exponential factor and free-fitting parameters). This expression is then fitted to the dataset in Fig. 3c in our previous study[16], in which $J_{1.7}$ were measured with only nitric acid, ammonia and water vapours added to the chamber, and the temperature was progressively decreased from 258 K to 249 K. Because the ammonia and nitric acid concentrations were kept almost constant during the temperature transition, we treat the $f([HNO_3],[NH_3])$ term as a constant to reduce the degrees of freedom. This expression with its two free parameters leads to a good agreement with the data, $R_2 = 0.96$. And the fitted $-E/R$ and $f([HNO_3],[NH_3])$ are 14,000 K and 3.2×10^{-26}, respectively.

Next, we apply the same $k(T)$ term to the HNO_3–H_2SO_4–NH_3 parameterization (equation (9)), assuming that the multicomponent nucleation follows a similar temperature dependence:

$$J_{1.7} = 2.9 \times 10^{-98} e^{\left(\frac{14{,}000}{T}\right)}[H_2SO_4]^3[HNO_3]^2[NH_3]^4 \quad (9)$$

Although this temperature-dependent parameterization may not be the final description of this process, it tracks the trend of $J_{1.7}$ well. In the event of 4×10^6 cm^{-3} H_2SO_4, 1.5×10^9 cm^{-3} HNO_3 and 5×10^8 cm^{-3} NH_3, the multicomponent nucleation is quenched ($J_{1.7} < 0.01$ cm^{-3} s^{-1}) above 268 K. This is consistent with the observations that nitric acid

and ammonia only contribute to the growth of ammonium sulfate particles at 278 K (ref. [16]). At 223 K, the parameterized $J_{1.7}$ is 306 cm^{-3} s^{-1}, matching our measurement in Fig. 2. And for the temperature in the upper troposphere and lower stratosphere (198 K), the parameterized $J_{1.7}$ is 8×10^5 cm^{-3} s^{-1}, which is still much slower than its kinetic limit of about 10^9–10^{10} cm^{-3} s^{-1}.

The EMAC global model

The ECHAM/MESSy Atmospheric Chemistry (EMAC) model is a numerical chemistry and climate simulation system that includes sub-models describing tropospheric and middle atmosphere processes and their interaction with oceans, land and human influences[72]. It uses the second version of the Modular Earth Submodel System (MESSy2) to link multi-institutional computer codes. Atmospheric circulation is calculated by the 5th generation of the European Centre Hamburg general circulation model (ECHAM5 (ref. [73])) and atmospheric chemical kinetics are solved for every model time step. For the present study, we applied EMAC (ECHAM5 version 5.3.02, MESSy version 2.54.0) in the T42L31ECMWF-resolution, for example, with a spherical truncation of T42 (corresponding to a quadratic Gaussian grid of approximately 2.8° by 2.8° in latitude and longitude) with 31 vertical hybrid pressure levels up to 10 hPa. EMAC uses a modal representation of aerosols dynamics (GMXe) that describes the aerosol size distribution as seven interacting log-normal distributions, of which four modes are soluble and three modes are insoluble. New particles are added directly to the nucleation mode. The applied model setup comprises the sub-model New Aerosol Nucleation (NAN) that includes new parameterizations of aerosol particle formation rates published in recent years[74]. These parameterizations include ion-induced nucleation. The ion-pair production rate, needed to calculate the ion-induced or ion-mediated nucleation, is described using the sub-model IONS, which provides ion-pair production rates[74].

The TOMCAT global model

The TOMCAT model is a global 3D offline chemical transport model[75,76]. It is run at approximately 2.8° spatial resolution, such as EMAC on a T42 grid, driven by ECMWF ERA-Interim reanalysis meteorological fields for the year 2008. We also used 31 hybrid sigma-pressure levels from the surface to 10 hPa. The dissolved fraction of gases in cloud water is calculated by means of an equilibrium Henry's law approach and set to zero for temperatures below −20 °C. The model includes GLOMAP aerosol microphysics[77] with nitrate and ammonium from the HyDIS solver[78] and the representation of new particle formation used by Gordon et al.[3]. The HyDIS solver adopts a sophisticated approach to the dissolution of nitric acid and ammonia into the aerosol phase that is a hybrid between a dynamic representation of the process, which accounts for the time needed for mass transport, and an equilibrium representation, which does not[78]. The main limitation of the solver is that it assumes all aerosol particles are liquid, which is probably a poor approximation in cold, dry conditions frequently found in the upper troposphere.

The cloud trajectories framework

We conducted a sensitivity study on ammonia transport processes and estimated the fraction remaining of ammonia vapour after convection from the boundary layer to the upper troposphere, using a cloud trajectories framework described in detail in Bardakov et al.[79,80]. In brief, trajectories from a convective system simulated with the large-eddy simulation (LES) model MIMICA[81] were extracted and a parcel representing the cloud outflow was selected for further analysis (Extended Data Fig. 8a). The meteorological profiles and clouds microphysics scheme used here were the same as in Bardakov et al.[80], producing altitude-dependent distributions of water and ice hydrometeors depicted in Extended Data Fig. 8. Partitioning of gas between vapour and aqueous phase along the trajectory was calculated on the basis of Henry's law constant adjusted to a cloud pH, $H^* = H \times 1.7 \times 10^{(9-pH)}$ following the expression for ammonia from Seinfeld and Pandis[60].

We then investigated the factors governing ammonia transport through the simulated convective system by varying: (1) the pH for the liquid water hydrometeors (Extended Data Fig. 8c); (2) the total amount of water in the system (Extended Data Fig. 8d); (3) the retention of ammonia molecules by the ice hydrometeors (Extended Data Fig. 8e). In our base-case simulation, the pH was assumed to have an altitude-dependent profile, reflecting the higher abundance of acids close to the surface and ranging from 4.5 to 5, in accordance with the representative pH values in the EMAC simulation. The base-case water content was as in Bardakov et al.[80] and the ice retention coefficient 0.05 in accordance with Ge et al.[13], with no further uptake on ice.

Atmospheric interpretation

This work focuses on the Asian monsoon region in part because this region is fairly extensive, but also because ammonia concentrations measured in this region are by far the highest in the upper troposphere. Although we frame this synergistic HNO_3–H_2SO_4–NH_3 nucleation in a scenario that suits the Asian monsoon upper troposphere, the physics applies more broadly — the colder the conditions are, the more important this mechanism is likely to be. To explore the importance of this synergistic nucleation to the atmosphere, we combine our experimental results, cloud resolving modelling and global-scale chemical transport modelling. On the basis of these constraints, the rate-limiting elements of new particle formation seem to be convective transport of ammonia and the production rate of particles in the mixing zone between convective outflow and the background upper free troposphere; however, confirmation of this will require extensive field and modelling studies.

Generally, nitric acid ranges between about 10^8 and 10^9 cm^{-3} (refs. [14,15]) and sulfuric acid between about 10^5 and 10^6 cm^{-3} (refs. [82,83]) in the tropical upper troposphere. The typical acid-excess conditions leave the principal uncertainty being ammonia levels, which are not yet well constrained. Although satellite-based ammonia measurements have provided a spatial distribution on a global scale, they are limited to cloud-free areas owing to blockage of the ammonia signal by optically thick clouds. However, deep convection followed by cloud glaciation may be a major source of upper tropospheric ammonia. This process may then not be captured by satellites as it occurs near clouds, with short time duration and high spatial heterogeneity. This may also explain why the in situ-measured ammonia concentrations are up to 40 times higher than those from satellite measurements[6].

Ammonia has no known chemical source in the atmosphere but is instead transported by cloud processes from the surface, whereas nitric acid and sulfuric acid vapours are formed primarily by out-of-cloud oxidation. Consequently, it is probable that this synergistic nucleation occurs initially in the outflow of convective clouds, in which the released ammonia mixes with pre-existing (background) nitric acid and sulfuric acid. Subsequently, as ammonia is titrated over several *e*-folding times (governed by the condensation sink in this mixing zone) and the outflow air fully mixes with the background air, nucleation conditions will shift from the ammonia-rich regime to the ammonia-limited regime. These highly dynamic processes are thus the key to constraining the climatic effects of this synergistic nucleation in Asian monsoon and potentially other convective regions. Nevertheless, current ambient measurements confirm the presence of ample ammonia, as well as particles comprised largely of ammonium nitrate[4], and our experiments show that synergistic HNO_3–H_2SO_4–NH_3 nucleation is a viable mechanism for new particle formation in the Asian monsoon upper troposphere. As global ammonia emissions continue to increase owing to agricultural growth and the warmer climate[84,85], the importance of this particle formation mechanism will increase.

Further, as there is almost no in situ composition measurement of clusters or newly formed particles in the upper troposphere, we can

only infer the major particle formation pathway from indirect evidence such as composition of precursor vapours or larger particles. Previously established mechanisms include binary and ternary sulfuric acid nucleation, which drive new particle formation over marine or anthropogenically influenced regions[1,4,86,87], nucleation by oxygenated organics, which dominates over pristine vegetated areas such as the Amazon basin[2,10,88], and nucleation by iodine oxidation products, which may be especially important in marine convection[89,90]. Over the Asian monsoon regions, however, mixed emissions of both inorganic and organic vapours may well complicate the particle formation mechanism. However, it has been demonstrated that ammonium nitrate can often explain more than half of the particulate volume in the upper troposphere[6]. This means that the HNO_3–NH_3 concentration is probably higher than the sum of all other condensable vapours (that is, sulfuric acid and oxygenated organics). And given that HNO_3–H_2SO_4–NH_3 nucleation is orders of magnitude faster than binary and ternary sulfuric acid nucleation at observed ammonia levels, we therefore infer that synergistic HNO_3–H_2SO_4–NH_3 nucleation is a major particle formation pathway in the Asian monsoon upper troposphere. It seems unlikely that this inorganic pathway and the organic pathways are antagonistic in growth, and without strong indications otherwise, it seems probable that they are more or less additive for nucleation itself. However, to further investigate interactions between different nucleation schemes, we would rely on further information on the source and identity of organic vapours that are present in the Asian monsoon upper troposphere.

Data availability

The full dataset shown in the figures is publicly available at https://doi.org/10.5281/zenodo.5949440. Source data are provided with this paper.

Code availability

The EMAC (ECHAM/MESSy) model is continuously further developed and applied by a consortium of institutions. The use of MESSy and access to the source code is licensed to all affiliates of institutions that are members of the MESSy Consortium. Institutions can become a member of the MESSy Consortium by signing the MESSy Memorandum of Understanding. More information can be found on the MESSy Consortium website (https://www.messy-interface.org). All code modifications presented in this paper will be included in the next version of MESSy. The TOMCAT model (http://homepages.see.leeds.ac.uk/~lecmc/tomcat.html) is a UK community model. It is available to UK (or NERC-funded) researchers who normally access the model on common facilities or who are helped to install it on their local machines. As it is a complex research tool, new users will need help to use the model optimally. We do not have the resources to release and support the model in an open way. Any potential user interested in the model should contact Martyn Chipperfield. The model updates described in this paper are included in the standard model library. The cloud trajectories model is publicly available at https://doi.org/10.5281/zenodo.5949440. Codes for conducting the analysis presented in this paper can be obtained by contacting the corresponding author, Neil M. Donahue (nmd@andrew.cmu.edu).

30. Duplissy, J. et al. Effect of ions on sulfuric acid-water binary particle formation: 2. Experimental data and comparison with QC-normalized classical nucleation theory. *J. Geophys. Res. Atmos.* **212**, 1752–1775 (2016).
31. Dias, A. et al. Temperature uniformity in the CERN CLOUD chamber. *Atmos. Meas. Tech.* **10**, 5075–5088 (2017).
32. Kirkby, J. et al. Ion-induced nucleation of pure biogenic particles. *Nature* **530**, 521–526 (2016).
33. Schnitzhofer, R. et al. Characterisation of organic contaminants in the CLOUD chamber at CERN. *Atmos. Meas. Tech.* **7**, 2159–2168 (2014).
34. Jokinen, T. et al. Atmospheric sulphuric acid and neutral cluster measurements using CI-APi-TOF. *Atmos. Chem. Phys.* **12**, 4117–4125 (2012).
35. Kürten, A. et al. Neutral molecular cluster formation of sulfuric acid–dimethylamine observed in real time under atmospheric conditions. *Proc. Natl Acad. Sci.* **111**, 15019–15024 (2014).
36. Lopez-Hilfiker, F. D. et al. A novel method for online analysis of gas and particle composition: description and evaluation of a Filter Inlet for Gases and AEROsols (FIGAERO). *Atmos. Meas. Tech.* **7**, 983–1001 (2014).
37. Wang, M. et al. Reactions of atmospheric particulate stabilized Criegee intermediates lead to high-molecular-weight aerosol components. *Environ. Sci. Technol.* **50**, 5702–5710 (2016).
38. Kürten, A., Rondo, L., Ehrhart, S. & Curtius, J. Performance of a corona ion source for measurement of sulfuric acid by chemical ionization mass spectrometry. *Atmos. Meas. Tech.* **4**, 437–443 (2011).
39. Tröstl, J. et al. The role of low-volatility organic compounds in initial particle growth in the atmosphere. *Nature* **530**, 527–531 (2016).
40. Breitenlechner, M. et al. PTR3: an instrument for studying the lifecycle of reactive organic carbon in the atmosphere. *Anal. Chem.* **89**, 5824–5831 (2017).
41. Kürten, A. et al. Experimental particle formation rates spanning tropospheric sulfuric acid and ammonia abundances, ion production rates, and temperatures. *J. Geophys. Res. Atmos.* **121**, 12–377 (2016).
42. McMurry, P. H. & Grosjean, D. Gas and aerosol wall losses in Teflon film smog chambers. *Environ. Sci. Technol.* **19**, 1176–1181 (1985).
43. Simon, M. et al. Molecular insight into HOM formation and biogenic new-particle formation over a wide range of tropospheric temperatures. *Atmos. Chem. Phys.* **20**, 9183–9207 (2020).
44. Tang, M., Cox, R. & Kalberer, M. Compilation and evaluation of gas phase diffusion coefficients of reactive trace gases in the atmosphere: volume 1. inorganic compounds. *Atmos. Chem. Phys.* **14**, 9233–9247 (2014).
45. Junninen, H. et al. A high-resolution mass spectrometer to measure atmospheric ion composition. *Atmos. Meas. Tech.* **3**, 1039–1053 (2010).
46. Kürten, A. et al. Observation of new particle formation and measurement of sulfuric acid, ammonia, amines and highly oxidized organic molecules at a rural site in central Germany. *Atmos. Chem. Phys.* **16**, 12793–12813 (2016).
47. Dada, L. et al. Formation and growth of sub-3-nm aerosol particles in experimental chambers. *Nat. Protoc.* **15**, 1013–1040 (2020).
48. Mui, W., Mai, H., Downard, A. J., Seinfeld, J. H. & Flagan, R. C. Design, simulation, and characterization of a radial opposed migration ion and aerosol classifier (ROMIAC). *Aerosol Sci. Technol.* **51**, 801–823 (2017).
49. Wimmer, D. et al. Performance of diethylene glycol-based particle counters in the sub-3 nm size range. *Atmos. Meas. Tech.* **6**, 1793–1804 (2013).
50. Mai, H. & Flagan, R. C. Scanning DMA data analysis I. Classification transfer function. *Aerosol Sci. Technol.* **52**, 1382–1399 (2018).
51. Mai, H., Kong, W., Seinfeld, J. H. & Flagan, R. C. Scanning DMA data analysis II. Integrated DMA-CPC instrument response and data inversion. *Aerosol Sci. Technol.* **52**, 1400–1414 (2018).
52. Jurányi, Z. et al. A 17 month climatology of the cloud condensation nuclei number concentration at the high alpine site Jungfraujoch. *J. Geophys. Res. Atmos.* **116**, D10204 (2011).
53. Tröstl, J. et al. Fast and precise measurement in the sub-20 nm size range using a Scanning Mobility Particle Sizer. *J. Aerosol Sci.* **87**, 75–87 (2015).
54. Wiedensohler, A. et al. Mobility particle size spectrometers: harmonization of technical standards and data structure to facilitate high quality long-term observations of atmospheric particle number size distributions. *Atmos. Meas. Tech.* **5**, 657–685 (2012).
55. Jayne, J. T. et al. Development of an aerosol mass spectrometer for size and composition analysis of submicron particles. *Aerosol Sci. Technol.* **33**, 49–70 (2000).
56. DeCarlo, P. F. et al. Field-deployable, high-resolution, time-of-flight aerosol mass spectrometer. *Anal. Chem.* **78**, 8281–8289 (2006).
57. Rogers, D. C. Development of a continuous flow thermal gradient diffusion chamber for ice nucleation studies. *Atmos. Res.* **22**, 149–181 (1988).
58. DeMott, P. J. et al. The Fifth International Workshop on Ice Nucleation phase 2 (FIN-02): laboratory intercomparison of ice nucleation measurements. *Atmos. Meas. Tech.* **11**, 6231–6257 (2018).
59. Schiebel, T. *Ice Nucleation Activity of Soil Dust Aerosols*. PhD thesis, KIT-Bibliothek (2017).
60. Seinfeld, J. H. & Pandis, S. N. *Atmospheric Chemistry and Physics* 2nd edn (Wiley, 2006).
61. Connolly, P. J. et al. Studies of heterogeneous freezing by three different desert dust samples. *Atmos. Chem. Phys.* **9**, 2805–2824 (2009).
62. Koop, T., Luo, B., Tsias, A. & Peter, T. Water activity as the determinant for homogeneous ice nucleation in aqueous solutions. *Nature* **406**, 611–614 (2000).
63. Cziczo, D. J. & Abbatt, J. P. D. Infrared observations of the response of NaCl, $MgCl_2$, NH_4HSO_4, and NH_4NO_3 aerosols to changes in relative humidity from 298 to 238 K. *J. Phys. Chem. A* **104**, 2038–2047 (2000).
64. Zuberi, B., Bertram, A. K., Koop, T., Molina, L. T. & Molina, M. J. Heterogeneous freezing of aqueous particles induced by crystallized $(NH_4)_2SO_4$, ice, and letovicite. *J. Phys. Chem. A* **105**, 6458–6464 (2001).
65. Schlenker, J. C. & Martin, S. T. Crystallization pathways of sulfate–nitrate–ammonium aerosol particles. *J. Phys. Chem. A* **109**, 9980–9985 (2005).
66. Riccobono, F. et al. Oxidation products of biogenic emissions contribute to nucleation of atmospheric particles. *Science* **344**, 717–721 (2014).
67. Möhler, O. & Arnold, F. Gaseous sulfuric acid and sulfur dioxide measurements in the Arctic troposphere and lower stratosphere: implications for hydroxyl radical abundances. *Geophys. Res. Lett.* **19**, 1763–1766 (1992).
68. Williamson, C. J. et al. Large hemispheric difference in ultrafine aerosol concentrations in the lowermost stratosphere at mid and high latitudes. Atmos. Chem. Phys. Discuss. 1–44 (2021).
69. Wespes, C. et al. First global distributions of nitric acid in the troposphere and the stratosphere derived from infrared satellite measurements. *J. Geophys. Res. Atmos.* **112**, D13311 (2007).

70. Popp, P. et al. Stratospheric correlation between nitric acid and ozone. *J. Geophys. Res. Atmos.* **114**, D03305 (2009).
71. Hirsikko, A. et al. Atmospheric ions and nucleation: a review of observations. *Atmos. Chem. Phys.* **11**, 767–798 (2011).
72. Jöckel, P. et al. Development cycle 2 of the modular earth submodel system (MESSy2). *Geosci. Model Dev.* **3**, 717–752 (2010).
73. Roeckner, E. et al. Sensitivity of simulated climate to horizontal and vertical resolution in the ECHAM5 atmosphere model. *J. Clim.* **19**, 3771–3791 (2006).
74. Ehrhart, S. et al. Two new submodels for the Modular Earth Submodel System (MESSy): New Aerosol Nucleation (NAN) and small ions (IONS) version 1.0. *Geosci. Model Dev.* **11**, 4987–5001 (2018).
75. Chipperfield, M. New version of the TOMCAT/SLIMCAT off-line chemical transport model: Intercomparison of stratospheric tracer experiments. *Q. J. R. Meteorol. Soc.* **132**, 1179–1203 (2006).
76. Monks, S. A. et al. The TOMCAT global chemical transport model v1.6: description of chemical mechanism and model evaluation. *Geosci. Model Dev.* **10**, 3025–3057 (2017).
77. Mann, G. et al. Description and evaluation of GLOMAP-mode: a modal global aerosol microphysics model for the UKCA composition-climate model. *Geosci. Model Dev.* **3**, 519–551 (2010).
78. Benduhn, F. et al. Size-resolved simulations of the aerosol inorganic composition with the new hybrid dissolution solver HyDiS-1.0: description, evaluation and first global modelling results. *Geosci. Model Dev.* **9**, 3875–3906 (2016).
79. Bardakov, R. et al. A novel framework to study trace gas transport in deep convective clouds. *J. Adv. Model. Earth Syst.* **12**, e2019MS001931 (2020).
80. Bardakov, R., Thornton, J. A., Riipinen, I., Krejci, R. & Ekman, A. M. L. Transport and chemistry of isoprene and its oxidation products in deep convective clouds. *Tellus B Chem. Phys. Meteorol.* **73**, 1–21 (2021).
81. Savre, J., Ekman, A. M. L. & Svensson, G. Technical note: Introduction to MIMICA, a large-eddy simulation solver for cloudy planetary boundary layers. *J. Adv. Model. Earth Syst.* **6**, 630–649 (2014).
82. Bates, T. S., Huebert, B. J., Gras, J. L., Griffiths, F. B. & Durkee, P. A. International Global Atmospheric Chemistry (IGAC) project's first aerosol characterization experiment (ACE 1): overview. *J. Geophys. Res. Atmos.* **103**, 16297–16318 (1998).
83. Hoell, J. M. et al. Pacific Exploratory Mission in the tropical Pacific: PEM-Tropics A, August-September 1996. *J. Geophys. Res. Atmos.* **104**, 5567–5583 (1999).
84. Erisman, J. W., Sutton, M. A., Galloway, J., Klimont, Z. & Winiwarter, W. How a century of ammonia synthesis changed the world. *Nat. Geosci.* **1**, 636–639 (2008).
85. Warner, J. X. et al. Increased atmospheric ammonia over the world's major agricultural areas detected from space. *Geophys. Res. Lett.* **44**, 2875–2884 (2017).
86. Twohy, C. H. et al. Deep convection as a source of new particles in the midlatitude upper troposphere. *J. Geophys. Res. Atmos.* **107**, AAC 6-1–AAC 6-10 (2002).
87. Lee, S.-H. et al. Particle formation by ion nucleation in the upper troposphere and lower stratosphere. *Science* **301**, 1886–1889 (2003).
88. Waddicor, D. A. et al. Aerosol observations and growth rates downwind of the anvil of a deep tropical thunderstorm. *Atmos. Chem. Phys.* **12**, 6157–6172 (2012).
89. Wang, S. et al. Active and widespread halogen chemistry in the tropical and subtropical free troposphere. *Proc. Natl Acad. Sci.* **112**, 9281–9286 (2015).
90. He, X.-C. et al. Role of iodine oxoacids in atmospheric aerosol nucleation. *Science* **371**, 589–595 (2021).

Acknowledgements We thank the European Organization for Nuclear Research (CERN) for supporting CLOUD with important technical and financial resources. This research has received funding from the US National Science Foundation (nos. AGS-1801574, AGS-1801897, AGS-1602086, AGS-1801329, AGS-2132089 and AGS-1801280), the European Union's Horizon 2020 programme (Marie Skłodowska-Curie ITN no. 764991 'CLOUD-MOTION'), the European Commission, H2020 Research Infrastructures (FORCeS, no. 821205), the European Union's Horizon 2020 research and innovation programme (Marie Skłodowska-Curie no. 895875 'NPF-PANDA'), a European Research Council (ERC) project ATM-GTP contract (no. 742206), an ERC-CoG grant INTEGRATE (no. 867599), the Swiss National Science Foundation (nos. 200021_169090, 200020_172602 and 20FI20_172622), the Academy of Finland ACCC Flagship (no. 337549), the Academy of Finland Academy professorship (no. 302958), the Academy of Finland (nos. 1325656, 316114 and 325647), Russian MegaGrant project 'Megapolis – heat and pollution island: interdisciplinary hydroclimatic, geochemical and ecological analysis' (application reference 2020-220-08-5835), Jane and Aatos Erkko Foundation 'Quantifying carbon sink, CarbonSink+ and their interaction with air quality' INAR project, Samsung PM2.5 SRP, Prince Albert Foundation 'the Arena for the gap analysis of the existing Arctic Science Co-Operations (AASCO)' (no. 2859), the German Federal Ministry of Education and Research (CLOUD-16 project nos. 01LK1601A and 01LK1601C), the Knut and Alice Wallenberg Foundation Wallenberg Academy Fellows project AtmoRemove (no. 2015.0162), the Portuguese Foundation for Science and Technology (no. CERN/FIS-COM/0014/2017) and the Technology Transfer Project N059 of the Karlsruhe Institute of Technology (KIT). The FIGAERO-CIMS was supported by a Major Research Instrumentation (MRI) grant for the US NSF AGS-1531284, as well as the Wallace Research Foundation. The computations by R.Bardakov were performed on resources provided by the Swedish National Infrastructure for Computing (SNIC) at the National Supercomputer Center (NSC). I.R. thanks the Max Planck Society for a sabbatical award. M.W. thanks Siebel Scholars Foundation for financial support.

Author contributions M.W., B.B., J.K. and N.M.D. planned the experiments. M.W., B.B., G.M., B.R., B.S., X.-C.H., J.S., W.S., R.M., B.L., H.L., H.E.M., F.A., P.B., Z.B., L.C., L.-P.D.M., J.D., H.F., L.G.C., M.G., R.G., V.H., A.K., K.L., V.M., D.M., S.M., R.L.M., B.M., T.M., A.O., T.P., M.P., A.A.P., A.P., M.Simon, Y.S., A.T., N.S.U., F.V., R.W., D.S.W., S.K.W., A.W., Y.W., M.Z.-W., M.Sipilä, P.M.W., A.H., U.B., M.K., R.C.F., J.C., R.V., I.E.-H., J.K., K.K. O.M., S.S. and N.M.D. prepared the CLOUD facility or measuring instruments. M.W., B.B., G.M., B.R., B.S., X.-C.H., J.S., W.S., R.M., B.L., H.E.M., A.A., L.C., L.G.C., M.G., M.H., V.H., J.E.K., N.G.A.M., D.M., R.L.M., B.M., A.R., M.Schervish, M.Simon, A.T., N.S.U., F.V., D.S.W., S.K.W., A.W., M.Z.-W., P.M.W., J.K. and K.K. collected the data. M.W., M.X., B.B., G.M., B.R., B.S., R.Bardakov, J.S., W.S., L.D., R.Baalbaki, B.L., D.S.W., S.K.W., A.W., I.R., T.C. and N.M.D. analysed the data. M.W., M.X., B.B., R.Bardakov, X.-C.H., J.S., W.S., R.M., L.D., R. Baalbaki., B.L., H.L., H.E.M., A.M.L.E., H.F., M.H., K.H., A.K., N.S.U., R.W., A.W., A.H., U.B., M.K., R.C.F., J.C., R.V., I.R., H.G., J.L., I.E.-H., D.R.W., T.C., J.K., O.M., S.S. and N.M.D. contributed to the scientific discussion. M.W., B.B., R.Bardakov, W.S., R.M., B.L., H.L., K.H., A.K., U.B., R.C.F., J.C., R.V., I.R., H.G., J.L., I.E.-H., T.C., J.K., O.M. and N.M.D. wrote the manuscript.

Competing interests The authors declare no competing interests.

Additional information

Supplementary information The online version contains supplementary material available at https://doi.org/10.1038/s41586-022-04605-4.

Correspondence and requests for materials should be addressed to Neil M. Donahue.

Peer review information *Nature* thanks Bernd Kärcher and the other, anonymous, reviewers for their contribution to the peer review of this work. Peer reviewer reports are available.

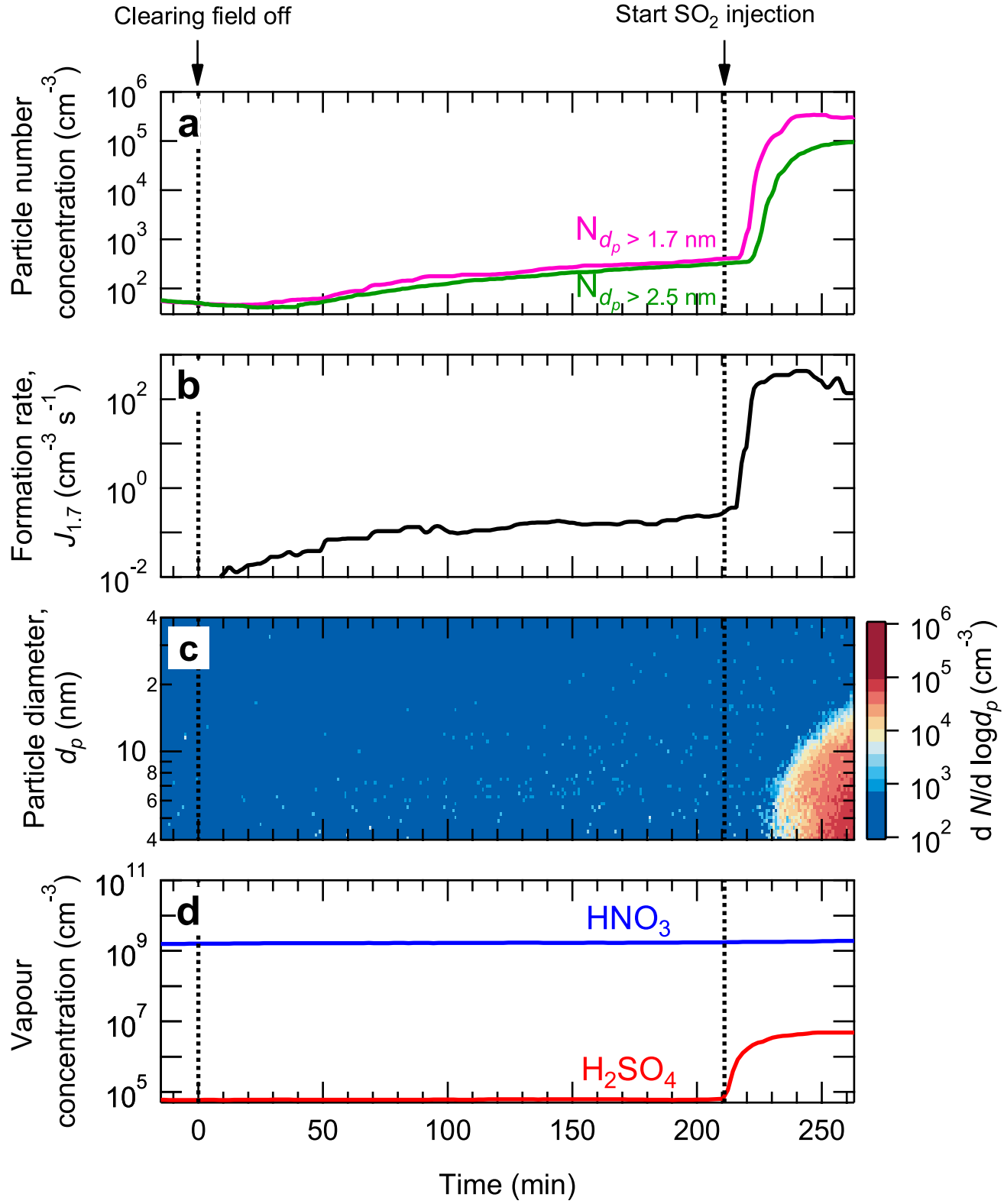

Extended Data Fig. 1 | See next page for caption.

Extended Data Fig. 1 | Enhancement of HNO_3–NH_3 particle formation by sulfuric acid. a, Particle number concentrations versus time at mobility diameters >1.7 nm (magenta) and >2.5 nm (green). The solid magenta trace is measured by a $PSM_{1.7}$ and the solid green trace is measured by a $CPC_{2.5}$. The fixed experimental conditions are about 6.5×10^8 cm^{-3} NH_3, 223 K and 25% relative humidity. **b**, Particle formation rate versus time at 1.7 nm ($J_{1.7}$), measured by a PSM. **c**, Particle size distribution versus time, measured by an SMPS. **d**, Gas-phase nitric acid and sulfuric acid versus time, measured by an I^- CIMS and a NO_3^- CIMS, respectively. We started the experiment by oxidizing NO_2 to produce 1.6×10^9 cm^{-3} HNO_3 in the presence of about 6.5×10^8 cm^{-3} ammonia. At time = 0 min, we turned off the high-voltage clearing field to allow the ion concentration to build up to a steady state between GCR production and wall deposition. The presence of ions (GCR condition) induces slow HNO_3–NH_3 nucleation, followed by relatively fast particle growth by nitric acid and ammonia condensation. We thus observe formation of both 1.7-nm and 2.5-nm particles by about one order of magnitude in about 3.5 h, with a slower approach to steady state because of the longer wall deposition time constant for the larger particles. Then, we increased H_2SO_4 in the chamber from 0 to 4.9×10^6 cm^{-3} by oxidizing progressively more injected SO_2 after 211 min, with a fixed production rate of nitric acid and injection rate of ammonia. Subsequently, particle concentrations increase by three orders of magnitude within 30 min. The overall systematic scale uncertainties of ±30% on particle formation rate, −33%/+50% on sulfuric acid concentration and ±25% on nitric acid concentration are not shown.

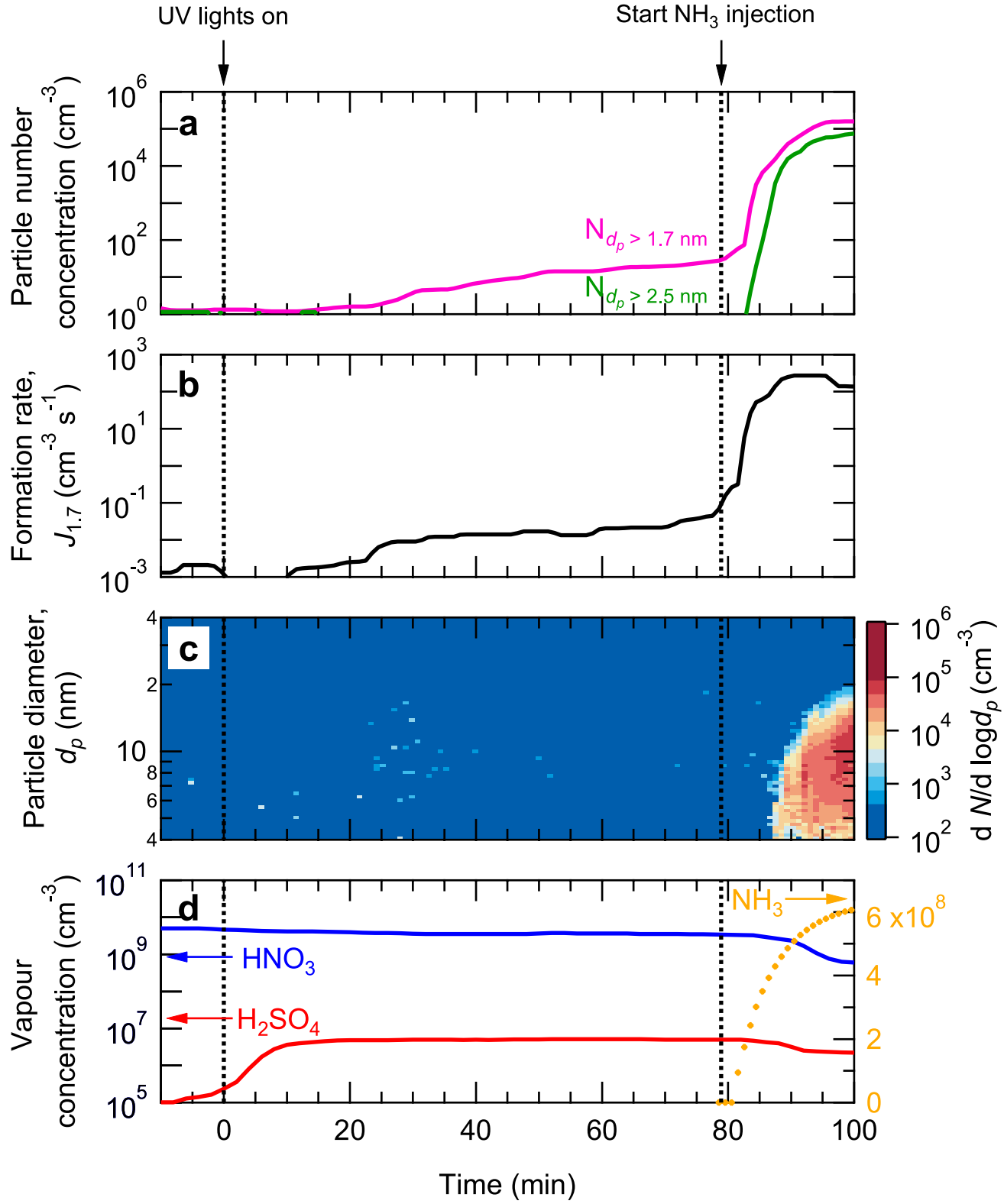

Extended Data Fig. 2 | See next page for caption.

Extended Data Fig. 2 | Enhancement of H_2SO_4–HNO_3 nucleation by ammonia. a, Particle number concentrations versus time at mobility diameters >1.7 nm (magenta) and >2.5 nm (green). The solid magenta trace is measured by a $PSM_{1.7}$ and the solid green trace is measured by a $CPC_{2.5}$. The fixed experimental conditions are 223 K and 25% relative humidity. **b**, Particle formation rate versus time at 1.7 nm ($J_{1.7}$), measured by a PSM. **c**, Particle size distribution versus time, measured by an SMPS. **d**, Gas-phase nitric acid and sulfuric acid versus time, measured by an I^- CIMS and a NO_3^- CIMS, respectively; gas-phase ammonia versus time, calculated with a first-order wall-loss rate. Before the experiment, we cleaned the chamber by rinsing the walls with ultra-pure water, followed by heating to 373 K and flushing at a high rate with humidified synthetic air for 48 h. We started with an almost perfectly clean chamber and only HNO_3, SO_2 and O_3 vapours present at constant levels. Sulfuric acid starts to appear by means of SO_2 oxidation soon after switching on the UV lights at time = 0 min, building up to a steady state of 5.0×10^6 cm^{-3} with the wall-loss timescale of about 10 min. Subsequently, we observe slow formation of 1.7-nm particles, yet they do not reach 2.5 nm during the course of a 2-h period with small growth rates and low survival probability. Then, owing to the injection of ammonia from 0 to around 6.5×10^8 cm^{-3} into the chamber after 80 min, a sharp increase in the rate of particle formation is observed with a fixed production rate of sulfuric acid and injection rate of nitric acid. The sulfuric acid concentration decreases slightly afterwards, owing to accumulated condensation sink from fast particle growth. The overall systematic scale uncertainties of ±30% on particle formation rate, −33%/50% on sulfuric acid concentration and ±25% on nitric acid concentration are not shown.

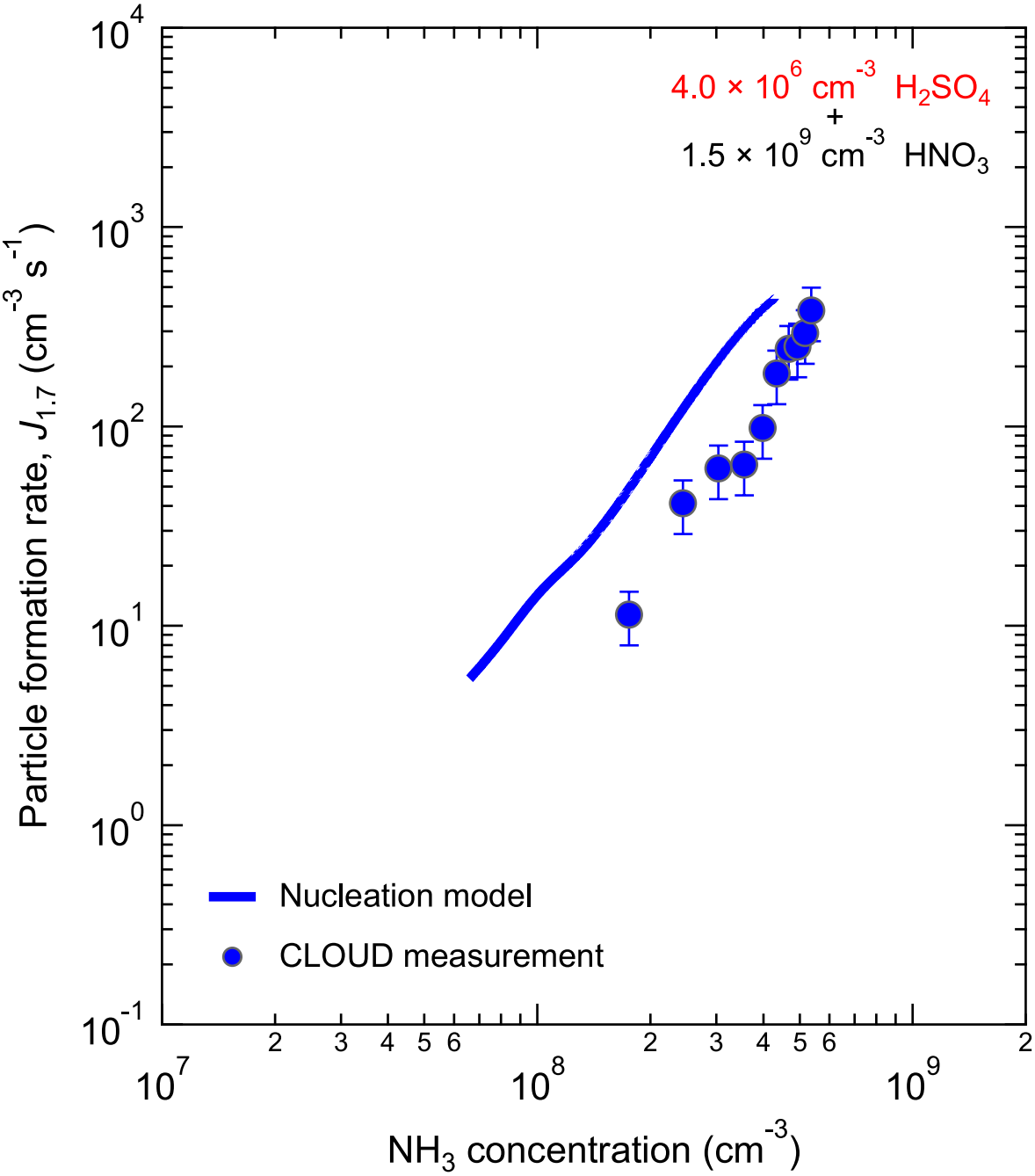

Extended Data Fig. 3 | Particle formation rates at 1.7 nm ($J_{1.7}$) versus ammonia concentration at 223 K and 25% relative humidity. Circles are the CLOUD measurements (the same as those in Fig. 2). The curve represents the model simulations on the basis of known thermodynamics and microphysics, including Kelvin effects, for nucleating clusters.

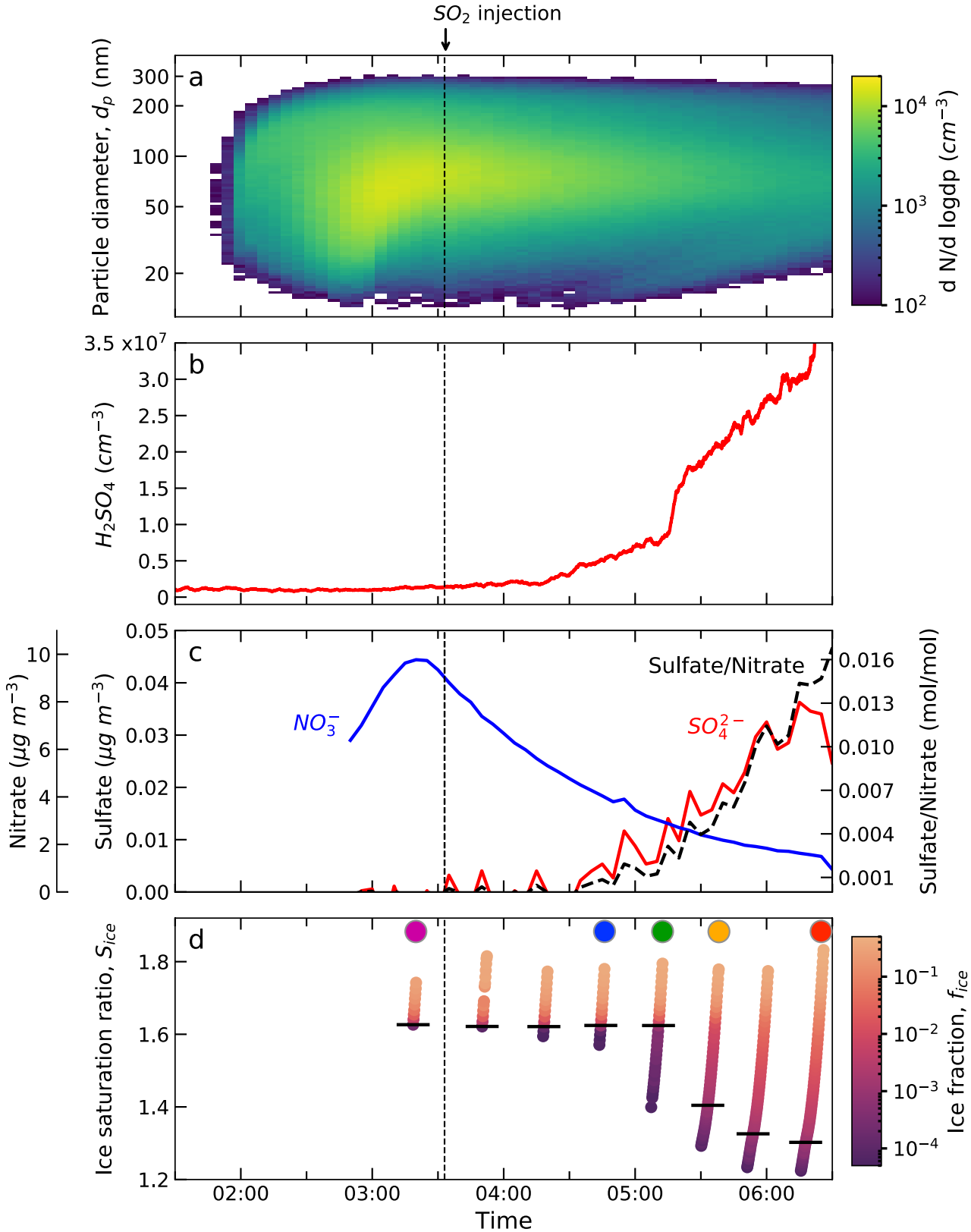

Extended Data Fig. 4 | Measurement of the ice nucleation ability of HNO_3–H_2SO_4–NH_3 particles versus sulfate-to-nitrate ratio. a, Particle size distribution versus time during the experiment, measured by an SMPS. **b**, Gas-phase sulfuric acid versus time, measured by a nitrate CIMS. **c**, Particle-phase chemical composition versus time, measured by an AMS. **d**, Fraction of INP at the nominal temperature of 215 K. The horizontal black dashes indicate the ice fraction threshold, $f_{ice} = 10^{-3}$. The coloured circles correspond to the sulfate-to-nitrate ratios shown in Fig. 4a.

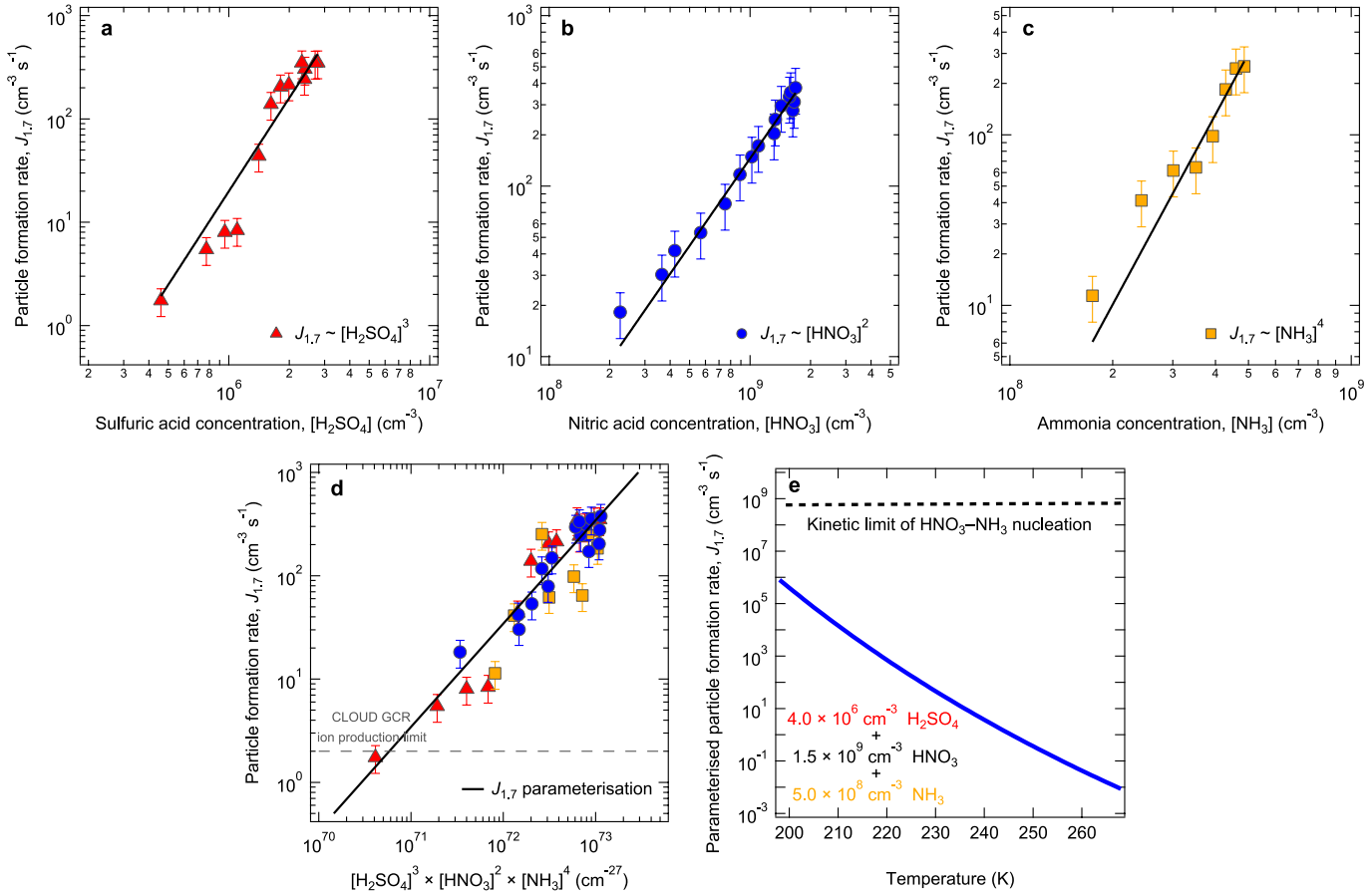

Extended Data Fig. 5 | Parameterization of the HNO_3–H_2SO_4–NH_3 particle formation rate. a–c Particle formation rate ($J_{1.7}$) as a function of H_2SO_4, HNO_3 and NH_3 vapour concentrations, respectively, at 223 K and 25% relative humidity. The red triangles, blue circles and yellow squares represent experiments while varying only the concentration of H_2SO_4 (Extended Data Fig. 1), HNO_3 (Fig. 1) and NH_3 (Extended Data Fig. 2), respectively. The H_2SO_4 concentration was varied between 4.6×10^5 and 2.9×10^6 cm^{-3}, HNO_3 between 2.3×10^8 and 1.7×10^9 cm^{-3} and NH_3 between 1.8×10^8 and 5.1×10^8 cm^{-3}. **d**, The multi-acid–ammonia parameterization (black line) on the basis of equation (6) with $k = 3.4 \times 10^{-71}$ s^{-1} cm^{24}. The grey dashed horizontal line shows a maximum of about 2 cm^{-3} s^{-1} ion-induced nucleation in the CLOUD chamber under GCR conditions, limited by the ion-pair production rate from GCR plus beam-background muons. The bars indicate 30% estimated total error on the particle formation rates, although the overall systematic scale uncertainties of −33%/+50% on sulfuric acid concentration and ±25% on nitric acid concentration are not shown. **e**, Temperature dependence of $J_{1.7}$ for HNO_3–H_2SO_4–NH_3 nucleation (blue curve) on the basis of equation (9) with $k = 2.9 \times 10^{-98}$ e$^{14{,}000/T}$ s^{-1} cm^{24}.

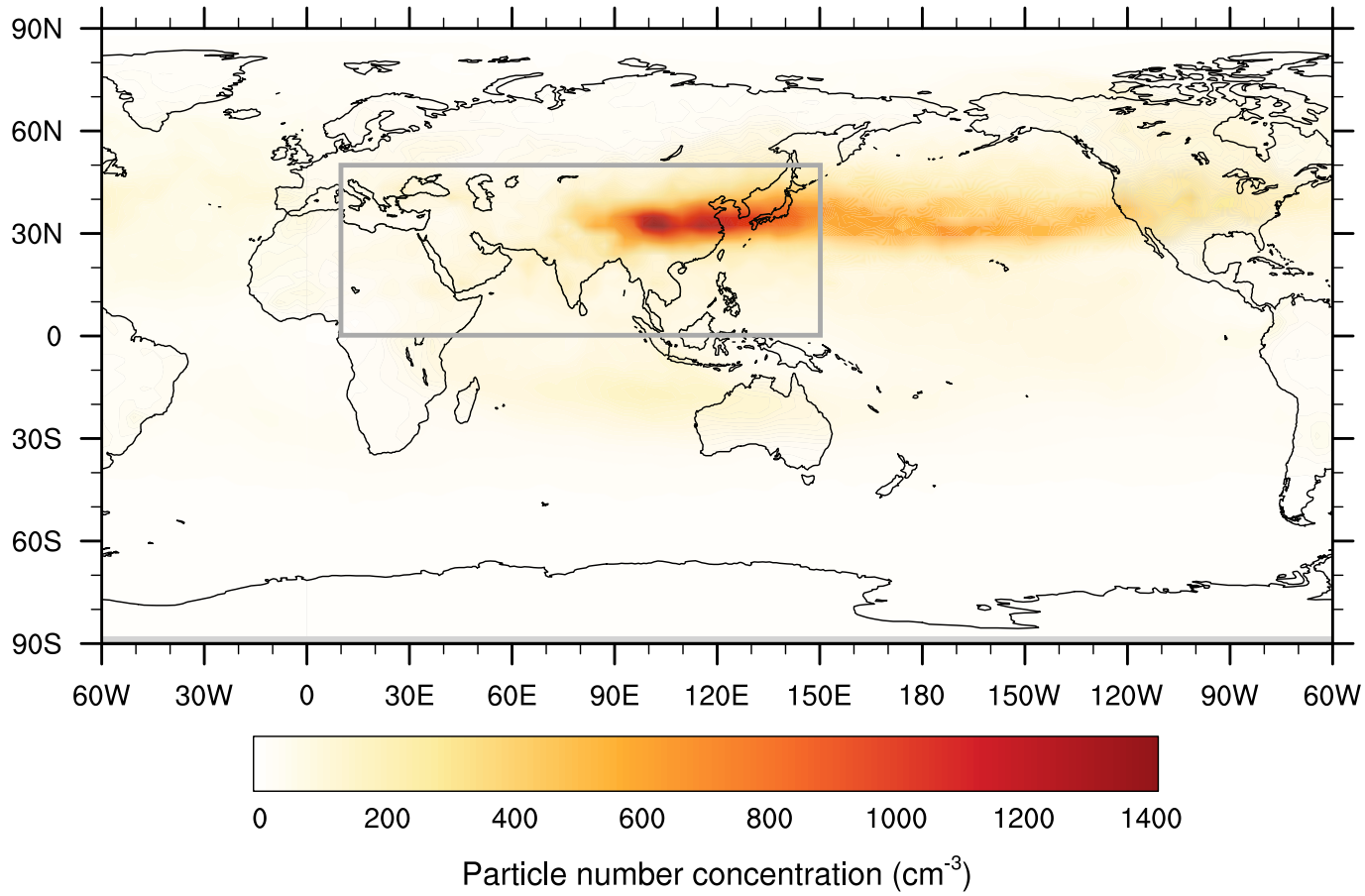

Extended Data Fig. 6 | Modelled contribution of HNO_3–H_2SO_4–NH_3 nucleation to upper tropospheric particles. Number concentrations of multi-acid new particles (nucleation mode) at 250-hPa altitude simulated in a global model (EMAC) with efficient vertical transport of ammonia. The particle formation rate is on the basis of the blue dashed curve in Fig. 2 and parameterization shown in Extended Data Fig. 5. The extra particle number concentrations are shown, that is, relative to the same model without multi-acid nucleation. High annually averaged particle numbers are expected in the monsoon region (grey rectangle) and adjacent regions.

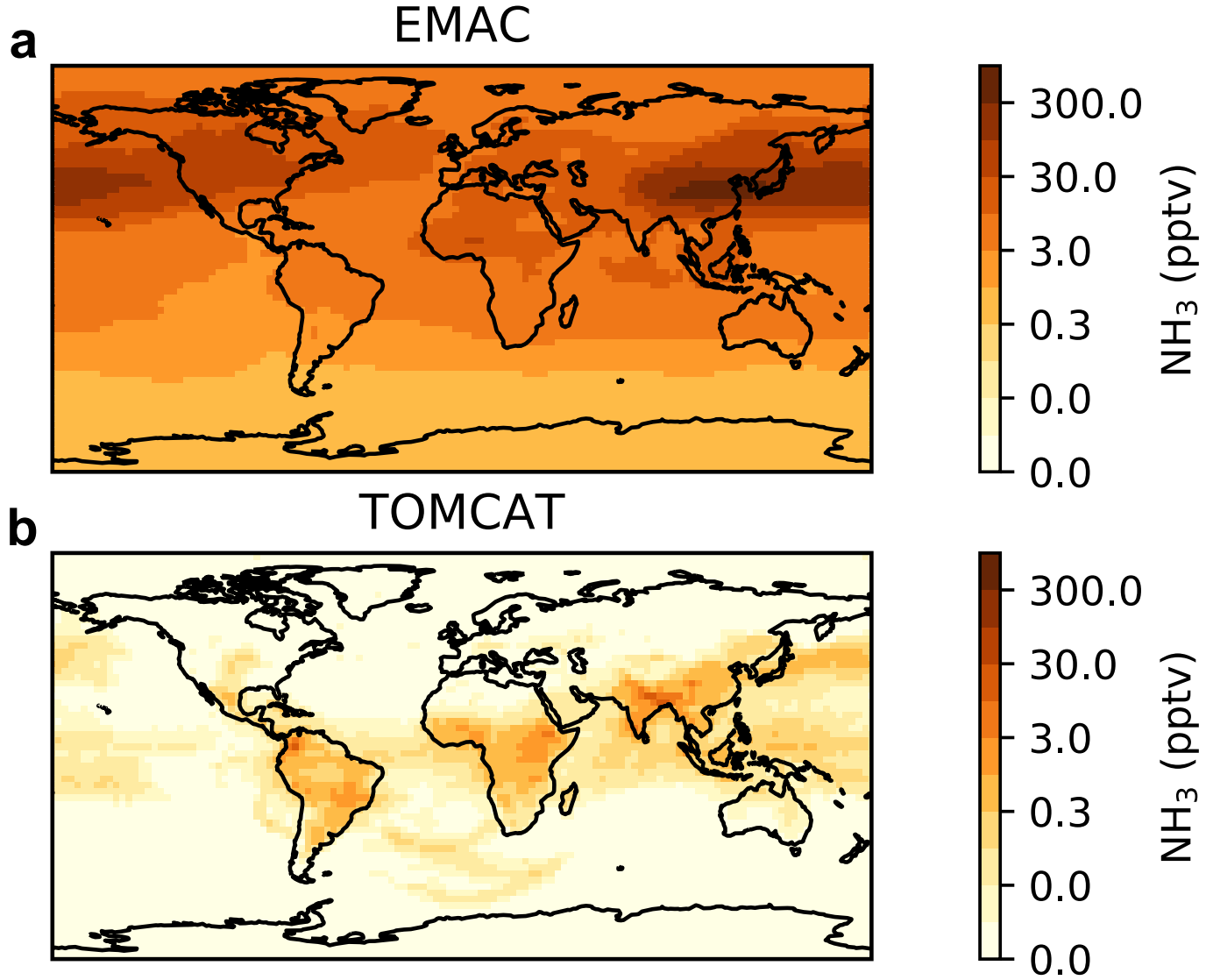

Extended Data Fig. 7 | Modelled annual mean ammonia mixing ratios at 250 hPa (11 km, about 223 K). a, The EMAC global model simulations are higher than the MIPAS satellite observations, although consistent with aircraft measurements[5,6]. **b**, The TOMCAT global model predicts much less ammonia (<1 pptv) in the upper troposphere.

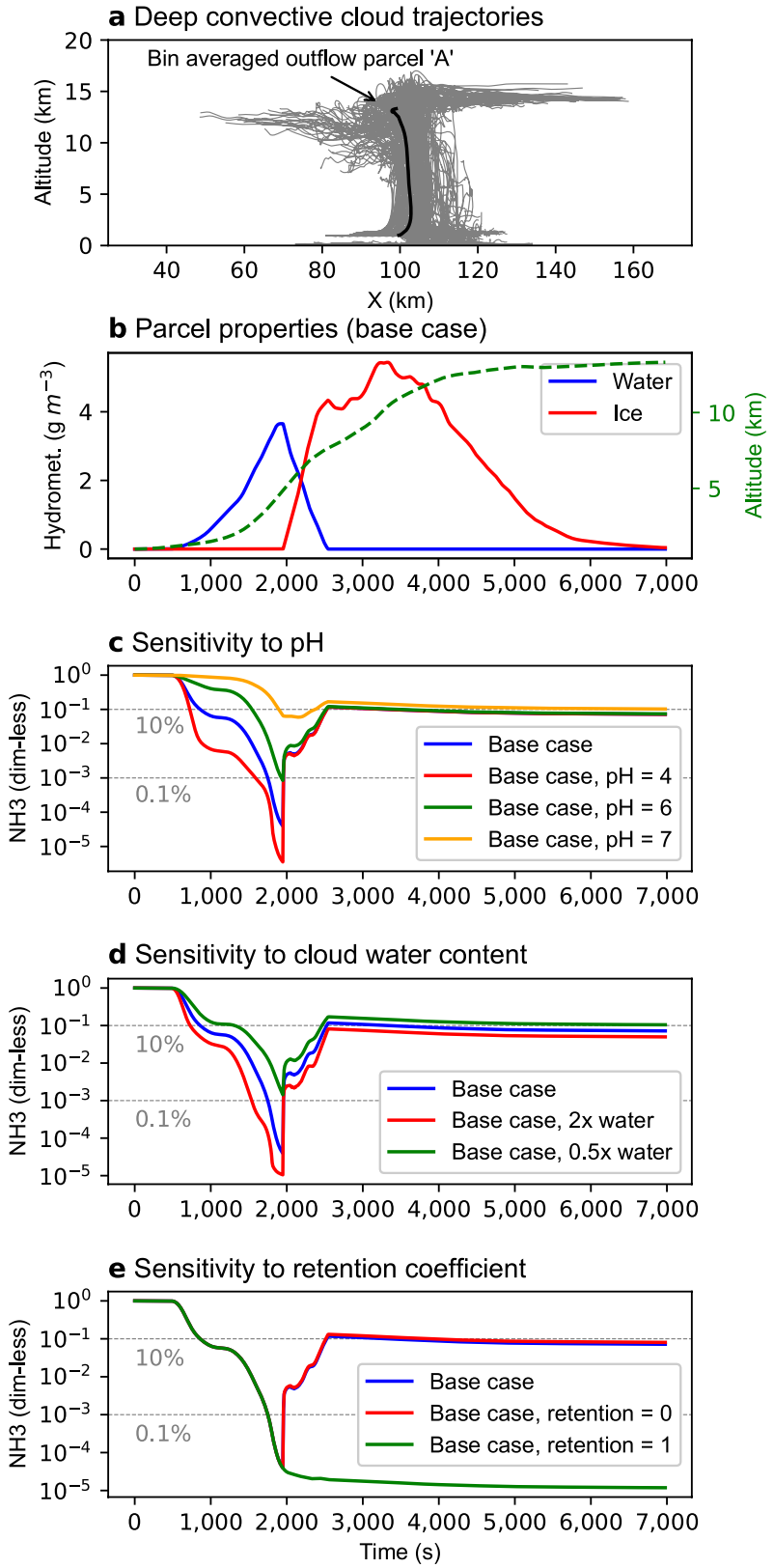

Extended Data Fig. 8 | Modelled transport of ammonia to the upper troposphere in deep convective clouds. a, Trajectories of the simulated convective cloud event (grey) and a selected parcel representing a buoyant parcel reaching the upper troposphere (black). **b**, The simulated evolution of parcel A altitude (green dashed trace) and the total mass concentration and phase of the cloud hydrometeors (red and blue curves). **c**–**e** Sensitivity of the predicted ammonia concentrations within parcel A to cloud water pH, total water amount and retention coefficient (by ice particles) as compared with the base-case simulation (blue trace in all figures).

7. Summary and outlook

Nanoparticles are generally formed by gas-to-particle conversion in the atmosphere by a process called New Particle Formation (NPF). In the NPF process, certain gases undergo oxidation reactions producing condensable vapors with low enough volatility to form very small particles. My work characterizes the chemical composition of freshly formed nanoparticles measured in the laboratory and field.

The chemical analysis of nanoparticles (particles with diameters smaller than 100 nm) is an analytical challenge because they are abundant in number but have very little mass. The Thermal Desorption-Differential Mobility Analyzer (TD-DMA) coupled to a nitrate Chemical Ionization Time-of-Flight mass spectrometer (CI-APi-TOF) was developed by Wagner et al. in 2018 to better address this challenge. In this work, I present four manuscripts, two of which report TD-DMA results and represent my main project as a lead author.

The first TD-DMA manuscript (Caudillo et al., 2021) reports gas and particle phase measurements from the oxidation of biogenic precursor gases (α-pinene and isoprene). The experiments were performed in the CLOUD chamber at CERN to investigate pure biogenic new particle formation. The TD-DMA was coupled to a nitrate CI-APi-TOF mass spectrometer to measure gases thermally desorbed from the aerosol. Thus, both gas and particle phase measurements used the same chemical ionization scheme and detection method for direct comparison. Using this method, we detected $C_{10}H_{16}O_{3\text{-}9}$, and $C_{20}H_{32}O_{5\text{-}13}$ compounds in the particle phase. Particularly for the experiment with isoprene added, C_5 ($C_5H_{10}O_{5\text{-}7}$) and C_{15} compounds ($C_{15}H_{24}O_{5\text{-}10}$) contribute importantly to the particles. This finding demonstrates the suitability of the TD-DMA for measuring newly formed nanoparticles and it confirms that isoprene suppresses new particle formation but contributes to the growth of newly formed particles.

The second TD-DMA manuscript (Caudillo et al., 2022) presents an intercomparison study of four different techniques that measured the chemical composition of secondary organic aerosols formed in the CLOUD chamber. The intercomparison examines the chemical composition and calculated volatility of different compounds found in the particles. We also applied Positive Matrix Factorization on TD-DMA and FIGAERO data to study the effect of chemical decomposition when using thermal desorption methods. Overall, the four methods agree on the most important compounds found in the nanoparticles. However, they did see different parts of the organic spectrum due to their specific features. Potential explanations for these differences are suggested.

The third manuscript (Ungeheuer et al., 2022) examines the role of lubricant oil in new particle formation in both laboratory and ambient settings to investigate the ability of lubricant oil to

form new particles. These new particles are an important source of ultrafine particles in the areas nearby large airports. In the ambient measurements taken downwind of Frankfurt International Airport, we found that the fraction of lubricant oil is largest in the smallest particles. In the laboratory, we also observed that evaporated lubricant oil nucleates and forms new particles rapidly. These results suggest that lubricant oil nucleation and subsequent particle growth can occur in the cooling exhaust plumes of aircraft turbofans.

The fourth manuscript (Wang et al., 2022) is a new particle formation study in the CLOUD chamber at CERN. This study shows that nitric acid, sulfuric acid, and ammonia interact synergistically and rapidly to form particles under upper free tropospheric conditions. These particles grow by condensation (driven by the availability of ammonia) up to CCN sizes and INP particles. The ability of these particles to act as a CCN and INP was also found to be as efficient as for desert dust. This mechanism helps account for previous observations of high concentrations of ammonia and ammonium nitrate over the Asia monsoon region.

There are several technical factors that were not addressed on this work, these factors might be considered for further TD-DMA studies:

A. *Temperature estimation of the filament:* for the studies reported in this work, the temperature of the filament was estimated based on the filament resistance and an intercomparison of TD-DMA and FIGAERO thermograms. In the future, we can use a sensitive sensor able to directly measure temperatures on a tiny surface as a more accurate measurement of thermal desorption temperature.
B. *Automation:* currently the TD-DMA measurements are performed in a semi-automatic mode. Software improvements will automate and therefore reduce the operator's intervention.
C. *Further calibration experiments:* reproducible experiments are needed to determine the relation between T_{max} (the temperature of maximum desorption signal) and the saturation concentration at different temperatures and relative humidity. Additionally, calibrations can quantify the contribution of the different compounds detected in the particle-phase.

Besides the technical factors to be considered for future TD-DMA measurements, I suggest some TD-DMA research questions:

A. *Measurements in the field:* so far, the TD-DMA has been applied only in laboratory experiments. A further step will be to bring it to the field. PMF analysis will be a helpful tool to better assess the sources and fate of complex organic mixtures in ambient particles.
B. *Volatility approach:* as mentioned previously, we can calibrate the TD-DMA by measuring the T_{max} of chemical standards that have a known saturation concentration. This calibration is critical for understanding the volatility distribution of different species

in the particle phase. For the manuscripts presented in this work, TD-DMA measurements have so far relied on calculating volatility using the parametrization introduced by Donahue et al. (2011) and modified by Stolzenburg et al. (2018). This approach estimates volatility using the number of carbon and oxygen atoms in specific molecules and accounting for the temperature using the Clausius–Clapeyron equation. We are interested in how an experimental calibration compares to this parameterization and which method provides a better estimation of volatility for TD-DMA measurements.

C. *Thermal decomposition:* in Caudillo et al., 2022, we used a PMF method to investigate thermal decomposition in TD-DMA and FIGAERO data. Specifically, the thermogram of $C_8H_{12}O_4$ shows significant contributions from compounds that are chemically distinct. This unique thermal desorption behavior may result from isomers that have different volatilities. It may also suggest larger species are thermally decomposing within the TD-DMA to produce fragments that desorb at different temperatures than the $C_8H_{12}O_4$ monomer. In the future, we can track some of the possible compounds that fragment and produce C8H12O4 to better understand thermal decomposition.

D. *Size-resolved measurements:* the TD-DMA performs size-resolved measurements for particles ranging from ~ 10 to 30 nm. Nevertheless, it is difficult to capture these small particles during rapid particle growth. Dedicated experiments and ambient measurements with high particle load but slow growth are ideal to collect particles with a specific size.

E. *Measurements of newly form aerosol and aged aerosol:* a flow tube system (FLOTUS at the CLOUD chamber) will be used to pre-age vapors before injecting them into the CLOUD chamber. The TD-DMA can certainly provide the chemical composition of these particles and contribute to the understanding of aging, transport, and chemical reactions in the atmosphere.

F. *Particle phase chemical reactions occurring on surfaces:* It is likely that aging occurs on the TD-DMA filament surface during long particle collection times. Similarly, to thermal decomposition, we have not investigated potential chemical transformations resulting from the TD-DMA sampling technique.

Lastly, in this work we demonstrated the suitability of the TD-DMA for measuring the chemical composition of newly formed particles. For multiple biogenic nucleation experiments at CLOUD, the TD-DMA measurements agreed with other methods on the most important compounds that are found in the nanoparticles. Future efforts should be made to better understand how our sampling method alters the chemical composition of the particles collected (e.g., thermal desorption processes or surface reactions). Closing the gap between sampling and detection as well as using complementary methods will provide a more accurate picture of the real processes occurring in the atmosphere.

8. Zusammenfassung und Ausblick

Nanopartikel werden im Allgemeinen durch die Umwandlung von Gasen zu Partikeln in der Atmosphäre durch einen Prozess namens *New Particle Formation* (NPF) gebildet. Beim NPF-Prozess durchlaufen bestimmte Vorläufergase Oxidationsreaktionen, bei denen kondensierbare Dämpfe entstehen, deren Flüchtigkeit gering genug ist, um sehr kleine Partikel zu bilden. In meiner Arbeit charakterisiere ich die chemische Zusammensetzung von frisch gebildeten Nanopartikeln, die im Labor und im Feld gemessen wurden.

Die chemische Analyse von Nanopartikeln (Partikel mit einem Durchmesser von weniger als 100 nm) stellt eine analytische Herausforderung dar, da sie zwar in großer Zahl vorhanden sind, aber nur eine sehr geringe Masse haben. Der *Thermal Desorption-Differential Mobility Analyzer* (TD-DMA), der mit einem Nitrat-Chemischen Ionisations-Flugzeit-Massenspektrometer (CI-APi-TOF) gekoppelt ist, wurde 2018 von Wagner et al. entwickelt, um diese Herausforderung besser zu meistern. In dieser Arbeit stelle ich vier Manuskripte vor, von denen zwei über TD-DMA-Ergebnisse berichten und mein Hauptprojekt als Erstautorin darstellen.

Das erste TD-DMA-Manuskript behandelt Gas- und Partikelphasenmessungen bei der Oxidation von biogenen Vorläufergasen (α-Pinen und Isopren). Die Experimente wurden in der CLOUD-Kammer am CERN durchgeführt, um die rein biogene Partikelneubildung zu untersuchen. Der TD-DMA wurde mit einem Nitrat-CI-APi-TOF-Massenspektrometer gekoppelt, um Gase zu messen, die thermisch aus dem Aerosol desorbiert wurden. Deshalb wurde für die Messungen in der Gas- und Partikelphase dasselbe chemische Ionisierungsschema und dieselbe Nachweismethode verwendet, um einen direkten Vergleich zu ermöglichen. Mit dieser Methode konnten wir Verbindungen mit den Summenformeln $C_{10}H_{16}O_{3–9}$ und $C_{20}H_{32}O_{5–13}$ in der Partikelphase nachweisen. Insbesondere bei dem Experiment mit zugesetztem Isopren tragen die Verbindungen mit den Summenformeln $C_5H_{10}O_{5–7}$ und $C_{15}H_{24}O_{5–10}$ wesentlich zu den Partikeln bei. Dieses Ergebnis zeigt die Eignung der TD-DMA zur Messung neu gebildeter Nanopartikel und bestätigt, dass Isopren die Bildung neuer Partikel unterdrückt, aber zum Wachstum neu gebildeter Partikel beiträgt.

Das zweite TD-DMA-Manuskript stellt eine Vergleichsstudie von vier verschiedenen Techniken zur Messung der chemischen Zusammensetzung sekundärer organischer Aerosole dar, die in der CLOUD-Kammer gebildet wurden. Der Vergleich untersucht die chemische Zusammensetzung und die berechnete Flüchtigkeit der verschiedenen in den Partikeln gefundenen Verbindungen. Wir haben auch die Positive Matrix-Faktorisierung (PMF) auf TD-DMA- und FIGAERO-Daten angewandt, um die Auswirkungen der chemischen Zersetzung bei der Verwendung von thermischen Desorptionsmethoden zu untersuchen. Insgesamt stimmen die vier Methoden bei den wichtigsten in den Nanopartikeln gefundenen Verbindungen überein. Allerdings wiesen sie

aufgrund ihrer spezifischen Merkmale unterschiedliche Teile des organischen Spektrums nach. Es wurden mögliche Erklärungen für diese Unterschiede vorgeschlagen.

Im dritten Manuskript wird die Rolle von Schmieröl bei der Bildung neuer Partikel mithilfe von Labor- und Feldmessungen untersucht. Diese sind eine wichtige Quelle für ultrafeine Partikel in der Nähe großer Flughäfen. Bei den Umgebungsmessungen im Windschatten des Frankfurter Flughafens haben wir festgestellt, dass der Anteil des Schmieröls in den kleinsten Partikeln am größten ist. Im Labor haben wir außerdem beobachtet, dass verdampftes Schmieröl schnell zu Nukleation führt und neue Partikel entstehen lässt. Diese Ergebnisse deuten darauf hin, dass die Nukleation von Schmieröl und das anschließende Partikelwachstum in den sich abkühlenden Abgasfahnen von Flugzeugturbinen auftreten können.

Das vierte Manuskript ist eine neue Studie zur Partikelbildung in der CLOUD-Kammer am CERN. Diese Studie zeigt, dass Salpetersäure, Schwefelsäure und Ammoniak synergetisch und schnell interagieren, um Partikel unter den Bedingungen der oberen freien Troposphäre zu bilden. Diese Partikel wachsen durch Kondensation (angetrieben durch die Verfügbarkeit von Ammoniak) bis zu Größen von Wolkenkondensationskeimen (CCN) und Eiskeimen (INP). Die Fähigkeit dieser Partikel, als CCN und INP zu wirken, erwies sich als ebenso effizient wie bei Wüstenstaub. Dieser Mechanismus trägt zur Erklärung früherer Beobachtungen bei, bei denen hohe Konzentrationen von Ammoniak und Ammoniumnitrat über der asiatischen Monsunregion festgestellt wurden.

Es gibt mehrere technische Faktoren, die in dieser Arbeit nicht berücksichtigt wurden; diese Faktoren könnten bei künftigen TD-DMA-Studien in Betracht gezogen werden:

A. *Schätzung der Temperatur des Filaments:* Für die in dieser Arbeit beschriebenen Studien wurde die Temperatur des Filaments auf der Grundlage des Filamentwiderstands und eines Vergleichs von TD-DMA- und FIGAERO-Thermogrammen abgeschätzt. In Zukunft kann ein sensitiver Sensor verwendet werden, der die Temperatur auf einer winzigen Oberfläche direkt messen kann, um die Temperatur der thermischen Desorption genauer zu bestimmen.
B. *Automatisierung:* Derzeit werden die TD-DMA-Messungen in einem halbautomatischen Modus durchgeführt. Softwareverbesserungen können die Messungen automatisieren und somit den Eingriff des*r Bedieners*in reduzieren.
C. *Weitere Kalibrierungsexperimente:* Es sind reproduzierbare Experimente erforderlich, um die Beziehung zwischen der Temperatur des maximalen Desorptionssignals, T_{max}, und der Sättigungskonzentration bei verschiedenen Temperaturen und relativer Luftfeuchtigkeit zu bestimmen. Darüber hinaus kann durch Kalibrierungen der Beitrag der verschiedenen in der Partikelphase nachgewiesenen Verbindungen quantifiziert werden.

Neben den technischen Faktoren, die bei künftigen TD-DMA-Messungen zu berücksichtigen sind, schlage ich einige TD-DMA-Forschungsfragen vor:

A. *Feldmessungen:* Bislang wurde der TD-DMA nur in Laborexperimenten eingesetzt. Ein weiterer Schritt wird darin bestehen, den TD-DMA im Feld einzusetzen. Die PMF-Analyse kann dabei ein hilfreiches Instrument sein, um die Quellen und das Schicksal komplexer organischer Mischungen in Umgebungspartikeln besser zu beurteilen.
B. *Volatilitätsansatz:* Wie bereits erwähnt, können wir den TD-DMA kalibrieren, indem wir T_{max} von chemischen Standards messen, die eine bekannte Sättigungskonzentration haben. Diese Kalibrierung ist entscheidend für das Verständnis der Volatilitätsverteilung verschiedener Verbindungen in der Partikelphase. In den in dieser Arbeit vorgestellten Manuskripten beruhen TD-DMA-Messungen bisher auf der Berechnung der Flüchtigkeit unter Verwendung der von Donahue et al. (2011) eingeführten und von Stolzenburg et al. (2018) modifizierten Parametrisierung. Dieser Ansatz schätzt die Flüchtigkeit anhand der Anzahl der Kohlenstoff- und Sauerstoffatome in bestimmten Molekülen und unter Berücksichtigung der Temperatur mithilfe der Clausius-Clapeyron-Gleichung. Ich bin daran interessiert, wie eine experimentelle Kalibrierung im Vergleich zu dieser Parametrisierung aussieht und welche Methode eine bessere Schätzung der Flüchtigkeit für TD-DMA-Messungen liefert.
C. *Thermische Zersetzung:* In Caudillo et al. (2022) wurde eine PMF-Methode zur Untersuchung der thermischen Zersetzung in TD-DMA- und FIGAERO-Daten verwendet. Insbesondere das Thermogramm von $C_8H_{12}O_4$ zeigt signifikante Beiträge von Verbindungen, die chemisch unterschiedlich sind. Dieses einzigartige thermische Desorptionsverhalten kann von Isomeren herrühren, die unterschiedliche Flüchtigkeiten haben. Es könnte auch darauf hindeuten, dass sich größere Spezies innerhalb des TD-DMA thermisch zersetzen, um Fragmente zu erzeugen, die bei anderen Temperaturen desorbieren als das Monomer $C_8H_{12}O_4$. In Zukunft können einige der Verbindungen untersucht werden, die möglicherweise für die Fragmentierung und das Entstehen von $C_8H_{12}O_4$ verantwortlich sind, um die thermische Zersetzung besser zu verstehen.
D. *Größenaufgelöste Messungen:* Der TD-DMA führt größenaufgelöste Messungen für Partikel im Bereich von ~10 bis 30 nm durch. Dennoch ist es schwierig, diese kleinen Partikel während eines schnellen Partikelwachstums zu erfassen. Spezielle Experimente und Umgebungsmessungen mit hoher Partikellast, aber langsamem Wachstum sind ideal, um Partikel mit einer bestimmten Größe zu sammeln.
E. *Messungen von neu gebildetem und gealtertem Aerosol:* Ein Strömungsrohrsystem (FLOTUS in der CLOUD-Kammer) wird verwendet, um Dämpfe vor der Injektion in die CLOUD-Kammer chemisch altern zu lassen. Der TD-DMA kann die chemische Zusammensetzung dieser Partikel liefern und zum Verständnis von Alterung, Transport und chemischen Reaktionen in der Atmosphäre beitragen.

F. *Chemische Reaktionen in der Partikelphase, die auf Oberflächen stattfinden*: Es ist wahrscheinlich, dass auf der Oberfläche des TD-DMA-Filaments während der langen Zeit der Partikelsammlung Alterungsprozesse stattfinden. Ähnlich wie bei der thermischen Zersetzung wurden mögliche chemische Umwandlungen, die sich aus der TD-DMA-Probentechnik ergeben, nicht untersucht.

In dieser Arbeit habe ich die Eignung des TD-DMA für die Messung der chemischen Zusammensetzung neu gebildeter Partikel nachgewiesen. Für mehrere biogene Nukleationsexperimente bei CLOUD stimmten die TD-DMA-Messungen mit anderen Methoden über die wichtigsten Verbindungen, die in den Nanopartikeln gefunden werden, überein. Künftige Anstrengungen sollten unternommen werden, um besser zu verstehen, wie unsere Probenahmemethode die chemische Zusammensetzung der gesammelten Partikel verändert (z. B. durch thermische Desorptionsprozesse oder Oberflächenreaktionen). Das Schließen der Lücke zwischen Probenahme und Nachweis sowie der Einsatz komplementärer Methoden werden ein genaueres Bild der realen Prozesse in der Atmosphäre liefern.

References

Albrecht, B. A.: Aerosols, Cloud Microphysics, and Fractional Cloudiness, Science, 245, 1227-1230, doi:10.1126/science.245.4923.1227, 1989.

Bianchi, F., Kurtén, T., Riva, M., Mohr, C., Rissanen, M. P., Roldin, P., Berndt, T., Crounse, J. D., Wennberg, P. O., and Mentel, T. F.: Highly oxygenated organic molecules (HOM) from gas-phase autoxidation involving peroxy radicals: A key contributor to atmospheric aerosol, Chemical reviews, 119, 3472-3509, 2019.

Caudillo, L., Rörup, B., Heinritzi, M., Marie, G., Simon, M., Wagner, A. C., Müller, T., Granzin, M., Amorim, A., Ataei, F., Baalbaki, R., Bertozzi, B., Brasseur, Z., Chiu, R., Chu, B., Dada, L., Duplissy, J., Finkenzeller, H., Gonzalez Carracedo, L., He, X. C., Hofbauer, V., Kong, W., Lamkaddam, H., Lee, C. P., Lopez, B., Mahfouz, N. G. A., Makhmutov, V., Manninen, H. E., Marten, R., Massabò, D., Mauldin, R. L., Mentler, B., Molteni, U., Onnela, A., Pfeifer, J., Philippov, M., Piedehierro, A. A., Schervish, M., Scholz, W., Schulze, B., Shen, J., Stolzenburg, D., Stozhkov, Y., Surdu, M., Tauber, C., Tham, Y. J., Tian, P., Tomé, A., Vogt, S., Wang, M., Wang, D. S., Weber, S. K., Welti, A., Yonghong, W., Yusheng, W., Zauner-Wieczorek, M., Baltensperger, U., El Haddad, I., Flagan, R. C., Hansel, A., Höhler, K., Kirkby, J., Kulmala, M., Lehtipalo, K., Möhler, O., Saathoff, H., Volkamer, R., Winkler, P. M., Donahue, N. M., Kürten, A., and Curtius, J.: Chemical composition of nanoparticles from α-pinene nucleation and the influence of isoprene and relative humidity at low temperature, Atmos. Chem. Phys., 21, 17099-17114, 10.5194/acp-21-17099-2021, 2021.

Caudillo, L., Surdu, M., Lopez, B., Wang, M., Thoma, M., Bräkling, S., Buchholz, A., Simon, M., Wagner, A. C., Müller, T., Granzin, M., Heinritzi, M., Amorim, A., Bell, D. M., Brasseur, Z., Dada, L., Duplissy, J., Finkenzeller, H., He, X. C., Lamkaddam, H., Mahfouz, N. G. A., Makhmutov, V., Manninen, H. E., Marie, G., Marten, R., Mauldin, R. L., Mentler, B., Onnela, A., Petäjä, T., Pfeifer, J., Philippov, M., Piedehierro, A. A., Rörup, B., Scholz, W., Shen, J., Stolzenburg, D., Tauber, C., Tian, P., Tomé, A., Umo, N. S., Wang, D. S., Wang, Y., Weber, S. K., Welti, A., Zauner-Wieczorek, M., Baltensperger, U., Flagan, R. C., Hansel, A., Kirkby, J., Kulmala, M., Lehtipalo, K., Worsnop, D. R., Haddad, I. E., Donahue, N. M., Vogel, A. L., Kürten, A., and Curtius, J.: An intercomparison study of four different techniques for measuring the chemical composition of nanoparticles, Atmos. Chem. Phys. Discuss., 2022, 1-24, 10.5194/acp-2022-498, 2022.

Chen, D. R., Pui, D. Y. H., Hummes, D., Fissan, H., Quant, F. R., and Sem, G. J.: Design and evaluation of a nanometer aerosol differential mobility analyzer (Nano-DMA), Journal of Aerosol Science, 29, 497-509, https://doi.org/10.1016/S0021-8502(97)10018-0, 1998.

Dickinson, R. E.: Chapter 11 - Interaction Between Future Climate and Terrestrial Carbon and Nitrogen, in: The Future of the World's Climate (Second Edition), edited by: Henderson-Sellers, A., and McGuffie, K., Elsevier, Boston, 289-308, 2012.

Donahue, N. M., Kroll, J., Pandis, S. N., and Robinson, A. L.: A two-dimensional volatility basis set–Part 2: Diagnostics of organic-aerosol evolution, Atmospheric Chemistry and Physics, 12, 615-634, 2012.

Duplissy, J., Merikanto, J., Franchin, A., Tsagkogeorgas, G., Kangasluoma, J., Wimmer, D., Vuollekoski, H., Schobesberger, S., Lehtipalo, K., Flagan, R. C., Brus, D., Donahue, N. M., Vehkamäki, H., Almeida, J., Amorim, A., Barmet, P., Bianchi, F., Breitenlechner, M., Dunne, E. M., Guida, R., Henschel, H., Junninen, H., Kirkby, J., Kürten, A., Kupc, A., Määttänen, A., Makhmutov, V., Mathot, S., Nieminen, T., Onnela, A., Praplan, A. P., Riccobono, F., Rondo, L., Steiner, G., Tome, A., Walther, H., Baltensperger, U., Carslaw, K. S., Dommen, J., Hansel, A., Petäjä, T., Sipilä, M., Stratmann, F., Vrtala, A., Wagner, P. E., Worsnop, D. R., Curtius, J., and Kulmala, M.: Effect of ions on sulfuric acid-water binary particle formation: 2. Experimental data and comparison with QC-normalized classical nucleation theory, Journal of Geophysical Research: Atmospheres, 121, 1752-1775, 10.1002/2015JD023539, 2016.

Ehn, M., Thornton, J. A., Kleist, E., Sipila, M., Junninen, H., Pullinen, I., Springer, M., Rubach, F., Tillmann, R., Lee, B., Lopez-Hilfiker, F., Andres, S., Acir, I.-H., Rissanen, M., Jokinen, T., Schobesberger, S., Kangasluoma, J., Kontkanen, J., Nieminen, T., Kurten, T., Nielsen, L. B., Jorgensen, S., Kjaergaard, H. G., Canagaratna, M., Maso, M. D., Berndt, T., Petaja, T., Wahner, A., Kerminen, V.-M., Kulmala, M., Worsnop, D. R., Wildt, J., and Mentel, T. F.: A large source of low-volatility secondary organic aerosol, Nature, 506, 476-479, 10.1038/nature13032, 2014.

Flagan, R. C.: Differential Mobility Analysis of Aerosols: A Tutorial, KONA Powder and Particle Journal, 26, 254-268, 10.14356/kona.2008023, 2008.

Guenther, A., Karl, T., Harley, P., Wiedinmyer, C., Palmer, P. I., and Geron, C.: Estimates of global terrestrial isoprene emissions using MEGAN (Model of Emissions of Gases and Aerosols from Nature), Atmos. Chem. Phys., 6, 3181-3210, 10.5194/acp-6-3181-2006, 2006.

Habre, R., Zhou, H., Eckel, S. P., Enebish, T., Fruin, S., Bastain, T., Rappaport, E., and Gilliland, F.: Short-term effects of airport-associated ultrafine particle exposure on lung function and inflammation in adults with asthma, Environ Int, 118, 48-59, 10.1016/j.envint.2018.05.031, 2018.

Harrison, A. G.: Chemical ionization mass spectrometry, Routledge, New York, 1992.

He, X.-C., Tham, Y. J., Dada, L., Wang, M., Finkenzeller, H., Stolzenburg, D., Iyer, S., Simon, M., Kürten, A., Shen, J., Rörup, B., Rissanen, M., Schobesberger, S., Baalbaki, R., Wang, D. S., Koenig, T. K., Jokinen, T., Sarnela, N., Beck, L. J., Almeida, J., Amanatidis, S., Amorim, A., Ataei, F., Baccarini, A., Bertozzi, B., Bianchi, F., Brilke, S., Caudillo, L., Chen, D., Chiu, R., Chu, B., Dias, A., Ding, A., Dommen, J., Duplissy, J., El Haddad, I., Gonzalez Carracedo, L.,

Granzin, M., Hansel, A., Heinritzi, M., Hofbauer, V., Junninen, H., Kangasluoma, J., Kemppainen, D., Kim, C., Kong, W., Krechmer, J. E., Kvashin, A., Laitinen, T., Lamkaddam, H., Lee, C. P., Lehtipalo, K., Leiminger, M., Li, Z., Makhmutov, V., Manninen, H. E., Marie, G., Marten, R., Mathot, S., Mauldin, R. L., Mentler, B., Möhler, O., Müller, T., Nie, W., Onnela, A., Petäjä, T., Pfeifer, J., Philippov, M., Ranjithkumar, A., Saiz-Lopez, A., Salma, I., Scholz, W., Schuchmann, S., Schulze, B., Steiner, G., Stozhkov, Y., Tauber, C., Tomé, A., Thakur, R. C., Väisänen, O., Vazquez-Pufleau, M., Wagner, A. C., Wang, Y., Weber, S. K., Winkler, P. M., Wu, Y., Xiao, M., Yan, C., Ye, Q., Ylisirniö, A., Zauner-Wieczorek, M., Zha, Q., Zhou, P., Flagan, R. C., Curtius, J., Baltensperger, U., Kulmala, M., Kerminen, V.-M., Kurtén, T., Donahue, N. M., Volkamer, R., Kirkby, J., Worsnop, D. R., and Sipilä, M.: Role of iodine oxoacids in atmospheric aerosol nucleation, Science, 371, 589-595, 10.1126/science.abe0298, 2021.

HEI: Understanding the Health Effects of Ambient Ultrafine Particles, Review Panel on Ultrafine Particles, Health Effects Institute, Boston, MA, 2013.

Heinritzi, M., Dada, L., Simon, M., Stolzenburg, D., Wagner, A. C., Fischer, L., Ahonen, L. R., Amanatidis, S., Baalbaki, R., Baccarini, A., Bauer, P. S., Baumgartner, B., Bianchi, F., Brilke, S., Chen, D., Chiu, R., Dias, A., Dommen, J., Duplissy, J., Finkenzeller, H., Frege, C., Fuchs, C., Garmash, O., Gordon, H., Granzin, M., El Haddad, I., He, X., Helm, J., Hofbauer, V., Hoyle, C. R., Kangasluoma, J., Keber, T., Kim, C., Kürten, A., Lamkaddam, H., Laurila, T. M., Lampilahti, J., Lee, C. P., Lehtipalo, K., Leiminger, M., Mai, H., Makhmutov, V., Manninen, H. E., Marten, R., Mathot, S., Mauldin, R. L., Mentler, B., Molteni, U., Müller, T., Nie, W., Nieminen, T., Onnela, A., Partoll, E., Passananti, M., Petäjä, T., Pfeifer, J., Pospisilova, V., Quéléver, L. L. J., Rissanen, M. P., Rose, C., Schobesberger, S., Scholz, W., Scholze, K., Sipilä, M., Steiner, G., Stozhkov, Y., Tauber, C., Tham, Y. J., Vazquez-Pufleau, M., Virtanen, A., Vogel, A. L., Volkamer, R., Wagner, R., Wang, M., Weitz, L., Wimmer, D., Xiao, M., Yan, C., Ye, P., Zha, Q., Zhou, X., Amorim, A., Baltensperger, U., Hansel, A., Kulmala, M., Tomé, A., Winkler, P. M., Worsnop, D. R., Donahue, N. M., Kirkby, J., and Curtius, J.: Molecular understanding of the suppression of new-particle formation by isoprene, Atmos. Chem. Phys., 20, 11809-11821, 10.5194/acp-20-11809-2020, 2020.

Hinds, W. C.: Aerosol Technology: Properties, Behavior, and Measurement of Airborne Particles, Wiley, 1999.

Huang, R.-J., Zhang, Y., Bozzetti, C., Ho, K.-F., Cao, J.-J., Han, Y., Daellenbach, K. R., Slowik, J. G., Platt, S. M., Canonaco, F., Zotter, P., Wolf, R., Pieber, S. M., Bruns, E. A., Crippa, M., Ciarelli, G., Piazzalunga, A., Schwikowski, M., Abbaszade, G., Schnelle-Kreis, J., Zimmermann, R., An, Z., Szidat, S., Baltensperger, U., Haddad, I. E., and Prévôt, A. S. H.: High secondary aerosol contribution to particulate pollution during haze events in China, Nature, 514, 218-222, 10.1038/nature13774, 2014.

Jokinen, T., Sipilä, M., Junninen, H., Ehn, M., Lönn, G., Hakala, J., Petäjä, T., Mauldin Iii, R. L., Kulmala, M., and Worsnop, D. R.: Atmospheric sulphuric acid and neutral cluster measurements using CI-APi-TOF, Atmos. Chem. Phys., 12, 4117-4125, 10.5194/acp-12-4117-2012, 2012.

Kiendler-Scharr, A., Wildt, J., Maso, M. D., Hohaus, T., Kleist, E., Mentel, T. F., Tillmann, R., Uerlings, R., Schurr, U., and Wahner, A.: New particle formation in forests inhibited by isoprene emissions, Nature, 461, 381-384, 2009.

Kirkby, J., Curtius, J., Almeida, J., Dunne, E., Duplissy, J., Ehrhart, S., Franchin, A., Gagné, S., Ickes, L., Kürten, A., Kupc, A., Metzger, A., Riccobono, F., Rondo, L., Schobesberger, S., Tsagkogeorgas, G., Wimmer, D., Amorim, A., Bianchi, F., Breitenlechner, M., David, A., Dommen, J., Downard, A., Ehn, M., Flagan, R. C., Haider, S., Hansel, A., Hauser, D., Jud, W., Junninen, H., Kreissl, F., Kvashin, A., Laaksonen, A., Lehtipalo, K., Lima, J., Lovejoy, E. R., Makhmutov, V., Mathot, S., Mikkilä, J., Minginette, P., Mogo, S., Nieminen, T., Onnela, A., Pereira, P., Petäjä, T., Schnitzhofer, R., Seinfeld, J. H., Sipilä, M., Stozhkov, Y., Stratmann, F., Tomé, A., Vanhanen, J., Viisanen, Y., Vrtala, A., Wagner, P. E., Walther, H., Weingartner, E., Wex, H., Winkler, P. M., Carslaw, K. S., Worsnop, D. R., Baltensperger, U., and Kulmala, M.: Role of sulphuric acid, ammonia and galactic cosmic rays in atmospheric aerosol nucleation, Nature, 476, 429-433, 10.1038/nature10343, 2011.

Kirkby, J., Duplissy, J., Sengupta, K., Frege, C., Gordon, H., Williamson, C., Heinritzi, M., Simon, M., Yan, C., Almeida, J., Tröstl, J., Nieminen, T., Ortega, I. K., Wagner, R., Adamov, A., Amorim, A., Bernhammer, A.-K., Bianchi, F., Breitenlechner, M., Brilke, S., Chen, X., Craven, J., Dias, A., Ehrhart, S., Flagan, R. C., Franchin, A., Fuchs, C., Guida, R., Hakala, J., Hoyle, C. R., Jokinen, T., Junninen, H., Kangasluoma, J., Kim, J., Krapf, M., Kürten, A., Laaksonen, A., Lehtipalo, K., Makhmutov, V., Mathot, S., Molteni, U., Onnela, A., Peräkylä, O., Piel, F., Petäjä, T., Praplan, A. P., Pringle, K., Rap, A., Richards, N. A. D., Riipinen, I., Rissanen, M. P., Rondo, L., Sarnela, N., Schobesberger, S., Scott, C. E., Seinfeld, J. H., Sipilä, M., Steiner, G., Stozhkov, Y., Stratmann, F., Tomé, A., Virtanen, A., Vogel, A. L., Wagner, A. C., Wagner, P. E., Weingartner, E., Wimmer, D., Winkler, P. M., Ye, P., Zhang, X., Hansel, A., Dommen, J., Donahue, N. M., Worsnop, D. R., Baltensperger, U., Kulmala, M., Carslaw, K. S., and Curtius, J.: Ion-induced nucleation of pure biogenic particles, Nature, 533, 521-526, 10.1038/nature17953, 2016.

Knutson, E. O., and Whitby, K. T.: Aerosol classification by electric mobility: apparatus, theory, and applications, Journal of Aerosol Science, 6, 443-451, https://doi.org/10.1016/0021-8502(75)90060-9, 1975.

Kulmala, M., Dada, L., Daellenbach, K. R., Yan, C., Stolzenburg, D., Kontkanen, J., Ezhova, E., Hakala, S., Tuovinen, S., Kokkonen, T. V., Kurppa, M., Cai, R., Zhou, Y., Yin, R., Baalbaki, R., Chan, T., Chu, B., Deng, C., Fu, Y., Ge, M., He, H., Heikkinen, L., Junninen, H., Liu, Y., Lu, Y., Nie, W., Rusanen, A., Vakkari, V., Wang, Y., Yang, G., Yao, L., Zheng, J., Kujansuu, J., Kangasluoma, J., Petäjä, T., Paasonen, P., Järvi, L., Worsnop, D., Ding, A., Liu, Y., Wang, L., Jiang, J., Bianchi, F., and Kerminen, V.-M.: Is reducing new particle formation a plausible

solution to mitigate particulate air pollution in Beijing and other Chinese megacities?, Faraday Discussions, 226, 334-347, 10.1039/D0FD00078G, 2021.

Kürten, A., Rondo, L., Ehrhart, S., and Curtius, J.: Performance of a corona ion source for measurement of sulfuric acid by chemical ionization mass spectrometry, Atmos. Meas. Tech., 4, 437-443, 10.5194/amt-4-437-2011, 2011.

Kürten, A., Jokinen, T., Simon, M., Sipilä, M., Sarnela, N., Junninen, H., Adamov, A., Almeida, J., Amorim, A., Bianchi, F., Breitenlechner, M., Dommen, J., Donahue, N. M., Duplissy, J., Ehrhart, S., Flagan, R. C., Franchin, A., Hakala, J., Hansel, A., Heinritzi, M., Hutterli, M., Kangasluoma, J., Kirkby, J., Laaksonen, A., Lehtipalo, K., Leiminger, M., Makhmutov, V., Mathot, S., Onnela, A., Petäjä, T., Praplan, A. P., Riccobono, F., Rissanen, M. P., Rondo, L., Schobesberger, S., Seinfeld, J. H., Steiner, G., Tomé, A., Tröstl, J., Winkler, P. M., Williamson, C., Wimmer, D., Ye, P., Baltensperger, U., Carslaw, K. S., Kulmala, M., Worsnop, D. R., and Curtius, J.: Neutral molecular cluster formation of sulfuric acid–dimethylamine observed in real time under atmospheric conditions, Proceedings of the National Academy of Sciences, 111, 15019-15024, 10.1073/pnas.1404853111, 2014.

Kürten, A., Bergen, A., Heinritzi, M., Leiminger, M., Lorenz, V., Piel, F., Simon, M., Sitals, R., Wagner, A. C., and Curtius, J.: Observation of new particle formation and measurement of sulfuric acid, ammonia, amines and highly oxidized organic molecules at a rural site in central Germany, Atmospheric Chemistry and Physics, 16, 12793-12813, 2016.

Lee, H. M., Soo Kim, C., Shimada, M., and Okuyama, K.: Bipolar diffusion charging for aerosol nanoparticle measurement using a soft X-ray charger, Journal of Aerosol Science, 36, 813-829, https://doi.org/10.1016/j.jaerosci.2004.10.011, 2005.

Leikauf, G. D., Kim, S.-H., and Jang, A.-S.: Mechanisms of ultrafine particle-induced respiratory health effects, Experimental & Molecular Medicine, 52, 329-337, 10.1038/s12276-020-0394-0, 2020.

Marten, R., Xiao, M., Rörup, B., Wang, M., Kong, W., He, X.-C., Stolzenburg, D., Pfeifer, J., Marie, G., Wang, D. S., Scholz, W., Baccarini, A., Lee, C. P., Amorim, A., Baalbaki, R., Bell, D. M., Bertozzi, B., Caudillo, L., Chu, B., Dada, L., Duplissy, J., Finkenzeller, H., Carracedo, L. G., Granzin, M., Hansel, A., Heinritzi, M., Hofbauer, V., Kemppainen, D., Kürten, A., Lampimäki, M., Lehtipalo, K., Makhmutov, V., Manninen, H. E., Mentler, B., Petäjä, T., Philippov, M., Shen, J., Simon, M., Stozhkov, Y., Tomé, A., Wagner, A. C., Wang, Y., Weber, S. K., Wu, Y., Zauner-Wieczorek, M., Curtius, J., Kulmala, M., Möhler, O., Volkamer, R., Winkler, P. M., Worsnop, D. R., Dommen, J., Flagan, R. C., Kirkby, J., Donahue, N. M., Lamkaddam, H., Baltensperger, U., and El Haddad, I.: Survival of newly formed particles in haze conditions, Environmental Science: Atmospheres, 2, 491-499, 10.1039/D2EA00007E, 2022.

Møller, K. L., Brauer, C., Mikkelsen, S., Bonde, J. P., Loft, S., Helweg-Larsen, K., and Thygesen, L. C.: Cardiovascular disease and long-term occupational exposure to ultrafine particles: A cohort study of airport workers, International Journal of Hygiene and Environmental Health, 223, 214-219, https://doi.org/10.1016/j.ijheh.2019.08.010, 2020.

Müller, T.: Experimental Chemical Characterization of Nanoparticles Generated from Car and Jet Oil, Master of Science, Institute for Environmental and Atmospheric Science of the department 11 - Geography and Earth Science, Johann Wolfgang Goethe-University, Frankfurt am Main, 2020.

Munson, M. S., and Field, F.-H.: Chemical ionization mass spectrometry. I. General introduction, Journal of the American Chemical Society, 88, 2621-2630, 1966.

Murray, K. K., Boyd, R. K., Eberlin, M. N., Langley, G. J., Li, L., and Naito, Y.: Definitions of terms relating to mass spectrometry (IUPAC Recommendations 2013), Pure and Applied Chemistry, 85, 1515-1609, doi:10.1351/PAC-REC-06-04-06, 2013.

Niu, X., Huang, Y., Lee, S. C., Sun, J., and Ho, K. F.: Surface Characterization of Secondary Organic Aerosols from Ozonolysis of Monoterpene and the Effects of Acute Lung Injury in Mice, Aerosol and Air Quality Research, 10.4209/aaqr.2019.12.0628, 2020.

Ohlwein, S., Kappeler, R., Kutlar Joss, M., Künzli, N., and Hoffmann, B.: Health effects of ultrafine particles: a systematic literature review update of epidemiological evidence, International journal of public health, 64, 547-559, 10.1007/s00038-019-01202-7, 2019.

Pöschl, U.: Atmospheric Aerosols: Composition, Transformation, Climate and Health Effects, Angewandte Chemie International Edition, 44, 7520-7540, https://doi.org/10.1002/anie.200501122, 2005.

Pye, H. O. T., Ward-Caviness, C. K., Murphy, B. N., Appel, K. W., and Seltzer, K. M.: Secondary organic aerosol association with cardiorespiratory disease mortality in the United States, Nature Communications, 12, 7215, 10.1038/s41467-021-27484-1, 2021.

Ramanathan, V., Crutzen, P. J., Kiehl, J. T., and Rosenfeld, D.: Aerosols, Climate, and the Hydrological Cycle, Science, 294, 2119-2124, doi:10.1126/science.1064034, 2001.

Reischl, G. P., Mäkelä, J. M., and Necid, J.: Performance of Vienna Type Differential Mobility Analyzer at 1.2–20 Nanometer, Aerosol Science and Technology, 27, 651-672, 10.1080/02786829708965503, 1997.

Riipinen, I., Pierce, J. R., Yli-Juuti, T., Nieminen, T., Häkkinen, S., Ehn, M., Junninen, H., Lehtipalo, K., Petäjä, T., Slowik, J., Chang, R., Shantz, N. C., Abbatt, J., Leaitch, W. R., Kerminen, V. M., Worsnop, D. R., Pandis, S. N., Donahue, N. M., and Kulmala, M.: Organic condensation: a vital link connecting aerosol formation to cloud condensation nuclei (CCN) concentrations, Atmos. Chem. Phys., 11, 3865-3878, 10.5194/acp-11-3865-2011, 2011.

Schervish, M., and Donahue, N. M.: Peroxy radical chemistry and the volatility basis set, Atmos. Chem. Phys., 20, 1183-1199, 10.5194/acp-20-1183-2020, 2020.

Schnitzhofer, R., Metzger, A., Breitenlechner, M., Jud, W., Heinritzi, M., De Menezes, L. P., Duplissy, J., Guida, R., Haider, S., Kirkby, J., Mathot, S., Minginette, P., Onnela, A., Walther, H., Wasem, A., Hansel, A., and the, C. T.: Characterisation of organic contaminants in the CLOUD chamber at CERN, Atmos. Meas. Tech., 7, 2159-2168, 10.5194/amt-7-2159-2014, 2014.

Schraufnagel, D. E.: The health effects of ultrafine particles, Experimental & Molecular Medicine, 52, 311-317, 10.1038/s12276-020-0403-3, 2020.

Shen, J., Scholz, W., He, X.-C., Zhou, P., Marie, G., Wang, M., Marten, R., Surdu, M., Rörup, B., Baalbaki, R., Amorim, A., Ataei, F., Bell, D. M., Bertozzi, B., Brasseur, Z., Caudillo, L., Chen, D., Chu, B., Dada, L., Duplissy, J., Finkenzeller, H., Granzin, M., Guida, R., Heinritzi, M., Hofbauer, V., Iyer, S., Kemppainen, D., Kong, W., Krechmer, J. E., Kürten, A., Lamkaddam, H., Lee, C. P., Lopez, B., Mahfouz, N. G. A., Manninen, H. E., Massabò, D., Mauldin, R. L., Mentler, B., Müller, T., Pfeifer, J., Philippov, M., Piedehierro, A. A., Roldin, P., Schobesberger, S., Simon, M., Stolzenburg, D., Tham, Y. J., Tomé, A., Umo, N. S., Wang, D., Wang, Y., Weber, S. K., Welti, A., Wollesen de Jonge, R., Wu, Y., Zauner-Wieczorek, M., Zust, F., Baltensperger, U., Curtius, J., Flagan, R. C., Hansel, A., Möhler, O., Petäjä, T., Volkamer, R., Kulmala, M., Lehtipalo, K., Rissanen, M., Kirkby, J., El-Haddad, I., Bianchi, F., Sipilä, M., Donahue, N. M., and Worsnop, D. R.: High Gas-Phase Methanesulfonic Acid Production in the OH-Initiated Oxidation of Dimethyl Sulfide at Low Temperatures, Environmental Science & Technology, 56, 13931-13944, 10.1021/acs.est.2c05154, 2022.

Simon, M., Heinritzi, M., Herzog, S., Leiminger, M., Bianchi, F., Praplan, A., Dommen, J., Curtius, J., and Kürten, A.: Detection of dimethylamine in the low pptv range using nitrate chemical ionization atmospheric pressure interface time-of-flight (CI-APi-TOF) mass spectrometry, Atmos. Meas. Tech., 9, 2135-2145, 10.5194/amt-9-2135-2016, 2016.

Simon, M., Dada, L., Heinritzi, M., Scholz, W., Stolzenburg, D., Fischer, L., Wagner, A. C., Kürten, A., Rörup, B., He, X. C., Almeida, J., Baalbaki, R., Baccarini, A., Bauer, P. S., Beck, L., Bergen, A., Bianchi, F., Bräkling, S., Brilke, S., Caudillo, L., Chen, D., Chu, B., Dias, A., Draper, D. C., Duplissy, J., El-Haddad, I., Finkenzeller, H., Frege, C., Gonzalez-Carracedo, L., Gordon, H., Granzin, M., Hakala, J., Hofbauer, V., Hoyle, C. R., Kim, C., Kong, W., Lamkaddam, H., Lee, C. P., Lehtipalo, K., Leiminger, M., Mai, H., Manninen, H. E., Marie, G.,

Marten, R., Mentler, B., Molteni, U., Nichman, L., Nie, W., Ojdanic, A., Onnela, A., Partoll, E., Petäjä, T., Pfeifer, J., Philippov, M., Quéléver, L. L. J., Ranjithkumar, A., Rissanen, M. P., Schallhart, S., Schobesberger, S., Schuchmann, S., Shen, J., Sipilä, M., Steiner, G., Stozhkov, Y., Tauber, C., Tham, Y. J., Tomé, A. R., Vazquez-Pufleau, M., Vogel, A. L., Wagner, R., Wang, M., Wang, D. S., Wang, Y., Weber, S. K., Wu, Y., Xiao, M., Yan, C., Ye, P., Ye, Q., Zauner-Wieczorek, M., Zhou, X., Baltensperger, U., Dommen, J., Flagan, R. C., Hansel, A., Kulmala, M., Volkamer, R., Winkler, P. M., Worsnop, D. R., Donahue, N. M., Kirkby, J., and Curtius, J.: Molecular understanding of new-particle formation from α-pinene between −50 and +25 °C, Atmos. Chem. Phys., 20, 9183-9207, 10.5194/acp-20-9183-2020, 2020.

Sindelarova, K., Granier, C., Bouarar, I., Guenther, A., Tilmes, S., Stavrakou, T., Müller, J. F., Kuhn, U., Stefani, P., and Knorr, W.: Global data set of biogenic VOC emissions calculated by the MEGAN model over the last 30 years, Atmos. Chem. Phys., 14, 9317-9341, 10.5194/acp-14-9317-2014, 2014.

Stolzenburg, D., Simon, M., Ranjithkumar, A., Kürten, A., Lehtipalo, K., Gordon, H., Ehrhart, S., Finkenzeller, H., Pichelstorfer, L., Nieminen, T., He, X. C., Brilke, S., Xiao, M., Amorim, A., Baalbaki, R., Baccarini, A., Beck, L., Bräkling, S., Caudillo Murillo, L., Chen, D., Chu, B., Dada, L., Dias, A., Dommen, J., Duplissy, J., El Haddad, I., Fischer, L., Gonzalez Carracedo, L., Heinritzi, M., Kim, C., Koenig, T. K., Kong, W., Lamkaddam, H., Lee, C. P., Leiminger, M., Li, Z., Makhmutov, V., Manninen, H. E., Marie, G., Marten, R., Müller, T., Nie, W., Partoll, E., Petäjä, T., Pfeifer, J., Philippov, M., Rissanen, M. P., Rörup, B., Schobesberger, S., Schuchmann, S., Shen, J., Sipilä, M., Steiner, G., Stozhkov, Y., Tauber, C., Tham, Y. J., Tomé, A., Vazquez-Pufleau, M., Wagner, A. C., Wang, M., Wang, Y., Weber, S. K., Wimmer, D., Wlasits, P. J., Wu, Y., Ye, Q., Zauner-Wieczorek, M., Baltensperger, U., Carslaw, K. S., Curtius, J., Donahue, N. M., Flagan, R. C., Hansel, A., Kulmala, M., Lelieveld, J., Volkamer, R., Kirkby, J., and Winkler, P. M.: Enhanced growth rate of atmospheric particles from sulfuric acid, Atmos. Chem. Phys., 20, 7359-7372, 10.5194/acp-20-7359-2020, 2020.

TSI: Advance Aerosol Neutralizer Model 3088, 2010.

Tuet, W. Y., Chen, Y., Fok, S., Champion, J. A., and Ng, N. L.: Inflammatory responses to secondary organic aerosols (SOA) generated from biogenic and anthropogenic precursors, Atmos. Chem. Phys., 17, 11423-11440, 10.5194/acp-17-11423-2017, 2017.

Twomey, S.: Pollution and the planetary albedo, Atmospheric Environment (1967), 8, 1251-1256, https://doi.org/10.1016/0004-6981(74)90004-3, 1974.

Wagner, A. C., Bergen, A., Brilke, S., Fuchs, C., Ernst, M., Hoker, J., Heinritzi, M., Simon, M., Bühner, B., and Curtius, J.: Size-resolved online chemical analysis of nanoaerosol particles: a thermal desorption differential mobility analyzer coupled to a chemical ionization time-of-flight mass spectrometer, Atmospheric Measurement Techniques, 11, 5489-5506, 2018.

Wang, M., Kong, W., Marten, R., He, X.-C., Chen, D., Pfeifer, J., Heitto, A., Kontkanen, J., Dada, L., Kürten, A., Yli-Juuti, T., Manninen, H. E., Amanatidis, S., Amorim, A., Baalbaki, R., Baccarini, A., Bell, D. M., Bertozzi, B., Bräkling, S., Brilke, S., Murillo, L. C., Chiu, R., Chu, B., De Menezes, L.-P., Duplissy, J., Finkenzeller, H., Carracedo, L. G., Granzin, M., Guida, R., Hansel, A., Hofbauer, V., Krechmer, J., Lehtipalo, K., Lamkaddam, H., Lampimäki, M., Lee, C. P., Makhmutov, V., Marie, G., Mathot, S., Mauldin, R. L., Mentler, B., Müller, T., Onnela, A., Partoll, E., Petäjä, T., Philippov, M., Pospisilova, V., Ranjithkumar, A., Rissanen, M., Rörup, B., Scholz, W., Shen, J., Simon, M., Sipilä, M., Steiner, G., Stolzenburg, D., Tham, Y. J., Tomé, A., Wagner, A. C., Wang, D. S., Wang, Y., Weber, S. K., Winkler, P. M., Wlasits, P. J., Wu, Y., Xiao, M., Ye, Q., Zauner-Wieczorek, M., Zhou, X., Volkamer, R., Riipinen, I., Dommen, J., Curtius, J., Baltensperger, U., Kulmala, M., Worsnop, D. R., Kirkby, J., Seinfeld, J. H., El-Haddad, I., Flagan, R. C., and Donahue, N. M.: Rapid growth of new atmospheric particles by nitric acid and ammonia condensation, Nature, 581, 184-189, 10.1038/s41586-020-2270-4, 2020.

Wang, M., Xiao, M., Bertozzi, B., Marie, G., Rörup, B., Schulze, B., Bardakov, R., He, X.-C., Shen, J., Scholz, W., Marten, R., Dada, L., Baalbaki, R., Lopez, B., Lamkaddam, H., Manninen, H. E., Amorim, A., Ataei, F., Bogert, P., Brasseur, Z., Caudillo, L., De Menezes, L.-P., Duplissy, J., Ekman, A. M. L., Finkenzeller, H., Carracedo, L. G., Granzin, M., Guida, R., Heinritzi, M., Hofbauer, V., Höhler, K., Korhonen, K., Krechmer, J. E., Kürten, A., Lehtipalo, K., Mahfouz, N. G. A., Makhmutov, V., Massabò, D., Mathot, S., Mauldin, R. L., Mentler, B., Müller, T., Onnela, A., Petäjä, T., Philippov, M., Piedehierro, A. A., Pozzer, A., Ranjithkumar, A., Schervish, M., Schobesberger, S., Simon, M., Stozhkov, Y., Tomé, A., Umo, N. S., Vogel, F., Wagner, R., Wang, D. S., Weber, S. K., Welti, A., Wu, Y., Zauner-Wieczorek, M., Sipilä, M., Winkler, P. M., Hansel, A., Baltensperger, U., Kulmala, M., Flagan, R. C., Curtius, J., Riipinen, I., Gordon, H., Lelieveld, J., El-Haddad, I., Volkamer, R., Worsnop, D. R., Christoudias, T., Kirkby, J., Möhler, O., and Donahue, N. M.: Synergistic HNO3–H2SO4–NH3 upper tropospheric particle formation, Nature, 605, 483-489, 10.1038/s41586-022-04605-4, 2022.

Appendix I. Summary of additional publications as a co-author

Survival of newly formed particles in haze conditions, Marten et al. (2022). Published on Environmental Science: Atmospheres on March 24th, 2022.

Here, CLOUD chamber experiments were performed to simulate typical ambient conditions of a polluted megacity. In megacities is frequently observed that new particle formation occurs despite high condensation sinks (presence of particles d > 100 nm).

For conducting the experiments, NO, SO_2, toluene, α-pinene, HONO, NH_3, O_3, and dimethylamine were mixed at 5 ºC and 60 % RH. The experiments showed that despite the high condensation sink, small particles can survive and grow up to larger sizes if there is sufficient HNO_3 and NH_3.

This means that, it is likely that under typical polluted conditions of a megacity, ammonium nitrate condensation can occur and increase survival of nucleated particles. Therefore, this mechanism might explain how both the particle number and poor visibility during haze are sustained.

Role of iodine oxoacids in atmospheric aerosol nucleation, He et al. (2021). Published on Science on February 5th, 2021.

CLOUD experiments were performed to simulate new particle formation in a marine ambient. The experiments were conducted at +10 ºC and -10 ºC, at 34 to 73% RH. Iodine (I_2) and ozone were introduced into the chamber, this produced iodine oxoacids such as iodic acid (HIO_3) and iodous acid (HIO_2).

He et al. (2021) showed that the nucleation rate of iodine oxoacids exceeds H_2SO_4-NH_3 nucleation at the same acid concentrations. Specifically, it was found that HIO_3 is the major iodine specie that drives both nucleation and growth of the newly formed particles.

In addition, the mechanism behind the formation of new particles by iodine oxoacids has been described in this article: by ion-induced nucleation (involving IO_3^- and the sequential addition of HIO_3) and, by neutral nucleation (with the repeated addition of HIO_2 followed by HIO_3).

Rapid growth of new atmospheric particles by nitric acid and ammonia condensation, Wang et al. (2020). Published on Nature on May 13th, 2020.

In this paper, Wang et al. (2020) reported CLOUD chamber experiments with mixtures of nitric acid, sulfuric acid and ammonia to simulate constituents of a polluted megacity.

The experiments were performed at temperatures from +20 ºC to -25 ºC and, it was found that at very cold temperatures (below -15 ºC), nitric acid and ammonia can nucleate in the absence of sulfuric acid. With nucleation rates close to 100 nm/h. This indicates that, pure ammonium nitrate nucleation can produce rapidly new particles at upper free tropospheric conditions.

Besides, it was found that at typical conditions of a megacity, nitric acid and ammonia can condense on the very small particles (that are more vulnerable to be lost by coagulation in ambientes with high coagulation sink). As a result, this mechanism increases their probability to survive and grow.

Molecular understanding of new-particle formation from α-pinene between -50 and +25 ºC, Simon et al. (2020). Published on Atmospheric Chemistry and Physics on August 3rd, 2020.

Simon et al. (2020) performed biogenic NPF experiments in the CLOUD chamber to produce Highly Oxygenated Organic Molecules (HOMs) by α-pinene ozonolysis.

Both autoxidation reaction forming HOMs and their nucleation rates depend strongly on the temperature. Thus, dedicated experiments were conducted in a wide range of temperatures from +25 °C to -50 °C at α-pinene levels between 100 to 2000 pptv and ozone levels between 30 - 40 ppbv.

Simon et al. (2020) observed that, the O/C ratio and yield of HOMs decrease as the temperature decreases. Despite the lower oxidation level and lower yield of HOMs (at low temperatures), the nucleation rates increase due to the reduction in volatility of all oxidized compounds. This is a compensating phenomenon which enhances the nucleation of HOMs at low temperature, representative for the upper free troposphere.

Enhanced growth rate of atmospheric particles from sulfuric acid, Stolzenburg et al. (2020). Published on Atmospheric Chemistry and Physics on June 25th, 2020.

CLOUD chamber experiments were performed to produce new particle formation from H_2SO_4-NH_3 at 5 ºC and 20 ºC. The goal of these experiments was to measure very precisely the growth rates of sulfuric acid particles with very small sizes (from 1.8 nm to 10 nm).

It was found that the evaporation of sulfuric acid particles above 2 nm is negligible, and growth proceeds kinetically even at low ammonia concentrations.

These results were implemented in a global model. It was found that predicted particle number concentrations in the upper free troposphere increases by more than 50 %. Besides these findings, Stolzenburg et al. (2020) set a new baseline for pure sulfuric acid condensation, which can help to identify the contribution of other gases to growth.

High Gas-Phase Methanesulfonic Acid Production in the OH-Initiated Oxidation of Dimethyl Sulfide at Low Temperatures, Shen et al. (2022). Published on Environmental Science & Technology on September 22nd, 2022.

In this Manuscript, Shen et al., 2022, showed experimental evidence of the strong temperature dependence of Methanesulfonic acid (MSA) production from Dimethyl Sulfide (DMS).

By performing controlled experiments in the CLOUD chamber at CERN and simulating with a numerical box model, Shen et al., 2022, suggests that when DMS is oxidized at low temperatures (< 0 ºC) some of the intermediate species (Methanesulfinic acid, MSIA), contribute to the final production of MSA while not affect substantially the production of H_2SO_4.

The enhancement of MSA at low temperatures was confirmed by following (experimentally) the kinetics of the gas-phase reactions and modeling the DMS oxidation mechanism. In general, there was a good agreement between the model, experimental results, and ambient observations when the additional pathways were considered in the chemical oxidation model.

This new updated DMS oxidation mechanism can be a key to understand the formation of gas-phase MSA and H_2SO_4 in the remote atmosphere.

Molecular understanding of the enhancement in organic aerosol mass at high relative humidity, Surdu et al. (2022). Submitted to Environmental Science & Technology on June 26th, 2022.

In this manuscript, Surdu et al., report gas and particle-phase real-time measurements of organic compounds. The experiments were performed in the CLOUD chamber at low temperatures (-10 ºC and -30 ºC) and at different RH. The purpose was to study the partitioning of pure biogenic oxidized organic molecules and provide a mechanism to understand the effect of relative humidity.

An increase in the mass of the Secondary Organic Aerosol by 45 and 85% was observed with increasing RH from 10-20% to 60-80% at -30 °C and -10 °C, respectively. These observations were attributed to the increased partitioning of semi-volatile compounds. The experimental results were explained by an aerosol growth model that accounts for kinetic limitations.

Nitrate radicals suppress biogenic new particle formation, Li & Huang, (2022). Submitted to Nature on June 26th, 2022.

Li & Huang showed how nitrate radicals (NO_3) suppress new particle formation in the α-pinene ozonolysis system. They showed three observational pieces of evidence that support this hypothesis: 1) experiments in the CLOUD chamber at CERN, 2) oxidation flow reactor experiments, and 3) direct ambient observations.

For the experiments performed under controlled conditions, they observed that the yield of ULVOCs decreases significantly when NO_3 radicals are present (compared to the experiments with ozone only). Besides, they reported nucleation rates, these quantities have a decreasing tendency when the nitrate radicals are present in the system. With the presence of NO_3 radicals, nitrogen-containing species are formed. These species have higher volatility than the equivalent from alpha-pinene ozonolysis. Thus, nitrate chemistry shifts the volatility distribution to higher volatility species. This impacts directly on their capability of participating in new particle formation. The evidence presented by Li & Huang answers why in the atmosphere is much more often observed new particle formation involving organic vapors during the daytime than during the nighttime.

Appendix II. Additional TD-DMA measurements

We performed experiments in the CLOUD chamber to simulate the formation of iodine oxoacids (HIO_2 and HIO_3) by oxidizing iodine atoms (I_2) in the presence of water and ozone at 5 ºC and 5% relative humidity. In the experiment I, new particles formed and reached sizes with diameter smaller than 100 nm. With the TD-DMA, we collected those particles and evaporated them to detect the chemical composition. Figure A1a shows the thermal desorption profile of the particles collected during the experiment. Most of the HIO_3 signal was observed only in the first heating curve. Therefore, we confirmed that the particles collected contain HIO_3 and the contribution of the background is negligible. Additionally, we conducted NPF experiments with mixtures of I_2, DMS, SO_2 and NH_3 at 5 ºC and 60% RH (Experiment II). Figure A1b displays the desorption profile of the compounds detected. By applying a ~ 2.5 minutes-TD-DMA heating curve, we were able to distinguish between the desorption profiles of Methanesulfonic acid (MSA), Sulfur trioxide (SO_3), Sulfuric acid (SA), and Iodic acid (HIO_3). These compounds were found to contribute importantly to the particle phase. However, it was not possible to quantify them accurately due to the saturation of the reagent ions during detection. The saturation was caused by the high particle load.

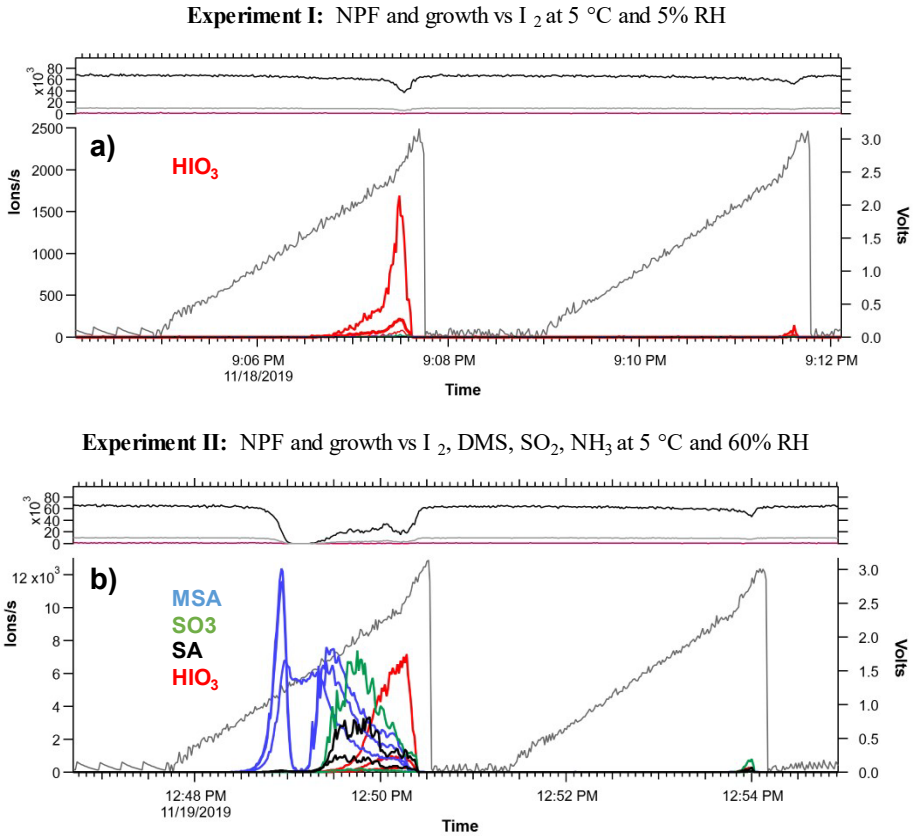

Figure A1. TD-DMA Thermal desorption profiles of the compounds found in the particle-phase during the experiments to simulate marine NPF, (a) Iodic acid (HIO3) and (b) Methanesulfonic acid (MSA), Sulfur trioxide (SO3), Sulfuric acid (SA), and HIO3. The majority of the compounds desorb during the first heating curve, this confirms that those compounds are attributable to the collected compounds.